ADVANCING ENGINEERED ENDOSYMBIONTS AS A PLATFORM TECHNOLOGY FOR THERAPEUTIC MACROPHAGE MODULATION

By

Cody Scott Madsen

A DISSERTATION

Submitted to
Michigan State University
in partial fulfillment of the requirements
for the degree of

Biomedical Engineering–Doctor of Philosophy

2022

ABSTRACT

ADVANCING ENGINEERED ENDOSYMBIONTS AS A PLATFORM TECHNOLOGY FOR THERAPEUTIC MACROPHAGE MODULATION

By

Cody Scott Madsen

This dissertation describes the construction of engineered endosymbionts (EES) as a platform technology for modulating macrophage function for therapeutic applications. Dr. Ashley Makela and I worked closely to advance the EES technology. Dr. Makela focused on the characterization of the EES ability to change macrophage function and I focused on developing the EES technology and working with Dr. Makela on characterization and using the EES in applications (Chapter 2 and 3). In Chapter 2, *Bacillus subtilis* was developed as a chassis organism for EES that escape phagosome destruction, reside in the cytoplasm of mammalian cells, and secrete proteins that are transported to the nucleus to impact host cell response and function. Two synthetic operons encoding either the mammalian transcription factors (TFs) *Stat-1* and *Klf6* or *Klf4* and *Gata-3* were recombined into the genome of *B. subtilis* expressing listeriolysin O (LLO) from *Listeria monocytogenes* and expressed from regulated promoters. Controlled expression of the mammalian proteins from *B. subtilis* LLO in the cytoplasm of J774A.1 macrophage/monocyte cells altered surface marker, cytokine and chemokine expression. Once the EES platform was developed and initially tested *in vitro* with a macrophage cell line, translating the EES to applications became the next step to understand the capacity of the new technology (Chapter 3). For increased translatability, the effect of the engineered *B. subtilis* LLO TF strains on murine bone marrow-derived macrophages (BMDMs) function was characterized. The TF strains shifted BMDM production of cytokines, chemokines and metabolic patterns. RNA-seq is still being analyzed to elucidate effects on gene expression. Furthermore, the ability of the *B. subtilis* LLO TF strains to alter the tumor microenvironment was characterized in a murine 4T1 orthotopic breast cancer model. The *B. subtilis* LLO strains

altered the tumor microenvironment by promoting immune cell invasion, altering the functional metabolism of cells within the tumor, and causing tumor growth stabilization. Additionally, safety of this EES platform was observed as multiple doses at bacterial concentrations 100-fold more than other bacterial therapies were injected without affecting the health of mice. Yet, during the development and characterization of the EES, the sugar (D-mannose) that was used to induce transcription in the EES once inside the host cell was observed to significantly impact macrophage physiology which created additional complexity and was not ideal for *in vivo* applications. Accordingly, Emily Greeson and I worked on developing a mechanism for non-invasive localized control of gene expression *in vivo*. Emily Greeson engineered *B. subtilis* with temperature sensitive repressors (TSRs) and characterized this new genetic switch. I then coated *B. subtilis* with superparamagnetic iron oxide nanoparticles (SPIONs) which could be stimulated by an alternating magnetic field (AMF) to generate thermal energy. Chapter 4 discusses this new approach, and we investigated the ability of magnetic hyperthermia to regulate TSRs of bacterial transcription. The TSR, TlpA39, was derived from a Gram-negative bacterium, and used here for thermal control of reporter gene expression in Gram-positive *B. subtilis. In vitro* heating of *B. subtilis* with TlpA39 controlling bacterial luciferase expression, resulted in a 14.6-fold (12 hour; h) and 1.8-fold (1 h) increase in reporter transcripts with a 9-fold (12 h) and 11.1-fold (1 h) increase in bioluminescence. To develop magnetothermal control, *B. subtilis* cells were coated with three SPION variations which was confirmed by electron microscopy coupled with energy dispersive X-ray spectroscopy. Furthermore, using long duration AMF, we demonstrated magnetothermal induction of the TSRs in SPION-coated *B. subtilis* with a maximum of 4.6-fold increases in bioluminescence. Pairing TSRs with magnetothermal energy using SPIONs for localized heating with AMF can lead to improved EES transcriptional control. The research described in this dissertation demonstrates a multi-disciplinary approach towards developing a new modular technology to alter mammalian cell function with the specific focus on macrophages.

This work is dedicated to those that inspired and supported me to step outside my comfort zone in my career path. Without the support of my family, friends and undergraduate research mentor (Dr. Michaela TerAvest), I would not have pursued and completed this degree.

ACKNOWLEDGEMENTS

Progressing through a doctorate program presents several challenges that can be viewed as opportunities to improve and learn, or as stumbling blocks meant to cause failure at some level. I was raised by both of my parents to take challenges as an opportunity to learn and improve but never be afraid to stumble and fall. Yet, always maintaining the intent to stand once more and learn again. Science will teach a researcher quickly that the main responsibility of research is to learn from challenges and absolutely be prepared to stumble and fall. Without accepting this first lesson from science, completing a dissertation can become an arduous process. I learned this lesson in my undergraduate research and was reminded of this on several occasions throughout my doctorate program. As a result, I implore readers of this dissertation to keep in mind these lessons from not only science but from life to believe in oneself, to always be willing to learn, to accept when failure is a possibility and to always be ready to stand again after one has fallen. I am grateful to those people and experiences that have taught me these important lessons and I look forward to continue learning.

I want to thank Dr. Christopher Contag and the members of the Contag lab that I worked closely with throughout this dissertation. Dr. Ashley Makela and Emily Greeson were instrumental in working on the engineered endosymbiont project and without them this work would have not progressed to the same extent. Dr. Chima Maduka was also a critical component in advancing metabolism studies associated with the project. Victoria Toomajian and Evran Ural were very supportive lab members that helped me think through studies and provide a sense of comic relief and/or distraction when necessary. I also want to thank the many collaborators that were associated with this work and especially thank the Hardy lab from Dr. Jonathan Hardy to the lab members (Dr. Kayla Conner and Dr. Jon Kaletka) in advancing this project through resource and idea sharing. I would like to thank our other collaborators including Dr. Daniel Portnoy for the EES chassis, Dr. Lee Kroos for *B. subtilis* plasmids and Dr. Maryam

Sayadi for being instrumental in RNA-seq analysis. I would also like to thank Dr. Jens Schmidt and Dr. Aitor Aguirre as committee members alongside Dr. Jonathan Hardy that provided invaluable suggestions and guidance throughout the completion of this dissertation.

I would like to thank the staff at MSU Flow Cytometry Core, Center for Advanced Microscopy, Advance Molecular Imaging Facility, Mass Spectrometry and Metabolomics Core and Research Technology Support Facility Genomic Core for providing crucial support in data acquisition and analysis. Additionally, the staff at these facilities provided training that allowed me to develop and advance skill sets for my future career.

Funding for this work came from the James and Kathleen Cornelius Endowment Fund, the MSU College of Engineering Dissertation Completion Fellowship and teaching fellowships from the MSU Department of Microbiology and Molecular Genetics.

Finally, I would like to emphasize my gratefulness to my friends and family. My friends have been a pillar of support throughout the completion of this dissertation. From friends abroad to those in the East Lansing area, I want to sincerely thank all of you for being a part of my support system and an integral part of my life, you know who you are. My family, specifically my brother and my parents, have been very supportive from the time I first entered MSU as a first-generation college student to now completing an eight-year degree. I cannot thank you enough for supporting me even when my decisions and career path was not the typical avenue that have been followed previously in the family. Your support and guidance in my daily life is why this work is dedicated to you.

TABLE OF CONTENTS

LIST OF TABLES

LIST OF FIGURES

KEY TO ABBREVIATIONS

EES	Engineered endosymbionts
BMDM	Bone marrow derived macrophage
CRISPR	Clustered Regularly Interspaced Short Palindromic Repeats
Cas	CRISPR-associated systems
EcN	*Escherichia coli* Nissle 1917
BCG	Bacille Calmette-Guerin
GRAS	Generally recognized as safe
LPS	Lipopolysaccharide
OCR	Oxygen consumption rate
ECAR	Extracellular acidification rate
ATP	Adenosine triphosphate
CFU	Colony forming units
TME	Tumor microenvironment
PCR	Polymerase Chain Reaction
RT-qPCR	Real-time quantitative Polymerase Chain Reaction
DNA	Deoxyribonucleic acid
LLO	Listeriolysin O
TF	Transcription factor
ANOVA	Analysis of Variance
TAM	Tumor associated macrophage
IPTG	Isopropyl β-D-1-thiogalactopyranoside
TSR	Temperature sensitive repressor
MPI	Magnetic particle imaging
MRI	Magnetic resonance imaging
AMF	Alternating magnetic field
SPION	Superparamagnetic iron oxide nanoparticle

CHAPTER 1

INTRODUCTION AND BACKGROUND: ENDOSYMBIONTS, MACROPHAGE PHYSIOLOGY AND SYNTHETIC BIOLOGY

Synthetic biology in human health

Synthetic biology has developed a variety of tools that can be used as and to advance therapeutics in human health applications. Some examples of these tools include genetic circuits such as logic gates/circuits, Clustered Regularly Interspaced Short Palindromic Repeats (CRISPR) and CRISPR-associated systems (Cas) along with nuclease dead Cas (dCas), biological scaffolds with small molecules and *ex vivo* engineered cells (i.e. chimeric antigen receptor T cells)[1–15]. Further, other approaches have encapsulated engineered eukaryotic cells in a semi-permeable membrane that allows proteins and molecules produced by prosthetic networks in the engineered eukaryotic cells to impact tissues and similar approaches with bacteria have been used to impact gut microbiome health through controlled delivery of small molecules and proteins[1,16]. Altogether, these tools were created to manipulate, guide and communicate with target cells towards a desired function. Moreover, while these tools have provided new opportunities to communicate change to cells, nature has provided examples of stable interactions which are controlled by intracellular communication in the form of endosymbionts that can be modeled to improve synthetic biology technologies in guiding cell function.

Endosymbionts and current applications

The endosymbiont theory of the origin of eukaryotic cells postulates that there was a close and long-term biological interaction (symbiosis) between separate single-cell organisms that led to eukaryotic cells and multicellular organisms by the genesis of organelles[17] and is referred to as endosymbiogenesis[18]. Organelles, specifically mitochondria, represent the first endosymbionts that formed as a result of stable interactions with host cells[19–21]. Over time, endosymbionts have developed throughout the entire biosphere from plants to insects to

animals[19,22–27]. Extensive omics approaches have characterized the complexities of these symbiotic relationships revealing the necessity of this interaction for survival of both host and endosymbiont[28–36]. Moreover, these studies have not only led to furthering the understanding of how eukaryotic cells developed and how these symbioses sustain the biosphere but also how symbiotic relationships along with endosymbionts can be used for human health applications[37–41]. The concept of using endosymbionts and symbionts for modifying eukaryotic organisms to improve human health has existed and been utilized in the last decade in insects and nematodes[42–45]. *Wolbachia spp*. is a model endosymbiont that lives symbiotically within mosquitoes and naturally blocks the transmission of dengue and Zika virus by the mosquito species *Aedes aegypti*[46]. Therefore, researchers have been infecting populations of mosquitoes with *Wolbachia spp*. and releasing them into the environment to further prevent transmission of the viruses through mating of the infected populations with the uninfected, further extending the *Wolbachia spp.*-carrying population[46,47]. Various symbionts have been engineered in applications ranging from improving honeybee immunity[48] to enhancing nematode biocontrol of dangerous crop pathogens[49], indirectly improving human health. Furthermore, extensive research has been done on natural endosymbionts in invertebrates and the benefits of the symbiotic relationships between endosymbiont and host which has even revealed clinically relevant compounds produced as a result of this relationship that can be produced into chassis organisms relevant in biomanufacturing[50–56]. Although the concept of endosymbiosis has been examined and utilized previously, only one recent study has investigated mimicking mitochondria by engineering a bacterium to become reliant on the host cell for survival thus creating an artificial endosymbiosis. In this study, *Escherichia coli* was engineered to exist in the cytoplasm of *Saccharomyces cerevisiae* and supply adenosine triphosphate as a replacement for the deficient mitochondria[57]. In return, *S. cerevisiae* produced an essential vitamin for *E. coli* to create a symbiotic relationship. This relationship was stable over several generations of *S.*

cerevisiae[57]. This study revealed that an extracellular bacterium could be engineered to live inside a eukaryotic cell and be used to understand symbiosis.

Bacterial and nanoparticle use in cancer therapy

Precedence exists for using bacteria to impact mammalian cell physiology for therapeutic approaches that are relevant even at the clinical level. Primarily extracellular bacteria-based therapies have been developed to improve human health from improving the gut microbiome[58–61] to treating cancer[62–65]. *Mycobacterium bovis* or Bacille Calmette-Guerin (BCG)[66,67] was originally developed as a tuberculosis vaccine but has now also been approved for bladder cancer treatment, and other clinical applications for bacteria treatment in cancer are being tested[62–65,68–70]. Furthermore, several advancements have been made in improving extracellular bacteria treatment of cancer from tropism to therapeutic delivery[71–74]. *E. coli* Nissle 1917 (EcN) is a probiotic Gram-negative bacterium that has been part of the advancements in extracellular bacterial cancer immunotherapy[75–78]. EcN has been modified to deliver chemotherapeutic drugs and proteins while improving safety as a probiotic[75–79]. Intracellular bacteria have also been used in cancer immunotherapy. Gram-positive intracellular bacterium, *Listeria monocytogenes,* has been used to mobilize the immune system to alter the cancer microenvironment and *Salmonella typhimurium* has been used extensively to disrupt viability of cancer cells along with therapeutic molecule delivery[80–86]. Still, several challenges exist to improve these therapies. Dose tolerance from live bacteria injection especially Gram-negative bacteria, utilizing known pathogens as chassis organisms, and lack of characterized mechanisms of impact on target microenvironment are all challenges that need to be addressed[87–90]. Yet, another approach exists that could be paired with bacteria for the advancement of cancer treatment.

Magnetic nanoparticles have broad applications in biomedicine including imaging, drug delivery, theranostics and therapeutic hyperthermia in cancer[91–93]. Nanoparticles have also been used to study and treat bacterial infections through the coating of bacterial membranes for imaging and as anti-microbial agents[94–100]. Superparamagnetic iron oxide nanoparticles (SPIONs) are useful imaging contrast agents for magnetic resonance imaging (MRI) and more recently in magnetic particle imaging (MPI)[101–106]. MPI detects SPIONs directly, providing a readout of both iron content and location with high specificity and sensitivity[101,107–109]. Further, MPI can guide the application of electromagnetic energy generated by alternating magnetic fields (AMF) to cause local temperature increase known as magnetic hyperthermia[110–112] to precisely heat the iron-containing area which has been used in cancer treatment[113]. The configuration, size and composition of SPIONs have a large effect on MPI performance[114–116] and magnetothermal heating[117]. Synomag-D is a commercially available multi-core “nanoflower” particle[118] and has demonstrated improved MPI performance[119,120] as well as high intrinsic power loss under magnetic hyperthermia[121,122]. Magnetothermal energy using SPIONs for localized heating with AMF as guided by MPI or MRI could be used for new approaches to bacteriotherapy.

The relevance of *B. subtilis* as a chassis organism

B. subtilis is a model Gram-positive, generally recognized as safe (GRAS)[123] organism[124] and is used for industrial protein production with numerous synthetic biology strategies for manipulating gene expression[125,126], global metabolic networks[127] and the entire genome[128–130] making it well-suited for utilizing complex genetic systems even for spatial and temporal regulation[127]. *B. subtilis* has been classically used for secreting complex proteins into the surrounding extracellular space through the general secretory (Sec) and twin-arginine translocation (Tat) pathways which provides a model system to use when secreting proteins[131].

Also, *B. subtilis* has been well characterized to the point of full genome annotation and databases (*e.g.* BsubCyc database) have been developed for metabolism analysis and protein production[132]. *B. subtilis* has been shown to contain multiple inducible systems including several sugar-regulated inducible systems[133]. *B. subtilis* even contains a promoter-regulator inducible system that is sensitive to D-mannose and D-mannose has been shown to be actively transported inside of mammalian cells[134,135]. Yet, other genetic switches are still needed to improve control mechanisms in *B. subtilis*. *B. subtilis* is highly resistant to environmental stressors such as heat with a heat shock response at 48ºC[136]. High heat resistance and well characterized protein production pathways may make *B. subtilis* an ideal chassis organism for thermal energy controlled protein production that could act as therapeutics[137–139]. *B. subtilis* also has multiple characterized inducible systems including several sugar-regulated inducible systems[133]. *B. subtilis* has been well studied for a variety of *in vitro* industry applications in areas such as pharmaceutical/nutraceutical production, recombinant protein production and secretion, and production of functional peptides and oligopeptides[140–143]. However, these inducible systems have limited control for both *in vitro* and *in vivo* applications due to potential host toxicity, cost and carbon-source dependence[144]. Temperature-sensitive repressors (TSRs) are a class of repressors that bind an operator-promoter region with temperature dependence, and show promise for *in vivo* control with local heating for localized delivery[145]. With the addition of thermal energy to the system, a structural change occurs that releases the repressor from DNA resulting in transcription[146]. Thus, TSRs are different from heat shock promoters (HSP) and rely on housekeeping sigma factors such as σA in *B. subtilis*[147,148]. TSRs offer a greater dynamic range than HSP and do not necessitate stress conditions for induction.[145,146] There is precedent for thermal control of *B. subtilis* with induction of gene expression at low and high temperatures in both native and recombinant systems[148–153]. Additionally, TSRs have been shown to be controlled previously in Gram-negative organisms with ultrasound to create localized thermal energy for transcriptional control[79,145].

The role of macrophages in tissue homeostasis

Due to phagocytic immune cells readily internalizing bacteria and demonstrating altered cell fate in response to bacteria, these cells represent a unique target cell type that has been used in bacterial therapy[80,81,154]. The immune system is delicately balanced in mammalian systems, both recognizing self and building tissues, and defending against disease and foreign invaders capable of damage. However, loss of immunological homeostasis (*i.e*. balance) may contribute to disease progression, and this has been largely studied in the context of macrophage function[155,156]. Macrophages are an abundant cell throughout the body, playing important roles in host immunity, tumor progression and modulation of the host response[157–159]. They are commonly recruited by stimuli in response to inflammation and contribute to progression, and therefore, they represent a significant component of the diseased microenvironment and the resulting outcome[155,156]. As a first line of defense, macrophages are phagocytic, acting to take up and destroy foreign invaders or damaged cells[154]. Macrophages are also remarkably plastic with the ability switch phenotypes and alternate between synthesizing proinflammatory or anti-inflammatory signals[160]. Their function is influenced by the microenvironment in which they reside, where they respond to a variety signals and stimuli and these are often co-opted by tumors to create anti-inflammatory microenvironments[154,161]. There are broadly two categories of macrophages, which dictate their function. Pro-inflammatory macrophages (M1) act in a fashion to destroy pathogens, including tumor cells, and anti-inflammatory (M2) macrophages decrease inflammation, support angiogenesis and promote tissue remodeling and repair[162–164]. Each phenotype of macrophages plays an important role in regulating several functions within tissues and treating disease. For example, inflammation is an important hallmark of cancer, and the phenotype of tumor associated macrophages (TAM) is thought to promote tumor growth, metastases and poor outcomes[165]. TAMs are broadly M2 polarized, and interleukin (IL)-10, IL-12p40 and granulocyte colony stimulating factor (G-CSF)

all have been shown to play important roles in impacting the tumor microenvironment through regulation of TAMs[165–167] which could be targeted by cancer immunotherapy. Arthritis represents immune polarization where homeostasis is driven to a pro-inflammatory condition[168]. Modulating macrophages towards the M2 phenotype could reduce inflammation in joints. Downregulation of tumor necrosis factor alpha (TNF-α) and upregulation of IL-10 shows promise for treating damaging inflammatory conditions such as arthritis[168,169]. However, manipulation of immune cells *in vivo* has been characterized by low efficacy and lack of innate control using current mechanisms[170].

Importance of bone marrow derived macrophages as models for *in vivo*

BMDMs[171,172] represent primary antigen presenting cells that signal to other important immune cells and regulate immune response[173,174]. These shifts in population function are distinguished by changes in gene expression, cell surface markers (*i.e.* cluster of differentiation (CD)86; pro-inflammatory or CD206; anti-inflammatory) and expression of cytokines/chemokines[175,176]. Furthermore, metabolism also acts as measure of shifts in BMDM activity and function. Metabolic reprogramming plays an important role in the progression of cancer through mechanisms such as the Warburg effect[177–179]. Immune cells such as BMDMs also experience the Warburg effect and other shifts in metabolism when activated by lipopolysaccharide (LPS) and other pro-inflammatory stimuli[180–187]. Metabolic deviations can be revealed by measuring transitions from oxidative phosphorylation to glycolysis (Warburg effect), changes in oxygen consumption rate (OCR) and extracellular acidification rate (ECAR) and variations in ATP production rate[188–192]. These metabolic shifts occur as a component of the dynamic response of macrophages to specific stimuli thus acting as another readout for macrophage behavior. As a result, BMDMs have been used as models to understand

macrophage importance in many applications including cancer[193–196], chronic inflammation[197,198], drug delivery[170,199], pathogen response[200–202] and tissue regeneration[170,203–205].

Transcription factors are a new option for therapeutic proteins

In the therapies mentioned above, bacteria are used to deliver checkpoint inhibitors, nanobodies, epitopes or even lyse as a way of altering the tumor microenvironment through disruption of tumor cell viability or in an attempt to activate immune cells[71–73,79,81]. These approaches have shown a level of efficacy and continue to be improved. Yet, delivering other types of payloads from bacteria could serve as alternatives or to be paired with current approaches. Due to transcription factors (TFs) regulating the expression of groups of genes to direct cellular fates[206–209]TFs are being used in ongoing clinical trials in new efforts to alter cellular function for therapies in cancer, wound repair, regeneration and immune modulation[210]. However, delivery mechanisms for TFs are limited and in need of new strategies[210]. *Pseudomonas aeruginosa* delivered TFs to induced pluripotent stem cells by a type III secretion system and drove differentiation to cardiomyocytes[211]. Ultimately, this study showed that a pathogenic, extracellular bacterium could deliver TFs that manipulated mammalian cells. Therefore, this study and the endosymbiosis study with *E. coli* mentioned above reveal an opportunity; the combined result of these studies would be stable, non-pathogenic engineered endosymbionts (EES) that can deliver TFs to alter cellular fate. The term EES in this work refers to bacteria that were designed and developed to exist in the cytoplasm of a mammalian cell over an extended period and remain viable.

The construction and application of engineered endosymbionts

B. subtilis expressing listeriolysin O (LLO) from *L. monocytogenes* is an engineered intracellular bacterium of interest which was chosen to be the chassis to develop functional

EES[212]. *B. subtilis* LLO was created previously by engineering *B. subtilis* ZB307 (derivative of *B. subtilis* strain 168)[213], allowing it to escape phagosomes in mammalian cells using the *hlyA* gene encoding for LLO protein under control of an isopropyl β-D-1-thiogalactopyranoside (IPTG) inducible promoter[212]. *B. subtilis* physiology is ideal for an EES as it is a GRAS, non-pathogenic, Gram-positive, soil bacterium that respires as a facultative anaerobe[123,214,215] and does not have a lipopolysaccharide- (LPS) mediated immune response[216]. To demonstrate both cytoplasmic persistence of the EES and host cell fate alteration, phagocytic immune cells[154] provided a useful model. Initially, variations of the EES were delivered to J774A.1 monocyte/macrophages previously because of the characterized mechanism to gain access to the cytoplasm[212], flexibility of using a cell line for optimizing EES interaction with the host cell and testing if TFs can be used to modulate macrophage response when expressed from the EES. Therefore, *B. subtilis* LLO was designed to express and deliver TFs in two operons for modulating macrophage phenotype towards pro- or anti-inflammatory states.

One operon encodes the TFs signal transducer and activator of transcription 1 (STAT-1) and Krüppel-like factor 6 (KLF6) which induce a general response to an inflammatory state in macrophages, and the second encodes Krüppel-like factor 4 (KLF4) and GATA binding protein 3 (GATA-3) which are both characterized to drive an anti-inflammatory response in macrophages[217–221]. Both STAT-1 which is controlled by pro-inflammatory IFN-γ and cytokines and KLF4 which is stimulated by anti-inflammatory cytokine IL-4 are upstream regulators that impact several pathways, while KLF6 and GATA-3 are more specific in regulation, which lends to a dual approach towards driving the desired cell fates[217–221]. The engineered *B. subtilis* LLO strains that expressed these TFs altered patterns of altered patterns of J774A.1 cell surface markers, cytokine and chemokine expression with some patterns of modulation towards anti- or pro-inflammatory phenotypes, indicating that the *B. subtilis* LLO TF expressing strains may be used to direct immune cell function and elucidate mechanisms of macrophage response to

intracellular bacteria. For translatability, EES impact on BMDMs[171,172] was characterized. The strains impacted BMDM gene expression, cytokine/chemokine expression and functional metabolism with some patterns of modulation towards anti- or pro-inflammatory phenotypes with clear indication of complex response to the bacteria and TFs. Furthermore, murine 4T1 orthotopic breast cancer tumor microenvironments[222–224] were altered by the engineered *B. subtilis* LLO strains by promoting immune cell invasion, altering the functional metabolism of cells within the tumor and causing tumor growth stabilization. Additionally, safety of this EES platform was observed as multiple doses at bacterial concentrations 100-fold more than other bacterial therapies were injected without affecting the health of mice. The EES showed promise as a new approach for modulating macrophage function by expressing TFs to be used in bacterial therapy applications and to decipher bacterial impact on tumor microenvironments. Additionally, further measures of controlling the EES both *in vitro* and *in vivo* were advanced. TSRs[145,146] were engineered into *B. subtilis* and were observed to control transcription of the bacterial bioluminescence operon in a temperature responsive manner. Further, pairing the TSRs with magnetic hyperthermia generated by AMF stimulating SPIONs coating *B. subtilis* showed magnetothermal control. These advancements provide an avenue towards the development of noninvasive genetic control mechanism for the EES when being used during *in vivo* applications.

REFERENCES

REFERENCES

1. Cubillos-Ruiz, A. *et al.* Engineering living therapeutics with synthetic biology. *Nat. Rev. Drug Discov.* **20**, 941–960 (2021).

2. Nielsen, A. A. K. *et al.* Genetic circuit design automation. *Science (80-.).* **352**, aac7341 (2016).

3. Doudna, J. A. & Charpentier, E. The new frontier of genome engineering with CRISPR-Cas9. *Science (80-.).* **346**, 1258096 (2014).

4. Tim, W., J., W. J., M., S. D. & S., L. E. Genetic Screens in Human Cells Using the CRISPR-Cas9 System. *Science (80-.).* **343**, 80–84 (2014).

5. Turtle, C. J. *et al.* CD19 CAR–T cells of defined CD4+:CD8+ composition in adult B cell ALL patients. *J. Clin. Invest.* **126**, 2123–2138 (2016).

6. Lee, D. W. *et al.* T cells expressing CD19 chimeric antigen receptors for acute lymphoblastic leukaemia in children and young adults: a phase 1 dose-escalation trial. *Lancet* **385**, 517–528 (2015).

7. Fesnak, A. D., June, C. H. & Levine, B. L. Engineered T cells: the promise and challenges of cancer immunotherapy. *Nat. Rev. Cancer* **16**, 566–581 (2016).

8. Brophy, J. A. N. & Voigt, C. A. Principles of genetic circuit design. *Nat. Methods* **11**, 508–520 (2014).

9. Xu, X. & Qi, L. S. A CRISPR–dCas Toolbox for Genetic Engineering and Synthetic Biology. *J. Mol. Biol.* **431**, 34–47 (2019).

10. Wang, B., Kitney, R. I., Joly, N. & Buck, M. Engineering modular and orthogonal genetic logic gates for robust digital-like synthetic biology. *Nat. Commun.* **2**, 1–9 (2011).

11. Stanton, B. C. *et al.* Genomic mining of prokaryotic repressors for orthogonal logic gates. *Nat. Chem. Biol.* **10**, 99–105 (2014).

12. Tamsir, A., Tabor, J. J. & Voigt, C. A. Robust multicellular computing using genetically encoded NOR gates and chemical ‘wires’. *Nature* **469**, 212–215 (2011).

13. Jones, T. S., Oliveira, S., Myers, C. J., Voigt, C. A. & Densmore, D. Genetic circuit design automation with Cello 2.0. *Nat. Protoc.* **17**, 1097–1113 (2022).

14. Jiang, F. & Doudna, J. A. CRISPR-Cas9 structures and mechanisms. *Annu Rev Biophys* **46**, 505–529 (2017).

15. Ran, F. *et al.* Genome engineering using the CRISPR-Cas9 system. *Nat. Protoc.* **8**, 2281–2308 (2013).

16. Lienert, F., Lohmueller, J. J., Garg, A. & Silver, P. A. Synthetic biology in mammalian cells: Next generation research tools and therapeutics. *Nature Reviews Molecular Cell Biology* (2014) doi:10.1038/nrm3738.

17. Sagan, L. On the origin of mitosing cells. *J. Theor. Biol.* **14**, 225-IN6 (1967).

18. Corsaro, D., Venditti, D., Padula, M. & Valassina, M. Intracellular Life. *Crit. Rev. Microbiol.* **25**, 39–79 (1999).

19. Moya, A., Peretó, J., Gil, R. & Latorre, A. Learning how to live together: Genomic insights into prokaryote-animal symbioses. *Nature Reviews Genetics* (2008) doi:10.1038/nrg2319.

20. Horner, D. S., Hirt, R. P., Kilvington, S., Lloyd, D. G. & Embley, T. M. Molecular data suggest an early acquisition of the mitochondrion endosymbiont. *Proc. R. Soc. London. Ser. B Biol. Sci.* **263**, 1053–1059 (1996).

21. Roger, A. J., Muñoz-Gómez, S. A. & Kamikawa, R. The origin and diversification of mitochondria. *Curr. Biol.* **27**, R1177–R1192 (2017).

22. Bordenstein, S. & Rosengaus, R. B. Discovery of a novel Wolbachia supergroup in Isoptera. *Curr. Microbiol.* **51**, 393–398 (2005).

23. Bordenstein, S. R. & Wernegreen, J. J. Bacteriophage flux in endosymbionts (Wolbachia): infection frequency, lateral transfer, and recombination rates. *Mol. Biol. Evol.* **21**, 1981–1991 (2004).

24. Nowack, E. C. M. & Melkonian, M. Endosymbiotic associations within protists. *Philosophical Transactions of the Royal Society B: Biological Sciences* (2010).

25. Nowack, E. C. M. & Weber, A. P. M. Genomics-informed insights into endosymbiotic organelle evolution in photosynthetic eukaryotes. *Annu. Rev. Plant Biol.* **69**, 51–84 (2018).

26. D Ainsworth, T. *et al.* The coral core microbiome identifies rare bacterial taxa as ubiquitous endosymbionts. *ISME J.* **9**, 2261–2274 (2015).

27. Poole, P., Ramachandran, V. & Terpolilli, J. Rhizobia: from saprophytes to endosymbionts. *Nat. Rev. Microbiol.* **16**, 291–303 (2018).

28. Schmitz-Esser, S., Penz, T., Spang, A. & Horn, M. A bacterial genome in transition - An exceptional enrichment of IS elements but lack of evidence for recent transposition in the symbiont Amoebophilus asiaticus. *BMC Evol. Biol.* (2011).

29. HORN, M. & WAGNER, M. Bacterial Endosymbionts of Free-living Amoebae1. *J. Eukaryot. Microbiol.* **51**, 509–514 (2004).

30. Lo, N., Bandi, C., Watanabe, H., Nalepa, C. & Beninati, T. Evidence for cocladogenesis between diverse dictyopteran lineages and their intracellular endosymbionts. *Mol. Biol. Evol.* **20**, 907–913 (2003).

31. Vigneron, A. *et al.* Insects recycle endosymbionts when the benefit is over. *Curr. Biol.* **24**, 2267–2273 (2014).

32. Łukasik, P., van Asch, M., Guo, H., Ferrari, J. & Charles J. Godfray, H. Unrelated facultative endosymbionts protect aphids against a fungal pathogen. *Ecol. Lett.* **16**, 214–218 (2013).

33. Pruneau, L. *et al.* Understanding Anaplasmataceae pathogenesis using “Omics” approaches. *Front. Cell. Infect. Microbiol.* **4**, 86 (2014).

34. Gabr, A., Grossman, A. R. & Bhattacharya, D. Paulinella, a model for understanding plastid primary endosymbiosis. *J. Phycol.* **56**, 837–843 (2020).

35. Bhattacharya, D., Archibald, J. M., Weber, A. P. M. & Reyes-Prieto, A. How do endosymbionts become organelles? Understanding early events in plastid evolution. *BioEssays* (2007).

36. Méheust, R., Zelzion, E., Bhattacharya, D., Lopez, P. & Bapteste, E. Protein networks identify novel symbiogenetic genes resulting from plastid endosymbiosis. *Proc. Natl. Acad. Sci.* (2016).

37. Boyd, B. M. & Reed, D. L. Taxonomy of lice and their endosymbiotic bacteria in the post-genomic era. *Clin. Microbiol. Infect.* **18**, 324–331 (2012).

38. Zeng, Z. *et al.* Bacterial endosymbiont Cardinium cSfur genome sequence provides insights for understanding the symbiotic relationship in Sogatella furcifera host. *BMC Genomics* **19**, 1–16 (2018).

39. Fan, H.-W. *et al.* Genomic analysis of an ascomycete fungus from the rice planthopper reveals how it adapts to an endosymbiotic lifestyle. *Genome Biol. Evol.* **7**, 2623–2634 (2015).

40. Henriquez, F. L. *et al.* Paradigms of protist/bacteria symbioses affecting human health: Acanthamoeba species and Trichomonas vaginalis. *Front. Microbiol.* **11**, 616213 (2021).

41. Kobayashi, D. Y. & Crouch, J. A. Bacterial/fungal interactions: from pathogens to mutualistic endosymbionts. *Annu. Rev. Phytopathol.* **47**, 63–82 (2009).

42. Elston, K. M. *et al.* Engineering insects from the endosymbiont out. *Trends Microbiol.* **30**, 79–96 (2022).

43. Epis, S. *et al.* Chimeric symbionts expressing a Wolbachia protein stimulate mosquito immunity and inhibit filarial parasite development. *Commun. Biol.* **3**, 1–10 (2020).

44. Wang, S. *et al.* Driving mosquito refractoriness to Plasmodium falciparum with engineered symbiotic bacteria. *Science (80-.).* **357**, 1399–1402 (2017).

45. Durvasula, R. V *et al.* Prevention of insect-borne disease: an approach using transgenic symbiotic bacteria. *Proc. Natl. Acad. Sci.* **94**, 3274–3278 (1997).

46. Jiggins, F. M. The spread of Wolbachia through mosquito populations. *PLoS Biology* (2017).

47. Flores, H. A. & O’Neill, S. L. Controlling vector-borne diseases by releasing modified mosquitoes. *Nat. Rev. Microbiol.* **16**, 508–518 (2018).

48. Leonard, S. P. *et al.* Engineered symbionts activate honeybee immunity and limit pathogens. *Science (80-.).* **367**, 573–576 (2020).

49. Machado, R. A. R. *et al.* Engineering bacterial symbionts of nematodes improves their biocontrol potential to counter the western corn rootworm. *Nat. Biotechnol.* **38**, 600–608 (2020).

50. Xu, T.-T., Chen, J., Jiang, L.-Y. & Qiao, G.-X. Diversity of bacteria associated with Hormaphidinae aphids (Hemiptera: Aphididae). *Insect Sci.* **28**, 165–179 (2021).

51. Ip, J. C.-H. *et al.* Host-Endosymbiont Genome Integration in a Deep-Sea Chemosymbiotic Clam. *Mol. Biol. Evol.* **38**, 502—518 (2021).

52. Yang, K. *et al.* Wolbachia and Spiroplasma could influence bacterial communities of the spider mite Tetranychus truncatus. *Exp. Appl. Acarol.* **83**, 197–210 (2021).

53. Shi, X.-B. *et al.* Aphid endosymbiont facilitates virus transmission by modulating the volatile profile of host plants. *BMC Plant Biol.* **21**, 67 (2021).

54. Chao, L.-L., Castillo, C. T. & Shih, C.-M. Molecular detection and genetic identification of Wolbachia endosymbiont in Rhipicephalus sanguineus (Acari: Ixodidae) ticks of Taiwan. *Exp. Appl. Acarol.* **83**, 115–130 (2021).

55. Izraeli, Y. *et al.* Wolbachia influence on the fitness of Anagyrus vladimiri (Hymenoptera: Encyrtidae), a bio-control agent of mealybugs. *Pest Manag. Sci.* **77**, 1023–1034 (2021).

56. Kennedy, J., Marchesi, J. R. & Dobson, A. D. W. Metagenomic approaches to exploit the biotechnological potential of the microbial consortia of marine sponges. *Applied Microbiology and Biotechnology* (2007).

57. Mehta, A. P. *et al.* Engineering yeast endosymbionts as a step toward the evolution of mitochondria. *Proc. Natl. Acad. Sci. U. S. A.* (2018).

58. Shen, T.-C. D. *et al.* Engineering the gut microbiota to treat hyperammonemia. *J. Clin. Invest.* **125**, 2841–2850 (2015).

59. Sheth, R. U., Cabral, V., Chen, S. P. & Wang, H. H. Manipulating Bacterial Communities by in situ Microbiome Engineering. *Trends Genet.* **32**, 189–200 (2016).

60. Puurunen, M. K. *et al.* Safety and pharmacodynamics of an engineered E. coli Nissle for the treatment of phenylketonuria: a first-in-human phase 1/2a study. *Nat. Metab.* **3**, 1125–1132 (2021).

61. Charbonneau, M. R. *et al.* Development of a mechanistic model to predict synthetic biotic activity in healthy volunteers and patients with phenylketonuria. *Commun. Biol.* **4**, 898 (2021).

62. Sedighi, M. *et al.* Therapeutic bacteria to combat cancer; current advances, challenges, and opportunities. *Cancer Med.* **8**, 3167–3181 (2019).

63. Sawant, S. S., Patil, S. M., Gupta, V. & Kunda, N. K. Microbes as Medicines: Harnessing the Power of Bacteria in Advancing Cancer Treatment. *Int. J. Mol. Sci.* **21**, (2020).

64. Yaghoubi, A. *et al.* Bacteriotherapy in Breast Cancer. *Int J Mol Sci* **20**, (2019).

65. Soleimanpour, S., Hasanian, S. M., Avan, A., Yaghoubi, A. & Khazaei, M. Bacteriotherapy in gastrointestinal cancer. *Life Sci* **254**, 117754 (2020).

66. Zhang, Z. H., Yin, L., Zhang, L. L. & Song, J. Efficacy and safety of Bacillus Calmette-Guerin for bladder cancer: A protocol of systematic review. *Med.* **99**, e21930 (2020).

67. Sfakianos, J. P. *et al.* Bacillus Calmette-Guerin (BCG): Its fight against pathogens and cancer. *Urol. Oncol.* **39**, 121–129 (2021).

68. La Mantia, I. *et al.* The role of bacteriotherapy in the prevention of adenoidectomy. *Eur Rev Med Pharmacol Sci* **23**, 44–47 (2019).

69. Andaloro, C., Santagati, M., Stefani, S. & La Mantia, I. Bacteriotherapy with Streptococcus salivarius 24SMB and Streptococcus oralis 89a oral spray for children with recurrent streptococcal pharyngotonsillitis: a randomized placebo-controlled clinical study. *Eur. Arch. oto-rhino-laryngology Off. J. Eur. Fed. Oto-Rhino-Laryngological Soc. Affil. with Ger. Soc. Oto-Rhino-Laryngology - Head Neck Surg.* **276**, 879–887 (2019).

70. Yaghoubi, A. *et al.* Bacteria as a double-action sword in cancer. *Biochim Biophys Acta Rev Cancer* **1874**, 188388 (2020).

71. Chowdhury, S. *et al.* Programmable bacteria induce durable tumor regression and systemic antitumor immunity. *Nat. Med.* **25**, 1057–1063 (2019).

72. Din, M. O. *et al.* Synchronized cycles of bacterial lysis for in vivo delivery. *Nature* **536**, 81–85 (2016).

73. Chien, T. *et al.* Enhancing the tropism of bacteria via genetically programmed biosensors. *Nat. Biomed. Eng.* **6**, 94–104 (2022).

74. Danino, T., Lo, J., Prindle, A., Hasty, J. & Bhatia, S. N. In vivo gene expression dynamics of tumor-targeted bacteria. *ACS Synth. Biol.* **1**, 465–470 (2012).

75. He, L. *et al.* Intestinal probiotics E. coli Nissle 1917 as a targeted vehicle for delivery of p53 and Tum-5 to solid tumors for cancer therapy. *J. Biol. Eng.* **13**, 1–13 (2019).

76. Yu, X., Lin, C., Yu, J., Qi, Q. & Wang, Q. Bioengineered Escherichia coli Nissle 1917 for tumour-targeting therapy. *Microb. Biotechnol.* **13**, 629–636 (2020).

77. Danino, T. *et al.* Programmable probiotics for detection of cancer in urine. *Sci. Transl. Med.* **7**, 289ra84-289ra84 (2015).

78. Zhang, Y. *et al.* Escherichia coli Nissle 1917 targets and restrains mouse B16 melanoma and 4T1 breast tumors through expression of azurin protein. *Appl. Environ. Microbiol.* **78**, 7603–7610 (2012).

79. Abedi, M. H. *et al.* Ultrasound-controllable engineered bacteria for cancer immunotherapy. *Nat. Commun.* **13**, 1–11 (2022).

80. Flickinger, J. C., Rodeck, U. & Snook, A. E. Listeria monocytogenes as a Vector for Cancer Immunotherapy: Current Understanding and Progress. *Vaccines* vol. 6 (2018).

81. Morrow, Z. T., Powers, Z. M. & Sauer, J.-D. Listeria monocytogenes Cancer Vaccines: Bridging Innate and Adaptive Immunity. *Curr. Clin. Microbiol. Reports* **6**, 213–224 (2019).

82. Hayashi, K. *et al.* Cancer metastasis directly eradicated by targeted therapy with a modified Salmonella typhimurium. *J. Cell. Biochem.* **106**, 992–998 (2009).

83. Nagakura, C. *et al.* Efficacy of a genetically modified Salmonella typhimurium in an orthotopic human pancreatic cancer in nude mice. *Anticancer Res.* **29**, 1873–1878 (2009).

84. Liang, K. *et al.* Genetically engineered Salmonella Typhimurium: Recent advances in cancer therapy. *Cancer Lett.* **448**, 168–181 (2019).

85. Nguyen, V. H. *et al.* Genetically engineered Salmonella typhimurium as an imageable therapeutic probe for cancer. *Cancer Res.* **70**, 18–23 (2010).

86. Guo, Y. *et al.* Targeted cancer immunotherapy with genetically engineered oncolytic Salmonella typhimurium. *Cancer Lett.* **469**, 102–110 (2020).

87. Harimoto, T. *et al.* A programmable encapsulation system improves delivery of therapeutic bacteria in mice. *Nat. Biotechnol.* (2022).

88. Toso, J. F. *et al.* Phase I study of the intravenous administration of attenuated Salmonella typhimurium to patients with metastatic melanoma. *J. Clin. Oncol.* **20**, 142–152 (2002).

89. Yelin, I. *et al.* Genomic and epidemiological evidence of bacterial transmission from probiotic capsule to blood in ICU patients. *Nat. Med.* **25**, 1728–1732 (2019).

90. Low, K. B. *et al.* Lipid A mutant Salmonella with suppressed virulence and TNFα induction retain tumor-targeting in vivo. *Nat. Biotechnol.* **17**, 37–41 (1999).

91. Mahmoudi, M., Hofmann, H., Rothen-Rutishauser, B. & Petri-Fink, A. Assessing the in vitro and in vivo toxicity of superparamagnetic iron oxide nanoparticles. *Chem. Rev.* **112**, 2323–2338 (2012).

92. Prijic, S. & Sersa, G. Magnetic nanoparticles as targeted delivery systems in oncology. *Radiol. Oncol.* **45**, 1–16 (2011).

93. Cardoso, V. F. *et al.* Advances in Magnetic Nanoparticles for Biomedical Applications. *Adv. Healthc. Mater.* **7**, (2018).

94. Moore, J. D. *et al.* Time-dependent bacterial transcriptional response to CuO nanoparticles differs from that of Cu 2+ and provides insights into CuO nanoparticle toxicity mechanisms. *Environ. Sci. Nano* **4**, 2321–2335 (2017).

95. Wang, C. *et al.* Combined use of vancomycin-modified Ag-coated magnetic nanoparticles and secondary enhanced nanoparticles for rapid surface-enhanced Raman scattering detection of bacteria. *Int. J. Nanomedicine* **13**, 1159 (2018).

96. Wang, L. *et al.* Bacterial inactivation using silver-coated magnetic nanoparticles as functional antimicrobial agents. *Anal. Chem.* **83**, 8688–8695 (2011).

97. Lee, J.-J. *et al.* Synthetic ligand-coated magnetic nanoparticles for microfluidic bacterial separation from blood. *Nano Lett.* **14**, 1–5 (2014).

98. Guo, N. *et al.* Magnetism and NIR dual-response polypyrrole-coated Fe3O4 nanoparticles for bacteria removal and inactivation. *Mater. Sci. Eng. C* **126**, 112143 (2021).

99. Arakha, M. *et al.* Antimicrobial activity of iron oxide nanoparticle upon modulation of nanoparticle-bacteria interface. *Sci. Rep.* **5**, 1–12 (2015).

100. Slavin, Y. N., Asnis, J., Häfeli, U. O. & Bach, H. Metal nanoparticles: understanding the mechanisms behind antibacterial activity. *J. Nanobiotechnology* **15**, 1–20 (2017).

101. Zheng, B. *et al.* Magnetic particle imaging tracks the long-term fate of in vivo neural cell implants with high image contrast. *Sci. Rep.* **5**, 1–9 (2015).

102. Tay, Z. W. *et al.* Superferromagnetic Nanoparticles Enable Order-of-Magnitude Resolution & Sensitivity Gain in Magnetic Particle Imaging. *Small Methods* 1 (2021).

103. Kratz, H. *et al.* Novel magnetic multicore nanoparticles designed for MPI and other biomedical applications: From synthesis to first in vivo studies. *PLoS One* **13**, e0190214–e0190214 (2018).

104. Casula, M. F. *et al.* Manganese doped-iron oxide nanoparticle clusters and their potential as agents for magnetic resonance imaging and hyperthermia. *Phys. Chem. Chem. Phys.* **18**, 16848–16855 (2016).

105. Makela, A. V *et al.* Magnetic Particle Imaging of Macrophages Associated with Cancer: Filling the Voids Left by Iron-Based Magnetic Resonance Imaging. *Mol. imaging Biol.* (2020).

106. Sehl, O. C., Makela, A. V., Hamilton, A. M. & Foster, P. J. Trimodal Cell Tracking In Vivo: Combining Iron- and Fluorine-Based Magnetic Resonance Imaging with Magnetic Particle Imaging to Monitor the Delivery of Mesenchymal Stem Cells and the Ensuing Inflammation. *Tomogr. (Ann Arbor, Mich.)* **5**, (2019).

107. Borgert, J. *et al.* Fundamentals and applications of magnetic particle imaging. *J. Cardiovasc. Comput. Tomogr.* **6**, 149–153 (2012).

108. Yu, E. Y. *et al.* Magnetic particle imaging: a novel in vivo imaging platform for cancer detection. *Nano Lett.* **17**, 1648–1654 (2017).

109. Ludewig, P. *et al.* Magnetic Particle Imaging for Real-Time Perfusion Imaging in Acute Stroke. *ACS Nano* **11**, 10480–10488 (2017).

110. Alphandéry, E., Chebbi, I., Guyot, F. & Durand-Dubief, M. Use of bacterial magnetosomes in the magnetic hyperthermia treatment of tumours: a review. *Int. J. Hyperth. Off. J. Eur. Soc. Hyperthermic Oncol. North Am. Hyperth. Gr.* **29**, 801–809 (2013).

111. Hergt, R. & Dutz, S. Magnetic particle hyperthermia—biophysical limitations of a visionary tumour therapy. *J. Magn. Magn. Mater.* **311**, 187–192 (2007).

112. Hergt, R. *et al.* Magnetic properties of bacterial magnetosomes as potential diagnostic and therapeutic tools. *J. Magn. Magn. Mater.* **293**, 80–86 (2005).

113. Tay, Z. W. *et al.* Magnetic Particle Imaging-Guided Heating in Vivo Using Gradient Fields for Arbitrary Localization of Magnetic Hyperthermia Therapy. *ACS Nano* **12**, 3699–3713 (2018).

114. Eberbeck, D., Wiekhorst, F., Wagner, S. & Trahms, L. How the size distribution of magnetic nanoparticles determines their magnetic particle imaging performance. *Appl. Phys. Lett.* **98**, 182502 (2011).

115. Ferguson, R. M., Minard, K. R., Khandhar, A. P. & Krishnan, K. M. Optimizing magnetite nanoparticles for mass sensitivity in magnetic particle imaging. *Med. Phys.* **38**, 1619–1626 (2011).

116. Tomitaka, A. *et al.* Variation of Magnetic Particle Imaging Tracer Performance With Amplitude and Frequency of the Applied Magnetic Field. *IEEE Trans. Magn.* **51**, (2015).

117. Gavilán, H. *et al.* How size, shape and assembly of magnetic nanoparticles give rise to different hyperthermia scenarios. *Nanoscale* **13**, 15631–15646 (2021).

118. Gavilán, H. *et al.* Colloidal Flower-Shaped Iron Oxide Nanoparticles: Synthesis Strategies and Coatings. *Part. Part. Syst. Charact.* **34**, 1700094 (2017).

119. Liu, S. *et al.* Long circulating tracer tailored for magnetic particle imaging. *Nanotheranostics* **5**, 348–361 (2021).

120. Matschegewski, C. *et al.* Biocompatibility of magnetic iron oxide nanoparticles for biomedical applications. *Curr. Dir. Biomed. Eng.* **5**, 573–576 (2019).

121. Bender, P. *et al.* Relating Magnetic Properties and High Hyperthermia Performance of Iron Oxide Nanoflowers. *J. Phys. Chem. C* **122**, 3068–3077 (2018).

122. Ota, S. *et al.* Quantitation method of loss powers using commercial magnetic nanoparticles based on superparamagnetic behavior influenced by anisotropy for hyperthermia. *J. Magn. Magn. Mater.* **538**, 168313 (2021).

123. Elshaghabee, F. M. F., Rokana, N., Gulhane, R. D., Sharma, C. & Panwar, H. Bacillus As Potential Probiotics: Status, Concerns, and Future Perspectives. *Front. Microbiol.* **8**, 1490 (2017).

124. Earl, A. M., Losick, R. & Kolter, R. Ecology and genomics of Bacillus subtilis. *Trends Microbiol.* **16**, 269–275 (2008).

125. Lowary, P. T. & Uhlenbeck, O. C. An RNA mutation that increases the affinity of an RNA–protein interaction. *Nucleic Acids Res.* **15**, 10483–10493 (1987).

126. Radeck, J. *et al.* The Bacillus BioBrick Box: generation and evaluation of essential genetic building blocks for standardized work with Bacillus subtilis. *J. Biol. Eng.* **7**, 29 (2013).

127. Martin, B. J. *et al.* Global Network Reorganization During Dynamic Adaptations of Bacillus subtilis Metabolism. *Science (80-.).* **335**, 1099–1103 (2012).

128. Jakutyte-Giraitiene, L. & Gasiunas, G. Design of a CRISPR-Cas system to increase resistance of Bacillus subtilis to bacteriophage SPP1. *J. Ind. Microbiol. Biotechnol.* **43**, 1183–1188 (2016).

129. Zhang, K., Duan, X. & Wu, J. Multigene disruption in undomesticated Bacillus subtilis ATCC 6051a using the CRISPR/Cas9 system. *Sci. Rep.* **6**, 27943 (2016).

130. Watzlawick, H. & Altenbuchner, J. Multiple integration of the gene ganA into the Bacillus subtilis chromosome for enhanced β-galactosidase production using the CRISPR/Cas9 system. *AMB Express* **9**, 158 (2019).

131. Kolkman, M. A. B. *et al.* The twin-arginine signal peptide of Bacillus subtilis YwbN can direct either Tat- or Sec-dependent secretion of different cargo proteins: Secretion of active subtilisin via the B. subtilis Tat pathway. *Appl. Environ. Microbiol.* (2008).

132. Barbe, V. *et al.* From a consortium sequence to a unified sequence: The Bacillus subtilis 168 reference genome a decade later. *Microbiology* (2009).

133. Vavrová, Ľ., Muchová, K. & Barák, I. Comparison of different Bacillus subtilis expression systems. *Res. Microbiol.* (2010).

134. Sun, T. & Altenbuchner, J. Characterization of a mannose utilization system in bacillus subtilis. *J. Bacteriol.* (2010).

135. Panneerselvam, K. & Freeze, H. H. Mannose enters mammalian cells using a specific transporter that is insensitive to glucose. *J. Biol. Chem.* (1996).

136. Schumann, W. The Bacillus subtilis heat shock stimulon. *Cell Stress Chaperones* **8**, 207–217 (2003).

137. Souza, C. C. de, Guimarães, J. M., Pereira, S. D. S. & Mariúba, L. A. M. The multifunctionality of expression systems in Bacillus subtilis: Emerging devices for the production of recombinant proteins. *Exp. Biol. Med. (Maywood).* **246**, 2443–2453 (2021).

138. Gang, F. *et al.* An operator-based expression toolkit for Bacillus subtilis enables fine-tuning of gene expression and biosynthetic pathway regulation. *Proc. Natl. Acad. Sci.* **119**, e2119980119 (2022).

139. Lam, K. H. E., Chow, K. C. & Wong, W. K. R. Construction of an efficient Bacillus subtilis system for extracellular production of heterologous proteins. *J. Biotechnol.* **63**, 167–177 (1998).

140. Niu, T. *et al.* Engineering a Glucosamine-6-phosphate Responsive glmS Ribozyme Switch Enables Dynamic Control of Metabolic Flux in Bacillus subtilis for Overproduction of N-Acetylglucosamine. *ACS Synth. Biol.* **7**, 2423–2435 (2018).

141. Wenzel, M., Müller, A., Siemann-Herzberg, M. & Altenbuchner, J. Self-inducible Bacillus subtilis expression system for reliable and inexpensive protein production by high-cell-density fermentation. *Appl. Environ. Microbiol.* **77**, 6419–6425 (2011).

142. van Dijl, J. & Hecker, M. Bacillus subtilis: from soil bacterium to super-secreting cell factory. *Microb. Cell Fact.* **12**, 3 (2013).

143. Park, S. A. *et al.* Bacillus subtilis as a robust host for biochemical production utilizing biomass. *Crit. Rev. Biotechnol.* **41**, 827–848 (2021).

144. Seo, S.-O. & Schmidt-Dannert, C. Development of a synthetic cumate-inducible gene expression system for Bacillus. *Appl. Microbiol. Biotechnol.* **103**, 303–313 (2019).

145. Piraner, D. I., Abedi, M. H., Moser, B. A., Lee-Gosselin, A. & Shapiro, M. G. Tunable thermal bioswitches for in vivo control of microbial therapeutics. *Nat. Chem. Biol.* **13**, 75–80 (2017).

146. Piraner, D. I., Wu, Y. & Shapiro, M. G. Modular Thermal Control of Protein Dimerization. *ACS Synth. Biol.* **8**, 2256–2262 (2019).

147. Haldenwang, W. G. The sigma factors of Bacillus subtilis. *Microbiol. Rev.* **59**, 1–30 (1995).

148. D., H. J. *et al.* Global Transcriptional Response of Bacillus subtilis to Heat Shock. *J. Bacteriol.* **183**, 7318–7328 (2001).

149. Li, W. *et al.* Characterization of two temperature-inducible promoters newly isolated from B. subtilis. *Biochem. Biophys. Res. Commun.* **358**, 1148–1153 (2007).

150. Völker, U. *et al.* Cloning and characterization of heat-inducible promoters of Bacillus subtilis. *FEMS Microbiol. Lett.* **106**, 287–293 (1993).

151. Breitling, R., Sorokin, A. V & Behnke, D. Temperature-inducible gene expression in Bacillus subtilis mediated by the c1857-encoded repressor of bacteriophage lambda. *Gene* **93**, 35–40 (1990).

152. Thuy Le, A. T. & Schumann, W. A novel cold-inducible expression system for Bacillus subtilis. *Protein Expr. Purif.* **53**, 264–269 (2007).

153. Budde, I., Steil, L., Scharf, C., Völker, U. & Bremer, E. Adaptation of Bacillus subtilis to growth at low temperature: a combined transcriptomic and proteomic appraisal. *Microbiology* **152**, 831–853 (2006).

154. Epelman, S., Lavine, K. J. & Randolph, G. J. Origin and Functions of Tissue Macrophages. *Immunity* **41**, 21–35 (2014).

155. Kim, Y.-B. *et al.* Programming of macrophages by UV-irradiated apoptotic cancer cells inhibits cancer progression and lung metastasis. *Cell. Mol. Immunol.* **16**, 851–867 (2019).

156. Ginhoux, F. & Guilliams, M. Tissue-Resident Macrophage Ontogeny and Homeostasis. *Immunity* **44**, 439–449 (2016).

157. Wynn, T. A., Chawla, A. & Pollard, J. W. Macrophage biology in development, homeostasis and disease. *Nature* **496**, 445–455 (2013).

158. Chu, Z. *et al.* Primed macrophages directly and specifically reject allografts. *Cell. Mol. Immunol.* **17**, 237–246 (2020).

159. Hume, D. A. Differentiation and heterogeneity in the mononuclear phagocyte system. *Mucosal Immunol.* **1**, 432–441 (2008).

160. Lavin, Y. *et al.* Tissue-Resident Macrophage Enhancer Landscapes Are Shaped by the Local Microenvironment. *Cell* **159**, 1312–1326 (2014).

161. Pawelek, J. *et al.* Co-Opting Macrophage Traits in Cancer Progression: A Consequence of Tumor Cell Fusion? in *Contributions to Microbiology* vol. 13 138–155 (2006).

162. Mosser, D. M. & Edwards, J. P. Exploring the full spectrum of macrophage activation. *Nature Reviews Immunology* (2008).

163. Zhang, X. & Mosser, D. M. Macrophage activation by endogenous danger signals. *Journal of Pathology* (2008).

164. Moreira, A. P. & Hogaboam, C. M. Macrophages in allergic asthma: Fine-tuning their pro- and anti-inflammatory actions for disease resolution. *Journal of Interferon and Cytokine Research* (2011).

165. Laoui, D. *et al.* Tumor-associated macrophages in breast cancer: Distinct subsets, distinct functions. *Int. J. Dev. Biol.* (2011).

166. Karagiannidis, I. *et al.* G-CSF and G-CSFR Induce a Pro-Tumorigenic Macrophage Phenotype to Promote Colon and Pancreas Tumor Growth. *Cancers* vol. 12 (2020).

167. Kanemaru, H. *et al.* Antitumor effect of Batf2 through IL-12 p40 up-regulation in tumor-associated macrophages. *Proc. Natl. Acad. Sci.* **114**, E7331 LP-E7340 (2017).

168. Georgopoulos, S., Plows, D. & Kollias, G. Transmembrane TNF is sufficient to induce localized tissue toxicity and chronic inflammatory arthritis in transgenic mice. *J. Inflamm.* (1996).

169. Iyer, S. S. & Cheng, G. Role of interleukin 10 transcriptional regulation in inflammation and autoimmune disease. *Crit. Rev. Immunol.* **32**, 23–63 (2012).

170. Spiller, K. L. & Koh, T. J. Macrophage-based therapeutic strategies in regenerative medicine. *Adv. Drug Deliv. Rev.* **122**, 74–83 (2017).

171. Gonçalves, R. & Mosser, D. M. The Isolation and Characterization of Murine Macrophages. *Curr. Protoc. Immunol.* **111**, 14.1.1-14.1.16 (2015).

172. Zhang, X., Goncalves, R. & Mosser, D. M. The Isolation and Characterization of Murine Macrophages. *Curr. Protoc. Immunol.* **83**, 14.1.1-14.1.14 (2008).

173. Germic, N., Frangez, Z., Yousefi, S. & Simon, H.-U. Regulation of the innate immune system by autophagy: monocytes, macrophages, dendritic cells and antigen presentation. *Cell Death Differ.* **26**, 715–727 (2019).

174. Frucht, D. M. *et al.* IFN-γ production by antigen-presenting cells: mechanisms emerge. *Trends Immunol.* **22**, 556–560 (2001).

175. Mantovani, A. *et al.* The chemokine system in diverse forms of macrophage activation and polarization. *Trends Immunol.* **25**, 677–686 (2004).

176. Das, A. *et al.* High-Resolution Mapping and Dynamics of the Transcriptome, Transcription Factors, and Transcription Co-Factor Networks in Classically and Alternatively Activated Macrophages. *Front. Immunol.* **9**, 22 (2018).

177. Escoll, P. & Buchrieser, C. Metabolic reprogramming of host cells upon bacterial infection: Why shift to a Warburg-like metabolism? *FEBS J.* **285**, 2146–2160 (2018).

178. Chen, Z., Lu, W., Garcia-Prieto, C. & Huang, P. The Warburg effect and its cancer therapeutic implications. *J. Bioenerg. Biomembr.* **39**, 267–274 (2007).

179. Kim, J. & Dang, C. V. Cancer's molecular sweet tooth and the Warburg effect. *Cancer Res.* **66**, 8927–8930 (2006).

180. Liu, Y. *et al.* Metabolic reprogramming in macrophage responses. *Biomark. Res.* **9**, 1–17 (2021).

181. Liu, D. *et al.* Comprehensive proteomics analysis reveals metabolic reprogramming of tumor-associated macrophages stimulated by the tumor microenvironment. *J. Proteome Res.* **16**, 288–297 (2017).

182. Errea, A. *et al.* Lactate inhibits the pro-inflammatory response and metabolic reprogramming in murine macrophages in a GPR81-independent manner. *PLoS One* **11**, e0163694 (2016).

183. Kelly, B. & O'neill, L. A. Metabolic reprogramming in macrophages and dendritic cells in innate immunity. *Cell Res.* **25**, 771–784 (2015).

184. Galván-Peña, S. & O'Neill, L. A. J. Metabolic reprograming in macrophage polarization. *Front. Immunol.* **5**, 420 (2014).

185. Blagih, J. & Jones, R. G. Polarizing macrophages through reprogramming of glucose metabolism. *Cell Metab.* **15**, 793–795 (2012).

186. Lorenz, M. C., Bender, J. A. & Fink, G. R. Transcriptional response of Candida albicans upon internalization by macrophages. *Eukaryot. Cell* **3**, 1076–1087 (2004).

187. Ip, W. K. E., Hoshi, N., Shouval, D. S., Snapper, S. & Medzhitov, R. Anti-inflammatory effect of IL-10 mediated by metabolic reprogramming of macrophages. *Science (80-.).* **356**, 513–519 (2017).

188. Curi, R. *et al.* A past and present overview of macrophage metabolism and functional outcomes. *Clin. Sci.* **131**, 1329–1342 (2017).

189. Lauterbach, M. A. *et al.* Toll-like receptor signaling rewires macrophage metabolism and promotes histone acetylation via ATP-citrate lyase. *Immunity* **51**, 997–1011 (2019).

190. Pelletier, M., Billingham, L. K., Ramaswamy, M. & Siegel, R. M. Extracellular flux analysis to monitor glycolytic rates and mitochondrial oxygen consumption. in *Methods in enzymology* vol. 542 125–149 (Elsevier, 2014).

191. Tannahill, G. M. *et al.* Succinate is an inflammatory signal that induces IL-1β through HIF-1α. *Nature* **496**, 238–242 (2013).

192. Divakaruni, A. S., Paradyse, A., Ferrick, D. A., Murphy, A. N. & Jastroch, M. Chapter Sixteen - Analysis and Interpretation of Microplate-Based Oxygen Consumption and pH Data. in *Mitochondrial Function* (eds. Murphy, A. N. & Chan, D. C. B. T.-M. in E.) vol. 547 309–354 (Academic Press, 2014).

193. Cho, H. J. *et al.* Bone marrow-derived, alternatively activated macrophages enhance solid tumor growth and lung metastasis of mammary carcinoma cells in a Balb/C mouse orthotopic model. *Breast cancer Res.* **14**, 1–12 (2012).

194. Weiser-Evans, M. C. M. *et al.* Depletion of cytosolic phospholipase A2 in bone marrow–derived macrophages protect against lung cancer progression and metastasis. *Cancer Res.* **69**, 1733–1738 (2009).

195. Redente, E. F. *et al.* Tumor progression stage and anatomical site regulate tumor-associated macrophage and bone marrow-derived monocyte polarization. *Am. J. Pathol.* **176**, 2972–2985 (2010).

196. Pathria, P., Louis, T. L. & Varner, J. A. Targeting Tumor-Associated Macrophages in Cancer. *Trends Immunol.* **40**, 310–327 (2019).

197. Davies, L. C. *et al.* Distinct bone marrow-derived and tissue-resident macrophage lineages proliferate at key stages during inflammation. *Nat. Commun.* **4**, 1–10 (2013).

198. Redente, E. F. *et al.* Differential polarization of alveolar macrophages and bone marrow-derived monocytes following chemically and pathogen-induced chronic lung inflammation. *J. Leukoc. Biol.* **88**, 159–168 (2010).

199. Xia, Y. *et al.* Engineering Macrophages for Cancer Immunotherapy and Drug Delivery. *Adv. Mater.* **32**, 2002054 (2020).

200. Kuhn, M. & Goebel, W. Induction of cytokines in phagocytic mammalian cells infected with virulent and avirulent Listeria strains. *Infect. Immun.* **62**, 348–356 (1994).

201. Demuth, A., Goebel, W., Beuscher, H. U. & Kuhn, M. Differential regulation of cytokine and cytokine receptor mRNA expression upon infection of bone marrow-derived macrophages with Listeria monocytogenes. *Infect. Immun.* **64**, 3475–3483 (1996).

202. Fortier, A., Faucher, S. P., Diallo, K. & Gros, P. Global cellular changes induced by Legionella pneumophila infection of bone marrow-derived macrophages. *Immunobiology* **216**, 1274–1285 (2011).

203. Sun, D. *et al.* Bone marrow-derived cell regulation of skeletal muscle regeneration. *FASEB J.* **23**, 382–395 (2009).

204. Gibon, E. *et al.* Aging affects bone marrow macrophage polarization: relevance to bone healing. *Regen. Eng. Transl. Med.* **2**, 98–104 (2016).

205. Das, A. *et al.* Monocyte and macrophage plasticity in tissue repair and regeneration. *Am. J. Pathol.* **185**, 2596–2606 (2015).

206. Tugal, D., Liao, X. & Jain, M. K. Transcriptional control of macrophage polarization. *Arterioscler. Thromb. Vasc. Biol.* (2013) doi:10.1161/ATVBAHA.113.301453.

207. Mitchell, P. J. & Tjian, R. Transcriptional regulation in mammalian cells by sequence-specific DNA binding proteins. *Science (80-.).* **245**, 371–378 (1989).

208. Fleetwood, A. J., Lawrence, T., Hamilton, J. A. & Cook, A. D. Granulocyte-macrophage colony-stimulating factor (CSF) and macrophage CSF-dependent macrophage phenotypes

display differences in cytokine profiles and transcription factor activities: implications for CSF blockade in inflammation. *J. Immunol.* **178**, 5245–5252 (2007).

209. Heinz, S. *et al.* Simple combinations of lineage-determining transcription factors prime cis-regulatory elements required for macrophage and B cell identities. *Mol. Cell* **38**, 576–589 (2010).

210. Rilo-Alvarez, H., Ledo, A. M., Vidal, A. & Garcia-Fuentes, M. Delivery of transcription factors as modulators of cell differentiation. *Drug Deliv. Transl. Res.* **11**, 426–444 (2021).

211. Jin, Y. *et al.* Enhanced differentiation of human pluripotent stem cells into cardiomyocytes by bacteria-mediated transcription factors delivery. *PLoS One* (2018).

212. Bielecki, J., Youngman, P., Connelly, P. & Portnoy, D. A. Bacillus subtilis expressing a haemolysin gene from Listeria monocytogenes can grow in mammalian cells. *Nature* (1990).

213. Zuber, P. & Losick, R. Role of AbrB in Spo0A- and Spo0B-dependent utilization of a sporulation promoter in Bacillus subtilis. *J. Bacteriol.* (1987).

214. Gallegos-Monterrosa, R., Mhatre, E. & Kovács, Á. T. Specific Bacillus subtilis 168 variants form biofilms on nutrient-rich medium. *Microbiol. (United Kingdom)* (2016).

215. Nakano, M. M. & Zuber, P. ANAEROBIC GROWTH OF A “STRICT AEROBE” (BACILLUS SUBTILIS). *Annu. Rev. Microbiol.* **52**, 165–190 (1998).

216. Travassos, L. H. *et al.* Toll-like receptor 2-dependent bacterial sensing does not occur via peptidoglycan recognition. *EMBO Rep.* **5**, 1000–1006 (2004).

217. Li, H., Jiang, T., Li, M. Q., Zheng, X. L. & Zhao, G. J. Transcriptional regulation of macrophages polarization by microRNAs. *Frontiers in Immunology* (2018).

218. Date, D. *et al.* Kruppel-like transcription factor 6 regulates inflammatory macrophage polarization. *J. Biol. Chem.* (2014).

219. Liao, X. *et al.* Krüppel-like factor 4 regulates macrophage polarization. *J. Clin. Invest.* (2011).

220. Yang, M. *et al.* Deficiency of GATA3-Positive Macrophages Improves Cardiac Function Following Myocardial Infarction or Pressure Overload Hypertrophy. *J. Am. Coll. Cardiol.* (2018).

221. VanDeusen, J. B. *et al.* STAT-1-mediated repression of monocyte interleukin-10 gene expression in vivo. *Eur. J. Immunol.* **36**, 623–630 (2006).

222. Tao, K., Fang, M., Alroy, J. & Sahagian, G. G. Imagable 4T1 model for the study of late-stage breast cancer. *BMC Cancer* **8**, 228 (2008).

223. Zhang, H. *et al.* Oncolytic adenoviruses synergistically enhance anti-PD-L1 and anti-CTLA-4 immunotherapy by modulating the tumour microenvironment in a 4T1 orthotopic mouse model. *Cancer Gene Ther.* **29**, 456–465 (2022).

224. Perez, G. I. *et al.* In Vitro and In Vivo Analysis of Extracellular Vesicle-Mediated Metastasis Using a Bright, Red-Shifted Bioluminescent Reporter Protein. *Adv. Genet.* **3**, 2100055 (2022).

CHAPTER 2

ENGINEERED ENDOSYMBIONTS THAT ALTER MAMMALIAN CELL SURFACE MARKER, CYTOKINE AND CHEMOKINE EXPRESSION

PUBLICATION NOTICE

The following dissertation chapter describes the construction of engineered endosymbionts as a platform technology to alter mammalian cell protein production by delivering transcription factors to the nuclei of the host cells. I constructed the engineered endosymbionts from a *B. subtilis* chassis, developed methods for characterization and characterized the interaction with the host cells. Dr. Ashley Makela worked jointly with me to develop methods for characterization and characterize effects on the host cells. Emily Greeson supported the construction of the engineered endosymbionts. Both Dr. Jonathan Hardy and Dr. Christopher Contag supervised and aided in the conception and development of the engineered endosymbionts.

The following chapter will be published in “Madsen, C. S., Makela, A. V, Greeson, E. M., Hardy, J. W. & Contag, C. H. Engineered endosymbionts that alter mammalian cell surface marker, cytokine and chemokine expression. *Nature Communications Biology*. *Accepted*. (2022).” and reprint permission was granted for use in this dissertation. This chapter was also published as a preprint in “Madsen, C. S., Makela, A. V, Greeson, E. M., Hardy, J. W. & Contag, C. H. Engineered endosymbionts capable of directing mammalian cell gene expression. *bioRxiv* 2021.10.05.463266 (2021).” and reprint permission is reserved to the authors for use in this dissertation.

ABSTRACT

Developing modular tools that direct mammalian cell function and activity through controlled delivery of essential regulators would improve methods of guiding tissue regeneration, enhancing cellular-based therapeutics and modulating immune responses. To address this challenge, *Bacillus subtilis* was developed as a chassis organism for engineered endosymbionts (EES) that escape phagosome destruction, reside in the cytoplasm of mammalian cells, and secrete proteins that are transported to the nucleus to impact host cell response and function. Two synthetic operons encoding either the mammalian transcription factors *Stat-1* and *Klf6* or *Klf4* and *Gata-3* were recombined into the genome of *B. subtilis* expressing listeriolysin O (LLO) from *Listeria monocytogenes* and expressed from regulated promoters. Controlled expression of the mammalian proteins from *B. subtilis* LLO in the cytoplasm of J774A.1 macrophage/monocyte cells altered surface marker, cytokine and chemokine expression. Modulation of host cell fates displayed some expected patterns towards anti- or pro-inflammatory phenotypes by each of the distinct transcription factor pairs with further demonstration of complex regulation caused by a combination of the EES interaction and transcription factors. Expressing mammalian transcription factors from engineered intracellular *B. subtilis* as engineered endosymbionts comprises a new tool for directing host cell gene expression for therapeutic and research purposes.

INTRODUCTION

The endosymbiont theory of the origin of eukaryotic cells postulates that there was a close and long-term biological interaction (symbiosis) between separate single-cell organisms that led to the genesis of organelles[1]. This process can be mimicked in the laboratory, as was demonstrated by engineering *Escherichia coli* to survive within cells of *Saccharomyces cerevisiae*[2]. In addition, bacteria can be engineered to express mammalian transcription factors (TFs) that alter cell fate. Extracellular *Pseudomonas aeruginosa* that deliver TFs via type III secretion into induced pluripotent stem cells (iPSCs) can direct the differentiation of the iPSCs into cardiomyocytes[3]. Together, these studies support the development of non-pathogenic engineered endosymbionts (EES) that persist in the host cell cytoplasm and influence control of mammalian gene expression. The term EES refers to the functional combination of bacteria that remain viable in the cytoplasm of mammalian cells with the engineered production of modulators (proteins, metabolites or nucleic acids) that can redirect host cell biology.

To demonstrate both cytoplasmic persistence of the EES and host cell fate alteration, phagocytic immune cells[4] provide a useful model. Because phagocytic immune cells readily internalize bacteria and demonstrate altered cell fate that is the result of specific TFs, these cells represent a testable system for EES function[4]. The immune response is delicately balanced in mammalian systems, both recognizing self and building tissues and defending against disease and foreign invaders capable of damage. Macrophages are commonly recruited by stimuli in response to inflammation and contribute to progression or suppression of associated pathologies[5], thus representing a significant component of the inflammatory microenvironment[6]. Macrophages may prove to be a key cell for molecular therapies directed at modifying cellular functions, since these cells are present within injured, damaged and malignant tissues and can be modulated to switch phenotypes to alter the disease course[7]. Macrophages are plastic, with the ability to alternate between synthesizing pro-inflammatory or

anti-inflammatory signals[8] and their function is influenced by the microenvironment in which they reside. Pro-inflammatory macrophages (M1) act in a fashion to destroy pathogens, and anti-inflammatory (M2) macrophages decrease inflammation, support angiogenesis and promote tissue remodeling and repair[9,10]. This dichotomy is known as macrophage polarization. Polarized inflammation effector states are distinguished by changes in cell surface markers including, cluster of differentiation (CD)86 for M1 or CD206 for M2, or through differential expression of cytokines and chemokines[11].

Bacillus subtilis expressing listeriolysin O (LLO) from *Listeria monocytogenes* is an engineered intracellular bacterium[12,13]. LLO lyses the phagocytic vacuole, releasing internalized bacteria into the cytosol. The *hlyA* gene encoding LLO was placed under control of an isopropyl β-D-1-thiogalactopyranoside- (IPTG) inducible promoter and inserted into the genome of *B. subtilis*[12,13]. Since *B. subtilis* expressing LLO can access the cytoplasm and does not have a lipopolysaccharide- (LPS) mediated immune response[14], it was chosen as a chassis organism for the development of a cell fate-controlling EES. Additionally, *B. subtilis* is a non-pathogenic, Gram-positive, soil bacterium that respires as a facultative anaerobe making it capable of replicating in the host cell cytoplasm[15]. This bacterium has been classically used for secreting complex proteins into the surrounding extracellular space through the general secretory (Sec) and twin-arginine translocation (Tat) pathways[16]. *B. subtilis* has been well characterized to the point of full genome annotation and databases (*e.g.* BsubCyc database) have been developed for metabolism analysis and protein production[17]. Several sugar-regulated inducible systems[18] including D-mannose, which has been shown to be actively transported inside of mammalian cells, provide additional techniques to regulate EES gene expression[19,20]. *B. subtilis* is an ideal chassis organism for development of an EES.

Bacteria have been developed that impact mammalian cell physiology for therapeutic approaches, bacteriotherapy, and advances in this field support the development of EES for cellular control. Bacille Calmette-Guerin (BCG, the *Mycobacterium bovis* strain used as a

tuberculosis vaccine) bacteriotherapy has become standard of care for bladder cancer, and other clinical applications for bacteriotherapy are being tested[21–27]. Here, the EES can be used to modulate mammalian cell function by expressing engineered operons that encode mammalian TFs that are delivered to the nuclei of mammalian cells (Fig. 2.1, 2.2). Due to TFs regulating the expression of groups of genes to direct cellular fates[28–31], TFs are being used in ongoing clinical trials in new efforts to alter cellular function for therapies in cancer, wound repair, regeneration and immune modulation[32]. However, delivery mechanisms for TFs are limited and in need of new strategies[32]. Therefore, an EES was designed to express and deliver TFs in two operons for modulating macrophage phenotype towards pro- or anti-inflammatory states. One operon encodes the TFs signal transducer and activator of transcription 1 (STAT-1) and Krüppel-like factor 6 (KLF6) which induce a general response to an inflammatory state in macrophages, and the second encodes Krüppel-like factor 4 (KLF4) and GATA binding protein 3 (GATA-3) which are both characterized to drive an anti-inflammatory response in macrophages[33–37]. Both STAT-1 and KLF4 are upstream regulators that impact several pathways, while KLF6 and GATA-3 are more specific in regulation, which lends to a dual approach towards driving the desired cell fates[33–37]. When expressed from intracellular EES these TFs altered patterns of cell surface markers, cytokine and chemokine expression with some patterns of modulation towards anti- or pro-inflammatory phenotypes, indicating that the EES may be used to direct immune cell function and elucidate mechanisms of macrophage response to intracellular bacteria.

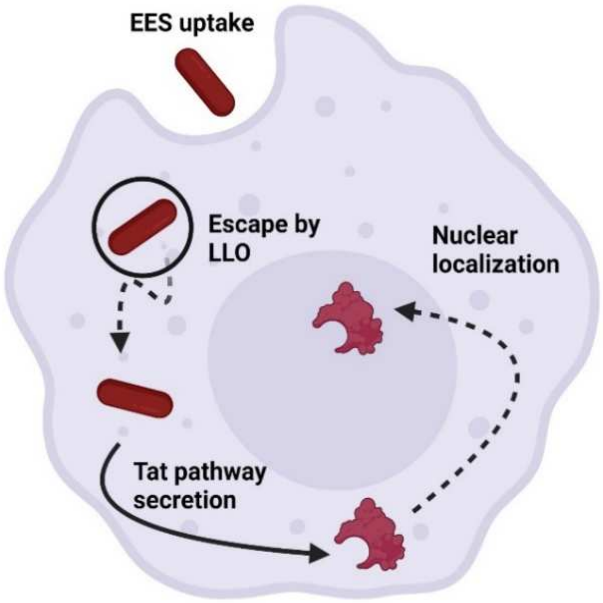

Figure 2.1. EES as a means of controlling gene expression in mammalian host cells

The EES enter phagocytic mammalian host cells and escape the phagosome using the LLO protein. The EES then secrete a reporter protein or transcription factor into the cytoplasm through the Tat pathway followed by localization to the host cell nuclei. Expression of mammalian transcription factors from the EES were shown to direct macrophage function.

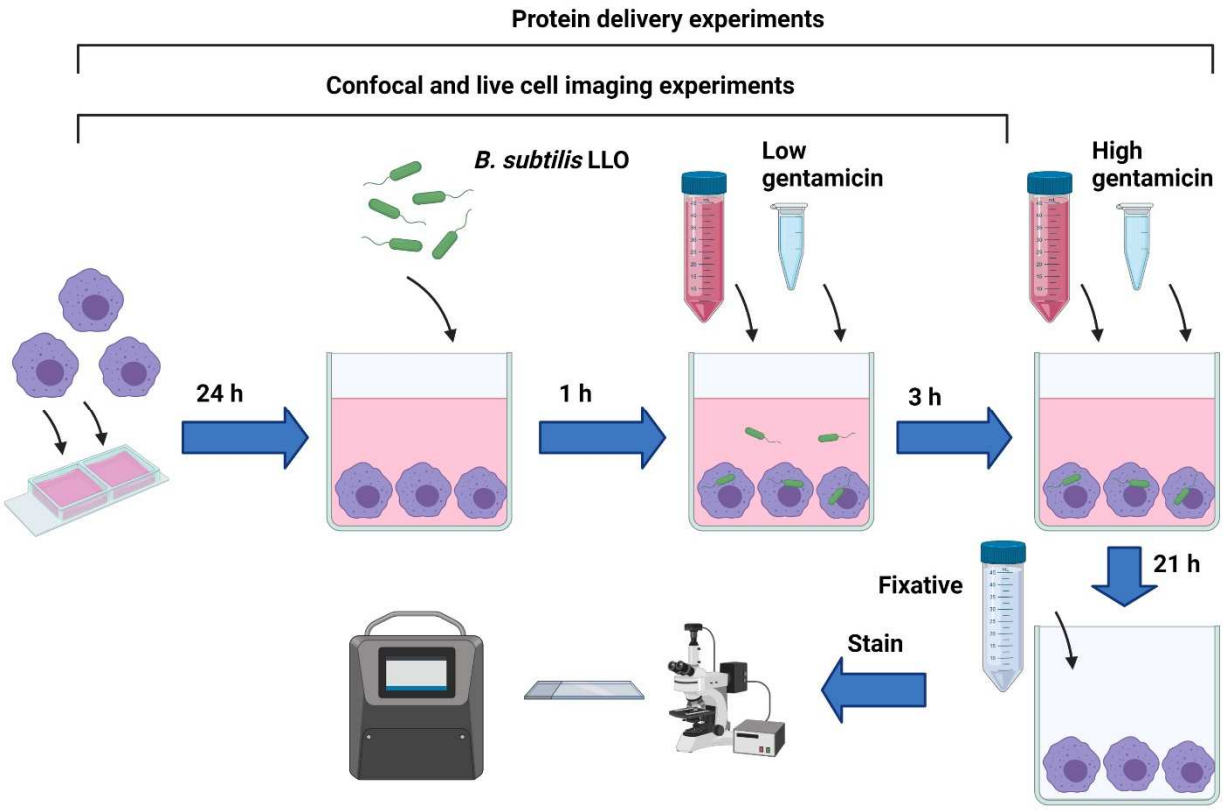

Figure 2.2. Diagram of method to deliver engineered bacteria and analyze interaction with host cells

General approach for co-*incubating B. subtilis* LLO with host J774A.1 cells and timeline for the interaction. EES are allowed to incubate with J774A.1 cells for 1 h with the appropriate inducer depending on condition before a low concentration of gentamicin is added to eliminate extracellular EES. Incubation continues for 3 more hours with a second inducer before a high concentration of gentamicin is used to eliminate intracellular EES. Incubation is continued for 21 h to determine impact on host cells by imaging or other methods such as flow cytometry and cytokine/chemokine profiling.

RESULTS

B. subtilis LLO escape from phagosomes of J774A.1 cells

Confocal microscopy confirmed the escape of *B. subtilis* LLO from phagosomes after uptake into J774A.1 cells[12]. To further elucidate the mechanism of escape, *B. subtilis* LLO (magenta) localization was compared to LAMP-1[38] positive structures (phagosomes, red) in J774A.1 cells (green) with and without IPTG induction of LLO expression (+IPTG and -IPTG). The LAMP-1 protein is crucial for phagosomal assembly and therefore will reveal when the LLO strain is contained within the phagosomes and when the phagosomes have been disrupted[39]. When LLO expression was induced by IPTG, many of the LLO strain were intact and present throughout the mammalian cells (Fig. 2.3, zoom-dotted line). Z-stack data analysis identified *B. subtilis* LLO throughout the cytoplasm of J774A.1 cells and not associated with LAMP-1 positive structures (Fig. 2.3, zoom-solid line). In contrast, without IPTG induction, few of the LLO strain were observed and many regions of punctate signal within LAMP-1 positive regions were observed (Fig. 2.3, zoom-solid line). Accordingly, the expression of LLO when induced by IPTG allows *B. subtilis* LLO to access the cytoplasm of the host cells.

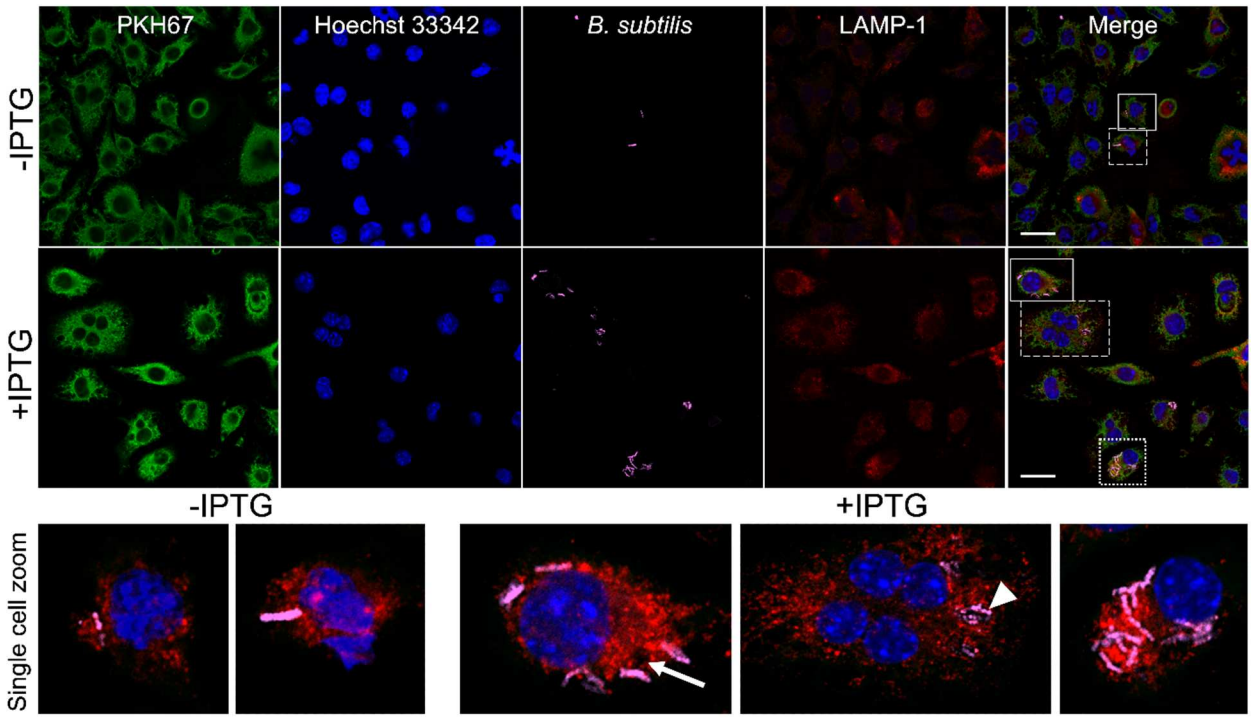

Figure 2.3. Confocal imaging identifies LLO strain phagosomal escape into the cytoplasm of J774A.1 cells

Confocal imaging was used to identify the PKH67 membrane stain (green; J774A.1 cells), nuclear Hoechst 33342 (blue), *B. subtilis* (magenta) and LAMP-1 (red). The LLO strain was introduced to J774A.1 cells at a multiplicity of infection (MOI) of 25:1 and treated without (-IPTG) or with IPTG (+IPTG). Examples of single cells are displayed as zoomed regions with Hoechst 33342, *B. subtilis* and LAMP-1 channels merged (below). Without IPTG, there were few *B. subtilis* positive regions (dashed line), mostly consisting of punctate regions of signal (solid line). When LLO was induced with IPTG (+IPTG), there was evidence of *B. subtilis* LLO escape. Empty LAMP-1 structures could be identified (solid line, white arrow) with adjacent *B. subtilis* LLO. There were also *B. subtilis* LLO which had not yet escaped the phagosome (dashed line, white arrowhead) but the majority of identified *B. subtilis* LLO were within the cytoplasm of the cells (dotted line). The z-depth was chosen for each zoomed image and each channel was adjusted to provide a representative image of each scenario. Scale bars = 20 μm.

Viability of J774A.1 cells and *B. subtilis* LLO replication in the host cell cytoplasm

Host cell viability was assessed after delivery of the LLO strain at different MOI at 2 different time points. At 1 hour (h) post-bacterial addition, there was significant change in host cell viability only at the highest MOI (50:1; Fig. 2.4, left panel). At 4 h post bacterial addition, both the 25:1 and 50:1 MOI conditions revealed significant losses in host cell viability (Fig. 2.4, left panel). The same trend was observed using flow cytometry to assess cell viability (Fig. 2.5). From these results, an MOI of 25:1 was chosen for the LLO strain delivering proteins to the nuclei of host cells. To determine the viability of *B. subtilis* LLO (LLO strain) in the cytoplasm, live cell imaging was performed to image the interaction of the fluorescently stained LLO strain in live J774A.1 cells. With IPTG induction, the LLO strain was observed to replicate in the host cell cytoplasm after phagosomal escape indicating active metabolism and viability (Fig. 2.4, right panel). An increase in the number of bacteria was visualized over time, after co-incubation with a 10:1 MOI. Zoomed regions demonstrate that each bacterium doubled twice during the two time points from 3 bacteria at 1 h to 12 at 2.5 h in this representative instance (Fig. 2.4, two right panels). Additionally, uptake of the LLO strain by the host cell was quantified in multiple conditions. The number of cells containing *B. subtilis* LLO with rod morphology and the number of bacteria per cell were determined (Table 2.1), alongside viability assessments using an MTS assay. At an MOI of 10:1, the doubling trend of the LLO strain was confirmed across the population as seen with the representative instance in Fig. 2.3 (Table 2.1). At each MOI tested, approximately 50% of the added LLO strain entered host cells and at MOIs of 25:1 or 50:1, nearly 100% of the host cells contained the LLO strain (Table 2.1).

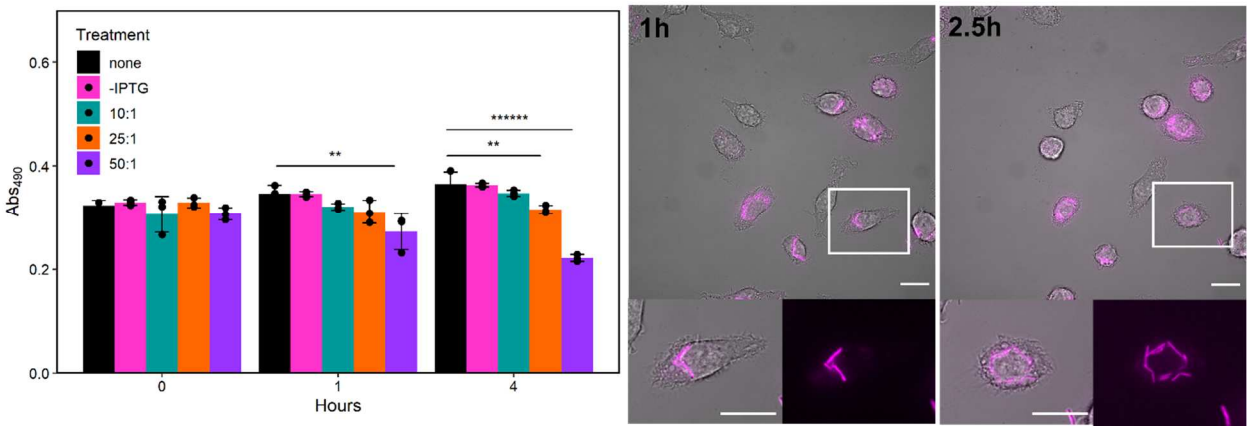

Figure 2.4. Host cell viability and replication of the LLO strain in the cytoplasm of J774A.1 cells

J774A.1 cell viability at multiple time points after treatment with the LLO strain under various conditions (left, MTS assay). Live cell microscopy revealed the LLO strain replicating in a single host cell by comparing images at 1 h and 2.5 h post bacterial addition (right). J774A.1 cells were visualized in brightfield, and the LLO strain using fluorescence (magenta); zoomed images reveal the LLO strain replication in the cytoplasm. Plotted data is mean ± SD from n=3 biological replicates; **p<0.01, ******p<0.000001. Scale bars = 20 μm.

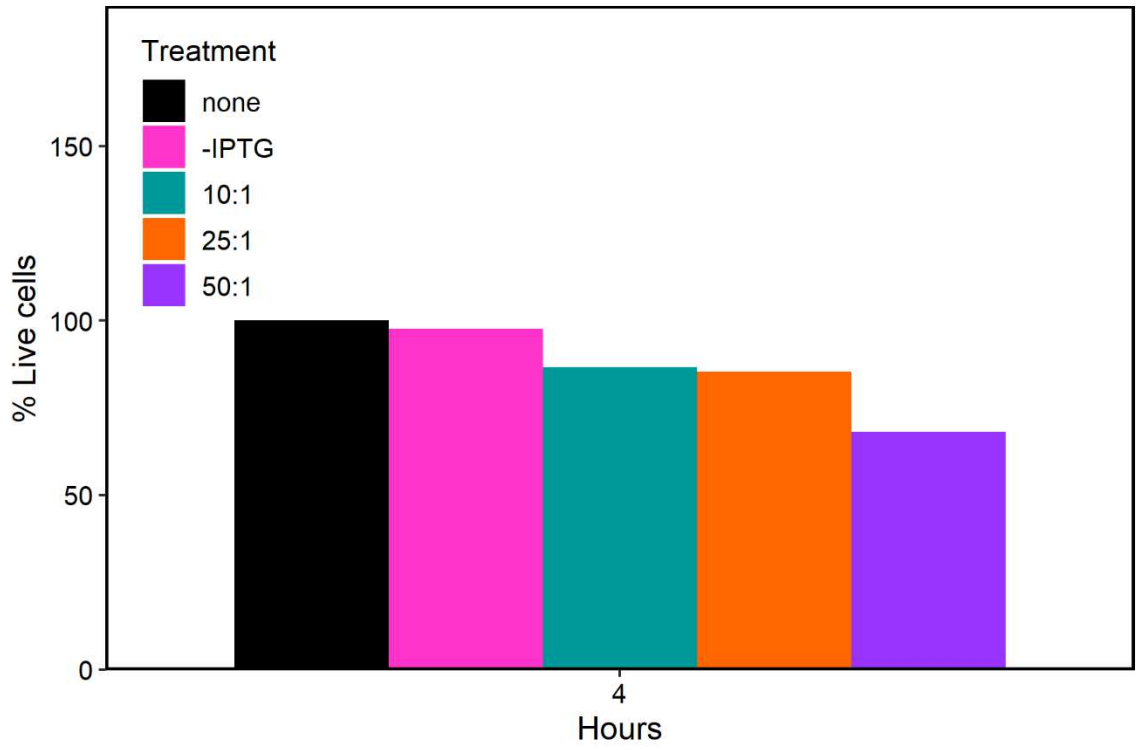

Figure 2.5. Flow cytometry analysis of viable J774A.1 cells

J774A.1 cells were treated with the LLO strain without IPTG (25:1 MOI) and with IPTG at different MOIs for 4 h J774A.1 were analyzed for viability using flow cytometry. Experiment was performed with one biological replicate (n=1) to test for the same trend as the MTS assay. Number of events>20,000 cells.

Table 2.1. Quantification table of LLO strain interaction with J774A.1 cells

Quantification of LLO strain presence within J774A.1 cells using a 25:1 MOI without IPTG, and different MOI with IPTG at 1 and 2 h post LLO-strain addition.

	-IPTG 25:1 MOI 1 h	-IPTG 25:1 MOI 2 h	10:1 MOI 1 h	10:1 MOI 2 h	25:1 MOI 1 h	25:1 MOI 2 h	50:1 MOI 1 h	50:1 MOI 2 h
J774A.1	290	235	452	501	570	500	588	130
LLO strain	4583	2527	2112	4753	6579	5985	14165	2830
LLO strain/J774A.1	15.80	10.75	4.67	9.49	11.54	11.97	24.10	21.77
%J774A.1 containing LLO strain	97.3	99.2	92.4	94.0	98.4	99.8	100	100

Engineered *B. subtilis* LLO secretes β-gal with delivery to the nuclei of J774A.1 cells

Protein secretion from *B. subtilis* LLO was used to further demonstrate bacterial viability within the cytoplasm and as an initial demonstration of protein delivery to the nucleus. *B. subtilis* LLO was engineered to produce and secrete β-galactosidase (β-gal) (strain designated LLO-*lacZ*) through the twin-arginine translocation (Tat) pathway by synthesizing the PhoD signal peptide[40] and the amino acids from 126-132 of the simian virus (SV) 40 nuclear localization signal (NLS)[41]. The production of β-gal by LLO-*lacZ,* with and without a nuclear localization signal (NLS; LLO-*lacZ*-NLS and LLO-*lacZ*-no NLS), was studied with IPTG or mannose control. The mannose-inducible system was amplified from the genome of the *B. subtilis* strain 168[19] to provide a genetic switch to control protein delivery to nucleus specifically. The mannose-inducible system was chosen due to the characterized uptake of this sugar in mammalian cells[20]. Localization of the reporter protein to J774A.1 nuclei was confirmed after coincubation with LLO-*lacZ* and end-point fluorescence microscopy (Fig. 2.6, 2.7). After incubation of

J774A.1 cells with mannose-induced LLO-*lacZ*-NLS (3 h), the nuclear to background fluorescence signal to noise ratio (SNR; Fig. 2.7) was higher than that observed for untreated J774A.1 cells, cells incubated with β-gal protein from supernatant of LLO-*lacZ*-NLS cultures, non-induced LLO-*lacZ*-NLS and LLO-*lacZ*-no NLS (Fig. 2.6). At 3 h, the mannose-inducible system was more efficient than the IPTG-inducible system as indicated by the intensity of fluorescent signals from the nuclei (Figure 2.8), and for this reason was used for the additional studies. Further, the addition of a high concentration of gentamicin (25 μg/mL) at 3 h after induction of β-gal eliminated intracellular bacteria and rescued the J774A.1 cells from overgrowth of the LLO-*lacZ*, allowing for another 21 h of trafficking of protein to the nucleus (Fig. 2.6, lower image panels; Fig. 2.7). Nuclear β-gal SNR of cells exposed to mannose-induced LLO-*lacZ*-NLS for 3 h and then incubated for 21 additional hours (Fig. 2.6) was higher than the controls of J774A.1 cells only (5.1-fold), cells incubated with the supernatant of induced LLO-*lacZ*-NLS, no mannose induction (2-fold) and cells exposed to the LLO-*lacZ*-no NLS strain (1.5-fold; Fig. 2.6). In summary, the mannose-inducible system in the LLO strain was shown to be controlled inside mammalian cells and to provide regulation of secreted proteins that are directed to the J774A.1 nuclei.

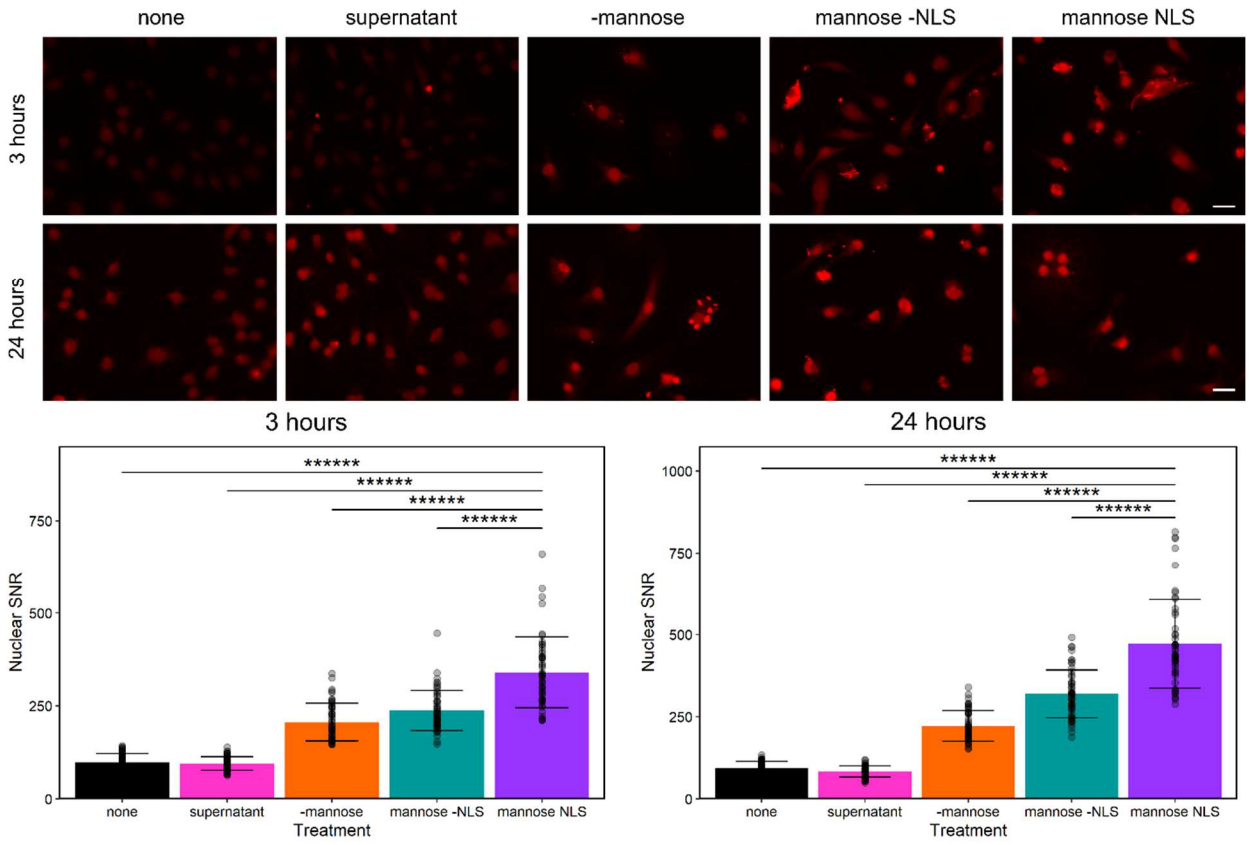

Figure 2.6. Intracellular localization of LLO-*lacZ* secreted β-gal

The presence of β-gal in the nuclei of host cells was determined by measuring fluorescent signals of anti-b-gal in the nuclei compared to background signals as a ratio (SNR). Fluorescence microscopy (top) and SNR (bottom) of the following: J774A.1 cells with no LLO strain (none), J774A.1 cells incubated with β-gal collected as supernatant from induced LLO-*lacZ*-NLS (supernatant), J774A.1 cells incubated with uninduced LLO-*lacZ*-NLS (-mannose), J774A.1 cells incubated with induced LLO-*lacZ*-no NLS (mannose -NLS) and J774A.1 cells incubated with induced LLO-*lacZ*-NLS (mannose NLS). Plotted data is mean ± SD from n=50 random individuals from a representative experiment; ******p<0.000001. Scale bars = 20 μm.

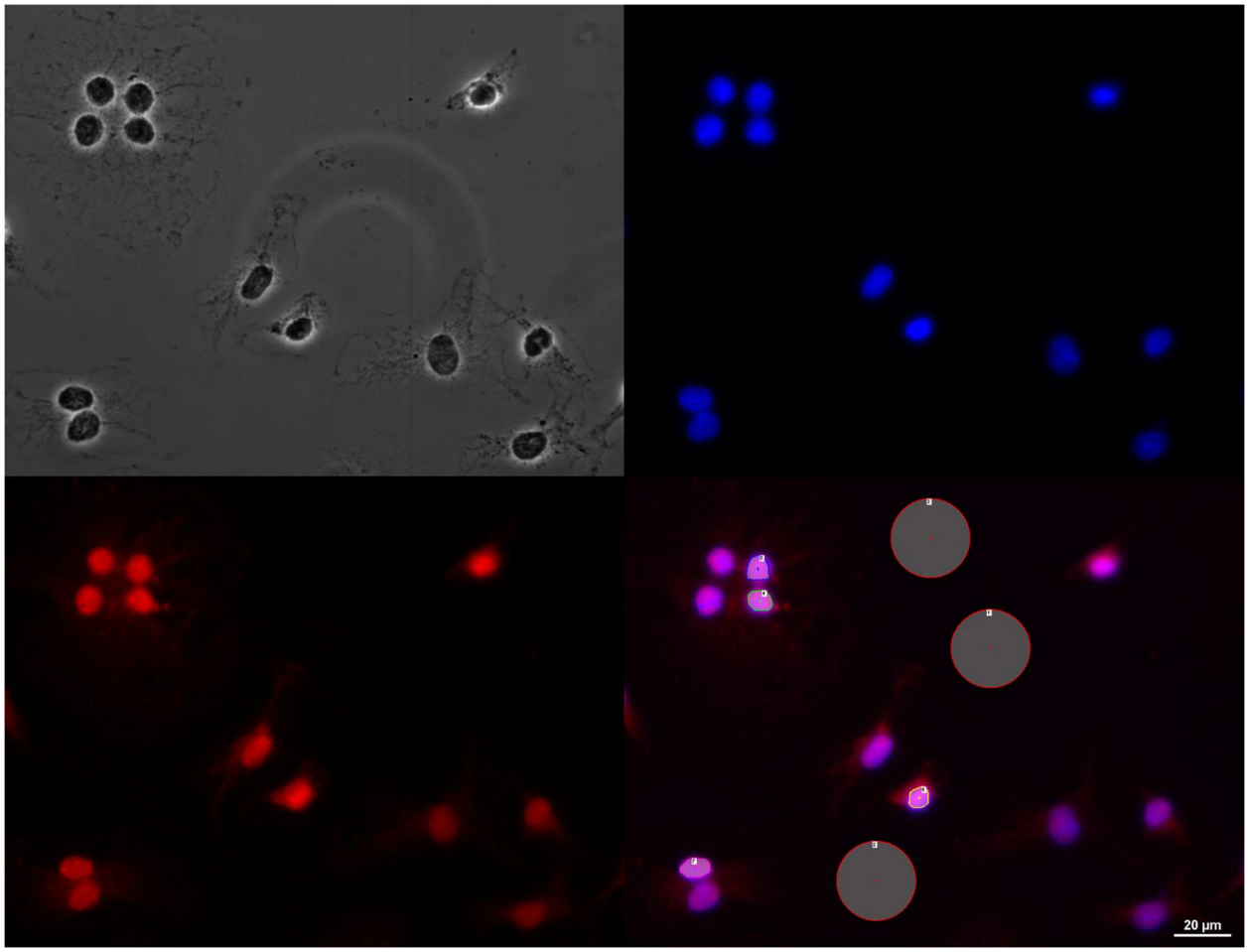

Figure 2.7. Quantification method for calculating SNR

Representative images showing quantification of β-gal fluorescence in nucleus by SNR. Phase contrast (upper left), Hoechst 33342 nuclear stain (upper right), Cy5 secondary antibody for β-gal (lower left) and overlay of Hoechst 3342 and Cy5 (lower right) as panels. Larger circles denoting background signal (noise) and smaller signals drawn around nuclei for quantification to generate SNR (lower right).

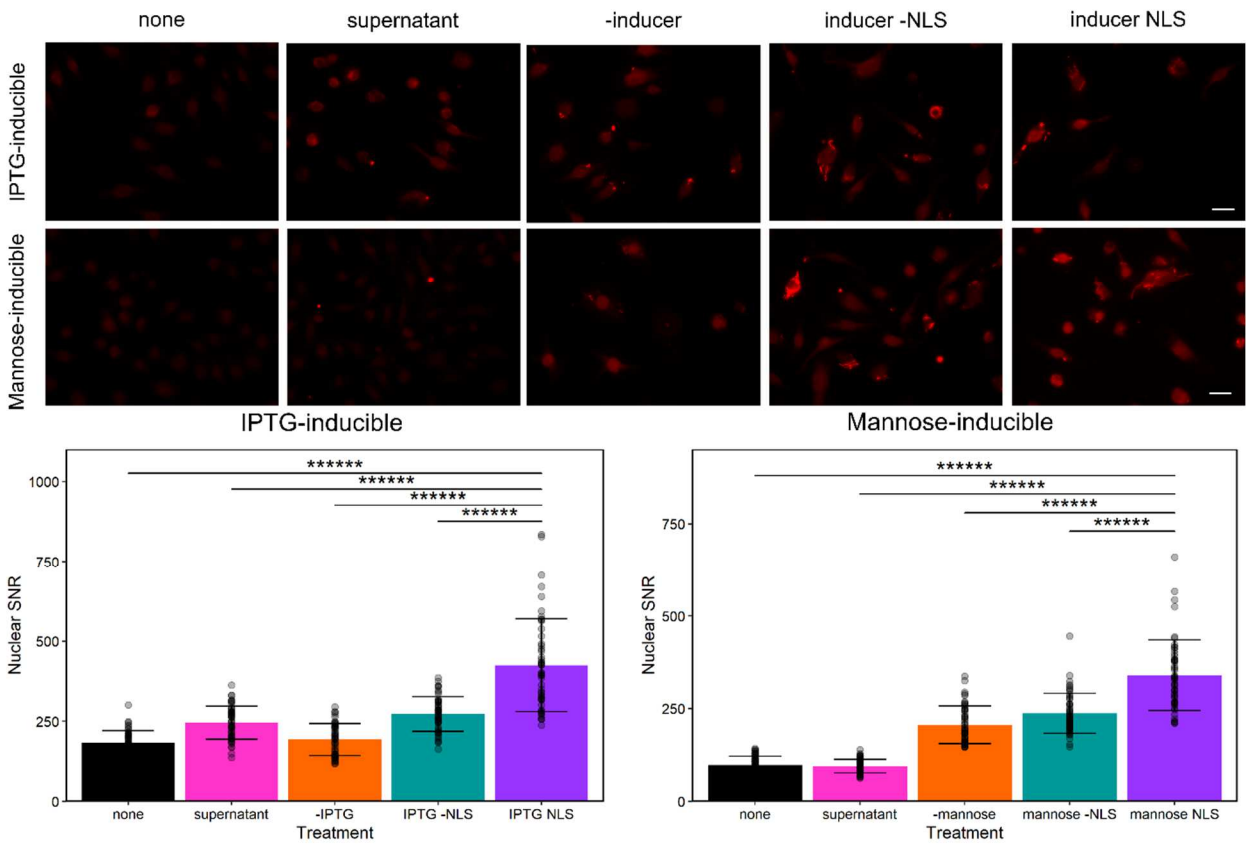

Figure 2.8. Intracellular LLO-*lacZ* secretes β-gal to nuclei of J774A.1 cell using IPTG- and mannose-inducible systems

Fluorescence of nuclei in J774A.1 cells with no LLO strain (none), J774A.1 cells incubated with β-gal collected as supernatant from induced LLO-*lacZ*-NLS (supernatant), J774A.1 cells incubated with uninduced LLO-*lacZ*-NLS (-mannose), J774A.1 cells incubated with induced LLO-*lacZ*-no NLS (mannose -NLS) and J774A.1 cells incubated with induced LLO-*lacZ*-NLS (mannose NLS). Plotted data is mean ± SD from n=50 random individuals from a representative experiment; ******p<0.000001. Scale bars = 20 μm.

Engineered *B. subtilis* LLO transcription factor delivery and modulation of J77A.1 cell marker expression

β-gal delivery by the LLO-*lacZ* strains demonstrated the possibility of an intracellular EES to functionally deliver proteins capable of transcriptional regulation to the nuclei of host cells. Accordingly, TFs were chosen to be delivered by the EES to alter host cell function. The LLO strain was engineered to secrete two distinct pairs of TFs known to impact macrophage function: STAT-1 and KLF6 (LLO-*SK*; pro-inflammatory) or KLF4 and GATA-3 (LLO-*KG*; anti-inflammatory) (Fig. 2.9). Introduction of the TF pairs into the genome of *B. subtilis* LLO minimally impacted bacterial growth rates, did not adversely affect J774A.1 cell viability compared to the LLO strain and did not alter the ability to escape destruction of phagosomes and persist in macrophages (percent cells containing bacteria and distribution of the fluorescence intensity relating to number of bacteria per cell; Fig. 2.10). After staining for protein expression, quantification of fluorescence confirmed production and delivery of STAT-1/KLF6 and KLF4/GATA-3 in cells containing LLO-*SK* or LLO-*KG*, respectively, after 3 h of TF delivery (Fig. 2.11). Quantification of nuclear SNR identified increases in nuclear fluorescence in all four TFs after delivery from the LLO-*SK* or LLO-*KG* strains with and without addition of D-mannose. D-mannose significantly increased delivery of all four TFs. Additionally, the positive controls for STAT-1/KLF6 (LPS and IFN-γ) and KLF4/GATA-3 (IL-4 and IL-13) produced some increase in nuclear SNR but significantly less than the LLO-*SK* and LLO-*KG* strains over the 3 h.

To determine the impact of engineered *B. subtilis* LLO strain TF delivery on J774A.1 modulation, surface marker expression was examined in cells containing various strains (168 strain, LLO strain, LLO-*SK* and LLO-*KG* strains in the presence and absence of mannose) and compared to M0 and M1+/M2+ polarized J774.1 cells at 24 or 48 h post-incubation. As determined by flow cytometry, engineered *B. subtilis* LLO strains expressing TFs exhibited

different patterns of J774A.1 surface marker expression when compared to the LLO strain (Fig. 2.12, 2.13). There was no difference in surface marker expression between *B. subtilis* strain 168 and the LLO strain at any time point. At 24 h post-incubation, a significant decrease in CD206 expression was observed in J774A.1 cells containing LLO-*SK*, with and without the addition of mannose ($p=0.0048$; not shown on plot), compared to the LLO strain. The same trend was observed at 48 h (Fig. 2.12A, C). Conversely, the mean fluorescence intensity (MFI) for CD206 staining was increased by LLO-*KG,* both with and without mannose ($p=0.0599$; not shown on graph), at levels comparable to those of the positive control at 24 h (M2+). However, the elevated levels were not sustained as indicated by the 48 h time point. CD86 expression levels were the same in all bacterial conditions at 24 h in comparison to resting cells with no significant differences in comparison to the M1 control (M1+; Fig. 2.12B, D). At 48 h, the LLO-*SK* strain significantly increased CD86 MFI in comparison to the LLO strain with or without mannose added. The *B. subtilis* 168 strain showed a significant difference in CD86 MFI in comparison to untreated control but not in comparison to the LLO strain. Differences in CD206 and CD86 expression at 24 and 48 h post treatment were analyzed to reveal temporal changes of each treatment (Fig. 2.13). CD206 expression was further increased in M2+ J774A.1 cells, whereas the LLO-*KG* with and without mannose were not able to sustain CD206 expression and showed a decrease at 48 h. CD86 expression was increased at 48 h in cell with the *B. subtilis* strain 168 and LLO-*SK* with, and without, mannose.

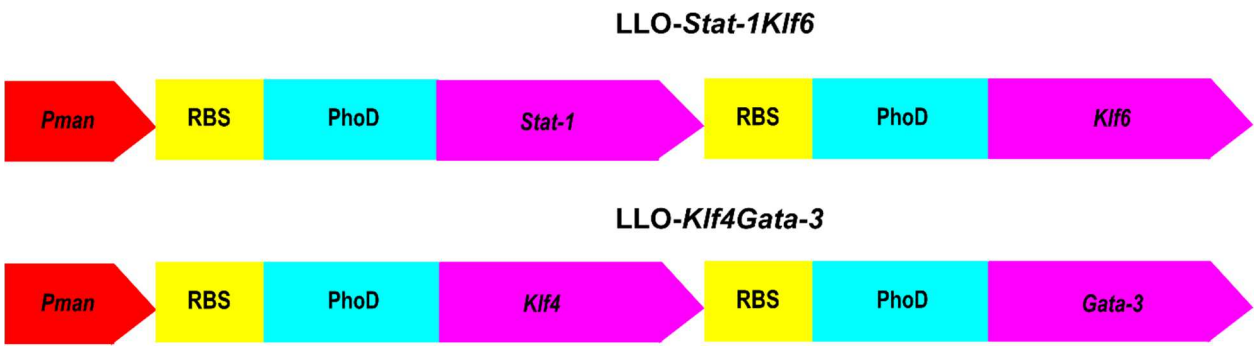

Figure 2.9. Visualization of polarization operons created for EES expression

The operons for polarization were designed to be transcriptionally controlled by the mannose promoter (*Pman*). Then a Gram-positive ribosomal binding site (RBS) and secretion peptide (PhoD) were synthesized in front of each gene in both operons.

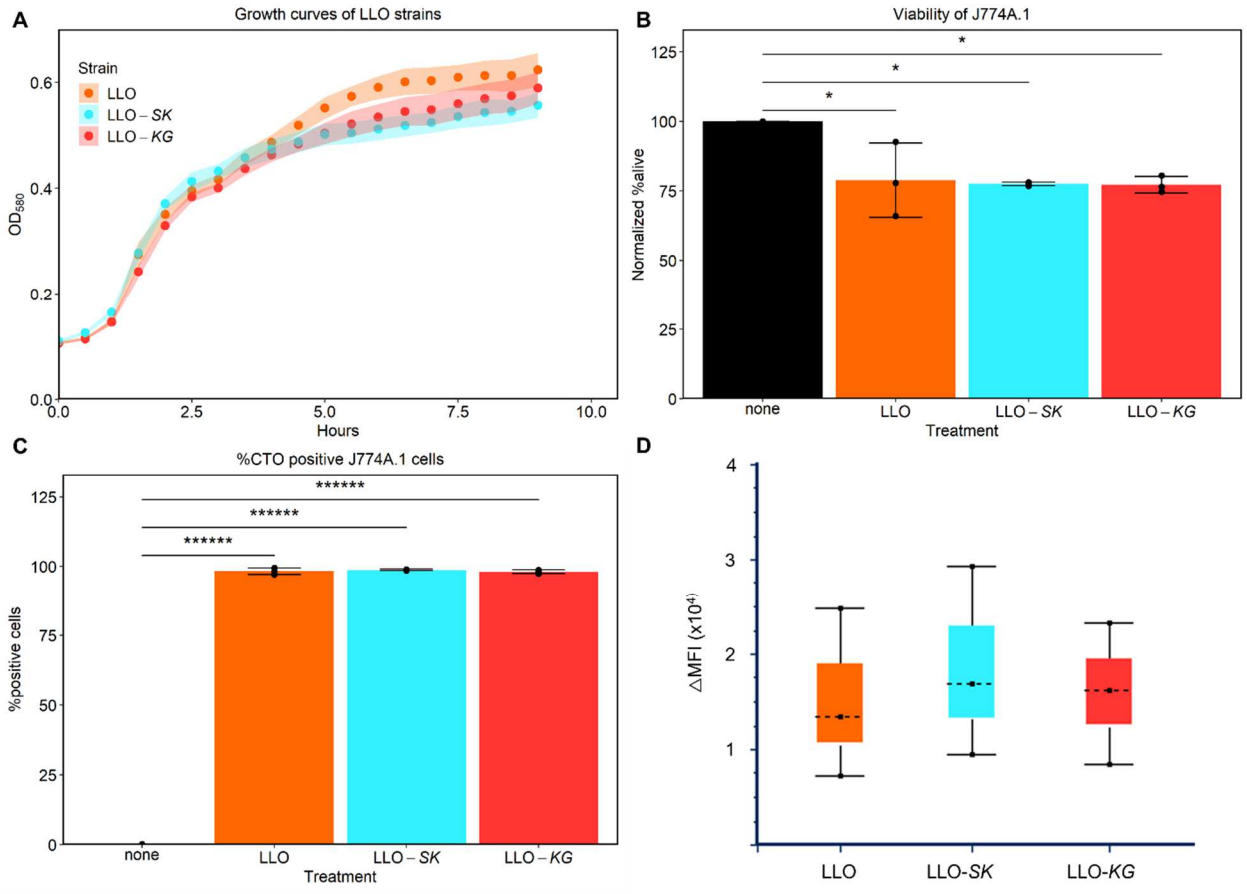

Figure 2.10. Characterization of engineered *B. subtilis* LLO strains activity in growth and interaction with J774A.1 cells

Growth rates of the LLO strain (LLO), LLO-*SK* and LLO- *KG* were evaluated for any differences (A). Flow cytometry was used to identify the strains impact on J774A.1 viability (B, percent viable cells) and ability to escape phagosomal destruction and persist in J774A.1 cells (C, percent cells that are positive for fluorescent LLO strains). Box and whisker plots (D) demonstrate distribution of CTO (CellTracker Orange) positive J774A.1 cells, relating to the presence of fluorescently labeled strains within the cells. ΔMFI represents the change in CTO intensity in the CTO positive population. Data is mean ± SD from either n=3 biological replicate or n=3 biological with n=8 technical for growth curve; *p<0.05, ******p<0.000001.

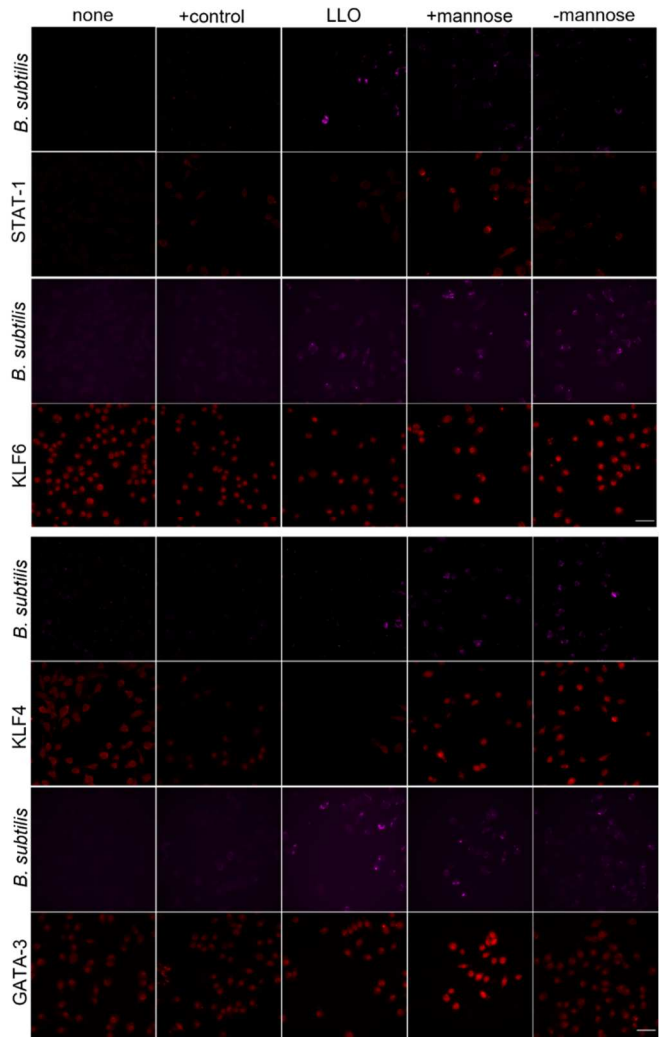

Figure 2.11. Engineered *B. subtilis* LLO production and secretion of mammalian transcription factors

Fluorescence microscopy (top) identifies *B. subtilis* (magenta) and transcription factors (red) in J774A.1 cells treated with nothing (none), positive control (STAT-1/KLF6: LPS and IFN-γ or KLF4/GATA-3: IL-4 and IL-13), LLO strain (LLO), LLO-*SK* or LLO-*KG* not induced (-mannose) or induced (+mannose). Each row dynamic range was scaled to the image with the highest fluorescence intensity to compare conditions. Scale bars=50 μm. Quantification of nuclear fluorescence (bottom) quantified from each transcription factor: STAT-1 (A), KLF6 (B), KLF4 (C) and GATA-3 (D). Plotted data is mean ± SD from n=158.4 +/- 63.6 (SD) random individuals in representative experiment; ******p<0.000001.

Figure 2.11 (cont'd)

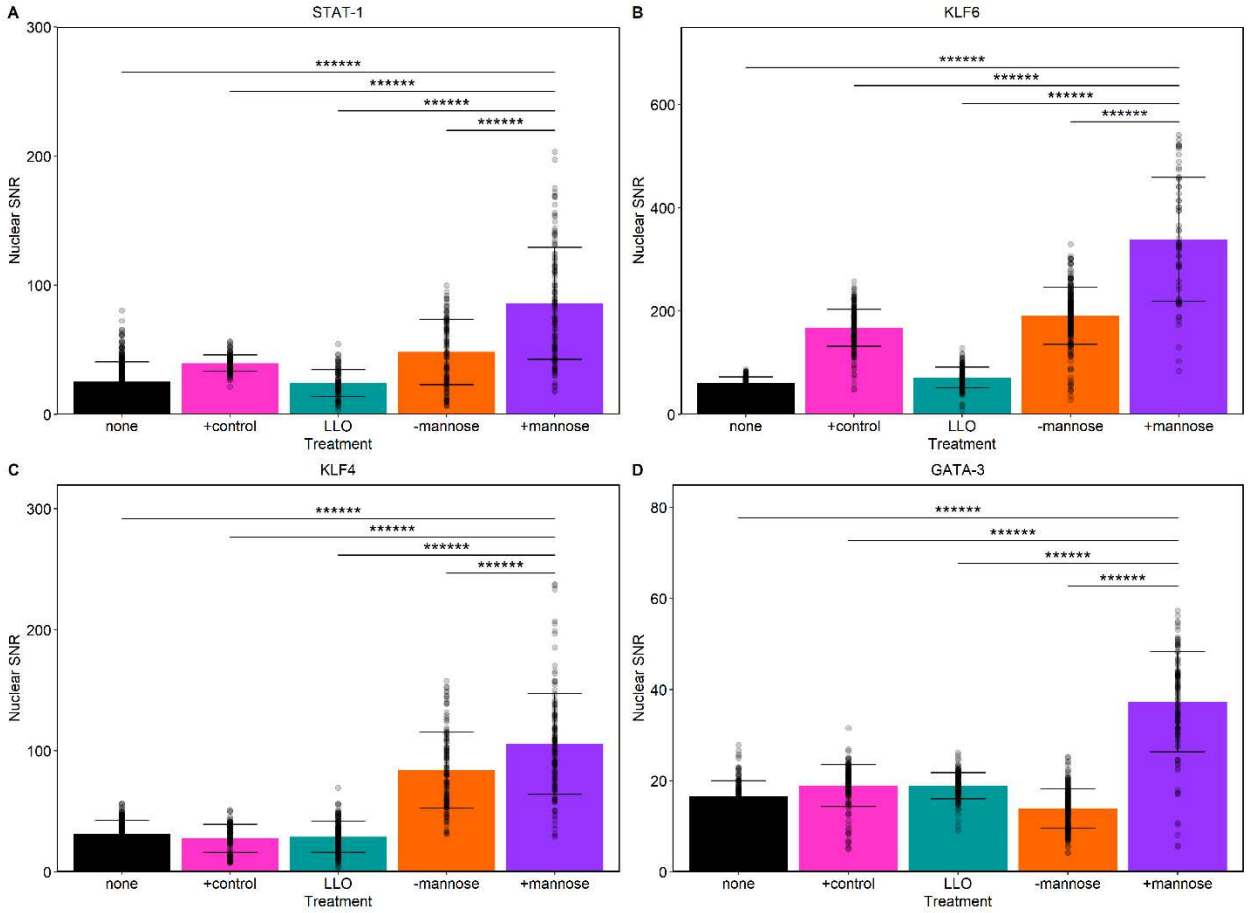

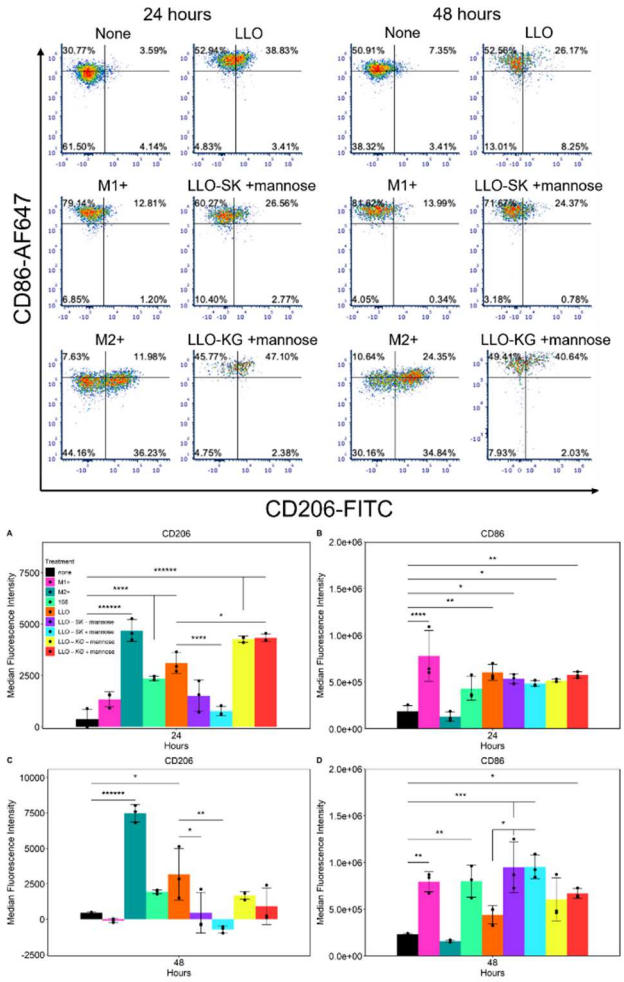

Figure 2.12. Flow cytometry demonstrated TF strain-mediated shifts of J774A.1 cell marker expression

Flow cytometric analysis revealed changes in CD86 and CD206 induced by expression of transcription factors from the EES (top panel). These data are representative examples, taken as the median value of n=3. Average CD86 or CD206 median fluorescence intensity (MFI) is compared among all treatments at each time point (bottom panel, n=3). J774A.1 cells were untreated (none), treated with LPS and IFN-γ (M1+), IL-4 and IL-13 (M2+), *B. subtilis* strain 168 (168), LLO strain (LLO), LLO-*SK* with and without mannose (LLO-*SK* -mannose, LLO-*SK* +mannose) and LLO-*KG* with and without mannose (LLO-*KG* -mannose, LLO-*KG* +mannose) at 24 and 48 h post initial treatment. Plotted data is mean ± SD; *p<0.05, **p<0.01, ***p<0.001, *****p<0.00001.

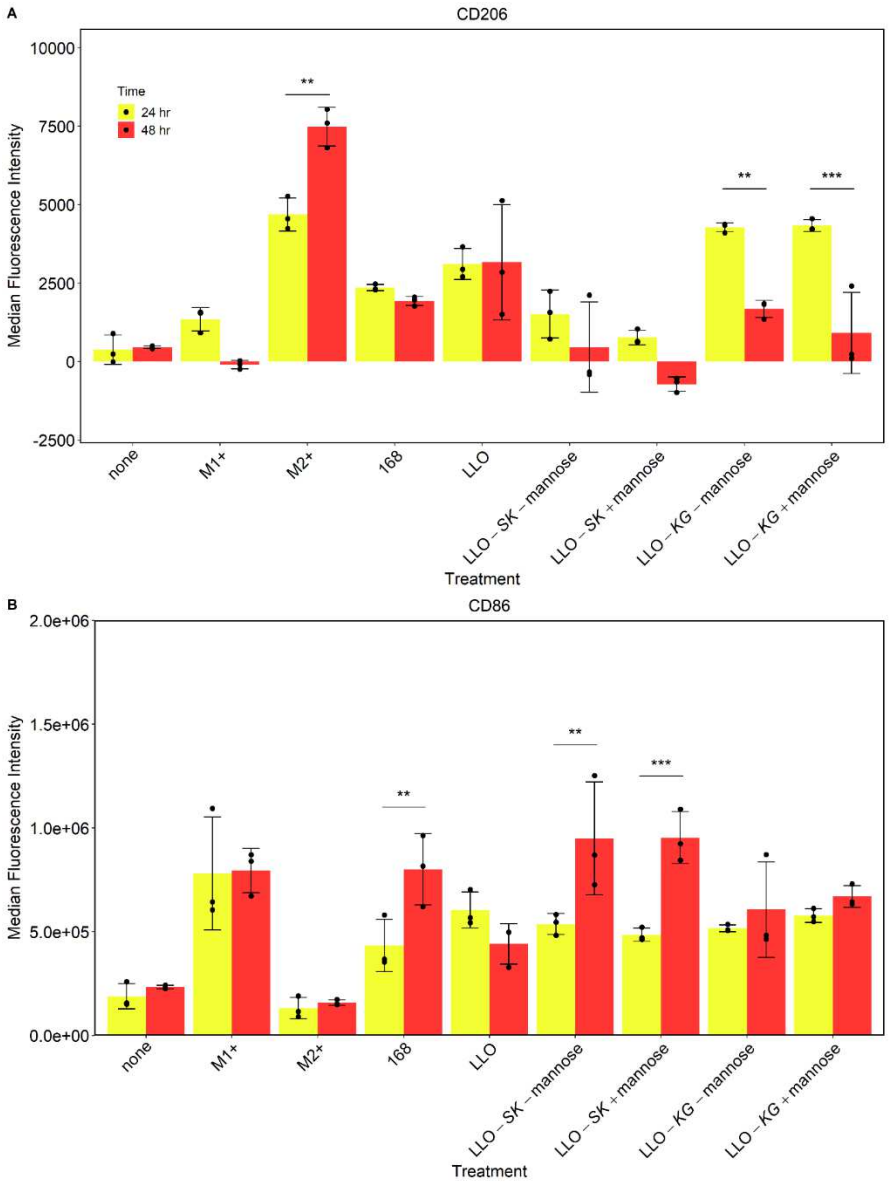

Figure 2.13. Flow cytometry reveals differences in impact of engineered *B. subtilis* LLO strains on J774A.1 cell marker expression between 24 and 48 h time points

Median fluorescence intensity of CD206 (A) and CD86 (B), comparing cell marker expression between 24 and 48 h time points. J774A.1 cells were treated with nothing (none), LPS and IFN-γ (M1+), IL-4 and IL-13 (M2+), LLO strain (LLO), LLO-*SK* with and without mannose (LLO-*SK* -mannose, LLO-*SK* +mannose) and LLO-*KG* with and without mannose (LLO-*KG* -mannose, LLO-*KG* +mannose. Plotted data is mean ± SD from n=3 biological replicates in representative experiment; **p<0.01, ***p<0.001.

Modulation of J77A.1 cell cytokine and chemokine expression using engineered B. subtilis LLO strains

Functional readouts for macrophage polarization and resulting cell fate change include shifts in cytokine and chemokine expression[7,11,42]. Therefore, to characterize the effect of LLO-*SK* and LLO-*KG* on macrophage function, cytokine and chemokines produced by the J774A.1 cells were profiled when treated with the engineered strains relative to the LLO strain. *B. subtilis* strain 168 yielded similar marker expression profiles in comparison to the LLO strain and a Δ*hlyA* mutant (i.e. no LLO expression) of *Listeria monocytogenes* has been shown to either not change cytokine and chemokine profiles in a macrophage cell line, or to change profiles of these proteins equally to the wild-type *L. monocytogenes* in bone marrow derived macrophages[43,44]. Therefore, the 168 strain was not used in further comparisons, because the lack of LLO was not expected to impact J774A.1 profiles. LLO-*SK* and LLO-*KG* were shown to alter J774A.1 cytokine and chemokine expression patterns relative to the LLO strain as well as positive controls (Fig. 2.14, 2.15). Addition of LLO-*SK* and LLO-*KG* strains to J774A.1 cells led to differential expression of cytokines compared to the cytokine profile observed when the LLO strain was used, as shown by levels of interleukin (IL)-10, IL-12p40 and tumor necrosis factor alpha (TNF-α) (Fig. 2.14A-D, 2.15). LLO-*SK* downregulated granulocyte colony stimulating factor (G-CSF) relative to both the LLO strain and LLO-*KG* (Fig. 2.14D-E). Although cytokine production was generally higher at 24 h compared to 48 h post bacterial exposure for most cytokines and chemokines, significant differences were observed at both time points from LLO-*SK* and LLO-*KG* in comparison to the LLO strain, and the M1 and M2 positive controls.

Some of the selected proteins were not impacted by any condition, including vascular endothelial growth factor (VEGF). Several cytokines were only significantly changed at one of the two time points in certain conditions, including IL-6 and macrophage inflammatory protein-2 (MIP-2/CXCL2) (Fig. 2.15F-G, O-P). D-mannose alone altered the relative levels of certain

cytokines including IL-1α and IL-1β; significant results were observed in treatment conditions when D-mannose was added and caused the same impact on certain cytokines (*e.g.* Fig. 2.14F, and Fig. 2.15C-D). Lastly, some cytokines such as eotaxin-1 (CCL11), IFN-γ and leukemia inhibitory factor (LIF) were not detected at any significant level in the J774A.1 cells (not shown). MIP-1α production at 24 h was outside the concentration range of the standards even after dilution (not shown). IL-4 only appeared in the M2+ condition in which it was added. IL-13 exhibited the same trend of minimal expression at 24 h among all treatment conditions other than M2+ (Fig. 2.15H-I). All *B. subtilis* LLO strains caused a significant change in most cytokine levels relative to the resting state and positive controls.

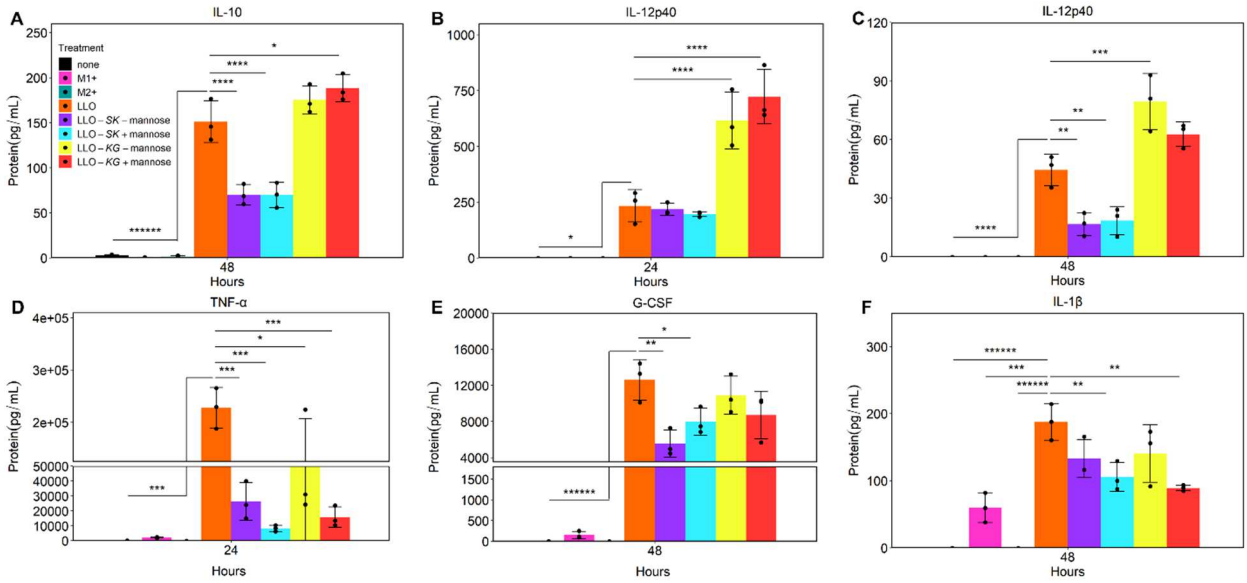

Figure 2.14. TF-expressing strains modulated cytokine and chemokine expression in J774A.1 cells

Cytokine and chemokine protein concentrations were assayed by Luminex in untreated J774A.1 cells (none), and in cells treated with LPS and IFN-γ (M1+), IL-4 and IL-13 (M2+), LLO strain (LLO), LLO-*SK* with and without mannose (LLO-*SK* -mannose, LLO-*SK* +mannose) and LLO-*KG* with and without mannose (LLO-*KG* -mannose, LLO-*KG* +mannose) at 24 and 48 h-post initial treatment. The most prominent protein changes are shown; 14 of the 17 proteins in the panel revealed gene-specific distinctions between the LLO-*SK* and LLO-*KG* strains. Plotted data is mean ± SD from n=3 biological replicates; *p<0.05, **p<0.01, ***p<0.001, ****p<0.0001, ******p<0.000001. Significance shown is comparing LLO treatment to all other treatments.

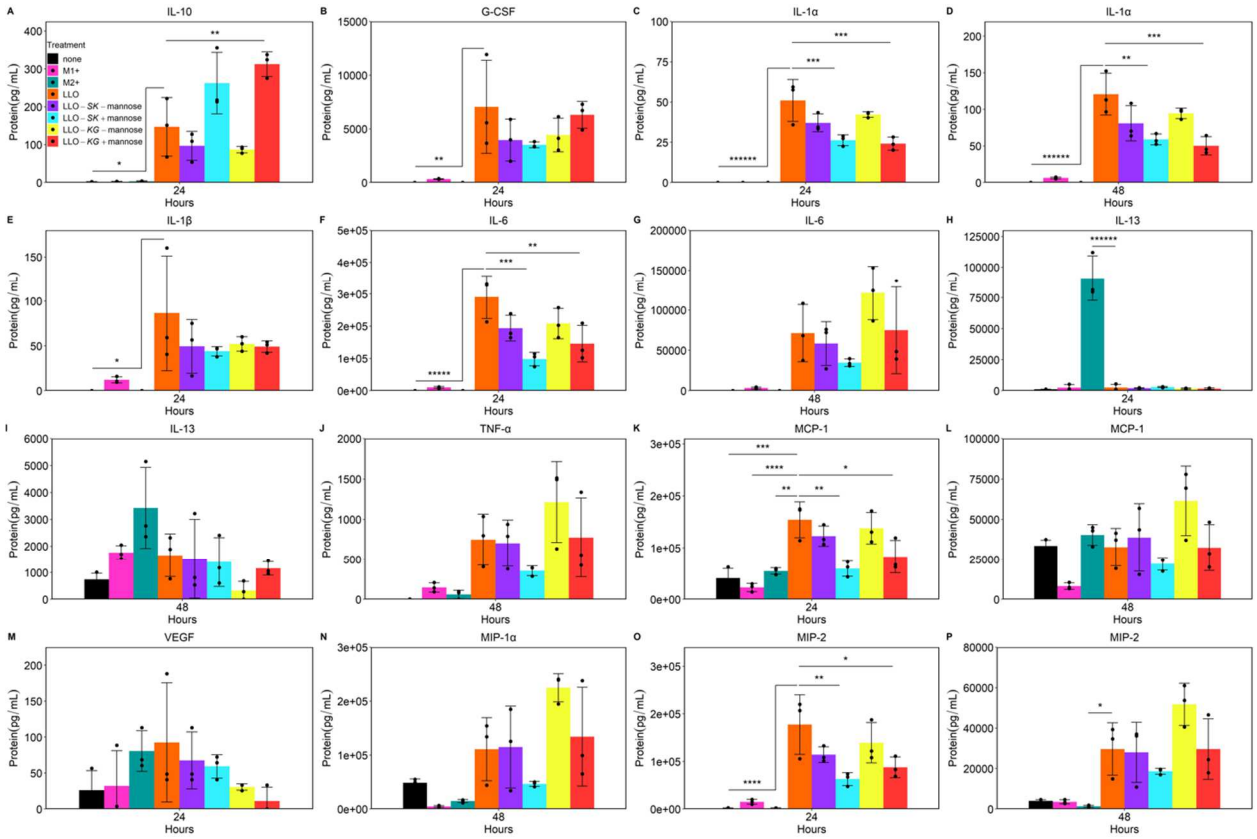

Figure 2.15. Remainder of Luminex cytokine profiling assay characterizing EES impact on J774A.1 cell cytokine and chemokine expression

Cytokine protein concentration was quantified after J774A.1 cells were treated with nothing (none), LPS and IFN-γ (M1+), IL-4 and IL-13 (M2+), LLO strain (LLO), LLO-*SK* with and without mannose (LLO-*SK* -mannose, LLO-*SK* +mannose) and LLO-*KG* with and without mannose (LLO-*KG* -mannose, LLO-*KG* +mannose) at 24 and 48 h post initial treatment. Data is mean ± SD from n=3 biological replicates; *p<0.05, **p<0.01, ***p<0.001, ****p<0.0001, *****p<0.00001, ******p<0.000001. Significance shown is comparing LLO strain condition to all other conditions.

DISCUSSION

For the EES to impact macrophage function, the EES needs to access the cytoplasm by phagosomal escape and remain metabolically active to deliver protein to the host cell cytoplasm, which can then traffic to the nucleus. Induction of LLO expression allowed the LLO strain to maintain its morphology within the cytoplasm of the host cell[38] (Fig. 2.3), indicating escape from phagosome-mediated destruction. After phagosomal escape, the LLO strain was observed to replicate in live J774A.1 cells indicating intracellular viability of the LLO strain (Fig. 2.4 right panel, Table 2.1). Additionally, the J774A.1 cells were found to contain an average of 11 bacteria (the LLO strain) per cell with 99% of cells containing bacteria indicating effective uptake and persistence (Table 2.1). The LLO strain delivering nuclear targeted β-gal protein to the nucleus was further evidence of bacterial and macrophage viability in the co-cultures (Fig. 2.6). The presence of viable LLO strain in the host cells did affect the host cell viability; without regulation of the LLO strain replication, the fate of host cells was eventually cell death, due to bacterial proliferation. This was apparent in 10-12% of J774A.1 cells at the final time point (4 h) with 25:1 MOI (Fig. 2.4 left panel). To address this problem, the cultures were treated with a high concentration of gentamicin (25 μg/mL), above the amount used to kill extracellular bacteria (4 μg/mL), for the purpose of eliminating the intracellular bacteria. To further develop an EES chassis, replication would need to be controlled to optimize the interaction between the EES and host cell. Genetic control of specific component of the EES replication machinery, could be used to control replication while still maintaining protein production; an optimized EES could include a genetic switch controlling an essential gene responsible for initiation of replication[45].

During immune responses, STAT-1 is part of the pro-inflammatory response and is a potent modulator that is directly upregulated by exposure to pro-inflammatory cytokines such as

IFN-γ. This response was shown at 3 h in this study (Fig. 2.11), while KLF6 has been shown to be upregulated in M1 polarized macrophages[33,34,37]. Therefore, these two factors were used in LLO-*SK* to compare to IFN-γ and LPS in driving the pro-inflammatory phenotype. The activity of KLF4 is directly stimulated by the signal cascade in cells treated with the cytokine IL-4 and while this stimulation did not produce significant immunofluorescence at 3 h (Fig. 2.11), this TF has been reported to promote M2 polarization. GATA-3 is also highly upregulated in M2 macrophages[35,36], which is the reason these two TF were used in LLO-*KG* to compare to IL-4 and IL-13 in driving the anti-inflammatory phenotype. Delivery of LLO-*SK* and LLO-*KG* strains to J774A.1 cells produced higher levels of these TFs in the nuclei than levels produced by the known signal cascade inducers (IFN-γ and LPS; IL-4 and IL-13). Accordingly, this result demonstrated the potential of *B. subtilis* LLO to impact host cell function within the 3 h timeframe of interaction between the LLO strains and host cells.

In this study macrophage plasticity was modulated using TFs expressed from the EES. Cell surface markers are commonly used to differentiate M1 and M2 polarization[7,11]. Cell surface expression levels of CD86 and CD206 were altered by the bacterial conditions, and the LLO-*SK* and LLO-*KG* were observed to regulate CD206 (Fig. 2.12) expression as expected based on the known activity of the expressed TFs. At 24 h, CD86 response was more complex as it is expected to be upregulated as a general response to bacteria. However, by 48 h the LLO-*SK* strain had increased expression significantly compared to the LLO strain (Fig. 2.12, 2.13). The *B. subtilis* 168 strain also increased expression between 24 and 48 h but not significantly relative to the LLO strain. The surface protein CD206 has been shown to recognize the surface carbohydrates of pathogens and be triggered by proteases produced by *B. subtilis*[46,47]. This would explain the increase in CD206 expression caused by the *B. subtilis* 168 strain and LLO strain in comparison to the untreated controls. Additionally, while CD86 is regulated directly by inflammatory responses to the engineered *B. subtilis* LLO, the plasticity of the macrophages

could cause CD86 expression to change over time[11]. It has been suggested that products of *B. subtilis* such as sublancin or exopolysaccharide (EPS), or the treatment of macrophages with *B. subtilis* spores can result in either M1 or M2 activation[48]. Even with these complexities, clear changes were observed that indicate that LLO-*SK* and LLO-*KG* impacted surface marker expression in comparison to the LLO strain.

Although changes in cytokine and chemokine expression vary along the spectrum of macrophage polarization, there are well documented cytokines which are used to broadly identify M1 or M2 macrophages[7,11,49]. These identifying cytokines and chemokines are important when studying disease as they provide information on the function and characteristics of macrophage populations[42,50]. The M1 and M2 polarization classifications represent a trend in immune responses but is complex and contains some mixed signals, likely due to bacterial stimulation which can cause these classifications to be incomplete or oversimplified[49,51]. Complexities in macrophage activation, phenotype and plasticity were encountered in this study. In some instances, the LLO-*SK* and LLO-*KG* strains impacted the host cell as predicted in comparison to the LLO strain alone (Fig. 2.14, 2.15). The upregulation of IL-10 by LLO-*KG* and down regulation by LLO-*SK* was an expected result along with G-CSF being downregulated by LLO-*SK*[35,37,52,53]. The LLO strain increased IL-10 and G-CSF which are expected results because IL-10 and G-CSF have been shown to be produced in response to bacteria[53–55]. However, in some cases there were results that were not anticipated, and the pleiotropic effects of each selected TF need to be considered. The change in IL-12p40 levels is an example of an unexpected result based on known signaling cascades. IL-12p40 is known to be produced during inflammatory phenotypes by nuclear factor kappa light chain enhancer of activated B cells (NF-κB)[56]. Therefore, the increase in production of IL-12p40 by LLO-*KG* is unexpected; however, it is possible GATA-3 could affect IL-12p40 production. The IL-12p40 promoter has a canonical GATA binding site but GATA-3 has not been studied with this promoter[56]. The LLO-

SK strain showed some downregulation of IL-12p40 at 48 h which could be due to STAT-1 driving alternative cytokine production such as IL-27p28[56,57]. TNF-α downregulation by LLO-*KG* is another expected result[35] but downregulation by LLO-*SK* in comparison to the LLO strain indicates further complexity and potential pleiotropic effects of STAT-1. This could be due to TNF-α being regulated by NF-κB[58–60]. Furthermore, there may have been metabolic impact on cytokine production due to the addition of D-mannose, which impairs glucose metabolism and is known to suppress the succinate-driven HIF1α activation of IL-1β leading to downregulation of IL-1β[61,62]. Accordingly, results indicated that D-mannose had a significant impact on IL-1β and other cytokines and chemokines, which is an important consideration for future EES studies that rely on sugar-inducible systems. Metabolic reprogramming is most likely playing a significant role in response to the chemical inducer of the engineered *B. subtilis* LLO TF operons and possibly the LLO strain alone[62].

Overall, dynamic responses were observed for many of the cytokines and chemokines in response to the LLO strain with the LLO-*SK* and LLO-*KG* strains able to modify expression further in comparison to the LLO strain in some key examples indicating TF specificity. One component of the differential responses were elevated expression of cytokines and chemokines in response to all bacterial strains compared to the positive controls of IFN-γ and LPS (M1+) or IL-4 and IL-13 (M2+). Additionally, the differences in responses to treatment with bacteria compared to the positive controls was larger in the cytokine and chemokine profiles than were observed with the cell surface markers. Enhanced signaling proteins (cytokines and chemokines) response from macrophages, and other professional antigen presenting cells, compared to cell surface marker expression has been previously observed[63–65]. Other factors that could contribute to the observed complex response involves *B. subtilis* stimulating Toll-like receptor 2 (TLR2) in contrast to IFN-γ and LPS stimulating TLR4[66]. Additionally, viable bacteria can cause a more dynamic response than just bacterial products alone[67]. Altogether, even with

the dynamic responses from the J774A.1 cells in response to complex signals, the LLO-*SK* and LLO-*KG* strains were able to change trends in macrophage surface markers, and cytokine/chemokine profiles in comparison to the LLO strain. This observation is further supported by not observing significant differences in J774A.1 viability, percentage of cells containing fluorescently labeled bacteria and distribution of fluorescence intensity (relating to number of bacteria per cell) when comparing the LLO, LLO-*SK* and LLO-*KG* strains (Fig. 2.10). Future studies should focus on characterizing the impact of these strains in primary macrophages such as bone marrow derived macrophages to clearly understand application potential. In addition, more TF pairings informed by thorough studies that elucidate the complexity of macrophage response should be constructed and tested to optimize the response from the macrophages for the desired application.

Controlling inflammation could be an important biomedical application of the LLO-*SK* and LLO-*KG* strains. For example, inflammation is an important hallmark of cancer, and the phenotype of tumor associated macrophages (TAM) is thought to promote tumor growth, metastases and poor outcomes[68]. TAMs are broadly M2 polarized, and IL-10, IL-12p40 and G-CSF all have been shown to play important roles in impacting the tumor microenvironment through regulation of TAMs[68–70] which could be targeted by the LLO-*SK* for cancer bacteriotherapy[26]. Arthritis represents immune polarization where homeostasis is driven to a pro-inflammatory condition[71]. Here, modulating macrophages towards the M2 phenotype could reduce inflammation in joints. Downregulation of TNF-α and upregulation of IL-10 LLO-*KG* shows promise for treating damaging inflammatory conditions such as arthritis[54,71]. Manipulation of immune cells *in vivo* has been characterized by low efficacy and lack of innate control[72] and the use of EES could circumvent these issues since engineered bacteria can be taken up by phagocytic cells and direct gene expression towards a therapeutic phenotype.

The use of an EES is advantageous when compared to alternative methods of manipulating mammalian cell fates and function. Current methods of manipulating mammalian cell fate include viral vectors, growth factors or signaling molecules[73]. Additionally, chimeric antigen receptor T (CAR-T) cells and CRISPR technologies have proven to be potential futures for some therapeutics and are clinically relevant, but each has some limitations[74]. Viral vectors have been shown to be slow as therapeutics within the immune system, specifically in targeting and modulating macrophages, compared to exogenous cytokines[75]. An alternative method of manipulating cellular fates using prosthetic networks increases the variety of cargo that can be delivered and provides some control with limitations[73]. The EES can build on the precedence of prosthetic networks by having the capability to be constructed to generate complex sets of proteins and molecules once in the cytoplasm of mammalian cells for improved control; continuously supplying TFs, or alternatively providing a method for delivering CRISPR-Cas9[76,77], which could improve directing cell fates.

Studies of pathogens and their virulence factors should inform future development of the EES. The EES will utilize this characterization for defined control within the host cell cytoplasm. This study demonstrated the utility of an EES to alter mammalian cell fates. The use of the EES as a tool to change mammalian cell function may have use in the treatment of diseases by altering the function of mammalian cells. *B. subtilis* serves as an ideal chassis for development and optimization of the EES capable of surviving in the cytoplasm and delivering proteins to the nuclei of mammalian cells to alter cellular fates.

MATERIALS AND METHODS

B. subtilis LLO constructs

Constructs were inserted into the genome of *B. subtilis* LLO at the *amyE* locus using a homologous recombination plasmid (pDR111[78], a gift from Dr. Lee Kroos). The pDR111 plasmid was transformed into *B. subtilis* using a natural competence protocol and constructs were selected by spectinomycin then confirmed by PCR amplification out of the genome[79]. *B. subtilis* expressing IPTG-inducible LLO was provided by Dr. Daniel Portnoy. The constructs include the *lacZ*, *Stat-1Klf6* and *Klf4Gata-3* genetic cassettes. *B. subtilis* LLO was designed to secrete β-gal to the nucleus through the twin-arginine translocation (Tat) pathway by synthesizing the PhoD signal peptide[40] and the amino acids from 126-132 of the simian virus (SV) 40 nuclear localization signal (NLS)[41] together and connecting both to *lacZ* when inserting into pDR111 using Gibson assembly after *lacZ* was amplified from the pST5832 plasmid (a gift from Carolyn Bertozzi & Jessica Seeliger, Addgene plasmid #36256). The same construct was engineered without the SV40 signal to confirm specific delivery to the nucleus. The *lacZ* gene and the synthesized PhoD signal peptide plus SV40 NLS were cloned into the NheI restriction site in pDR111 using Gibson assembly. Initially, the β-gal secretion strain was controlled by an IPTG-inducible promoter (Phyper-spank). However, previous studies have shown the IPTG system is limited in controlling protein production so these constructs were engineered to be controlled by the mannose-inducible system amplified from *B. subtilis* ZB307 strain genome[19]. The mannose promoter and regulator were cloned into the pDR111 plasmid to replace the Phyper-spank promoter and LacI regulator using Gibson assembly. Accordingly, the *lacZ* gene with the same design was cloned in the NheI restriction site present in the pDR111 mannose plasmid using Gibson assembly. The *Stat*-1 and *Klf6* genes were synthesized by IDT as a custom gene and Gblock respectively from the coding sequences obtained from Uniprot. The *Stat-1Klf6* operon

was fused by ligation at an introduced EagI restriction site between the genes during cloning into the pDR111 mannose plasmid by restriction cloning into the SalI and NheI restriction sites. The *Klf4* and *Gata-3* genes were synthesized as Gblocks from IDT and fused using the same method as the *Stat-1Klf6* operon. The *Klf4Gata-3* operon was cloned into the pDR111 mannose plasmid using restriction cloning at the SalI and SbfI restriction sites after the SbfI cut site was introduced into the multiple cloning site by inverse PCR then digesting both ends with SbfI and re-ligating the pDR111 mannose plasmid. All constructs were confirmed by restriction digest, sequencing and functionality tests.

Growth conditions for *B. subtilis* 168*, B. subtilis* LLO and engineered strains

B. subtilis LLO was grown under the same conditions for all experiments. Each *B. subtilis* LLO construct was grown in Luria-Bertani Miller broth (LB) with the appropriate antibiotic. *B. subtilis* LLO was grown in LB with chloramphenicol (10 µg/mL) and all constructs that were integrated into the *amyE* were grown with spectinomycin (100 µg/mL). The overnight cultures were grown for 16 h at 37°C and 250 RPM. All constructs were integrated into the genome of *B. subtilis* LLO which allowed for expression of constructs without antibiotics during co-incubation with J774A.1 cells. *B. subtilis* 168 (ATCC-23857, ATCC, Manassas, VA, USA) was grown in LB with no antibiotic selection overnight for 16 h at 37°C and 250 RPM.

Delivery protocol for *B. subtilis* LLO and engineered strains

The following conditions were utilized to induce *B. subtilis* LLO delivery, unless otherwise described. J774A.1 monocyte/macrophage cells (ATCC-TIB-67, ATCC Manassas, VA, USA) were maintained at 37°C and 5% CO_2 in DMEM (ThermoFisher, MA, USA), supplemented with 10% fetal bovine serum (FBS). Cells were tested negative for mycoplasma using the MycoAlert PLUS Mycoplasma Detection Kit (Lonza, USA). Once cells were confluent,

they were seeded onto a plate or 4-well chambered imaging slide and allowed to adhere overnight (described below) when an estimation of total number of cells was made based on confluency. *B. subtilis* LLO was added at an optimized MOI of 25:1 for all experiments besides testing of host cell viability, along with IPTG (500 μM) to induce expression of LLO with or without protein of interest. *B. subtilis* LLO and J774A.1 cells were then co-incubated at 37°C and 5% CO_2 for 1 h J774A.1 cells were then washed three times with PBS and new medium was added containing gentamicin (4 μM) to eliminate any remaining extracellular *B. subtilis* LLO. Co-incubation continued for 3 h at 37°C and 5% CO_2 prior to imaging or preparation for microscopy (described below) (Fig. 2.2).

Antibody staining for *B. subtilis* LLO phagosomal escape

After fixation with 4% paraformaldehyde (PFA), cells were permeabilized using 0.3% Triton X-100 (ThermoFisher) followed by a blocking step containing 0.3% Triton X-100 and 5% normal goat serum (ThermoFisher, cat#31872,). *B. subtilis* LLO location was determined by incubating a rabbit anti-subtilisin antibody (1:50, Antibodies-online, PA, USA, cat#ABIN958907) at 4°C overnight followed by a goat anti-rabbit IgG Dylight 650 (1:4000, Novus, CO, USA, cat#NBP1-76058) secondary antibody at room temperature (RT) for 2 h. Phagosome formation or destruction was shown by incubating an anti-Lamp-1[38] antibody (1:100, AbCam, MA, USA, cat#ab25245) at 4°C overnight followed by a goat anti-rat IgG Alexa Fluor 555 (1:1000, Invitrogen, CA, USA, cat#A-21434) secondary antibody at RT for 2 h. Nuclei were counterstained by incubating cells with Hoechst 33342 (1 μg/mL) for 10 minutes (min) at RT. Membranes of the cells were stained by incubating cells with PKH67 green-fluorescent cell linker kit (10 μM, Sigma MO, USA) for 10 min at room temperature. Slides were then coverslipped using Fluoromount-D mounting media (Southern Biotech, AL, USA). Slides were imaged using confocal microscopy (described below).

Confocal imaging

Confocal microscopy was performed using a Nikon A1 CLSM (Nikon, NY, USA) microscope to determine *B. subtilis* LLO escape from the phagosome complex by imaging J774A.1 cells that had been treated with the *B. subtilis* LLO with and without IPTG. Imaging was performed using a 60x oil objective and 1.5x zoom and using filter sets for DAPI (Hoechst 33342), GFP (PKH67), TRITC (Alexa Fluor 555 for LAMP-1) and Cy5 (Dylight 650 for *B. subtilis*). Z-stacks were taken at 0.5 µm steps to confirm location of *B. subtilis* LLO within host cells. Images were analyzed using NIS-Elements AR Software (Nikon) and background noise was reduced by using Nikon denoise.ai algorithm. The 3-dimensional volume images and cutaways were produced by the Alpha display mode. The Alpha display mode was also used to generate 3-dimensional videos to display z-depth location of the *B. subtilis* LLO during escape from the phagosomes.

J774A.1 viability by MTS assay and Flow cytometry and uptake rate of engineered B. subtilis LLO strains

The effect of *B. subtilis* LLO on J774A.1 cell viability was determined after EES delivery. Conditions examined were: multiple time points of interaction between *B. subtilis* LLO and host cells (0, 1 and 4 h), different MOIs (10:1, 25:1, 50:1), no IPTG induction and no treatment, with biological triplicates (n=3) for each time and condition. At each time point, J774A.1 cells were washed once with PBS then MTS reagent (Abcam) was added to cells at a 10-fold dilution with DMEM followed by incubation for 30 min at 37°C then absorbance was measured at 490 nm. All treatment conditions were compared to J774A.1 cells alone to elucidate any differences in loss of viability of the J774A.1 cells due to the treatment conditions. Flow cytometry was used to analyze cell viability after engineered *B. subtilis* delivery at 10:1, 25:1 and 50:1, compared to no IPTG induction and no treatment at the 4 h time point (n=1) or after the addition of LLO, LLO-*SK*

and LLO-*KG* (all at 25:1 MOI with IPTG; n=3) compared to no treatment. Furthermore, uptake of *B. subtilis* LLO, LLO-*SK* and LLO-*KG* by J774A.1 cells was assessed after staining bacteria with CellTracker Orange CMRA Dye (CTO, Invitrogen, C34564, 2 μM incubated at 37°C and 250 RPM for 25 min). Following staining, the strains were washed three times before adding to J774A.1 cells at 25:1 MOI for 4 h incubation. Cells were collected, washed once with 1X PBS and incubated with Zombie NIR viability dye (1:750, Biolegend, San Diego, CA, USA; cat#423105) in PBS for 20 min, at 4°C in the dark. Cells were washed twice followed by fixation using 4% PFA and resuspended in 100 μL flow buffer for analysis using the Cytek Aurora Cytometer (Cytek Biosciences, CA, USA). All samples were assessed for percent live cells. Cells which were incubated with CTO bacteria were assessed for percent CTO positive cells (indicating J774A.1 cells containing bacteria) and CTO MFI was used as a relative measure of CTO bacteria per cell. Standard one-way ANOVA with Tukey post-hoc test was used to determine statistically different values.

Live Cell Imaging

B. subtilis LLO was internalized into J774A.1 cells as described above, using a 96-well black glass-bottom plate (40,000 cells/well; Greiner Bio-One, Austria, cat#655892). *B. subtilis* LLO was stained with CellTracker Orange CMRA Dye (CTO, Invitrogen, C34564) as described above then added to J774A.1 cells. Live cell imaging was performed on a Leica DMi8 Thunder microscope equipped with a DFC9000 GTC sCMOS camera and LAS-X software (Leica, Wetzlar, Germany). Cells were maintained at 37°C and 5% CO_2 in Fluorobrite medium during the imaging session. Fluorescent images of CTO were acquired using a TRITC filter set. Brightfield and fluorescent images were acquired consecutively, using a 63x oil objective every 1 h beginning at 1 h post co-incubation and continuing until 4 h post incubation. Z-stacks were taken at all time points at 0.4 μm steps to confirm *B. subtilis* LLO presence within cytoplasm. *B.*

subtilis LLO presence in J774A.1 cells was quantified using Fiji (ImageJ) software and cell counter plugin by counting >1.5 µm rods throughout z-depth. An area of 2090 µm by 1254 µm in each well was imaged and used to perform this quantification.

Engineered *B. subtilis* LLO β-gal protein secretion

B. subtilis LLO engineered to secrete β-gal (LLO-*lacZ*) with and without a NLS (LLO-*lacZ*-NLS and LLO-*lacZ*-no NLS) were internalized into J774A.1 cells as described above, using 4-well chambered slides (75,000 cells/well, ThermoFisher, cat #154917). Incubation was also performed using the supernatant from a 16 h mannose-induced LLO-*lacZ*-NLS culture. The second incubation step was 3 h and began after adding gentamicin (4 µg/mL) and with and without D-mannose (1% w/v) for the β-gal secretions strains. During extended studies, the cells were washed gently 3 times with 1X PBS then a high concentration of gentamicin (25 µg/mL) was added after 3 h and incubation continued for an additional 21 h. The cells were then fixed with 4% PFA for 10 min prior to preparation for microscopy (described below).

β-gal antibody staining

After fixation with 4% PFA, cells were permeabilized using 0.3% Triton X-100 (ThermoFisher) followed by a blocking step containing 0.3% Triton X-100 and 5% normal goat serum (ThermoFisher). β-gal secretion to the nucleus was identified using fluorescence imaging after incubation with an anti-β-galactosidase (*E. coli*) antibody-rabbit (1:100, Biorad, CA, USA, cat#AHP1292GA) at 4ºC overnight followed by a goat anti-rabbit IgG Dylight 650 (1:3000, Novus) secondary antibody at RT for 2 h Nuclei were counterstained by incubating cells with Hoechst 33342 (1 µg/mL) for 10 min at room temperature. Slides were then coverslipped using Fluoromount-D mounting media (Southern Biotech, AL, USA). Epi-fluorescent microscopy was performed using a Nikon Eclipse Ci-L microscope equipped with a CoolSNAP DYNO camera for

fluorescent imaging and NIS elements BR 5.21.02 software (Nikon). Images were acquired with a 40x phase contrast objective and for fluorescent imaging DAPI and Cy5 filter sets were used. Nuclear SNR was quantified by imaging in random areas in each corner of the well and in the center of the well. At least 5 random images totaling an area of 1085 μm by 825 μm were utilized in drawing regions of interest (ROIs) around nuclei of J774A.1 cells to quantify Cy5 fluorescence by utilizing Hoechst 33342 counterstain to determine nuclei location. Nuclear SNR was calculated by using mean fluorescence intensity of ROI region around nuclei of J774A.1 cells in each of the five random images (n=50 random individuals) divided by standard deviation (SD) of noise in the well. SD of noise in well was determined by drawing 3 ROIs (550 μm^2) in background areas of each image then calculating SD of the mean fluorescence from all ROIs drawn in background areas. Statistics was determined using Brown-Forsythe and Welch ANOVA with Dunnett T3 post-hoc test and all treatment conditions were compared.

Engineered *B. subtilis* LLO-modulation of J774A.1 cell protein expression

The LLO strain, LLO-*SK* and LLO-*KG* were internalized into J774A.1 cells as described above (*B. subtilis* LLO β-gal protein secretion), using a 6-well plate (Corning Costar #3516). TFs were secreted for 3 h then allowed to be trafficked for an additional 21 h as described above (*B. subtilis* LLO β-gal protein secretion). For flow cytometry, Accutase (Sigma, cat#A6964) was used to detach J774A.1 cells for analysis (described below). For Luminex cytokine profiling (Millipore Sigma, MA, USA), the supernatant was removed at both 24 and 48 h and then analysis was performed to quantify cytokines produced (described below). Non-stimulated J774A.1 cells were assumed to be at resting state. J774A.1 cells were polarized with interferon-gamma (IFN-γ) and lipopolysaccharide (LPS) (M1+, 100 ng/mL each) or interleukin (IL)-4 and/or IL-13 (M2+, 100 ng/mL each) to be used as positive controls. Furthermore, J774A.1 cells were treated with the *B. subtilis* 168 strain in flow cytometry characterization to compare to LLO

strain. The EES with operons were treated with and without mannose as described in *B. subtilis* LLO β-gal secretion and the LLO strain was not as no difference in impact on J774A.1 cells was observed in previous flow experiments. All treatment conditions were performed in biological triplicates (n=3).

Growth curves

B. subtilis LLO, LLO-*SK* and LLO-*KG* overnight cultures were grown for 16 h at 37°C and 250 RPM in triplicate (n=3). All cultures were diluted 1:20 then allowed to grow into logarithmic phase for 3 h Subsequently the cultures were normalized to OD_{580} = 0.1 then 100 µL was transferred into columns of a 96 well plate (Falcon, #351172) for a total of 24 replicates (n=3 biological, n=8 technical). Cultures were grown in a PerkinElmer VICTOR Nivo plate reader at 37°C and 300 RPM with OD_{580} measurements (580 nm was used due to plate reader limitations) taken every 30 min. Measurements were performed until growth rates began to slow in late logarithmic phase in the 100 µL (9 h for all samples). All replicates were plotted to visualize differences in growth rates between strains as mean ± SD.

Flow cytometry

After addition of the engineered *B. subtilis* LLO strains and controls, followed by incubation for 24 or 48 h, cells were collected and stained in a 96-well round bottom plate. Treatment addition was staggered so that flow staining and data acquisition could be performed at the same time for 24 and 48 h cells. All staining steps were performed in 100 µL volume at 4°C in the dark. Samples were first incubated with Zombie NIR viability dye (1:750, Biolegend) for 20 min. Cells were washed once with flow buffer, followed by incubation with TruStain FcX™ PLUS (anti-mouse CD16/32) Antibody (Biolegend, cat#156603; 0.25 µg/sample) for 10 min. Alexa Fluor® 647 anti-mouse CD86 Antibody (0.125 µg/sample; Biolegend; cat#105020) and

FITC anti-mouse CD206 (MMR) antibody (0.1 µg/sample, Biolegend; cat#141703) were then added and incubated for 20 min. Cells were washed twice with flow staining buffer and fixed with 4% PFA for 10 min and resuspended in a final volume of 100 µL for flow cytometry analysis using the Cytek Aurora spectral flow cytometer (Cytek). Single stained controls and unstained controls for all conditions were used to assess fluorescent spread and for gating strategies. Flow cytometry data was analyzed with the software FCSExpress (DeNovo Software, CA, USA). A standard one-way ANOVA with Tukey's multiple comparisons test was used to determine statistically different MFI values amongst all groups within each time point. A two-way ANOVA with Šidák's multiple comparisons test was used to compare the 24 and 48 h data for each surface marker. The data presented herein were obtained using instrumentation in the MSU Flow Cytometry Core Facility. The facility is funded in part through the financial support of Michigan State University's Office of Research & Innovation, College of Osteopathic Medicine, and College of Human Medicine.

Luminex cytokine profiling assay

Cell culture supernatant was stored at -20°C until ready for use. Supernatant was analyzed for CCL2 (MCP-1), CCL3 (MIP-1a), CCL11 (Eotaxin), CXCL2/MIP-2, G-CSF, IL-1α, IL-1β, IL-4, IL-6, IL-10, IL-12p40, IL-12p70, IL-13, INFγ, LIF, TNF-α and VEGFα cytokine expression. Cytokine levels of cell supernatants were measured using a MCYTOMAG-70K-17 Mouse Cytokine Magnetic Multiplex Assay (Millipore Sigma) using a Luminex 200 analyzer instrument (Luminex Corp, USA) according to the manufacturer's instructions. Standard one-way ANOVA with Tukey post-hoc test was used to determine statistically different values amongst all treatment groups.

ICC confirming EES manufacturing and delivering TFs

Protocol for engineered *B. subtilis* LLO modulation of J774A.1 cell protein expression was used as the template protocol for this experiment. The experiment was performed using a 96-well black glass-bottom plate (40,000 cells/well; Greiner Bio-One). However, J774A.1 cells were fixed at 3 h post mannose addition to reveal engineered *B. subtilis* LLO delivering TFs to host cells using antibodies against the transcription factor of interest. Each transcription factor was stained for with the appropriate antibody individually within the wells. The strains was stained prior to addition to host cells using Invitrogen CellTracker Orange CMRA Dye (Invitrogen) as in live cell imaging. After fixing, cells were permeabilized using 0.3% Triton X-100 (ThermoFisher) followed by a blocking step containing 0.3% Triton X-100 and 5% normal goat serum (ThermoFisher). Cells were then incubated with rabbit anti-*Stat-1* (1:50, MyBiosource, CA, USA, cat#MBS125754), rabbit anti-*Klf6* (1:50, MyBiosource, cat#MBS8307089), rabbit anti-*Klf4* (1:20, MyBiosource, cat#MBS2014661) or rabbit anti-*Gata-3* (1:100, MyBiosource, cat#MBS8204267) at 4ºC overnight followed by a goat anti-rabbit IgG Dylight 650 (1:3000, Novus) secondary antibody at RT for 2 h Nuclei were stained by incubating cells with Hoechst 33342 (1 µg/mL) for 10 min at room temperature. Membranes of the cells were stained by incubating cells with PKH67 green-fluorescent cell linker kit (10 µM) for 10 min at room temperature. Imaging was performed using Leica DMi8 Thunder microscope equipped with Leica DFC9000 GTC sCMOS camera and Leica LAS-X software (Leica) with the following light emitting diodes for excitation: Hoechst 33342 (395 nm), PKH67 (475 nm), CellTracker Orange CMRA Dye (555 nm) and Dylight 650 for TFs (635 nm) filters were used and imaged using a 40X objective to confirm LLO-*SK* and LLO-*KG* delivery of TFs. Images were quantified using Fiji (ImageJ). Thresholding was performed on the Hoechst 33342 images to identify the nuclei. Nuclear ROIs were used to quantify fluorescence intensity in the Dylight 650 channel. Nuclear SNR was calculated using mean nuclear fluorescence/standard deviation of the

background signal. Background signal was quantified from one data set for each TF. A mean of 158.4 +/- 63.6 (SD) cells were analyzed per data set. Outliers were identified using the ROUT methods (Q=1%) and outliers removed for analysis using a one-way ANOVA and Tukey's multiple comparisons test.

Statistical analysis

Statistical analyses were performed using Prism software (9.2.0, GraphPad Inc., La Jolla, CA). Statistical tests are identified for each method. Data are expressed as mean +/- standard deviation; $p<.05$ was considered a significant finding. Plotting was performed using R version 4.0.4 with the following packages: ggplot2, dplyr, reshape2, ggsignif, plotrix and ggpubr.

Availability of data and materials

All raw data, *B. subtilis* LLO constructs and R scripts will be made available upon request by the corresponding author. Plasmids used to produce *B. subtilis* LLO constructs will be submitted to Addgene after manuscript publication. All R scripts were written with established packages.

Competing interests

The authors declare no competing interests.

Acknowledgements

The authors would like to thank Dr. Daniel A. Portnoy for the *B. subtilis* LLO strain, Dr. Jens Schmidt for advice on imaging and Dr. Lee Kroos for *B. subtilis* plasmid pDR111. The authors would also like to thank Dr. Melinda Frame of the Michigan State University Center for

Advanced Microscopy for confocal imaging, Dr. Matthew Bernard of the Michigan State University Flow Cytometry Core for flow cytometry aid and Luminex cytokine profiling analysis. The authors would like to acknowledge Chima V. Maduka for his thoughtful and thorough review of the manuscript and providing crucial insights. Fig. 2.1 and 2.2 were created using BioRender.com.

Funding

The authors would like to acknowledge the James and Kathleen Cornelius Endowment for financially supporting this research.

Affiliations

Department of Biomedical Engineering, Michigan State University, East Lansing, MI, USA. Department of Microbiology and Molecular Genetics, Michigan State University, East Lansing, MI, USA. Institute for Quantitative Health Science and Engineering, Michigan State University, East Lansing, MI, USA

Contributions

Cody S. Madsen conceptualized *Bacillus subtilis* as a chassis organism, developed all the EES constructs as the platform technology, jointly developed and performed all experiments, jointly developed and analyzed all data to make figures and was one of the primary authors of the manuscript. Dr. Ashley V. Makela jointly developed and performed all experiments, jointly developed and analyzed all data to make figures and was one of the primary authors of the manuscript. Emily M. Greeson significantly contributed to the development of the EES platform technology, jointly developed and significantly contributed to

the writing and editing of this manuscript. Dr. Jonathan W. Hardy acquired the *B. subtilis* LLO strain from Dr. Daniel A. Portnoy, significantly contributed to the development of the EES platform technology and significantly contributed as an author to this manuscript. Dr. Christopher H. Contag conceptualized the initial concept of the EES, supervised the studies, contributed to the experimental design, provided the resources, reviewed data and edited the manuscript.

REFERENCES

REFERENCES

1. Sagan, L. On the origin of mitosing cells. *J. Theor. Biol.* **14**, 225-IN6 (1967).

2. Mehta, A. P. *et al.* Engineering yeast endosymbionts as a step toward the evolution of mitochondria. *Proc. Natl. Acad. Sci. U. S. A.* (2018).

3. Jin, Y. *et al.* Enhanced differentiation of human pluripotent stem cells into cardiomyocytes by bacteria-mediated transcription factors delivery. *PLoS One* (2018).

4. Epelman, S., Lavine, K. J. & Randolph, G. J. Origin and Functions of Tissue Macrophages. *Immunity* **41**, 21–35 (2014).

5. Chen, S., Yang, J., Wei, Y. & Wei, X. Epigenetic regulation of macrophages: from homeostasis maintenance to host defense. *Cell. Mol. Immunol.* **17**, 36–49 (2020).

6. Ginhoux, F. & Guilliams, M. Tissue-Resident Macrophage Ontogeny and Homeostasis. *Immunity* **44**, 439–449 (2016).

7. Martinez, F. O., Sica, A., Mantovani, A. & Locati, M. Macrophage activation and polarization. *Frontiers in Bioscience* (2008).

8. Lavin, Y. *et al.* Tissue-Resident Macrophage Enhancer Landscapes Are Shaped by the Local Microenvironment. *Cell* **159**, 1312–1326 (2014).

9. Mosser, D. M. & Edwards, J. P. Exploring the full spectrum of macrophage activation. *Nature Reviews Immunology* (2008).

10. Moreira, A. P. & Hogaboam, C. M. Macrophages in allergic asthma: Fine-tuning their pro- and anti-inflammatory actions for disease resolution. *Journal of Interferon and Cytokine Research* (2011).

11. Mantovani, A. *et al.* The chemokine system in diverse forms of macrophage activation and polarization. *Trends Immunol.* **25**, 677–686 (2004).

12. Bielecki, J., Youngman, P., Connelly, P. & Portnoy, D. A. Bacillus subtilis expressing a haemolysin gene from Listeria monocytogenes can grow in mammalian cells. *Nature* (1990).

13. Zuber, P. & Losick, R. Role of AbrB in Spo0A- and Spo0B-dependent utilization of a sporulation promoter in Bacillus subtilis. *J. Bacteriol.* (1987).

14. Travassos, L. H. *et al.* Toll-like receptor 2-dependent bacterial sensing does not occur via peptidoglycan recognition. *EMBO Rep.* **5**, 1000–1006 (2004).

15. Gallegos-Monterrosa, R., Mhatre, E. & Kovács, Á. T. Specific Bacillus subtilis 168 variants form biofilms on nutrient-rich medium. *Microbiol. (United Kingdom)* (2016).

16. Kolkman, M. A. B. *et al.* The twin-arginine signal peptide of Bacillus subtilis YwbN can direct either Tat- or Sec-dependent secretion of different cargo proteins: Secretion of active subtilisin via the B. subtilis Tat pathway. *Appl. Environ. Microbiol.* (2008).

17. Barbe, V. *et al.* From a consortium sequence to a unified sequence: The Bacillus subtilis 168 reference genome a decade later. *Microbiology* (2009).

18. Vavrová, Ľ., Muchová, K. & Barák, I. Comparison of different Bacillus subtilis expression systems. *Res. Microbiol.* (2010).

19. Sun, T. & Altenbuchner, J. Characterization of a mannose utilization system in bacillus subtilis. *J. Bacteriol.* (2010).

20. Panneerselvam, K. & Freeze, H. H. Mannose enters mammalian cells using a specific transporter that is insensitive to glucose. *J. Biol. Chem.* (1996).

21. Soleimanpour, S., Hasanian, S. M., Avan, A., Yaghoubi, A. & Khazaei, M. Bacteriotherapy in gastrointestinal cancer. *Life Sci* **254**, 117754 (2020).

22. La Mantia, I. *et al.* The role of bacteriotherapy in the prevention of adenoidectomy. *Eur Rev Med Pharmacol Sci* **23**, 44–47 (2019).

23. Andaloro, C., Santagati, M., Stefani, S. & La Mantia, I. Bacteriotherapy with Streptococcus salivarius 24SMB and Streptococcus oralis 89a oral spray for children with recurrent streptococcal pharyngotonsillitis: a randomized placebo-controlled clinical study. *Eur. Arch. oto-rhino-laryngology Off. J. Eur. Fed. Oto-Rhino-Laryngological Soc. Affil. with Ger. Soc. Oto-Rhino-Laryngology - Head Neck Surg.* **276**, 879–887 (2019).

24. Yaghoubi, A. *et al.* Bacteriotherapy in Breast Cancer. *Int J Mol Sci* **20**, (2019).

25. Yaghoubi, A. *et al.* Bacteria as a double-action sword in cancer. *Biochim Biophys Acta Rev Cancer* **1874**, 188388 (2020).

26. Sawant, S. S., Patil, S. M., Gupta, V. & Kunda, N. K. Microbes as Medicines: Harnessing the Power of Bacteria in Advancing Cancer Treatment. *Int. J. Mol. Sci.* **21**, (2020).

27. Sedighi, M. *et al.* Therapeutic bacteria to combat cancer; current advances, challenges, and opportunities. *Cancer Med.* **8**, 3167–3181 (2019).

28. Tugal, D., Liao, X. & Jain, M. K. Transcriptional control of macrophage polarization. *Arterioscler. Thromb. Vasc. Biol.* (2013).

29. Mitchell, P. J. & Tjian, R. Transcriptional regulation in mammalian cells by sequence-specific DNA binding proteins. *Science (80-.).* **245**, 371–378 (1989).

30. Fleetwood, A. J., Lawrence, T., Hamilton, J. A. & Cook, A. D. Granulocyte-macrophage colony-stimulating factor (CSF) and macrophage CSF-dependent macrophage phenotypes display differences in cytokine profiles and transcription factor activities: implications for CSF blockade in inflammation. *J. Immunol.* **178**, 5245–5252 (2007).

31. Heinz, S. *et al.* Simple combinations of lineage-determining transcription factors prime cis-regulatory elements required for macrophage and B cell identities. *Mol. Cell* **38**, 576–589 (2010).

32. Rilo-Alvarez, H., Ledo, A. M., Vidal, A. & Garcia-Fuentes, M. Delivery of transcription factors as modulators of cell differentiation. *Drug Deliv. Transl. Res.* **11**, 426–444 (2021).

33. Li, H., Jiang, T., Li, M. Q., Zheng, X. L. & Zhao, G. J. Transcriptional regulation of macrophages polarization by microRNAs. *Frontiers in Immunology* (2018).

34. Date, D. *et al.* Kruppel-like transcription factor 6 regulates inflammatory macrophage polarization. *J. Biol. Chem.* (2014).

35. Liao, X. *et al.* Krüppel-like factor 4 regulates macrophage polarization. *J. Clin. Invest.* (2011).

36. Yang, M. *et al.* Deficiency of GATA3-Positive Macrophages Improves Cardiac Function Following Myocardial Infarction or Pressure Overload Hypertrophy. *J. Am. Coll. Cardiol.* (2018).

37. VanDeusen, J. B. *et al.* STAT-1-mediated repression of monocyte interleukin-10 gene expression in vivo. *Eur. J. Immunol.* **36**, 623–630 (2006).

38. Kortebi, M. *et al.* Listeria monocytogenes switches from dissemination to persistence by adopting a vacuolar lifestyle in epithelial cells. *PLoS Pathog.* **13**, e1006734–e1006734 (2017).

39. Huynh, K. K. *et al.* LAMP proteins are required for fusion of lysosomes with phagosomes. *EMBO J.* **26**, 313–324 (2007).

40. Tjalsma, H., Bolhuis, A., Jongbloed, J. D. H., Bron, S. & van Dijl, J. M. Signal Peptide-Dependent Protein Transport in Bacillus subtilis: a Genome-Based Survey of the Secretome. *Microbiol. Mol. Biol. Rev.* (2000).

41. Kalderon, D., Roberts, B. L., Richardson, W. D. & Smith, A. E. A short amino acid sequence able to specify nuclear location. *Cell* (1984).

42. Turner, M. D., Nedjai, B., Hurst, T. & Pennington, D. J. Cytokines and chemokines: At the crossroads of cell signalling and inflammatory disease. *Biochim. Biophys. Acta - Mol. Cell Res.* **1843**, 2563–2582 (2014).

43. Demuth, A., Goebel, W., Beuscher, H. U. & Kuhn, M. Differential regulation of cytokine and cytokine receptor mRNA expression upon infection of bone marrow-derived macrophages with Listeria monocytogenes. *Infect. Immun.* **64**, 3475–3483 (1996).

44. Kuhn, M. & Goebel, W. Induction of cytokines in phagocytic mammalian cells infected with virulent and avirulent Listeria strains. *Infect. Immun.* **62**, 348–356 (1994).

45. Witz, G., Van Nimwegen, E. & Julou, T. Initiation of chromosome replication controls both division and replication cycles in e. Coli though a double-adder mechanism. *Elife* (2019).

46. Corvey, C., Stein, T., Düsterhus, S., Karas, M. & Entian, K.-D. Activation of subtilin precursors by Bacillus subtilis extracellular serine proteases subtilisin (AprE), WprA, and Vpr. *Biochem. Biophys. Res. Commun.* **304**, 48–54 (2003).

47. Stahl, P. D. & Ezekowitz, R. A. B. The mannose receptor is a pattern recognition receptor involved in host defense. *Curr. Opin. Immunol.* **10**, 50–55 (1998).

48. Hong, J. E. *et al.* Alveolar Macrophages Treated With Bacillus subtilis Spore Protect Mice Infected With Respiratory Syncytial Virus A2. *Front. Microbiol.* **10**, 447 (2019).

49. Smith, T. D., Tse, M. J., Read, E. L. & Liu, W. F. Regulation of macrophage polarization and plasticity by complex activation signals. *Integr. Biol. (Camb).* **8**, 946–955 (2016).

50. Ramesh, G., MacLean, A. G. & Philipp, M. T. Cytokines and chemokines at the crossroads of neuroinflammation, neurodegeneration, and neuropathic pain. *Mediators Inflamm.* **2013**, 480739 (2013).

51. Benoit, M., Desnues, B. & Mege, J.-L. Macrophage Polarization in Bacterial Infections. *J. Immunol.* **181**, 3733 LP – 3739 (2008).

52. Rőszer, T. Understanding the Mysterious M2 Macrophage through Activation Markers and Effector Mechanisms. *Mediators Inflamm.* **2015**, 816460 (2015).

53. Martins, A., Han, J. & Kim, S. O. The multifaceted effects of granulocyte colony-stimulating factor in immunomodulation and potential roles in intestinal immune homeostasis. *IUBMB Life* **62**, 611–617 (2010).

54. Iyer, S. S. & Cheng, G. Role of interleukin 10 transcriptional regulation in inflammation and autoimmune disease. *Crit. Rev. Immunol.* **32**, 23–63 (2012).

55. Zhu, Q. *et al.* IL-6 and IL-10 Are Associated with Gram-Negative and Gram-Positive Bacteria Infection in Lymphoma. *Front. Immunol.* **13**, (2022).

56. Becker, C. *et al.* Regulation of IL-12 p40 Promoter Activity in Primary Human Monocytes: Roles of NF-κB, CCAAT/Enhancer-Binding Protein β, and PU.1 and Identification of a Novel Repressor Element (GA-12) That Responds to IL-4 and Prostaglandin E₂ *J. Immunol.* **167**, 2608 LP – 2618 (2001).

57. Fraternale, A. *et al.* Molecules Altering the Intracellular Thiol Content Modulate NF-kB and STAT-1/IRF-1 Signalling Pathways and IL-12 p40 and IL-27 p28 Production in Murine Macrophages. *PLoS One* **8**, e57866 (2013).

58. Ramana, C. V, Chatterjee-Kishore, M., Nguyen, H. & Stark, G. R. Complex roles of Stat1 in regulating gene expression. *Oncogene* **19**, 2619–2627 (2000).

59. Samuel, T. *et al.* Control of specificity and magnitude of NF-κB and STAT1-mediated gene activation through PIASy and PIAS1 cooperation. *Proc. Natl. Acad. Sci.* **104**, 11643–11648 (2007).

60. Falvo, J. V, Tsytsykova, A. V & Goldfeld, A. E. Transcriptional control of the TNF gene. *Curr. Dir. Autoimmun.* **11**, 27–60 (2010).

61. O'Neill, L. A. J. & Pearce, E. J. Immunometabolism governs dendritic cell and macrophage function. *J. Exp. Med.* **213**, 15–23 (2015).

62. Torretta, S. *et al.* D-mannose suppresses macrophage IL-1β production. *Nat. Commun.* **11**, 6343 (2020).

63. Foss, D. L., Zilliox, M. J. & Murtaugh, M. P. Differential regulation of macrophage interleukin-1 (IL-1), IL-12, and CD80-CD86 by two bacterial toxins. *Infect. Immun.* **67**, 5275–5281 (1999).

64. Murtaugh, M. P. & Foss, D. L. Inflammatory cytokines and antigen presenting cell activation. *Vet. Immunol. Immunopathol.* **87**, 109–121 (2002).

65. Bromander, A., Holmgren, J. & Lycke, N. Cholera toxin stimulates IL-1 production and enhances antigen presentation by macrophages in vitro. *J. Immunol.* **146**, 2908–2914 (1991).

66. Udayan, S. *et al.* Macrophage cytokine responses to commensal Gram-positive Lactobacillus salivarius strains are TLR2-independent and Myd88-dependent. *Sci. Rep.* **11**, 1–16 (2021).

67. Zhou, Q., Desta, T., Fenton, M., Graves, D. T. & Amar, S. Cytokine profiling of macrophages exposed to Porphyromonas gingivalis, its lipopolysaccharide, or its FimA protein. *Infect. Immun.* **73**, 935–943 (2005).

68. Laoui, D. *et al.* Tumor-associated macrophages in breast cancer: Distinct subsets, distinct functions. *Int. J. Dev. Biol.* (2011) doi:10.1387/ijdb.113371dl.

69. Karagiannidis, I. *et al.* G-CSF and G-CSFR Induce a Pro-Tumorigenic Macrophage Phenotype to Promote Colon and Pancreas Tumor Growth. *Cancers* vol. 12 (2020).

70. Kanemaru, H. *et al.* Antitumor effect of < em>Batf2 through IL-12 p40 up-regulation in tumor-associated macrophages. *Proc. Natl. Acad. Sci.* **114**, E7331 LP-E7340 (2017).

71. Georgopoulos, S., Plows, D. & Kollias, G. Transmembrane TNF is sufficient to induce localized tissue toxicity and chronic inflammatory arthritis in transgenic mice. *J. Inflamm.* (1996).

72. Spiller, K. L. & Koh, T. J. Macrophage-based therapeutic strategies in regenerative medicine. *Adv. Drug Deliv. Rev.* **122**, 74–83 (2017).

73. Lienert, F., Lohmueller, J. J., Garg, A. & Silver, P. A. Synthetic biology in mammalian cells: Next generation research tools and therapeutics. *Nature Reviews Molecular Cell Biology* (2014).

74. Mollanoori, H., Shahraki, H., Rahmati, Y. & Teimourian, S. CRISPR/Cas9 and CAR-T cell, collaboration of two revolutionary technologies in cancer immunotherapy, an instruction for successful cancer treatment. *Hum. Immunol.* **79**, 876–882 (2018).

75. Boehler, R. M. *et al.* Lentivirus delivery of IL-10 to promote and sustain macrophage polarization towards an anti-inflammatory phenotype. *Biotechnol. Bioeng.* **111**, 1210–1221 (2014).

76. Jakutyte-Giraitiene, L. & Gasiunas, G. Design of a CRISPR-Cas system to increase resistance of Bacillus subtilis to bacteriophage SPP1. *J. Ind. Microbiol. Biotechnol.* **43**, 1183–1188 (2016).

77. Liu, C., Zhang, L., Liu, H. & Cheng, K. Delivery strategies of the CRISPR-Cas9 gene-editing system for therapeutic applications. *J. Control. Release* **266**, 17–26 (2017).

78. Rokop, M. E., Auchtung, J. M. & Grossman, A. D. Control of DNA replication initiation by recruitment of an essential initiation protein to the membrane of Bacillus subtilis. *Mol. Microbiol.* (2004).

79. Harwood, C. R. & Cutting, S. M. Molecular biological methods for Bacillus. (1990).

CHAPTER 3

UTILIZING ENGINEERED ENDOSYMBIONTS TO MODULATE PRIMARY MACROPHAGE FUNCTION AND ALTER TUMOR MICROENVIRONMENTS

ABSTRACT

Modulating gene expression in macrophages can be used to improve tissue regeneration and redirect tumor microenvironments (TME) toward positive therapeutic outcomes. We have developed engineered endosymbionts (EES) as a platform technology for the purpose of controlling the fates and function of macrophages. In chapter 2, engineered *Bacillus subtilis* strains expressed listeriolysin O (LLO) from *Listeria monocytogenes* and mammalian transcription factors (TFs), resided in the cytoplasm of J774A.1 monocyte/macrophage cells and modulated surface marker, cytokine and chemokine expression indicating functional change in the host cells. For increased translatability, the effect of the engineered *B. subtilis* LLO TF strains on murine bone marrow-derived macrophages (BMDMs) function was characterized using flow cytometry, chemokine/cytokine profiling, metabolic assays and RNA-Seq. The TF strains shifted BMDM gene expression, production of cytokine and chemokines and metabolic patterns which indicated that primary macrophages could be guided towards beneficial therapeutic outcomes. Therefore, the ability of the engineered *B. subtilis* LLO TF strains to alter the TME was characterized in a murine 4T1 orthotopic breast cancer model. The *B. subtilis* LLO strains altered the TME by promoting immune cell invasion, altering the functional metabolism of cells within the tumor and causing tumor growth stabilization. Additionally, safety of this EES platform was observed as multiple doses at bacterial concentrations 100-fold more than other bacterial therapies were injected without affecting the health of mice. The *B. subtilis* LLO TF strains as EES showed promise as a unique therapeutic approach for cancer immunotherapy that could be expanded to modulate mammalian cells for other biomedical applications.

INTRODUCTION

The concept of using endosymbionts and symbionts for modifying eukaryotic organisms to improve human health has existed and been utilized in the last decade in insects and nematodes[1–4]. *Wolbachia spp*. is a model endosymbiont that lives symbiotically within mosquitoes and naturally blocks the transmission of dengue and Zika virus by the mosquito species *Aedes aegypti*[5]. Therefore, researchers have been infecting populations of mosquitoes with *Wolbachia spp*. and releasing them into the environment to further prevent transmission of the viruses through mating of the infected populations with the uninfected, further extending the *Wolbachia spp.*-carrying population[5,6]. Various symbionts have been engineered in applications ranging from improving honeybee immunity[7] to enhancing nematode biocontrol of dangerous crop pathogens[8], indirectly improving human health. Furthermore, extensive research has been done on natural endosymbionts in invertebrates and the benefits of the symbiotic relationships between endosymbiont and host which has even revealed clinically relevant compounds produced as a result of this relationship that can be produced into chassis organisms relevant in biomanufacturing[9–15]. Previously, we developed non-pathogenic engineered endosymbionts (EES) that persisted in the cytoplasm of mammalian cells and altered macrophage surface marker, cytokine and chemokine expression for potential use in human health applications.

Variations of the EES were delivered to J774A.1 monocyte/macrophages previously[16] because of the characterized mechanism to gain access to the cytoplasm and flexibility of using a cell line for optimizing EES interaction with the host cell. For translatability, EES impact on primary bone marrow derived macrophages (BMDMs)[17,18] was characterized. BMDMs represent primary antigen presenting cells that signal to other important immune cells and regulate immune response[19,20]. Accordingly, BMDMs alternate between synthesizing pro-inflammatory or anti-inflammatory signals[21] and function as pro-inflammatory macrophages (M1) to destroy

pathogens or anti-inflammatory (M2) macrophages to decrease inflammation, support angiogenesis and promote tissue remodeling and repair[22,23]. These shifts in population function are distinguished by changes in gene expression, cell surface markers and expression of cytokines/chemokines[24–27]. Furthermore, metabolism also acts as measure of shifts in BMDM activity and function. Metabolic reprogramming plays an important role in the progression of cancer through mechanisms such as the Warburg effect[28–30]. Immune cells such as BMDMs also experience the Warburg effect and other shifts in metabolism when activated by lipopolysaccharide (LPS) and other pro-inflammatory stimuli[31–38]. Metabolic deviations can be revealed by measuring transitions from oxidative phosphorylation to glycolysis (Warburg effect), changes in oxygen consumption rate (OCR), changes in extracellular acidification rate (ECAR) and variations in adenosine triphosphate (ATP) production rate[39–43]. These metabolic shifts occur as a component of the dynamic response of macrophages to specific stimuli thus acting as another readout for macrophage behavior. As a result, BMDMs have been used as models to understand macrophage importance in many applications including cancer[44–47], chronic inflammation[48,49], drug delivery[50,51], pathogen response[52–54] and tissue regeneration[51,55–57].

Extracellular bacteria-based therapies have been developed to improve human health from improving the gut microbiome[58–61] to treating cancer[62–65]. *Mycobacterium bovis* or Bacille Calmette-Guerin (BCG)[66,67] was originally developed as a tuberculosis vaccine but has now also been approved for bladder cancer treatment, and other clinical applications for bacteria treatment in cancer are being tested[62–65,68–70]. Furthermore, several advancements have been made in improving extracellular bacteria treatment of cancer from tropism to therapeutic delivery[71–75]. *E. coli* Nissle 1917 (EcN) is a probiotic Gram-negative bacterium that has been part of the advancements in extracellular bacterial cancer immunotherapy[76–79]. EcN has been modified to deliver chemotherapeutic drugs and proteins while improving safety as a probiotic[75–79]. Intracellular bacteria have also been used in cancer immunotherapy. Gram-positive

intracellular bacterium, *Listeria monocytogenes,* has been used to mobilize the immune system to alter the cancer microenvironment and *Salmonella typhimurium* has been used extensively to disrupt viability of cancer cells along with therapeutic molecule delivery[80–86]. Yet, several challenges still exist to improve these therapies. Dose tolerance from live bacteria injection especially Gram-negative bacteria, utilizing known pathogens as chassis organisms, and lack of characterized mechanisms of impact on target microenvironment are all challenges that need to be addressed[87–90]. The *Bacillus subtilis* expressing listeriolysin O (LLO)[91,92] chassis of the EES is a non-pathogenic, generally recognized as safe (GRAS), Gram-positive, soil bacterium that respires as a facultative anaerobe and does not have a lipopolysaccharide- (LPS) mediated immune response which provides an alternative to some of the challenges described above[93,94]. The EES concept of using an intracellular approach to stimulate macrophages and mobilize the immune system to alter the cancer microenvironment parallels some efforts in *L. monocytogenes*[80,81] for cancer treatment but with a non-pathogenic platform that is classically used for secretion of complex proteins[95].

In the therapies mentioned above, bacteria are used to deliver checkpoint inhibitors, nanobodies, epitopes or even lyse as a way of altering the tumor microenvironment (TME) through disruption of tumor cell viability or in an attempt to activate immune cells[71–73,75,81]. These approaches have shown a level of efficacy and continue to be improved. Yet, delivering other types of payloads from bacteria could serve as alternatives or to be paired with current approaches. Previously, engineered *B. subtilis* LLO strains were used to deliver transcription factors (TFs) due to TFs potency in regulating genes to direct cellular fates[96–99] which has led to TFs being used in clinical trials for therapies in cancer, wound repair, regeneration and immune modulation[100]. These engineered *B. subtilis* LLO strains expressed and delivered signal transducer and activator of transcription 1 (STAT-1) together with Krüppel-like factor 6 (KLF6) for pro-inflammatory activation and Krüppel-like factor 4 (KLF4) together with GATA binding

protein 3 (GATA-3) for anti-inflammatory activation in macrophages[101–105]. The engineered *B. subtilis* LLO strains altered patterns of BMDM gene expression, cytokine/chemokine expression and functional metabolism with some patterns of modulation towards anti- or pro-inflammatory phenotypes with clear indication of complex response to the bacteria and TFs. Furthermore, murine 4T1 orthotopic breast cancer TMEs[106–108] were altered by the engineered *B. subtilis* LLO strains by promoting immune cell invasion with some tumor growth regression measured. Additionally, safety of this EES platform was observed as multiple doses at bacterial concentrations 100-fold more than other bacterial therapies were injected without affecting the health of mice. The EES showed promise as a new approach for modulating macrophage function by expressing TFs to be used in bacterial therapy applications and to decipher bacterial impact on TMEs (Fig. 3.1, 3.2).

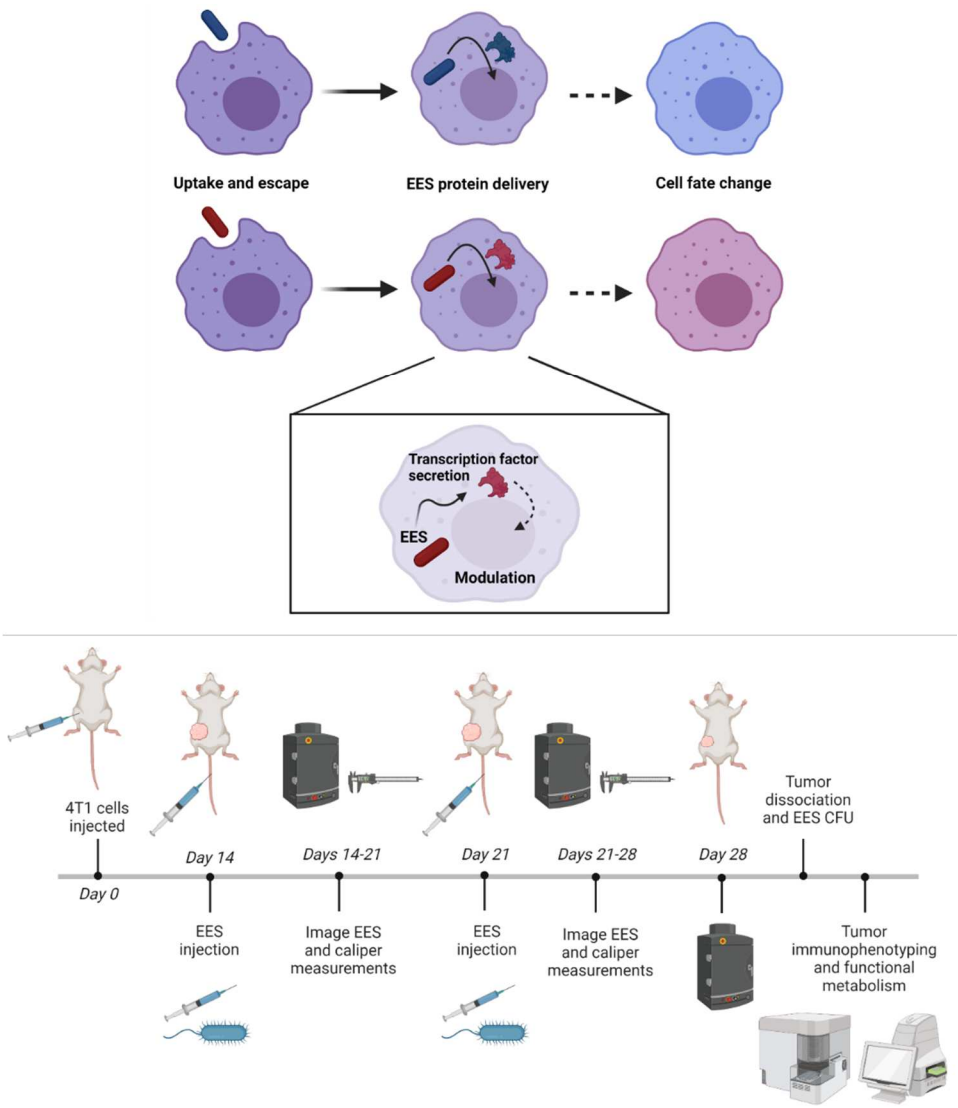

Figure 3.1. EES approach to modulating macrophage function and current EES application to alter tumor microenvironments

The EES are taken up by macrophages and escape into the cytoplasm to deliver transcription factors (TFs) to modulate host cell function. For an *in vivo* application, the EES ability to localize to and alter the TME was tested in a 4T1 orthotopic breast cancer model. The EES localization and persistence was tracked with the *In Vivo* Imaging System (IVIS). Tumor growth was measured by calipers. Tumors were characterized by immunophenotyping (flow cytometry), functional metabolism (Seahorse real-time metabolic assays) and EES colony forming units (CFU).

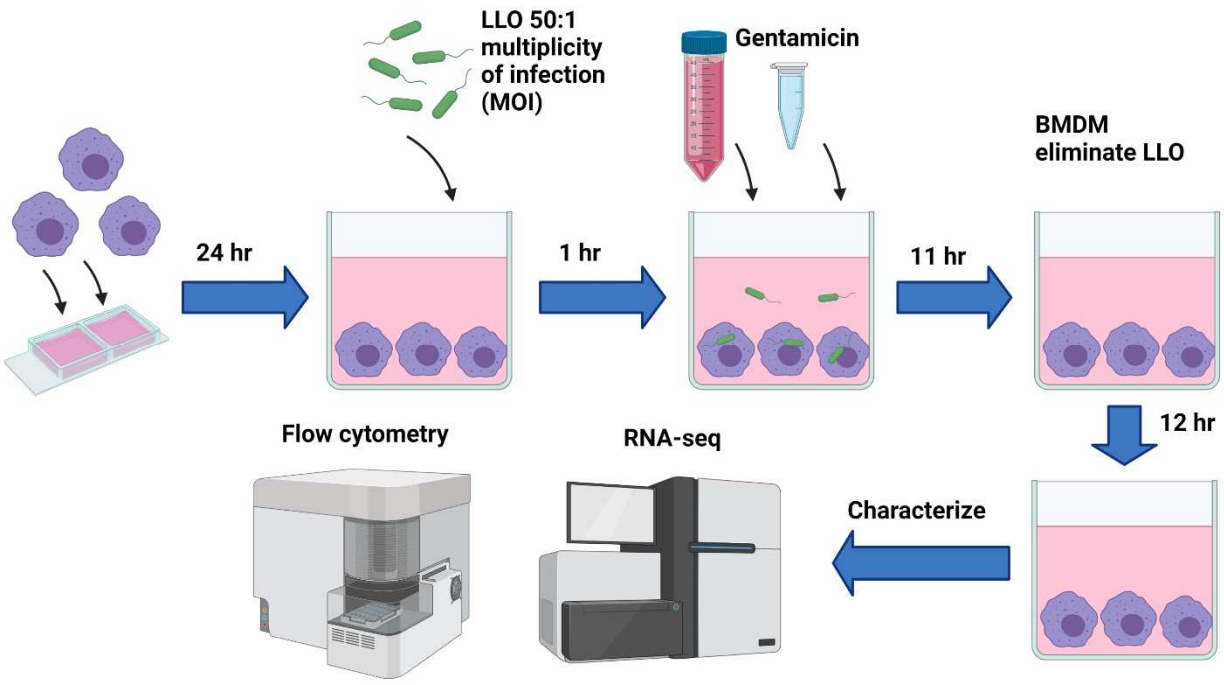

Figure 3.2. Diagram of method to deliver *B. subtilis* LLO strains to bone marrow derived macrophages and analyze interaction

General approach for co-incubating *B. subtilis* LLO with host bone marrow derived macrophages (BMDMs) and timeline for the interaction. Bacteria were incubated with BMDMs for 1 h then gentamicin is added to eliminate extracellular bacteria. With 11 additional hours of incubation, BMDMs were observed to eliminate all intracellular bacteria. Analysis was performed at multiple times intervals but in most cases, incubation was continued for an additional 12 h to determine impact on host cells by methods such as flow cytometry and RNA-sequencing.

RESULTS

B. subtilis expressing LLO escaped phagosome destruction, but autophagy mechanisms eliminated *B. subtilis* LLO

Fluorescent microscopy confirmed that *B. subtilis* LLO escaped phagosomal destruction in BMDMs (Fig. 3.3) by evaluation of colocalization between bacteria (white) and LAMP-1[109] positive structures (phagosomes, magenta) which indicate assembly of the phagosomes[110]. The escape was conditional on transcription induction by isopropyl β-D-1-thiogalactopyranoside (IPTG) of the *hlyA* gene encoding LLO which was also observed for macrophage cell lines previously[16,91]. Without IPTG addition (-IPTG), few *B. subtilis* rods were observed and most were outside cells with punctate regions of *B. subtilis* signal associated with LAMP-1 positive regions at 4 h and by 12 h only remnants of bacteria were observed (Fig. 3.3, orange arrows). Conversely, when IPTG was added (+IPTG), *B. subtilis* rods were observed in several cells not localized with LAMP-1 pockets with some cells containing many bacteria (Fig. 3.3). Yet, after *B. subtilis* LLO escaped to the cytoplasm (+IPTG), BMDMs responded to the escape and had removed most of the intracellular bacteria by 12 h (Fig. 3.3). Microtubule-associated protein light chain 3 (LC3) has been shown to coordinate autophagy response after phagosomal escape in macrophages infected with *L. monocytogenes* and other pathogens[111–114] so LC3B[111] was used to indicate that this mechanism was activated by the BMDMs to remove intracellular *B. subtilis* LLO by 12 h with some activation and destruction of *B. subtilis* LLO even at 4 h (Fig. 3.3 white arrows). Accordingly, the expression of LLO when induced by IPTG allowed *B. subtilis* LLO to access the cytoplasm of the BMDMs but resulted in *B. subtilis* LLO elimination within several hours. Nonetheless, live cell imaging validated that *B. subtilis* LLO remained viable within the cytoplasm as replication was observed in multiple cells in a representative imaging region of interest between 3 and 4.5 h post bacterial addition (Fig. 3.4). Additionally, BMDMs were

observed to actively pursue and share bacteria between cells to control bacterial proliferation and persistence (Fig. 3.4).

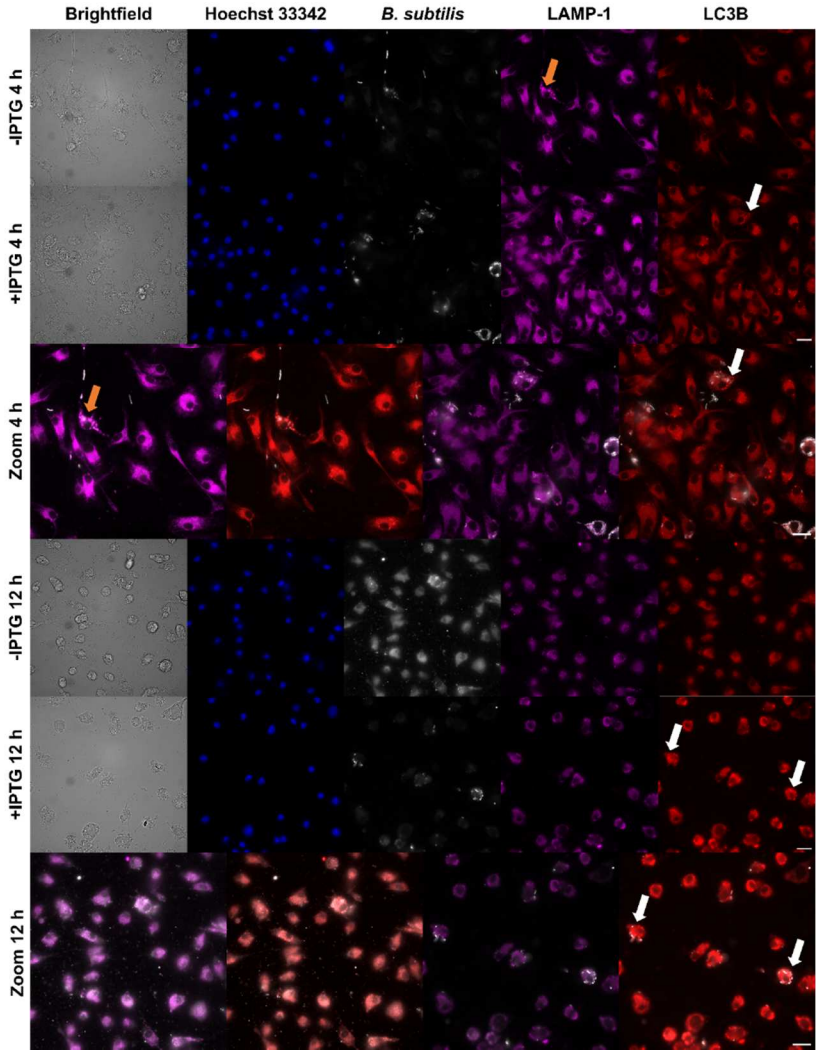

Figure 3.3. Fluorescent imaging identified *B. subtilis* LLO escape from BMDM phagosomes and destruction by autophagy mechanisms

Microscopy was used to image BMDMS after the LLO strain was delivered at a multiplicity of infection (MOI) of 50:1 and treated without (-IPTG) or with IPTG (+IPTG) with imaging at 4 and 12 h in brightfield, nuclei stained by Hoechst 33342 (blue), *B. subtilis* stained by CellTracker Orange CMRA Dye (white) and LAMP-1/LC3B stained by primary and secondary antibodies (magenta and red respectively). Overlays of *B. subtilis* and LAMP-1 or LC3B are shown with the two overlays for -IPTG on the left and +IPTG on the right for both time points. The z-depth was chosen for each overlayed image and each channel was adjusted to provide a representative image of each scenario. Scale bars = 20 μm.

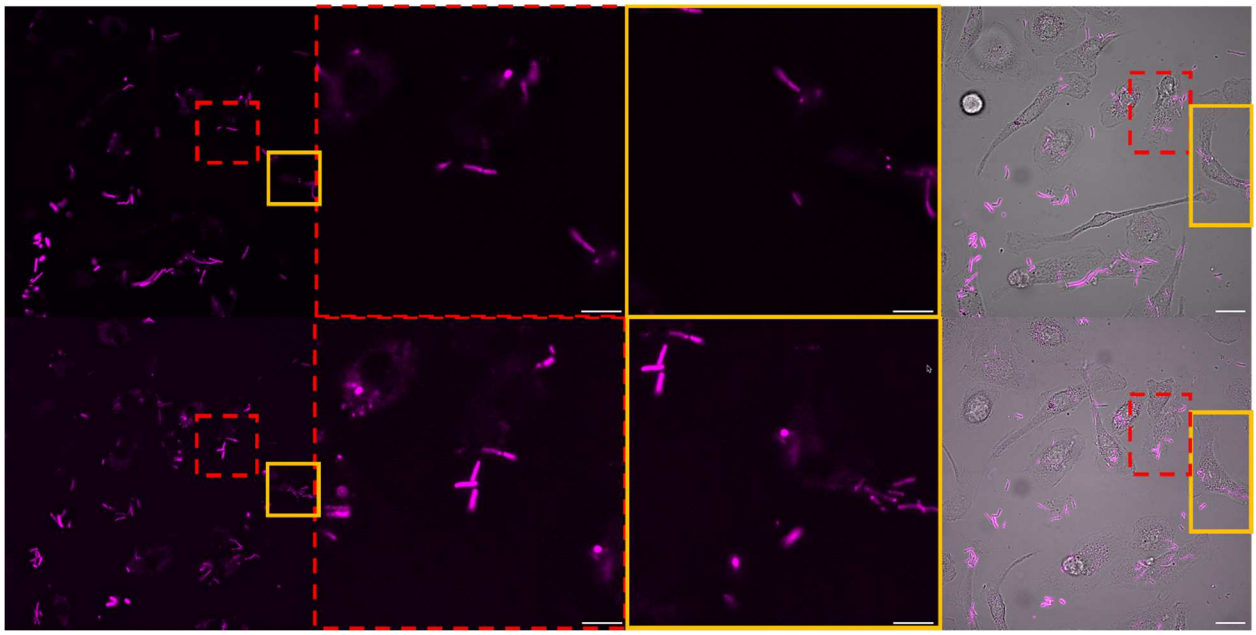

Figure 3.4. Live cell imaging of replicating *B. subtilis* LLO inside live BMDMs

Live cell microscopy revealed the LLO strain replicating in multiple host cells by comparing images at 3 h (top images) and 4.5 h (bottom images) post bacterial addition. BMDMs were visualized in brightfield, and the LLO strain using fluorescence (magenta); zoomed images reveal the LLO strain replication in the cytoplasm. Scale bars = 3 μm for zoomed images and representative scale bars = 20 μm for not zoomed images are in overlay images.

Flow cytometry analysis of BMDM viability and uptake after exposure to *B. subtilis* LLO and change in marker expression in response to engineered *B. subtilis* LLO strains

After, *B. subtilis* LLO (LLO strain) was observed to be taken up by BMDMs and escape phagosomal destruction but be eliminated over time by other responses, host cell viability and rate of uptake was assessed. Flow cytometry analysis was used to determine the number of BMDMs that were positive for CellTracker Orange (CTO) CMRA Dye stained LLO strain (Fig. 3.5). A multiplicity of infection (MOI) at 50:1 was found to be the optimal MOI which had also been shown in live cell imaging experiments with approximately 35% of BMDMs positive for bacteria while the 25:1 MOI resulted in half the cells being positive and 100:1 MOI producing a

similar number of positive cells as 50:1 (Fig. 3.5). BMDM viability was also assessed by flow cytometry at the optimal MOI (50:1) at 4 and 12 h with and without IPTG added to induce LLO expression. After 4 h of incubation with the bacteria, the LLO strain with IPTG induction did cause a small decrease (5% of total cells) in host cell viability (Fig. 3.5). However, at 12 h post incubation, the bacteria did not cause a decrease in host cell viability (Fig. 3.5).

Surface marker expression of BMDMs was evaluated by flow cytometry to begin determining shifts in macrophage function caused by engineered *B. subtilis* LLO strains at 24 and 48 h. The BMDMs were incubated with the LLO strain, LLO-*Stat-1Klf6* (LLO-*SK*)[16] strain and LLO-*Klf4Gata-3* (LLO-*KG*)[16] strain along with the inducer for transcription of the mammalian TFs, D-mannose, to account for shifts in marker expression caused by the sugar[16]. Additionally, the BMDMs were incubated with positive controls to trigger the pro-inflammatory (M1) and anti-inflammatory (M2) phenotypes indicated by expression of cluster of differentiation (CD)86 and CD206 respectively[27]. Lipopolysaccharide (LPS) and interferon-γ (IFN-γ) were used to induce the pro-inflammatory phenotype while interleukin (IL)-4 and IL-13 were used to induce the anti-inflammatory phenotype[115,116]. The positive controls caused significant increases in each appropriate marker while the *B. subtilis* LLO strains only caused minimal shifts in marker expression (Fig. 3.6). For CD86, LPS and IFN-γ increased marker expression by 20- and 10-fold at 24 and 48 h respectively (Fig. 3.6). All bacterial conditions resulted in no significant change in CD86 expression at both 24 and 48h and the LLO-*KG* strain caused a minor trend of decrease at 48 h. For CD206, IL-4 and IL-13 increased marker expression by 5- and 2-fold at 24 and 48 h respectively (Fig. 3.6). At 24 h, the bacterial conditions did increase CD206 significantly. The bacterial treatments with mannose increased the CD206 more than the bacterial treatments without mannose except in the LLO-*KG* strain. At 48 h, the bacterial treatments did not cause a significant change in CD206 expression, and the LLO-*KG* strain appeared to cause a minor decreasing trend. The ratio of CD86 to CD206 expression revealed

minor but more clear shifts between bacterial treatments as shown in the dot plots (Fig. 3.6). The LLO-*KG* strain showed a shift separate from that of the LLO strain alone by reducing the CD86+ population (determine by shown gating strategy) by 7% at 24 h while the LLO-*SK* did not show this trend. A similar but lesser trend was observed again at 48 h and the LLO-*SK* showed an increase in CD86+ population compared to LLO and LLO-*KG* at 48 h.

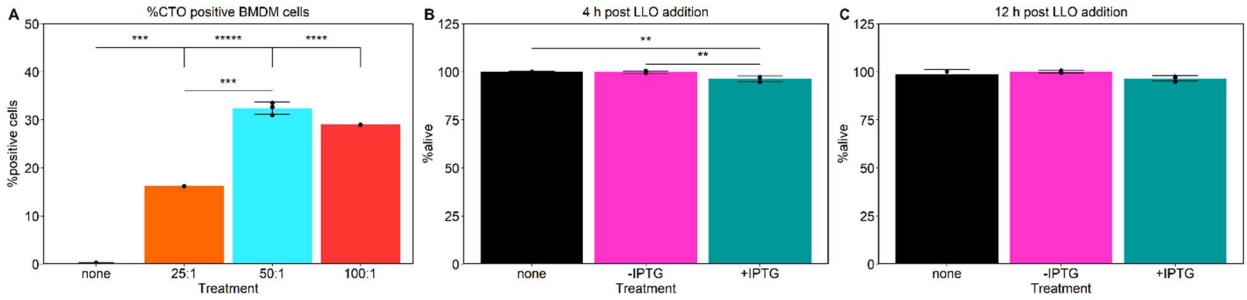

Figure 3.5. Uptake of *B. subtilis* LLO by BMDM and BMDM viability after uptake

BMDMs were treated with CellTracker Orange (CTO) CMRA Dye stained LLO strain with IPTG at different MOIs for 4 h to determine number of cells with bacteria (A). BMDMs were analyzed for viability using flow cytometry at 4 and 12 h at a 50:1 MOI (B-C). Experiments were performed with three biological replicates (n=3) except for 25:1 and 100:1 MOI in uptake experiment (A) which were performed with one biological replicate (n=1) as live cell data had already showed these trends. Data is mean ± SD; **p<0.01, ***p<0.001, ****p<0.0001, *****p<0.00001.

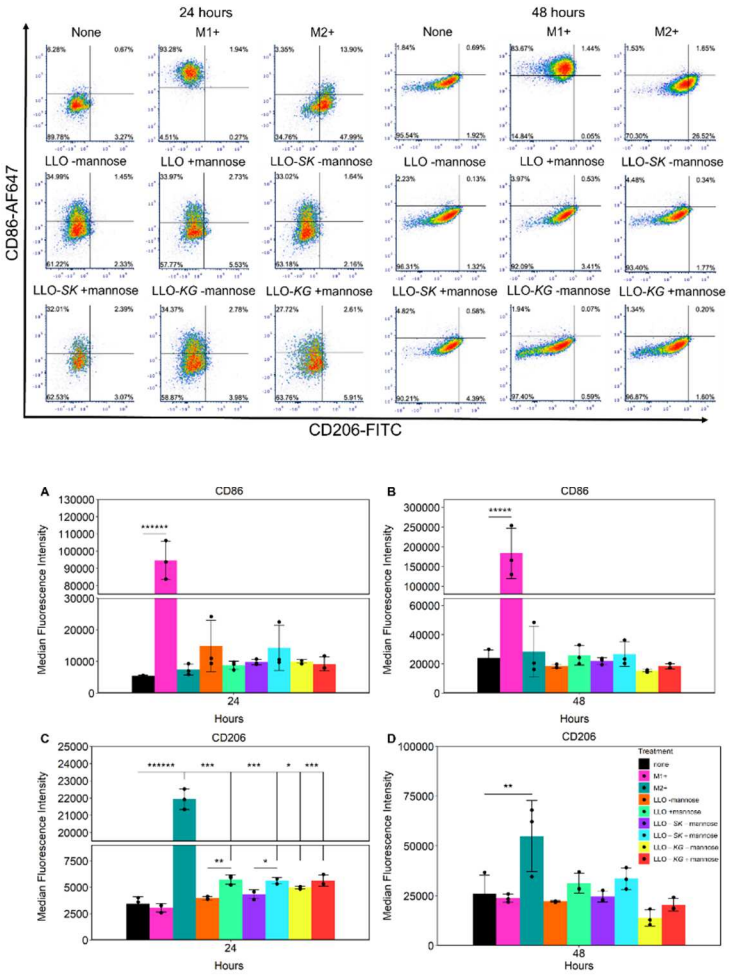

Figure 3.6. Flow cytometry indicated engineered *B. subtilis* LLO strains caused minor shifts in BMDMs cell marker expression

Flow cytometric analysis revealed some shifts in ratio of expression of CD86 and CD206 induced by engineered *B. subtilis* LLO strains. The dot plots are representative examples, taken as the median value of n=3. Plotted CD86 or CD206 median fluorescence intensity (MFI) is compared among all treatments at 24 and 48 h with (lower panel). BMDMs cells were untreated (none), treated with LPS and IFN-γ (M1+), IL-4 and IL-13 (M2+), *B. subtilis* strain 168 (168), LLO strain (LLO), LLO-*SK* with and without mannose (LLO-*SK* -mannose, LLO-*SK* +mannose) and LLO-*KG* with and without mannose (LLO-*KG* -mannose, LLO-*KG* +mannose) at 24 and 48 h post initial treatment. Plotted data is mean ± SD from n=3 biological replicates; *p<0.05, **p<0.01, ***p<0.001, *****p<0.00001, *****p<0.00001.

Engineered *B. subtilis* LLO strains modulate BMDM cytokine and chemokine production

Cytokine and chemokines are important for signaling to other immune cells in different tissue environments[24,26]. Therefore, profiling the BMDMs production of these proteins after exposure to the engineered *B. subtilis* LLO strains is essential for predicting some potential impacts *in vivo*. The BMDMs showed a significant increase in many cytokines and chemokines in response to the bacterial treatments (several hundred or thousand-fold in some instances) and in many cases more than the positive controls (Fig. 3.7, 3.8). Also, the engineered *B. subtilis* LLO strains showed differential regulation in some cytokines and chemokines and D-mannose was observed to be the primary regulator of certain cytokines and chemokines (Fig. 3.7, 3.8). LLO-*SK* and LLO-*KG* differentially regulated IL-10, macrophage inflammatory protein-1α (MIP-1α) and granulocyte colony stimulating factor (G-CSF) especially when transcription was induced by D-mannose in comparison to each other and with the same trends observed compared to the LLO strain at 24 h (Fig. 3.7A, E-F). The LLO-*KG* increased IL-6 in relation to LLO-*SK* and the LLO strain at 24 h (Fig. 3.7B). Tumor necrosis factor alpha (TNF-α) increased to all bacterial treatments at 24 h but at 48 h only the LLO-*SK* strain with mannose added was significant in comparison to the untreated and comparable to that of the positive control (Fig. 3.7C-D). MIP-2 (CXCL2) and monocyte chemoattractant protein-1 (MCP-1/CCL2) showed specific responses to D-mannose with the different engineered strains still causing different patternicity even with the complexity of the D-mannose at 24 h (Fig. 3.7G-H). D-mannose continue to impact the expression of these two proteins at 48 h as well (Fig. 3.8E-F).

While most cytokines and chemokines production were triggered more by the bacteria than the positive controls, IL-12p40 and vascular endothelial growth factor (VEGF) did not show these trends. Production of both IL-12p40 and VEGF at 24 and 48 h increased in response to M1 positive control by either hundreds or tens-fold respectively (Fig. 3.8M-P). The bacteria did

not cause such large increases. Yet, at 24 h, IL-12p40 did exhibit differential regulation by LLO-*SK* and LLO-*KG* observed previously[16]. LLO-*KG* increased production of IL-12p40 by 5-fold in comparison to the untreated which is significant when the hundreds-fold higher positive control is not included in the one-way analysis of variance (ANOVA) statistical analysis ($p<0.002$). However, many of the cytokines and chemokines such as IL-10, IL-6 and MCP-1 are examples that did not show any differences in the bacterial treatments at 48 h (Fig. 3.8A-F). Furthermore, some of the cytokines such as IL-15 and granulocyte-macrophage colony stimulating factor (GM-CSF) were not significantly produced in response to any treatments (Fig. 3.8G-H, K-L). Finally, IL-1β was significantly produced only in response to the bacterial treatments at both 24 and 48 h but no production difference was observed between the bacterial treatments (Fig. 3.8I-J).

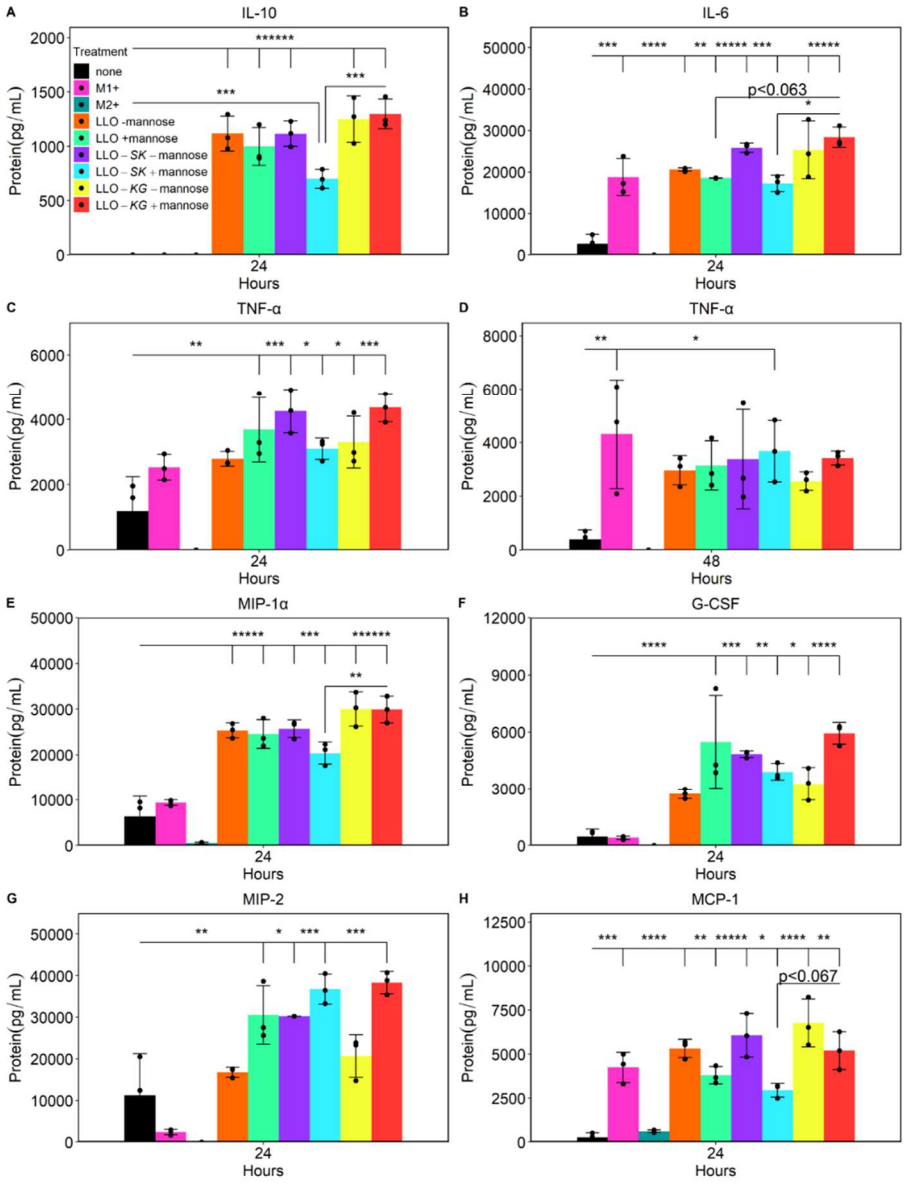

Figure 3.7. Engineered *B. subtilis* LLO strains altered BMDMs cytokine and chemokine production

Cytokine and chemokine protein concentration was quantified after BMDMs cells were untreated (none), treated with LPS and IFN-γ (M1+), IL-4 and IL-13 (M2+), LLO strain with and without mannose (LLO -mannose, LLO +mannose), LLO-*SK* with and without mannose (LLO-*SK* -mannose, LLO-*SK* +mannose) and LLO-*KG* with and without mannose (LLO-*KG* -mannose, LLO-*KG* +mannose) at 24 and 48 h post initial treatment. Data is mean ± SD from n=3 biological replicates; *p<0.05, **p<0.01, ***p<0.001, ****p<0.0001, *****p<0.00001, ******p<0.000001.

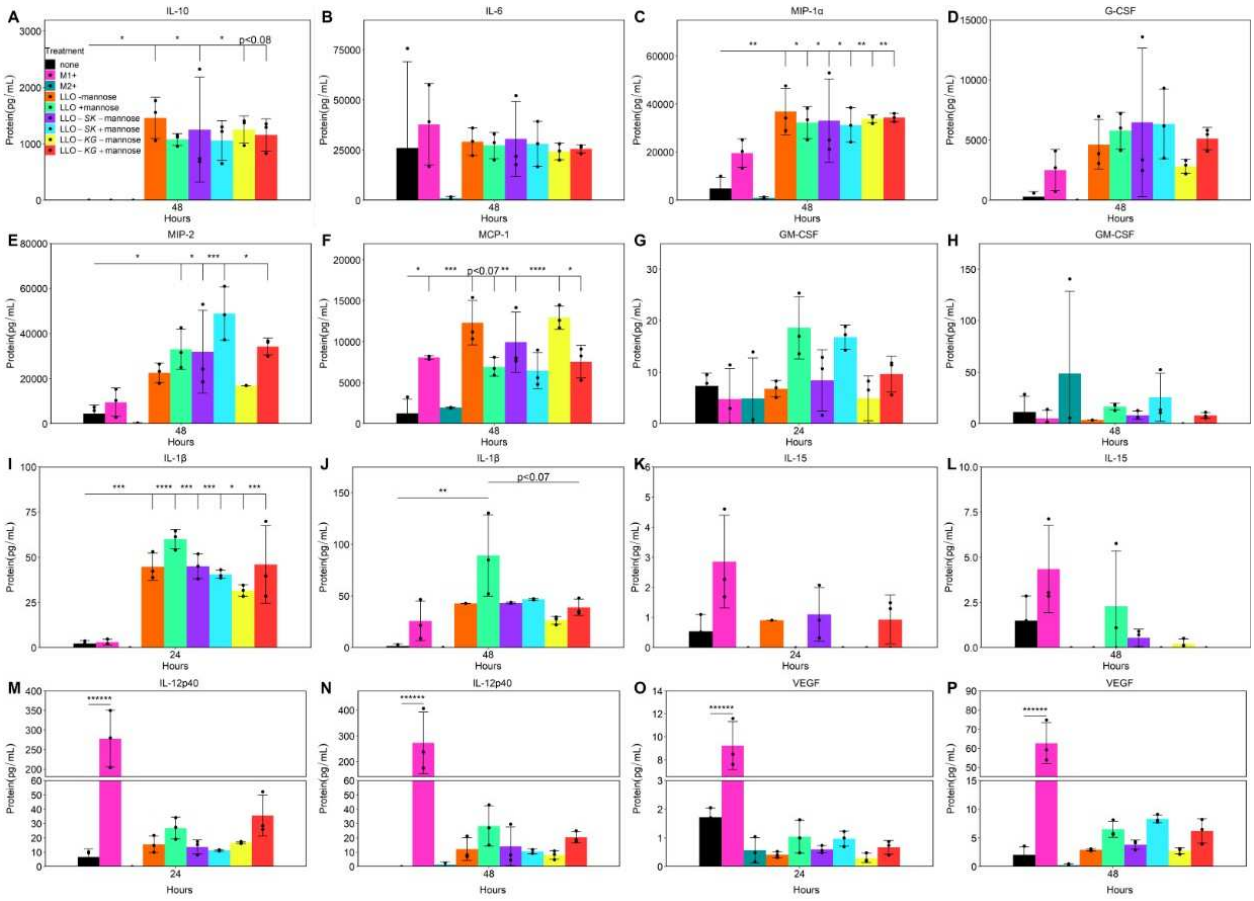

Figure 3.8. Further profiling of BMDMs cytokine and chemokine production after exposure to engineered *B. subtilis* LLO strains

Cytokine and chemokine protein concentration was quantified after BMDMs cells were untreated (none), treated with LPS and IFN-γ (M1+), IL-4 and IL-13 (M2+), LLO strain with and without mannose (LLO -mannose, LLO +mannose), LLO-*SK* with and without mannose (LLO-*SK* -mannose, LLO-*SK* +mannose) and LLO-*KG* with and without mannose (LLO-*KG* -mannose, LLO-*KG* +mannose) at 24 and 48 h post initial treatment. Data is mean ± SD from n=3 biological replicates; *p<0.05, **p<0.01, ***p<0.001, ****p<0.0001, *****p<0.00001, ******p<0.000001.

Engineered *B. subtilis* LLO strains adjust functional metabolism patterns in BMDMs

Functional metabolism provides valuable insight into the activity and response of macrophages to various stimuli[117]. Additionally, D-mannose has been shown to impact

macrophage metabolism and functional response[118] which should be considered in this study. As a result, BMDM functional metabolism was characterized in response to the engineered *B. subtilis* LLO strains and mannose with LPS serving as a control and comparison to other studies[35,36]. Overall, the D-mannose and engineered *B. subtilis* LLO strains modified BMDMs functional metabolism in unique patterns at both 12 and 24 h when oxygen consumption rate (OCR), extracellular acidification rate (ECAR), ATP production and shifts between glycolysis and oxidative phosphorylation were measured (Fig. 3.9, 3.10, Table 3.1-2). The bacterial treatments increased OCR and ECAR similar to that of the LPS treatment at 12 h while D-mannose produced similar results to the untreated. The LLO-*KG* strain with and without mannose increased OCR and ECAR more than any other conditions at 12 h (Fig. 3.9C-D). Conversely, at 24 h, D-mannose overtook all other treatments as the dominating stimulus driving metabolism change even in the bacterial treatments (Fig. 3.10C-D). The LLO-*KG* strain still caused trends of increase in OCR and ECAR but only without the addition of D-mannose.

To further unravel the complexity of the response to the bacteria alone and how the TFs may be impacting metabolism change, changes in OCR (ΔOCR) and ECAR (ΔECAR) were evaluated when electron transport chain inhibitors including Oligomycin (complex V) and Rotenone (complex I)/Antimycin A (AA; complex III) were added[119]. At 12 h, LLO-*KG* with and without D-mannose was the only treatment to cause a significant change in OCR when Oligomycin was added, and Rotenone/AA treatment resulted in similar results as basal OCR (Fig. 3.9E, G). Yet, when evaluating changes in ECAR at 12 h, Rotenone/AA addition revealed differential trends from the LLO-*SK* and LLO-*KG* strains and showed a distinct change from the D-mannose treatment (Fig. 3.9H). At 24 h, D-mannose continued to be the most important stimulus when evaluating changes in OCR after all inhibitors were added (Fig. 3.10E, G). However, the changes in ECAR after inhibitors at 24 h exhibited less dictation by D-mannose

and even some differential trends between the engineered *B. subtilis* LLO strains when Oligomycin was added (Fig. 3.10F).

Quantification of transference in energy generation between glycolysis and oxidative phosphorylation demonstrated that the bacterial treatments shifted metabolism to glycolysis from oxidative phosphorylation at 12 h (Table 3.1). The LLO-*KG* strain with mannose generated the most significant shift to glycolysis ($p<0.007$) and comparable to that of LPS ($p<0.005$) while LLO-*SK* did not produce a significant shift. Additionally, total ATP production rate followed the same trends as the LLO-*KG* with mannose increased ATP rates by 4-fold compared to the untreated ($p<0.01$) and the LLO strain with mannose increased ATP rates by 3-fold compared to the untreated at 12 h ($p<0.07$). D-mannose diverted all energy production to oxidative phosphorylation and reduced ATP production rate at 12 h (Table 3.1). Energetic shifts between glycolysis and oxidative phosphorylation and ATP production rates also paralleled the OCR and ECAR results at 24 h except in the LLO-*KG* with mannose treatment (Table 3.2). The treatment of D-mannose at 24 h shifted energy generation towards glycolysis instead of oxidative phosphorylation which was inverse of trends at 12 h. The LLO-*KG* strain inhibited that shift when treated with D-mannose which maintained similarity to the other bacterial treatments without D-mannose whereas the LLO strain and LLO-*SK* strain were impacted by the treatment of D-mannose significantly, $p<0.04$ and $p<0.004$ respectively (Table 3.2). However, ATP production rates were driven by D-mannose in all bacterial treatments and were like that of the D-mannose treatment alone.

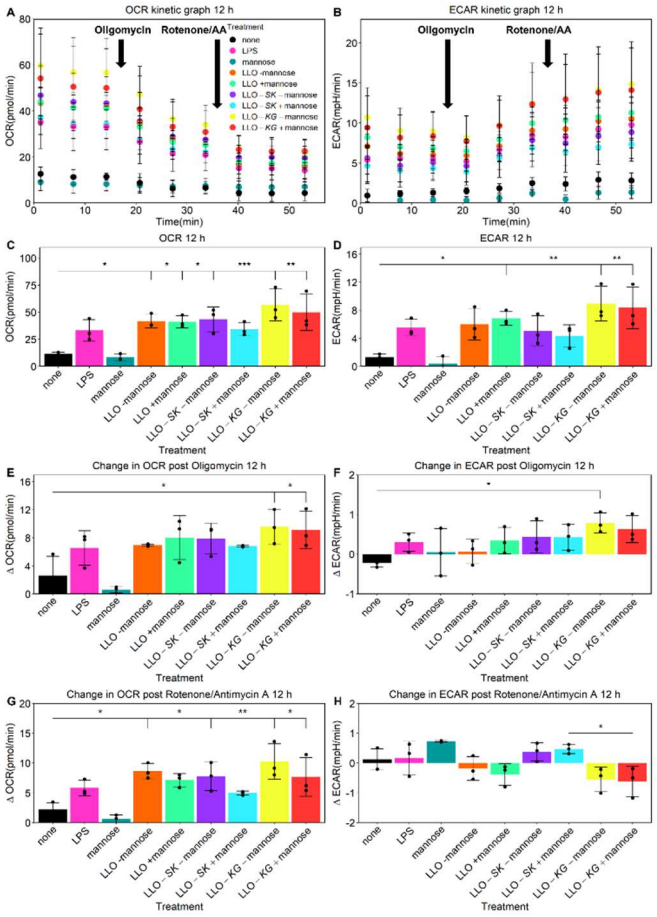

Figure 3.9. Shifts in functional metabolism patterns of BMDMs at 12 h after exposure to engineered *B. subtilis* LLO strains

Oxygen consumption rate (OCR) and extracellular acidification rate (ECAR) were measured before and after electron transport chain inhibitors, Oligomycin and Rotenone/antimycin A (AA), were added at points indicated on kinetic plot (A, B). OCR and ECAR quantification at the third measurement before addition of inhibitors was plotted (C, D). Further analysis was performed to quantify changes in OCR (ΔOCR) and ECAR (ΔECAR) after inhibitors were added (E-H). BMDMs were untreated (none), treated with LPS, mannose, LLO strain with and without mannose (LLO -mannose, LLO +mannose), LLO-*SK* with and without mannose (LLO-*SK* -mannose, LLO-*SK* +mannose) and LLO-*KG* with and without mannose (LLO-*KG* -mannose, LLO-*KG* +mannose). Data is mean ± SD from n=3 biological replicates; *p<0.05, **p<0.01, ***p<0.001.

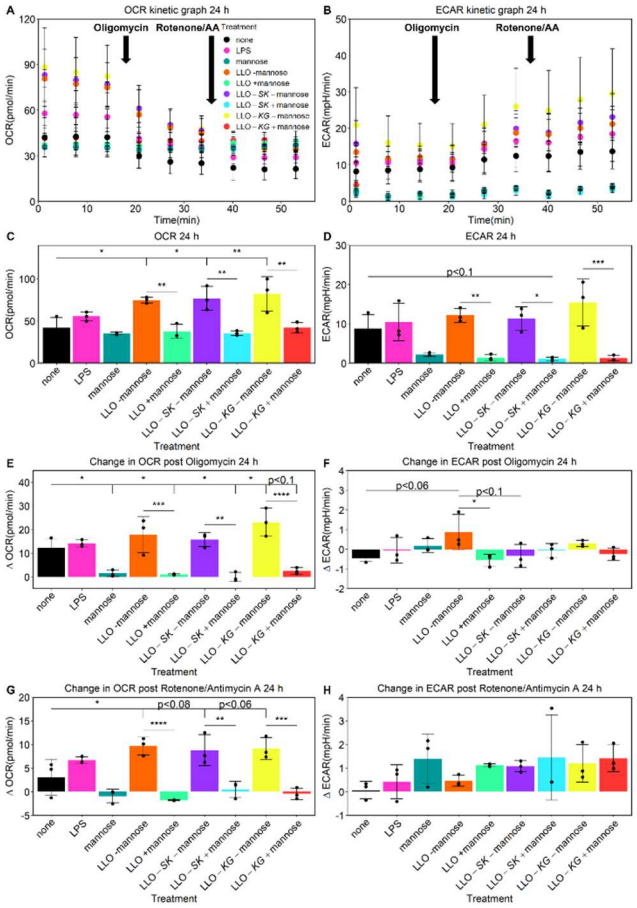

Figure 3.10. Functional metabolism patterns of BMDMs at 24 h after exposure to engineered *B. subtilis* LLO strains

Oxygen consumption rate (OCR) and extracellular acidification rate (ECAR) were measured before and after electron transport chain inhibitors, Oligomycin and Rotenone/antimycin A (AA), were added at points indicated on kinetic plot (A, B). OCR and ECAR quantification at the third measurement before addition of inhibitors was plotted (C, D). Further analysis was performed to quantify changes in OCR (ΔOCR) and ECAR (ΔECAR) after inhibitors were added (E-H). BMDMs were untreated (none), treated with LPS, mannose, LLO strain with and without mannose (LLO -mannose, LLO +mannose), LLO-*SK* with and without mannose (LLO-*SK* -mannose, LLO-*SK* +mannose) and LLO-*KG* with and without mannose (LLO-*KG* -mannose, LLO-*KG* +mannose). Data is mean ± SD from n=3 biological replicates; *p<0.05, **p<0.01, ***p<0.001, ****p<0.0001.

Table 3.1. Quantification table for functional metabolism shifts between glycolysis and oxidative phosphorylation and resulting differences in ATP production at 12 h

Quantification of shifts between glycolysis and oxidative phosphorylation and resulting impact on ATP production when BMDMs were untreated (none), treated with LPS, mannose, LLO strain with and without mannose (LLO -mannose, LLO +mannose), LLO-*SK* with and without mannose (LLO-*SK* -mannose, LLO-*SK* +mannose) and LLO-*KG* with and without mannose (LLO-*KG* -mannose, LLO-*KG* +mannose) at 12 h post addition of treatments.

	Basal Rates(Average) 12 h											
	glycoATP Production Rate(pmol/min)		mitoATP Production Rate (pmol/min)		Total ATP Production Rate(pmol/min)		XF ATP Rate Index		% Glycolysis		% Oxidative Phosphorylation	
Groups	Average	StDev	Average	StDev	Average	StDev	Average	StDev	Average	StDev	Average	StDev
Untreated	7.4	3.2	28.3	11.2	35.8	13.7	4.1	1.6	20.9	6.5	79.1	6.5
LPS 100ng/ mL	38.7	7.7	67.3	18.0	106.0	25.7	1.7	0.1	36.8	1.5	63.2	1.5
Mannose	2.9	8.6	6.0	1.1	8.9	9.8	-2.596	3.810	-46.335	127.003	146.3	127.0
LLO	39.1	17.9	90.1	18.5	129.2	36.0	2.5	0.8	29.3	6.0	70.7	6.0
LLO +mannose	48.1	6.9	88.5	17.9	136.6	24.2	1.8	0.2	35.4	2.6	64.6	2.6
LLO-SK	31.9	15.5	87.2	27.2	119.1	42.2	2.9	0.5	26.1	3.7	73.9	3.7
LLO-SK +mannose	28.7	12.0	66.9	15.1	95.7	25.3	2.6	0.9	29.2	7.1	70.8	7.1
LLO-KG	60.3	17.1	125.3	34.0	185.6	51.0	2.1	0.1	32.5	1.0	67.5	1.0
LLO-KG +mannose	59.4	20.5	105.2	43.3	164.6	63.6	1.8	0.2	36.4	2.2	63.6	2.2

Table 3.2. Quantification table for functional metabolism shifts between glycolysis and oxidative phosphorylation and resulting differences in ATP production at 24 h

Quantification of shifts between glycolysis and oxidative phosphorylation and resulting impact on ATP production when BMDMs were untreated (none), treated with LPS, mannose, LLO strain with and without mannose (LLO -mannose, LLO +mannose), LLO-*SK* with and without mannose (LLO-*SK* -mannose, LLO-*SK* +mannose) and LLO-*KG* with and without mannose (LLO-*KG* -mannose, LLO-*KG* +mannose) at 24 h post addition of treatments.

	Basal Rates(Average) 24 h											
	glycoATP Production Rate(pmol/min)		mitoATP Production Rate (pmol/min)		Total ATP Production Rate(pmol/min)		XF ATP Rate Index		% Glycolysis		% Oxidative Phosphorylation	
Groups	Average	StDev	Average	StDev	Average	StDev	Average	StDev	Average	StDev	Average	StDev
Untreated	68.0	27.3	93.2	31.3	161.1	56.7	1.4	0.3	42.0	5.7	58.0	5.7
LPS 100ng/ mL	79.1	42.2	109.2	11.7	188.3	53.3	1.6	0.6	40.2	9.7	59.8	9.7
Mannose	20.1	4.1	8.3	7.4	28.5	11.3	0.38	0.27	74.2	14.4	25.8	14.4
LLO	86.3	15.0	165.0	13.0	251.4	26.5	1.9	0.2	34.2	2.6	65.8	2.6
LLO +mannose	13.3	6.8	5.9	1.2	19.2	6.9	0.52	0.28	67.3	11.6	32.7	11.6
LLO-SK	78.9	22.2	167.0	35.2	246.0	55.3	2.2	0.4	31.8	3.6	68.2	3.6
LLO-SK +mannose	9.4	3.9	5.3	6.1	14.7	10.0	0.44	0.45	74.3	23.8	25.7	23.8
LLO-KG	113.0	45.1	190.5	64.2	303.5	109.3	1.7	0.2	36.8	2.0	63.2	2.0
LLO-KG +mannose	10.5	6.0	14.6	8.9	25.1	14.8	1.4	0.2	42.0	4.3	58.0	4.3

Tumor microenvironment functional metabolism was modified by engineered *B. subtilis* LLO strains when injected in vivo during pilot study

Metabolism has been linked to cancer progression and even to enhancing metastasis so manipulating metabolism could be a method of therapy in cancer[28–30,119]. Combining this knowledge with the results that the engineered *B. subtilis* LLO strains could modulate functional metabolism, the TME metabolism was characterized[119]. Bioluminescent, non-pathogenic *B. subtilis* LLO-*luxA-E*[120,121] (LLO-*lux*) was shown to localize to 4T1 orthotopic tumors and persist in the tumor for a week after intravenous (IV) injection of 10^8 bacteria into the tail vein while being cleared from healthy BALB/c mice in 24 h (Fig. 3.11). Previously, bacterial cancer treatments have been shown to be most effective at reducing tumor growth and altering the tumor environment when injected intratumorally (IT)[72,73,87,122]. Therefore, comparing the impact of the engineered *B. subtilis* LLO strains on the TME through different methods of delivery was essential for optimizing effectiveness. The LLO-*KG* strain was selected for the pilot study to be compared to the LLO-*lux* strain and D-mannose treatments because of the results in the cytokine/chemokine and *in vitro* functional metabolism studies (Fig. 3.7, 3.9). After dissociation of the tumors one week post the second weekly bacteria injection when tumor growth stabilization caused by the bacteria had been observed without impact on overall mouse health (Fig. 3.12), the tumor functional metabolism exhibited a reduction in the bacterial treatments with differences between strains and methods of delivery (Fig. 3.13).

D-mannose (with IPTG to compare to bacterial treatments) treatment in the mouse water increased both OCR and ECAR marginally but significantly in the tumors (Fig. 3.13C-D). To allow for proper comparison, the mice injected with the LLO-*lux*, and LLO-*KG* strains were treated with D-mannose in the same way as the D-mannose treatment alone. The LLO-*lux* strain and LLO-*KG* strain treatments both reduced OCR in the tumor TMEs when injected IV

(LLO-*lux* IV, LLO-*KG* IV) and the LLO strain caused the greatest reduction which was matched by the LLO-*KG* strain when injected IT (LLO-*KG* IT, Fig. 3.13C). LLO-*KG* IV increased ECAR compared to the untreated tumors while LLO-*lux* IV and LLO-*KG* IT decreased ECAR (Fig. 3.13D). Inhibitors were used again to provide further insights into changes in the respiratory chain with FCCP added as an uncoupler for mitochondrial oxidative phosphorylation[119] to increase understanding of potential mitochondrial stress. After addition of each inhibitor or the uncoupler while measuring OCR, the same trend in results as with basal OCR were observed for each of the changes in OCR (Fig. 3.13E, G, I). These changes included ATP production (calculated from change after Oligomycin addition), max respiration (calculated from change after FCCP addition) and spare capacity (calculated from change between basal OCR and OCR after FCCP). Changes in ECAR after each chemical addition produced more distinct trends between the different treatments. The LLO-*KG* IV treatment caused the greatest change in ECAR after Oligomycin addition, and these changes were significant compared to the LLO-*lux* IV treatment and nearly significant compared to the alternate delivery method for LLO-*KG* (Fig. 3.13F). Conversely, when FCCP and Rotenone/AA were added, the three bacterial treatments significantly reduced the change in ECAR compared to the untreated and D-mannose treatment with the LLO-*KG* IV treatment causing the least reduction (Fig. 3.13H, J).

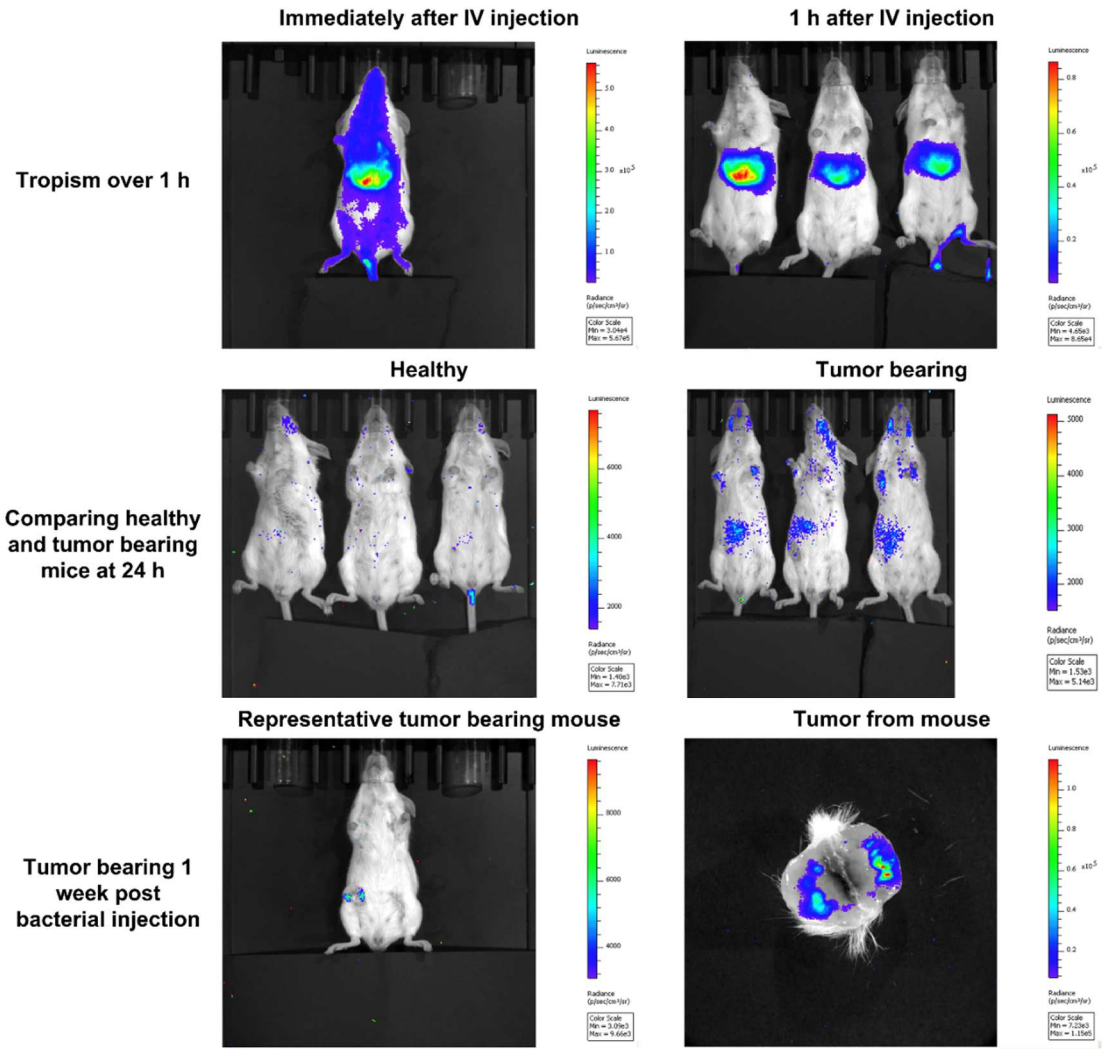

Figure 3.11. Bioluminescent imaging of LLO-*lux* strain after intravenous injection into representative healthy and tumor bearing mice

Representative healthy and 4T1 orthotopic tumor bearing BALB/c mice were injected with 10^8 LLO-*lux* intravenously and tracked using the *In Vivo* Imaging System (IVIS). Representative images are shown from immediately after injection, 1 h post injection, 24 h post injection and 1 week post injection. Healthy and tumor bearing mice showed the same trends immediately after injection and 1 h post injection. However, by 24 h, all bacterial signal is cleared from healthy mice. Finally, bacteria were shown to persist throughout the tumor 1 week post injection.

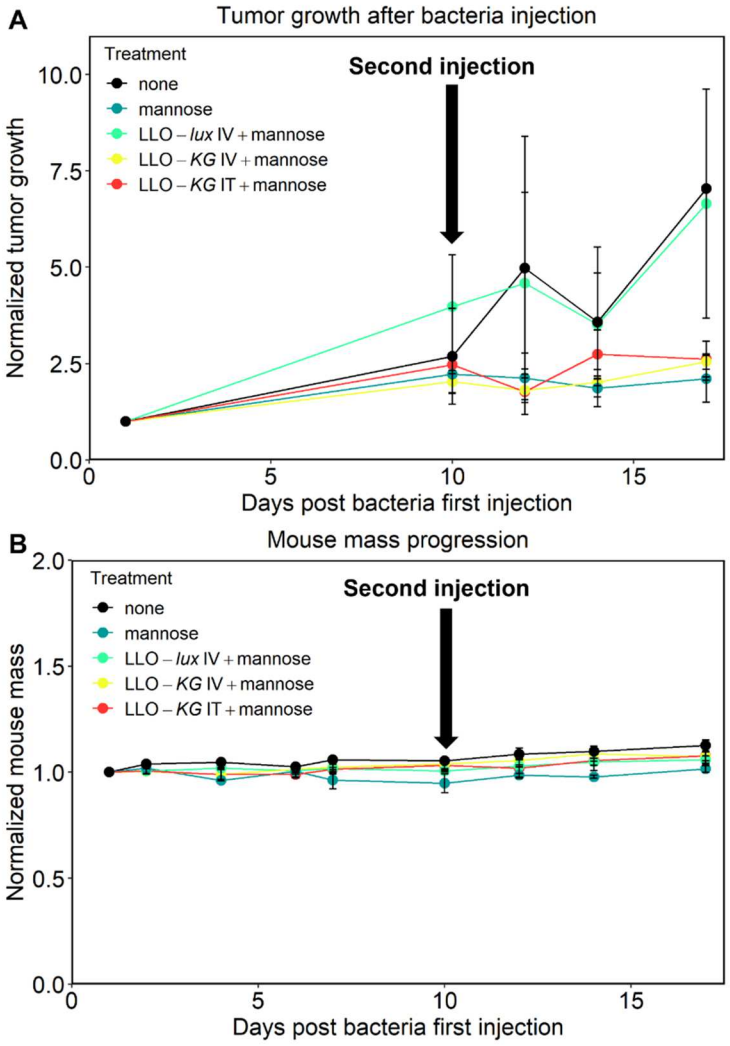

Figure 3.12. Engineered *B. subtilis* LLO strains stabilize tumor growth rate and mouse mass progression during tumor growth

Tumor size measurements by calipers were normalized to tumor sizes on first day of treatments to determine growth rate differences and second injection of bacteria is noted by the arrow (A). Mouse mass was normalized to mass on first day of bacterial injection to evaluate mass progression as an indicator of health (B). Tumors were untreated (none), treated with mannose, LLO-*lux* strain injected intravenously with mannose (LLO-*lux* IV +mannose), LLO-*KG* injected intravenously and intratumorally with mannose (LLO-*KG* IV +mannose, LLO-*KG* IT +mannose). Plotted data is mean ± SEM (A) or mean ± SD (B) from n=3 or n=2 (mannose only) tumors (A) or mice (B).

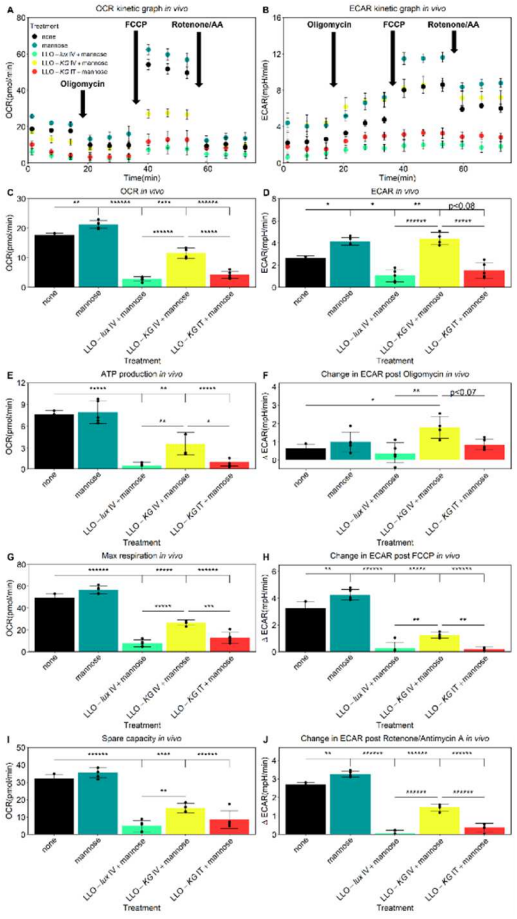

Figure 3.13. Bacteria-mediated reduction of functional metabolism in TMEs

Oxygen consumption rate (OCR) and extracellular acidification rate (ECAR) were measured before and after electron transport chain inhibitors, Oligomycin and Rotenone/antimycin A (AA), and uncoupler, FCCP, were added at points indicated on kinetic plot (A, B). OCR and ECAR quantification at the third measurement before addition of inhibitors and uncoupler was plotted (C, D). Further analysis was performed to quantify changes in OCR (ATP production, max respiration, spare capacity) and ECAR (ΔECAR) after inhibitors and uncoupler were added (E-H). Tumors were untreated (none), treated with mannose, LLO-*lux* strain injected intravenously with mannose (LLO-*lux* IV +mannose), LLO-*KG* injected intravenously and intratumorally with mannose (LLO-*KG* IV +mannose, LLO-*KG* IT +mannose). Data is mean ± SD from n>4 replicate wells seeded from one representative tumor; *p<0.05, **p<0.01, ***p<0.001, ****p<0.0001, *****p<0.00001, ******p<0.000001.

Tumor immunophenotyping identified immune cell population changes caused by engineered *B. subtilis* LLO strains during pilot study

Tumor immunophenotyping by flow cytometry provides important insights into different immune cell populations and can be used as a measure of efficacy in therapies by promoting immune cell invasion to alter the TME[123–125]. This method has even been used in bacterial cancer treatment to understand the benefits of using bacteria to activate immune cells towards treating cancer[71]. In parallel with the tumor functional metabolism characterization, the immunophenotyping was performed after dissociation of the tumors. Profiling of the tumor immune cell populations displayed that the engineered *B. subtilis* LLO strains can promote immune cell invasion causing alteration in cell populations in the tumors (Fig. 3.14). To analyze leukocytes, CD45 positive cells[123] were identified from the live tumor cell populations with the LLO-*KG* IV treatment causing a reproducible trend of increase in CD45+ cells and D-mannose also causes a slight increase (Fig. 3.14A). Once the leukocytes were identified, various T cell lineages were analyzed from all CD45+ cells. T cell populations (CD3+)[123] increased significantly in the D-mannose treatment and the LLO-*KG* IV treatment also causes a trending increase in total T cell population with a similar change observed in naïve T cells (CD4+)[123] and the LLO-*lux* IV treatment caused a small increase (Fig. 3.14B-C). For cytotoxic T cells (CD8+)[123], the treatments caused a modest decrease in this T cell population except the LLO-*KG* IT treatment (Fig. 3.14D). Dendritic cell (CD11c+/MHCII+)[123] populations were marginally increased by the LLO-*KG* IV and IT treatments in comparison to the LLO-*lux* IV and other treatments (Fig. 3.14E). Regulatory T cell (CD25+)[123] populations were altered by any of the treatments (Fig. 3.14F). Lastly, when analyzing the different tumor cells, distinct populations were observed to have increases in expression of the markers that identify these populations. All treatments besides LLO-*KG* IT increased CD45 expression to some extent with the LLO-*KG* IV causing the largest increase compared to the untreated tumors (Fig 3.14G). Similarly, all

treatments increased the expression of the CD8α+ cell populations to similar levels of significance compared to the untreated tumors (Fig. 3.14G). Overall, the engineered *B. subtilis* LLO strains altered the immune cell populations in the tumors while maintaining a similar concentration of bacteria between the strains and delivery methods in the tumors (Fig. 3.15).

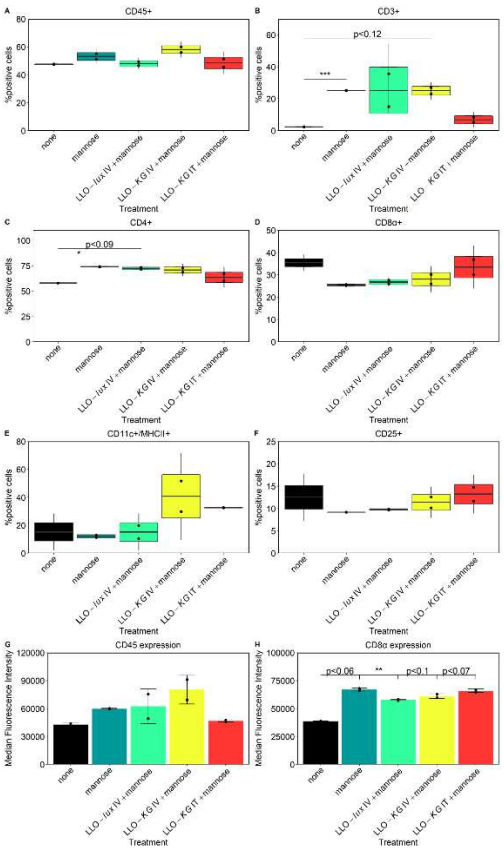

Figure 3.14. Tumor immunophenotyping revealed alterations in tumor immune cell populations

Tumor immunophenotyping by flow cytometry after tumor dissociation on tumors that were untreated (none), treated with mannose, LLO-*lux* strain injected intravenously with mannose (LLO-*lux* IV +mannose), LLO-*KG* injected intravenously and intratumorally with mannose (LLO-*KG* IV +mannose, LLO-*KG* IT +mannose). CD45 expression was analyzed on live cells to identify leukocytes. CD45+ cells were gated for CD11b (myeloid lineage cells) and CD3+ (T cells). CD3+ cells were analyzed for CD4 (helper) and CD8α (cytotoxic) T cells. Dendritic cell populations (CD11c+/MHCII+) and regulatory T cells (CD25+) were also quantified. Further analysis showed changes in marker expression by median fluorescence intensity in the populations of CD45+ and CD8α+ populations. Data is mean ± SD for box and two times ± SD for whiskers (A-F) while the marker expression is mean ± SD (G-H) from n=2 tumors from each treatment; *p<0.05, **p<0.01, ***p<0.001.

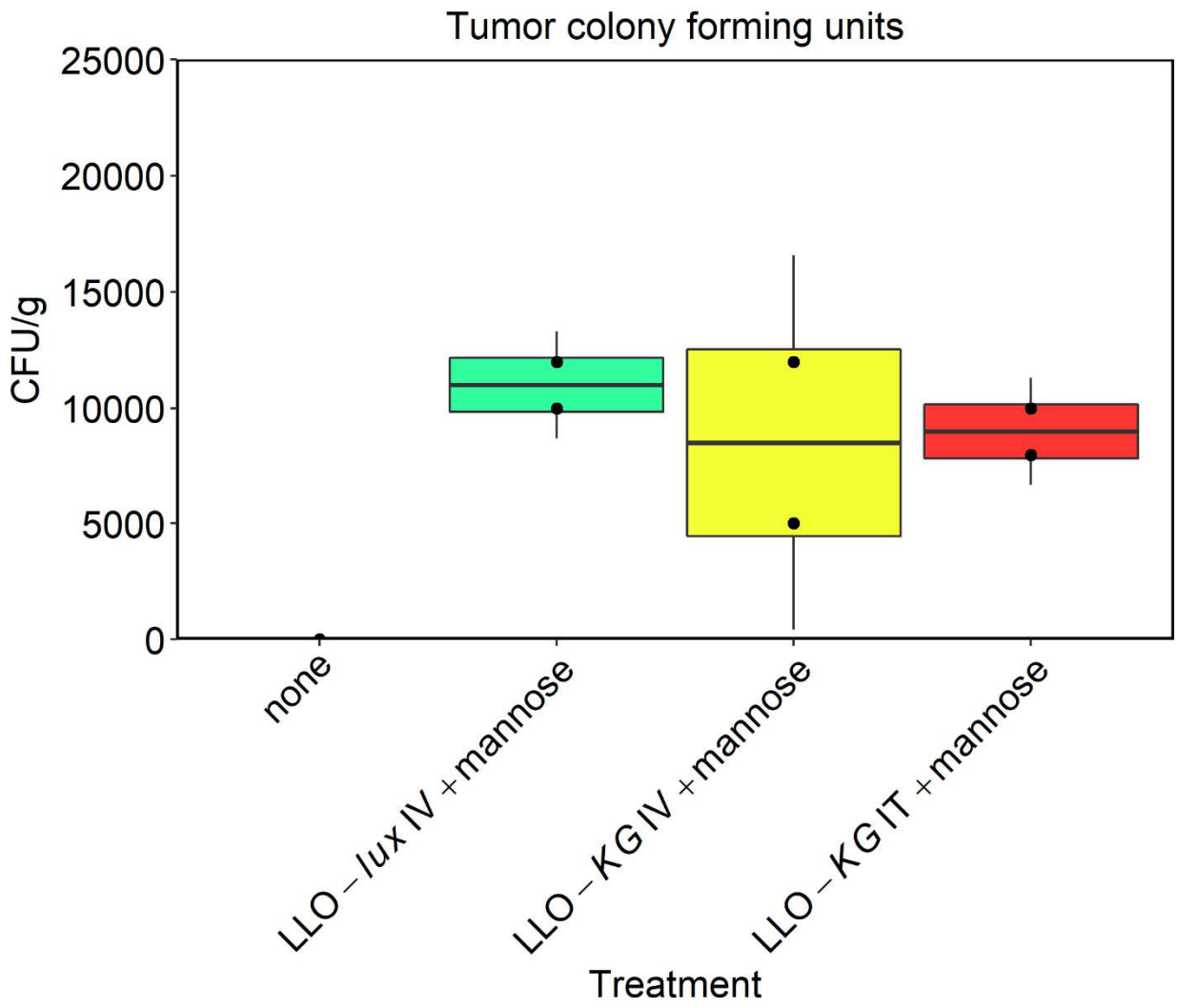

Figure 3.15. Colony forming units demonstrated bacterial persistence in tumors over a week after last injection

Colony forming units (CFU) were calculated and normalized to tumor weight (g) after second half of tumor that was not used for tumor immunophenotyping was homogenized then diluted and plated for bacteria growth. Tumors were untreated (none), LLO-*lux* strain injected intravenously with mannose (LLO-*lux* IV +mannose), LLO-*KG* injected intravenously and intratumorally with mannose (LLO-*KG* IV +mannose, LLO-*KG* IT +mannose). Data is mean ± SD for box and two times ± SD for whiskers from n=2 tumors that were plated in duplicate from each treatment.

DISCUSSION

For the EES platform to be effective at altering macrophage function and be used in applications such as cancer treatment, the EES must interact with the host cells intracellularly to deliver TFs. *B. subtilis* LLO gained access to the cytoplasm of BMDMs with IPTG induction of LLO expression (Fig. 3.3) and remained viable to deliver TFs as shown by replication (Fig. 3.4) with both events required to demonstrate translatability to primary macrophages such as BMDMs. Even with destruction by LC3 related autophagy mechanisms[111–114], the bacteria persisted for several hours which provided time for TF delivery. Furthermore, the natural removal of the bacteria indicated safety of the EES platform when used as a therapy. Yet, if the therapy measures required further interaction between the host cell and engineered *B. subtilis* LLO strains, proteins such as phospholipases (plc) A and B from *L. monocytogenes* could be introduced into the *B. subtilis* LLO chassis to evade the autophagy mechanisms[114] but replication would need to be considered. After confirmed escape of *B. subtilis* LLO from phagosomes with resulting replication but destruction through mechanisms triggered by LC3, the BMDMs high viability after these stages of interaction (~95%) displayed promise for altering BMDM function without losing the host cells (Fig. 3.5). Yet, the uptake rate into BMDMs of approximately 35% resulted in an important consideration for other *in vitro* characterization and when transitioning *in vivo* (Fig. 3.5). The consideration included whether engineered *B. subtilis* LLO strains delivering TFs to 35% of the host cell population would result in functional change throughout the population and would that result in efficacy *in vivo*. Accordingly, the results seen throughout the study indicated that the population function was adjusted by the different bacterial strains and the pilot *in vivo* study showed promising trends.

BMDMs marker expression exhibited only minor shifts from the bacterial treatments but strong responses to the characterized controls for increasing these markers. The engineered *B.*

subtilis LLO strains did not increase or decrease CD86 marker expression in comparison to untreated BMDMs and CD206 was increased by the strains but only at 24 h (Fig. 3.6). These responses by the BMDMs to the strains were greatly reduced in comparison to the macrophage cell line response previously[16]. The lack of CD86 expression in response to the non-pathogenic *B. subtilis* LLO from the BMDMs was unexpected because Toll-like receptor 2 (TLR2) triggers inflammatory responses[126,127] but a similar lack of CD86 marker expression has been observed when bacterial TLR agonists were used to stimulate initially resting BMDMs[128]. Unstimulated BMDMs appeared to produce a large response in cytokines but did not change marker expression unless pre-activation was performed before addition of the bacterial TLR agonists[128]. The same concept can also be applied to CD206 which had also been observed in the same previous study[128]. Yet, the CD206 expression response was a bit more complex. CD206 is the mannose binding receptor[129–131] which explains the increase seen in the mannose treatment conditions and acts as a receptor for bacterial surface carbohydrates[132] (Fig. 3.6). Even with these factors, the LLO-*KG* strain was the one strain that caused a significant increase in CD206 expression compared to the untreated in the treatments without D-mannose. CD206 has been recently implicated in promoting innate and adaptive antitumor immune responses when expressed by tumor associated macrophages (TAMs) which suggests translatability for the LLO-*KG* strain[129].

Cytokines and chemokines play essential roles in signaling between various immune cell populations[26,52,133,134]. These proteins have been categorized based on roles in disease progression and for classifying cells but with further evaluation, these proteins have been shown to exhibit pleiotropic effects in diseases progression and in cell classification[47,135–142]. Furthermore, complex stimuli such as live bacteria compounds with the pleiotropic effects to create unexpected responses from macrophages which makes the macrophage phenotype and function difficult to classify[143,144]. Yet, unraveling this complexity provides valuable insight into

outcomes *in vivo* and understanding therapeutic potential. The engineered *B. subtilis* LLO strains stimulated production of many disease especially tumor relevant cytokines and chemokines from the BMDMs with the TFs causing specific regulations (Fig. 3.7, 3.8). The bacterial treatments stimulated production of most of the cytokines and chemokines analyzed indicating the signaling response from the BMDMs to the bacteria. Accordingly, the LLO strain alone caused significant production of the cytokines and chemokines (Fig. 3.7, 3.8). LLO-*SK* and LLO-*KG* differentially regulated IL-10, MIP-1α, G-CSF and IL-12p40 at 24 h with IL-10, G-CSF and IL-12p40 occurring in a predicted pattern based on known regulation[16,103,105,145–147]. LLO-*SK* increased certain cytokines such as TNF-α especially at 48 h which could be useful in altering the TME[148,149]. LLO-*KG* upregulated IL-6 at 24 h which is a predicted result based on the known activity of KLF4[150] while the increase in MIP-1α is unexpected and little is known about transcription factor regulation of MIP-1α with only a few identified[151,152]. MCP-1 was downregulated by LLO-*SK* which is predicted based on the known regulation by nuclear factor kappa light chain enhancer of activated B cells (NF-κB) and STAT-1 can compete with these pathways[153,154]. Additionally, D-mannose regulated the expression of MCP-1 as all treatments with D-mannose downregulated MCP-1. D-mannose appeared to have a similar but opposite effect on MIP-2 as all treatments with D-mannose upregulated this cytokine indicating that D-mannose is playing a role in macrophage response. Overall, the engineered *B. subtilis* LLO strains generated production of beneficial cytokines and chemokines for altering the TME including TNF-α and IL-12p40[148,149,155]. Yet, the pleiotropic effects of some cytokines and chemokines adds ambiguity to whether others may also be beneficial. Two specific examples are IL-6 and MCP-1 because both are implicated in promoting immune cells such as T cells to invade the TME but can also promote tumor angiogenesis when expressed by cancer cells[153,156]. Some cytokines and chemokines such as MIP-1α, MIP-2, G-CSF and IL-10 are implicated in promoting poor outcomes in tumors when produced by TAMs or other cells so the downregulation by LLO-*SK* is beneficial[146,151,157–159]. Therefore, the LLO-*SK* strain appeared to

be the better strain for altering the TME, but the LLO-*KG* still produced beneficial cytokines and chemokines for this application. Nonetheless, the cytokines and chemokines are only one component in altering the TME so other analyses such as functional metabolism was necessary.

With the complexities seen in marker and cytokine/chemokine expression, functional metabolism provides another measure of macrophage phenotype in response to the engineered *B. subtilis* LLO strains and if the adjusted phenotypes could be relevant in tumors. In totality, the bacterial treatments caused increases in metabolism and the Warburg effect[31–38] similar to that of the LPS treatment at 12 h (Fig. 3.9). The LLO-*KG* strain promoted the most significant shift in metabolism with increased OCR, ECAR and ATP production (Fig. 3.9). The activity of KLF4 and GATA-3 provides explanations into the observed result. Both TFs are involved in macrophage metabolism and have been shown be associated with IL-4 cascades and work with STAT-6 to induce nuclear peroxisome proliferator-activated receptor γ (PPARγ) causing mitochondrial biogenesis which results in increased OCR and ATP production and a major reduction in OCR if electron transport inhibitors were added[103,117,160–162]. Additionally, these pathways that are classically associated with shifts to oxidative phosphorylation can be combined with inflammatory stimuli to increase glycolysis simultaneously which is then linked to cytokine and chemokine production such as IL-10, IL-6 and TNF-α[160]. These complex regulatory networks explain how the LLO-*KG* strain significantly increased OCR, ATP production (primarily contributed by increase in mitoATP production rate; Table 3.1) and glycolysis at 12 h then was able to diminish a shift from oxidative phosphorylation to glycolysis caused by D-mannose at 24 h after the bacteria had been eliminated. Additionally, the regulatory networks explain why the LLO-*KG* strain had the most significant reduction in OCR when Rotenone/AA (complex I and complex III inhibitors[163]) were added. ECAR exhibited a similar pattern of response to the treatments as OCR at 12 h but had more unique changes specific to different treatments when

inhibitors were added. ECAR was increased most significantly by the LLO-*KG* treatments in comparison to the untreated which is directed by the increase in glycolysis caused by LLO-*KG* treatments. When the inhibitors Rotenone/AA were added, differential change in ECAR between LLO-*SK* and LLO-*KG* was observed at 12 h which indicated that STAT-1 and KLF6 promoted the electron transport chain running in reverse electron flow as seen in classical pro-inflammatory macrophages because of a positive loss in ECAR[162]. This positive loss in ECAR caused by Rotenone/AA in the LLO-*SK* treatments occurred because complex I generates nicotinamide adenine dinucleotide (NADH) when in reverse electron flow for lactate dehydrogenase to utilize in converting pyruvate to lactate which contributes to ECAR through H^+ production[162,164]. D-mannose also caused the same positive loss in ECAR after Rotenone/AA addition at 12 h because D-mannose contributes to lactate production in macrophages[118]. The major reduction in OCR, ECAR and ATP production with a significant shift towards glycolysis (except in LLO-*KG* condition) at 24 h in the D-mannose treatments resulted from the suppression of glucose utilization seen previously in macrophages[118] (Fig. 3.10, Table 3.2). TAMs have been shown to enhance tumor progression through metabolic measures[160,162,165]. TAMs rely on glycolysis for energy production so therapeutic measures have been proposed to increase PPARγ induction to cause increased phagocytic activity which the LLO-*KG* caused in this study[160,162,165]. However, TAM metabolism is understudied, and complex so further studies are needed to understand the ideal target to adjust TAM metabolism[160,162,165]. These observations from the *in vitro* functional metabolism analyses continued to underscore the complexity of macrophage response and the coordination between metabolism and cytokine/chemokine response which is essential for tissue maintenance and further impact on disease.

After in-depth characterization of the engineered *B. subtilis* LLO interaction with and specific modulation of BMDMs, the translatability of the strains in mobilizing the immune system

to alter the TME was tested. Initially, the LLO-*lux* strain was used to visualize location of bacterial accumulation temporally. The non-pathogenic LLO-*lux* strain was observed to be cleared from healthy mice within 24 h but persisted in tumor bearing mice specifically within the tumors for a week post injection IV which established the potential for the engineered *B. subtilis* LLO strains to be utilized to alter the TME (Fig. 3.11). In the pilot study, LLO-*KG* was used to compared to LLO-*lux* and D-mannose alone because of the beneficial signaling proteins that were produced by the BMDMs and altered metabolism patterns induced after exposure to the strain. Injection methods of IV and IT were compared because of the efficacy shown in previous studies from IT injection[72,73,87,122] but IV adds an additional measure of translatability to show that the bacteria will accumulate wherever the TME is located. After injecting the strains and supplying D-mannose in the drinking water, tumor growth stabilization materialized in the LLO-*KG* treatments especially post the second bacterial injection with some indication of tumor regression in the few days immediately after injection (Fig. 3.12A). However, the LLO-*lux* strain did not produce the same result which signaled strain specificity. Additionally, the D-mannose treatment appeared to stabilize tumor growth (n=2) which has been observed in previous studies[166,167]. None of the treatments resulted in negative overall health effects on the mice which indicated the safety of the *B. subtilis* platform and the transcriptional inducer (Fig. 3.12B). Yet, the tumor metabolism and immunophenotyping analyses were needed to understand the effectiveness in the immune modulation goal of the EES platform. The dissociated tumors from the bacterial treatments all had reduced OCR and accordingly reduced ATP production, max respiration and spare capacity while the D-mannose treatment sustained or increased these properties compared to the untreated which may indicate a shift to glycolysis in the heterogenous TME caused by the bacteria (Fig. 3.13). However, only the LLO-*KG* IV treatment potentially increased glycolysis (ECAR increased) while the other bacterial treatments also reduced ECAR. These results were complex, but the LLO-*KG* IV result seemed to be most beneficial. Carcinoma cell metabolism is classically discussed as being driven by glycolysis, but

this is largely in homogeneous cell culture. In fact, several studies on subtypes of carcinoma especially breast cancer show a reliance on oxidative phosphorylation[168–170]. As a result, the LLO-*KG* IV could have caused a shift to glycolysis at the population level because immune cells were stimulated to invade and the immunophenotyping begins to support this hypothesis (Fig. 3.14). Additionally, as the inhibitors and uncoupler were added, the LLO-*KG* IV treatment continued to cause an increase in ECAR indicating further reliance on glycolysis but less than that of the untreated which could be attributed to immune cells or 4T1 cells. The LLO-*lux* IV and LLO-*KG* IT treatments increased ambiguity as these treatments showed low metabolism overall indicating potentially lower 4T1 metabolism or low immune cells metabolism. Ultimately, the metabolism must be paired with the immunophenotyping. The LLO-*KG* IV also was the most beneficial treatment based on immunophenotyping as total immune cells increased by 15% and had higher expression of CD45 which has shown to indicate activated immune cells[171–173] compared to all other treatments (Fig. 3.14). T cells (CD3+) were a significant portion of these immune cells with the population being largely naïve T cell (CD4+). Yet, a significant portion of the CD3+ were the beneficial tumor disrupting cytotoxic T cells[174–178] that highly expressed CD8α (Fig. 3.14). Dendritic cells were also increased which would be beneficial for altering the TME by activating T cells and increase innate and adaptive immune responses[179–181]. The D-mannose treatment also increased immune cells especially T cells which provides insight on how D-mannose alone alters the TME and contributes to tumor regression seen previously[166,167]. While these markers provide substantial insight into the TME alteration, further markers are being optimized which include CD19 for B cells[123], lymphocyte antigen 6 (Ly6) C and G for monocytic and granulocytic myeloid derived suppressor cells (MDSCs)[182], major histocompatibility complex II (MHCII) and CD206 for pro- and anti-inflammatory macrophages[130,183,184], forkhead box P3 (FOXP3) for improved classification of T cells[185,186] and natural cytotoxicity receptor (NKp46) for natural killer (NK) cells[187]. These markers will be paired with other markers already optimized to appropriately define these subsets of cells. Additionally,

the 4T1 cells can be classified by CD45- and MHCII+ cells which will be used in future studies[188]. Altogether the engineered *B. subtilis* LLO strains altered the TME in the pilot study due to strain specificity as the different strains and delivery method did not impact the number of bacteria present in the tumors (Fig. 3.15).

The functional assays established that the engineered *B. subtilis* LLO strains modulated macrophage function. Yet, on-going RNA-seq analysis will further reinforce changes seen in functional assays and provide an in-depth characterization of gene expression changes caused by the TF delivering strains compared to controls. The pilot study provided valuable insight into the alterations of the TME caused by the engineered *B. subtilis* LLO strains along with what conditions should be used and optimized going forward. Yet, a final study will be necessary to test efficacy from both LLO-*SK* and LLO-*KG* on tumor growth stabilization, alteration of TME by characterizing more immune cell populations by flow cytometry and repeating functional metabolism analysis. Furthermore, these expansions on EES *in vivo* studies will be performed with increased numbers of mice for each treatment and expanding conditions to include all bacterial treatments without D-mannose to understand the role of the sugar in the TME as seen in the pilot study especially in tumor growth stabilization. Also, more thorough safety characterization will be performed by determining if there are negative repercussions on the liver with all bacteria passing through this organ. Ultimately, the EES technology creates a new modular approach to altering macrophage function that can be used in human health applications.

MATERIALS AND METHODS

B. subtilis LLO constructs

B. subtilis expressing IPTG-inducible LLO was provided by Dr. Daniel Portnoy. *B. subtilis* LLO *Stat-1Klf6* (LLO-*SK*) and *B. subtilis* LLO *Klf4Gata-3* (LLO-*KG*) were constructed and utilized in our previous work[16]. These same strains were utilized in this study and the *B. subtilis* LLO *luxA-E* (LLO-*luxA-E*) strain was constructed using the same homologous recombination plasmid (pDR111[189], a gift from Dr. Lee Kroos) to insert the *luxA-E* operon into the *amyE* locus using a natural competence protocol[190]. The construct was selected by spectinomycin then confirmed by PCR amplification out of the genome. The *luxA-E* operon was amplified from a transposon plasmid used for bioluminescent imaging previously[191] then inserted in place of the *lacI* gene in the pDR111 plasmid using inverse PCR then Gibson cloning for constitutive expression from the Phyper-spank promoter. Accordingly, this construct was inserted in the *B. subtilis* LLO *amyE* locus (LLO-*luxA-E* or LLO-*lux*).

Growth conditions for *B. subtilis* LLO, LLO-*luxA-E* and TF strains

B. subtilis strains were grown under the same conditions for all experiments. Each *B. subtilis* LLO construct was grown in Luria-Bertani Miller broth (LB) with the appropriate antibiotic. *B. subtilis* LLO was grown in LB with chloramphenicol (10 µg/mL) while *B. subtilis* LLO *SK*, *KG* and *luxA-E* were grown with spectinomycin (100 µg/mL). The overnight cultures were grown for 16 h at 37°C and 250 RPM. The *B. subtilis* LLO *SK*, *KG* and *luxA-E* strains were added to macrophages *in vitro* or injected *In vivo* without antibiotics because constructs were integrated into the genome.

B. subtilis LLO, LLO-*SK* and LLO-*KG* addition to bone marrow derived macrophages *in vitro*

The following conditions were utilized to induce *B. subtilis* LLO, LLO-*SK* and LLO-*KG* delivery, unless otherwise described. BMDMs were sourced from male and female C57BL/6J mice (Jackson Laboratories) of 3-4 months based on previous established methods[17] and maintained at 37°C and 5% CO_2 in DMEM (ThermoFisher, MA, USA), supplemented with 10% fetal bovine serum (FBS), 1% penicillin-streptomycin and 100 U/mL recombinant macrophage colony-stimulating factor (M-CSF). BMDMs were maintained in these conditions for 7 days before being seeded at $5x10^4$ into 96-well plates or $7x10^5$-$1x10^6$ in 6-well plates and allowed to adhere overnight. The engineered *B. subtilis* LLO were added at an optimized MOI of 50:1 for all experiments besides the uptake rate experiment (described below), along with IPTG (500 μM) to induce expression of LLO with or without delivery of TFs. The bacterial strains and BMDMs were then co-incubated at 37°C and 5% CO_2 for 1 h J774A.1 cells were then washed three times with PBS and new medium was added containing gentamicin (5 μM) to eliminate any remaining extracellular bacteria. Co-incubation continued until BMDMs were evaluated by various analyses at various time points with the BMDMs eliminating intracellular engineered *B. subtilis* LLO within 11 additional hours (Fig. 3.2). Further details of TF delivery in specific experiments are described below.

Live cell imaging

B. subtilis LLO was added to BMDMs as described above, using a 96-well black glass-bottom plate (50,000 cells/well; Perkin Elmer, cat# 6005430). *B. subtilis* LLO was centrifuged (10,000 x g) for 2 min then resuspended in CellTracker Orange CMRA Dye (CTO, Invitrogen, C34564, 2 μM) in PBS then incubated at 37°C and 250 RPM for 25 min. Afterwards, *B. subtilis* LLO was centrifuged (10,000 x g) and washed three times before adding to BMDMs. Live cell imaging was performed on a Leica DMi8 Thunder microscope equipped with a DFC9000 GTC

sCMOS camera and LAS-X software (Leica, Wetzlar, Germany). BMDMs were maintained at 37°C and 5% CO_2 in Fluorobrite medium during the imaging session. Fluorescent images of CTO were acquired using a TRITC filter set. Brightfield and fluorescent images were acquired consecutively, using a 63x oil objective every 1.5 h starting at 3 h post bacterial addition until 9 h post bacterial addition. Z-stacks were taken at all time points at 0.4 µm steps to confirm *B. subtilis* LLO presence within cytoplasm. Zoomed in images were created using Fiji (ImageJ) software.

Confirming *B. subtilis* LLO phagosomal escape and destruction by LC3 mechanisms

CTO was used to confirm location of *B. subtilis* LLO as described above. After fixation with 4% paraformaldehyde (PFA), cells were permeabilized using 0.3% Triton X-100 (ThermoFisher) followed by a blocking step containing 0.3% Triton X-100 and 5% normal goat serum (ThermoFisher, cat#31872,). Primary antibodies were incubated at 4°C overnight followed by secondary antibodies incubated at room temperature (RT) for 2 h. Phagosome formation or destruction was shown by incubating an anti-Lamp-1[109] primary antibody (1:100, AbCam, MA, USA, cat#ab25245) followed by a goat anti-rat IgG Alexa Fluor 647 secondary antibody (1:5000, ThermoFisher, cat#A-21247). Autophagy mechanisms triggered by LC3 were elucidated by incubating an ant-LC3B primary antibody (1:1000, AbCam, MA, USA, cat#ab192890) followed by a goat anti-rabbit IgG Texas Red secondary antibody (1:2000, ThermoFisher, cat#T-2767). Nuclei were counterstained by incubating cells with Hoechst 33342 (1 µg/mL) for 10 minutes (min) at RT. Slides were then coverslipped using Fluoromount-D mounting media (Southern Biotech, AL, USA). Slides were imaged using a Leica DMi8 Thunder microscope equipped with a DFC9000 GTC sCMOS camera and LAS-X software (Leica, Wetzlar, Germany). Brightfield and fluorescent images were acquired using a 63x oil objective with the fluorescent images acquired by the DAPI (Hoechst 33342), TRITC (CTO), Texas Red

(LC3B) and Cy5 (LAMP-1) filter sets. Overlayed images were created using Fiji (ImageJ) software.

BMDMs viability and uptake rate of *B. subtilis* LLO by flow cytometry

Flow cytometry was used to test rate of uptake of *B. subtilis* LLO and change in BMDM viability after bacterial delivery. For viability, conditions examined were multiple time points of interaction between *B. subtilis* LLO and host cells (4 and 12 h), a 50:1 MOI and with or without IPTG induction compared to untreated with biological triplicates (n=3) for each time and condition. For uptake rate, conditions examined were multiple MOIs (25:1, 50:1, 100:1) compared to untreated after 4 h incubation with biological triplicate (n=3) for untreated and 50:1 MOI and one biological replicate (n=1) for 25:1 and 100:1 MOI. Cells were collected, washed once with 1X PBS and incubated with Zombie NIR viability dye (1:750, Biolegend, San Diego, CA, USA; cat#423105) in PBS for 20 min, at 4°C in the dark. Cells were washed twice followed by fixation using 4% PFA and resuspended in 100 µL flow buffer for analysis using the Cytek Aurora Cytometer (Cytek Biosciences, CA, USA). All samples were assessed for percent live cells. BMDMs which were incubated with CTO bacteria were assessed for percent CTO positive cells (BMDMs containing bacteria). Standard one-way ANOVA with Tukey post-hoc test was used to determine statistically different values.

Engineered *B. subtilis* LLO strains TF delivery and BMDM protein production modulation

The LLO strain, LLO-*SK* and LLO-*KG* were internalized into BMDMs as described above (*B. subtilis* LLO, LLO-*SK* and LLO-*KG* addition to bone marrow derived macrophages *in vitro*), using a 6-well plate (Corning Costar #3516). D-mannose (1% w/v) was added to controls and to induce TF secretion after the initial 1 h incubation between BMDMs and bacteria. TFs were delivered throughout the survival of the LLO-*SK* and LLO-*KG* strains and trafficked until

experiments were ended for analysis (12, 24 or 48 h). For flow cytometry, Accutase (Sigma, cat#A6964) with scraping was used to detach BMDMs for analysis (described below). For Luminex cytokine/chemokine profiling (Millipore Sigma, MA, USA), the supernatant was removed at both 24 and 48 h and then analysis was performed to quantify cytokines/chemokines produced (described below). BMDMs that were untreated were at resting state. BMDMs were polarized with IFN-γ and LPS (M1+) at 50 ng/mL and 100 ng/mL respectively or IL-4 and IL-13 (M2+) at 20 ng/mL each to be used as positive controls. All bacterial strains were treated with and without D-mannose as described above. All treatment conditions were performed in biological triplicates (n=3).

In vitro flow cytometry

After addition of the engineered *B. subtilis* LLO strains and controls, followed by incubation for 24 or 48 h, BMDMs were collected and stained in a 96-well round bottom plate. All staining steps were performed in 100 µL volume at 4°C in the dark. Samples were first incubated with Zombie NIR viability dye (1:750, Biolegend) for 20 min. Cells were washed once with flow buffer, followed by incubation with TruStain FcX™ PLUS (anti-mouse CD16/32) Antibody (Biolegend, cat#156603; 0.25 µg/sample) for 10 min. Alexa Fluor® 647 anti-mouse CD86 Antibody (0.125 µg/sample; Biolegend; cat#105020) and FITC anti-mouse CD206 (MMR) antibody (0.1 µg/sample, Biolegend; cat#141703) were then added and incubated for 20 min. Cells were washed twice with flow staining buffer and fixed with 4% PFA for 10 min and resuspended in a final volume of 100 µL for flow cytometry analysis using the Cytek Aurora spectral flow cytometer (Cytek). Single stained controls and unstained controls for all conditions were used to assess fluorescent spread and for gating strategies. Flow cytometry data was analyzed with the software FCSExpress (DeNovo Software, CA, USA). A standard one-way ANOVA with Tukey's multiple comparisons test was used to determine statistically different MFI

values amongst all groups within each time point. The data presented herein were obtained using instrumentation in the MSU Flow Cytometry Core Facility. The facility is funded in part through the financial support of Michigan State University's Office of Research & Innovation, College of Osteopathic Medicine, and College of Human Medicine.

Luminex cytokine/chemokine profiling assay

Cell culture supernatant was stored at -20°C until ready for use. Supernatant was analyzed for CCL2 (MCP-1), CCL3 (MIP-1a), CXCL2/MIP-2, G-CSF, GM-CSF IL-1β, IL-6, IL-10, IL-12p40, IL-15, TNF-α and VEGFα cytokine expression. Cytokine and chemokine levels of cell supernatants were measured using a MCYTOMAG-70K Mouse Cytokine Magnetic Multiplex Assay (Millipore Sigma) using a Luminex 200 analyzer instrument (Luminex Corp, USA) according to the manufacturer's instructions. Standard one-way ANOVA with Tukey post-hoc test was used to determine statistically different values amongst all treatment groups.

In vitro Seahorse functional metabolism assays

Engineered *B. subtilis* LLO strains were added to BMDMs in a 96-well plate as described above (Engineered *B. subtilis* LLO strains TF delivery and BMDM protein production modulation). LPS (100 ng/mL) and D-mannose (1% w/v) served as controls in this experiment. Basal measurements of oxygen consumption rate (OCR), extracellular acidification rate (ECAR) and were obtained in real-time using the Seahorse XFe-96 Extracellular Flux Analyzer (Agilent Technologies) and was normalized to cell number[38,42,192]. Prior to running the assay, cell culture medium was replaced by the Seahorse XF DMEM medium (pH 7.4) supplemented with 25 mM D-glucose and 4 mM Glutamine. The Seahorse ATP rate and cell energy phenotype assays were run according to manufacturer's instruction and all reagents for the Seahorse assays were sourced from Agilent Technologies. Wave software (Version 2.6.1) was used to process and

export Seahorse data. Standard one-way ANOVA with Tukey post-hoc test was used to determine statistically different values amongst all treatment groups.

RNA-sequencing

Engineered *B. subtilis* LLO strains were added to BMDMs in a 96-well plate as described above (Engineered *B. subtilis* LLO strains TF delivery and BMDM protein production modulation). The following treatments were used at concentrations described above in biological triplicate at both 12 and 24 h (n=3): untreated, D-mannose, LPS, LPS and IFN-γ (M1+), IL-4 and IL-13 (M2+), LLO without IPTG (does not escape phagosomes), LLO strain with and without mannose (LLO -mannose, LLO +mannose), LLO-*SK* with and without mannose (LLO-*SK* -mannose, LLO-*SK* +mannose) and LLO-*KG* with and without mannose (LLO-*KG* -mannose, LLO-*KG* +mannose). These conditions and time points totaled 72 samples of mouse total RNA that was extracted by a Qiagen RNeasy kit (Qiagen, cat#74104) with RNase-free DNase Set (Qiagen, cat#79254) for NGS library preparation and sequencing. Libraries were prepared using the Illumina TruSeq Stranded mRNA Library Preparation Kit with IDT for Illumina TruSeq Unique Dual Index adapters following manufacturer's recommendations. Completed libraries were QC'd and quantified using a combination of Qubit dsDNA HS and Agilent 4200 TapeStation HS DNA1000 assays. The libraries were pooled in equimolar quantities for multiplexed sequencing. The library pool was loaded onto one lane of a NovaSeq S4 flow cell; sequencing was performed in a 2x150bp paired end format using a NovaSeq 6000 v1.5 300 cycle reagent cartridge. Base calling was done by Illumina Real Time Analysis (RTA) v3.4.4 and output of RTA was demultiplexed and converted to FastQ format with Illumina Bcl2fastq v2.20.0. All samples reached >30 million read counts. RNA-seq data was analyzed using FastQC (v0.11.7), GNU parallel (20180422), Trimmomatic (0.39) and STAR (2.6.0c). Differentially expressed genes are still being analyzed and compared between treatment conditions.

In vivo 4T1-BGL tumor model and tumor growth measurements

Female BALB/c mice (6-8 weeks; Jackson Laboratories USA) were obtained and cared for in accordance with the standards of Michigan State University Institutional Animal Care and Use Committee. Mice were anesthetized with isoflurane administered at 2% in oxygen followed by an injection of 300,000 4T1-BGL cells (n=3 except for D-mannose treatment which was n=2; >90% viability, measured using the trypan blue exclusion assay) suspended in 50 µL PBS into the 4^{th} (inguinal) MFP, as previously reported[193]. Two weeks post cancer cell implantation (pi) engineered *B. subtilis* LLO strains treatment was initiated. Mice were randomly divided into groups dependent on strain injected and presence of D-mannose/IPTG: 1) no treatment, 2) +mannose +IPTG, 3) LLO-*lux* +mannose intravenous (IV) +IPTG, 4) LLO-*KG* IV +mannose +IPTG, 5) LLO-*KG* intratumoral (IT) +mannose +IPTG. Bacterial treatments were administered based on treatment as described above and performed under anaesthesia (as above), containing $1x10^8$ bacteria in 100 µL PBS for IV and 25 µL PBS for IT. After 24 h post bacterial treatment, groups which were to be given D-mannose and IPTG received an IP injection of each (2 g/kg D-mannose, 50 mg/kg IPTG) and added to water (20% w/v D-mannose, 40 mM IPTG). Seven days after the first bacterial treatment, a second bacterial treatment was given, followed by D-mannose and IPTG 24 hours after. After the initial bacterial injection, animal well-being was documented every 2-3 days by observing water consumption, grooming and weight measurements. Tumors were measured using calipers beginning on the first day of the first treatment and continued every observation day of the second week until end point. Tumor volume was calculated using the equation: tumor volume= $0.5(\text{length}\times\text{width}^2)$. A repeated measures two-way ANOVA with Tukey post-hoc test was used to determine any significance between treatments and time points. At endpoint, tumors were collected for immunophenotyping, histology, measurement of metabolism and colony forming units (below).

Livers were also collected for histology to determine damage to tissue from repeated bacterial injections.

Imaging and colony forming units of *B. subtilis* LLO strains *in vivo*

The engineered *B. subtilis* LLO strains were washed three times with PBS after overnight growth before resuspending at $1x10^8$ in 100 100 µL PBS for IV and 25 µL PBS for IT. The LLO-*lux* strain was imaged using the IVIS system (IVIS Spectrum) using auto-exposure settings (time = 120-300 sec, binning = medium, f/stop = 1, emission filter = open). The LLO-*lux* strain was imaged immediately after injection, 1 h post injection, 24 h post injection, 72 h post injection and at following regular time points that correlate with caliper measurements and animal well-being documentation. A final imaging time point was taken before euthanasia then after the tumors were removed and cut in half to elucidate location of bacteria throughout tumor. Tumors were then weighed and half of the tumor that was not used for immunophenotyping and metabolism characterization was used for bacterial CFU. Half of the tumor was homogenized in 1 mL of PBS using a 1.5 mm Zirconium bead tube (Benchmark, cat#D1032-15) by bead beating in a Benchmark Beadbug 6 Microtube Homogenizer at max speed for 10 min. The homogenized mixture was diluted 1:100 in 200 µL of PBS then plated on LB+Agar with spectinomycin (100 µg/mL) for all bacterial treatments and untreated control. CFUs were counted and concentrations in tumors was calculated based on dilutions then normalized to tumor mass. Standard one-way ANOVA with Tukey post-hoc test was used to determine any statistically different values amongst the treatment groups.

Tumor immunophenotyping and metabolism characterization

Tumors were collected from each group (n=3) for dissociation and immunophenotyping using flow cytometry analysis or metabolism characterization using the Seahorse Assay.

Tumors were minced followed by digestion using a solution containing DMEM, Collagenase III (Worthington Biochemical, cat#LS004182) and DNAse I ((Worthington Biochemical, cat#LS002139). Tumors were digested for 90 min at 37ºC, 5% CO_2 with mixing using a pipette every 30 min. The solution was passed through a 70 µm strainer followed by centrifugation and resuspension in ACK Lysing Buffer (ThermoFisher, cat#A1049201) for 1 min followed by addition of HBSS + 10% FBS. Cells were centrifuged, resuspended in PBS and counted using the Trypan Blue Assay. For immunophenotyping, $1x10^6$ cells were collected per sample and transferred into a Nunc MicroWell 96-well polypropylene plate (Millipore Sigma, cat#P6866-1CS) for staining. All staining steps were performed in 100 µL volume at 4°C in the dark. Samples were first incubated with LIVE/DEAD Fixable Blue Dead Cell Stain (0.75 µL/sample, ThermoFisher, cat#L23105) for 30 min. Cells were washed once with flow buffer, followed by incubation with TruStain FcX™ PLUS (anti-mouse CD16/32) Antibody (Biolegend, cat#156603; 0.25 µg/sample) for 10 min. A mixture of the following antibodies was then added to the samples for 20 min at manufacturer suggested concentrations: CD8a BUV737 (ThermoFisher, cat#367-0081-80), CD25 SuperBright 780 (ThermoFisher, cat#78-0251-82), CD3 APC/Fire 810 (Biolegend, cat#100267), Ly-6C PE/Cyanine7 (Biolegend, cat#128017), Ly-6G Alexa Fluor 700 (Biolegend, cat#127621), CD4 Brilliant Violet 510 (Biolegend, cat#100449), MHC-II (I-A/I-E) Spark Blue 550 (Biolegend, cat#107661), FOXP3 AF647 (Biolegend, cat#320014), NKp46 BV605 (Biolegend, cat#137619), CD11C BB700 (BD Bioscience, cat#566505), CD45 BUV395 (BD Bioscience, cat#564279) and CD19 BUV615 (BD Bioscience, cat#751213). Cells were washed twice with flow staining buffer and fixed with 4% PFA for 10 min and resuspended in a final volume of 100 µL for flow cytometry analysis using the Cytek Aurora spectral flow cytometer (Cytek). Single stained controls and unstained controls for all conditions were used to assess fluorescent spread and for gating strategies. Flow cytometry data was analyzed with the software FCSExpress (DeNovo Software). For Seahorse analysis, $5x10^4$ cells from one (n=1) representative heterogenous tumor dissociation was seeded into an appropriate 96-well plate in

technical replicates of at least four wells (n>4) with methods for setting up the Seahorse assay described above (*In vitro* Seahorse functional metabolism assays). The Seahorse Mito Stress assay was run according to manufacturer's instruction and all reagents for the Seahorse assays were sourced from Agilent Technologies. For immunophenotyping, Brown-Forsythe and Welch ANOVA with Dunnett T3 post-hoc test were used to compare all treatments. For the Seahorse analysis, a standard one-way ANOVA with Tukey post-hoc test was used to determine statistically different values amongst all treatment groups.

Statistical analysis

Statistical analyses were performed using Prism software (9.4.0, GraphPad Inc., La Jolla, CA). Statistical tests are identified for each method. Data are expressed as mean +/- standard deviation; $p<.05$ was considered a significant finding. Plotting was performed using R version 4.0.4 with the following packages: ggplot2, dplyr, reshape2, ggsignif, plotrix and ggpubr.

Availability of data and materials

All raw data, *B. subtilis* LLO constructs and R scripts will be made available upon request by the corresponding author. Plasmid used to produce the *B. subtilis* LLO-*luxA-E* constructs will be submitted to Addgene. All R scripts were written with a general format appropriate for the openly available, established packages mentioned above and can be made available on request.

Competing interests

The authors declare no competing interests.

Acknowledgements

The authors would like to thank Dr. Daniel A. Portnoy for the *B. subtilis* LLO strain and Dr. Lee Kroos for *B. subtilis* plasmid pDR111. The authors would also like to thank Dr. Matthew Bernard of the Michigan State University Flow Cytometry Core for flow cytometry aid, cytokine/chemokine profiling analysis and tumor immunophenotyping design; the MSU RTSF Genomics Core for performing RNA-seq and MSU ICER for computational support in RNA-seq analysis. The authors would like to acknowledge the James and Kathleen Cornelius Endowment for financially supporting this research. Fig. 1 and Supplementary Fig. 1 were created using BioRender.com.

Funding

The authors would like to acknowledge the James and Kathleen Cornelius Endowment for financially supporting this research.

Affiliations

Department of Biomedical Engineering, Michigan State University, East Lansing, MI, USA. Department of Microbiology and Molecular Genetics, Michigan State University, East Lansing, MI, USA. Institute for Quantitative Health Science and Engineering, Michigan State University, East Lansing, MI, USA

Contributions

Cody S. Madsen conceptualized the use of the EES as a bacterial cancer treatment, developed all the EES constructs as the platform technology, jointly developed and performed

all experiments, jointly developed and analyzed all data to make figures and was one of the primary authors of the manuscript. Dr. Ashley V. Makela jointly developed and performed all experiments, jointly developed and analyzed all data to make figures and was one of the primary authors of the manuscript. Dr. Chima V. Maduka significantly contributed to functional metabolism assays and significantly contributed to the writing and editing of this manuscript. Emily M. Greeson significantly contributed to the development of the EES platform technology, jointly developed and significantly contributed to the writing and editing of this manuscript. Anthony Tundo and Evran Ural both contributed to performing the *in vivo* studies and significantly contributed to the writing and editing of the manuscript. Dr. Maryam Sayadi developed the RNA-seq analysis pipeline and significantly contributed to writing and editing of this manuscript. Dr. Christopher H. Contag conceptualized the initial concept of the EES, supervised the studies, contributed to the experimental design, provided the resources, reviewed data and edited the manuscript.

REFERENCES

REFERENCES

1. Elston, K. M. *et al.* Engineering insects from the endosymbiont out. *Trends Microbiol.* **30**, 79–96 (2022).

2. Epis, S. *et al.* Chimeric symbionts expressing a Wolbachia protein stimulate mosquito immunity and inhibit filarial parasite development. *Commun. Biol.* **3**, 1–10 (2020).

3. Wang, S. *et al.* Driving mosquito refractoriness to Plasmodium falciparum with engineered symbiotic bacteria. *Science (80-.).* **357**, 1399–1402 (2017).

4. Durvasula, R. V *et al.* Prevention of insect-borne disease: an approach using transgenic symbiotic bacteria. *Proc. Natl. Acad. Sci.* **94**, 3274–3278 (1997).

5. Jiggins, F. M. The spread of Wolbachia through mosquito populations. *PLoS Biology* (2017).

6. Flores, H. A. & O'Neill, S. L. Controlling vector-borne diseases by releasing modified mosquitoes. *Nat. Rev. Microbiol.* **16**, 508–518 (2018).

7. Leonard, S. P. *et al.* Engineered symbionts activate honey bee immunity and limit pathogens. *Science (80-.).* **367**, 573–576 (2020).

8. Machado, R. A. R. *et al.* Engineering bacterial symbionts of nematodes improves their biocontrol potential to counter the western corn rootworm. *Nat. Biotechnol.* **38**, 600–608 (2020).

9. Xu, T.-T., Chen, J., Jiang, L.-Y. & Qiao, G.-X. Diversity of bacteria associated with Hormaphidinae aphids (Hemiptera: Aphididae). *Insect Sci.* **28**, 165–179 (2021).

10. Ip, J. C.-H. *et al.* Host-Endosymbiont Genome Integration in a Deep-Sea Chemosymbiotic Clam. *Mol. Biol. Evol.* **38**, 502—518 (2021).

11. Yang, K. *et al.* Wolbachia and Spiroplasma could influence bacterial communities of the spider mite Tetranychus truncatus. *Exp. Appl. Acarol.* **83**, 197–210 (2021).

12. Shi, X.-B. *et al.* Aphid endosymbiont facilitates virus transmission by modulating the volatile profile of host plants. *BMC Plant Biol.* **21**, 67 (2021).

13. Chao, L.-L., Castillo, C. T. & Shih, C.-M. Molecular detection and genetic identification of Wolbachia endosymbiont in Rhipicephalus sanguineus (Acari: Ixodidae) ticks of Taiwan. *Exp. Appl. Acarol.* **83**, 115–130 (2021).

14. Izraeli, Y. *et al.* Wolbachia influence on the fitness of Anagyrus vladimiri (Hymenoptera: Encyrtidae), a bio-control agent of mealybugs. *Pest Manag. Sci.* **77**, 1023–1034 (2021).

15. Kennedy, J., Marchesi, J. R. & Dobson, A. D. W. Metagenomic approaches to exploit the biotechnological potential of the microbial consortia of marine sponges. *Applied Microbiology and Biotechnology* (2007).

16. Madsen, C. S., Makela, A. V, Greeson, E. M., Hardy, J. W. & Contag, C. H. Engineered endosymbionts capable of directing mammalian cell gene expression. *bioRxiv* 2021.10.05.463266 (2021).

17. Gonçalves, R. & Mosser, D. M. The Isolation and Characterization of Murine Macrophages. *Curr. Protoc. Immunol.* **111**, 14.1.1-14.1.16 (2015).

18. Zhang, X., Goncalves, R. & Mosser, D. M. The Isolation and Characterization of Murine Macrophages. *Curr. Protoc. Immunol.* **83**, 14.1.1-14.1.14 (2008).

19. Germic, N., Frangez, Z., Yousefi, S. & Simon, H.-U. Regulation of the innate immune system by autophagy: monocytes, macrophages, dendritic cells and antigen presentation. *Cell Death Differ.* **26**, 715–727 (2019).

20. Frucht, D. M. *et al.* IFN-γ production by antigen-presenting cells: mechanisms emerge. *Trends Immunol.* **22**, 556–560 (2001).

21. Lavin, Y. *et al.* Tissue-Resident Macrophage Enhancer Landscapes Are Shaped by the Local Microenvironment. *Cell* **159**, 1312–1326 (2014).

22. Mosser, D. M. & Edwards, J. P. Exploring the full spectrum of macrophage activation. *Nature Reviews Immunology* (2008).

23. Moreira, A. P. & Hogaboam, C. M. Macrophages in allergic asthma: Fine-tuning their pro- and anti-inflammatory actions for disease resolution. *Journal of Interferon and Cytokine Research* (2011).

24. Mantovani, A. *et al.* The chemokine system in diverse forms of macrophage activation and polarization. *Trends Immunol.* **25**, 677–686 (2004).

25. Das, A. *et al.* High-Resolution Mapping and Dynamics of the Transcriptome, Transcription Factors, and Transcription Co-Factor Networks in Classically and Alternatively Activated Macrophages. *Front. Immunol.* **9**, 22 (2018).

26. Turner, M. D., Nedjai, B., Hurst, T. & Pennington, D. J. Cytokines and chemokines: At the crossroads of cell signalling and inflammatory disease. *Biochim. Biophys. Acta - Mol. Cell Res.* **1843**, 2563–2582 (2014).

27. Martinez, F. O., Sica, A., Mantovani, A. & Locati, M. Macrophage activation and polarization. *Frontiers in Bioscience* (2008).

28. Escoll, P. & Buchrieser, C. Metabolic reprogramming of host cells upon bacterial infection: Why shift to a Warburg-like metabolism? *FEBS J.* **285**, 2146–2160 (2018).

29. Chen, Z., Lu, W., Garcia-Prieto, C. & Huang, P. The Warburg effect and its cancer therapeutic implications. *J. Bioenerg. Biomembr.* **39**, 267–274 (2007).

30. Kim, J. & Dang, C. V. Cancer's molecular sweet tooth and the Warburg effect. *Cancer Res.* **66**, 8927–8930 (2006).

31. Liu, Y. *et al.* Metabolic reprogramming in macrophage responses. *Biomark. Res.* **9**, 1–17 (2021).

32. Liu, D. *et al.* Comprehensive proteomics analysis reveals metabolic reprogramming of tumor-associated macrophages stimulated by the tumor microenvironment. *J. Proteome Res.* **16**, 288–297 (2017).

33. Errea, A. *et al.* Lactate inhibits the pro-inflammatory response and metabolic reprogramming in murine macrophages in a GPR81-independent manner. *PLoS One* **11**, e0163694 (2016).

34. Kelly, B. & O'neill, L. A. Metabolic reprogramming in macrophages and dendritic cells in innate immunity. *Cell Res.* **25**, 771–784 (2015).

35. Galván-Peña, S. & O'Neill, L. A. J. Metabolic reprograming in macrophage polarization. *Front. Immunol.* **5**, 420 (2014).

36. Blagih, J. & Jones, R. G. Polarizing macrophages through reprogramming of glucose metabolism. *Cell Metab.* **15**, 793–795 (2012).

37. Lorenz, M. C., Bender, J. A. & Fink, G. R. Transcriptional response of Candida albicans upon internalization by macrophages. *Eukaryot. Cell* **3**, 1076–1087 (2004).

38. Ip, W. K. E., Hoshi, N., Shouval, D. S., Snapper, S. & Medzhitov, R. Anti-inflammatory effect of IL-10 mediated by metabolic reprogramming of macrophages. *Science (80-.).* **356**, 513–519 (2017).

39. Curi, R. *et al.* A past and present overview of macrophage metabolism and functional outcomes. *Clin. Sci.* **131**, 1329–1342 (2017).

40. Lauterbach, M. A. *et al.* Toll-like receptor signaling rewires macrophage metabolism and promotes histone acetylation via ATP-citrate lyase. *Immunity* **51**, 997–1011 (2019).

41. Pelletier, M., Billingham, L. K., Ramaswamy, M. & Siegel, R. M. Extracellular flux analysis to monitor glycolytic rates and mitochondrial oxygen consumption. in *Methods in enzymology* vol. 542 125–149 (Elsevier, 2014).

42. Tannahill, G. M. *et al.* Succinate is an inflammatory signal that induces IL-1β through HIF-1α. *Nature* **496**, 238–242 (2013).

43. Divakaruni, A. S., Paradyse, A., Ferrick, D. A., Murphy, A. N. & Jastroch, M. Chapter Sixteen - Analysis and Interpretation of Microplate-Based Oxygen Consumption and pH Data. in *Mitochondrial Function* (eds. Murphy, A. N. & Chan, D. C. B. T.-M. in E.) vol. 547 309–354 (Academic Press, 2014).

44. Cho, H. J. *et al.* Bone marrow-derived, alternatively activated macrophages enhance solid tumor growth and lung metastasis of mammary carcinoma cells in a Balb/C mouse orthotopic model. *Breast cancer Res.* **14**, 1–12 (2012).

45. Weiser-Evans, M. C. M. *et al.* Depletion of cytosolic phospholipase A2 in bone marrow–derived macrophages protect against lung cancer progression and metastasis. *Cancer Res.* **69**, 1733–1738 (2009).

46. Redente, E. F. *et al.* Tumor progression stage and anatomical site regulate tumor-associated macrophage and bone marrow-derived monocyte polarization. *Am. J. Pathol.* **176**, 2972–2985 (2010).

47. Pathria, P., Louis, T. L. & Varner, J. A. Targeting Tumor-Associated Macrophages in Cancer. *Trends Immunol.* **40**, 310–327 (2019).

48. Davies, L. C. *et al.* Distinct bone marrow-derived and tissue-resident macrophage lineages proliferate at key stages during inflammation. *Nat. Commun.* **4**, 1–10 (2013).

49. Redente, E. F. *et al.* Differential polarization of alveolar macrophages and bone marrow-derived monocytes following chemically and pathogen-induced chronic lung inflammation. *J. Leukoc. Biol.* **88**, 159–168 (2010).

50. Xia, Y. *et al.* Engineering Macrophages for Cancer Immunotherapy and Drug Delivery. *Adv. Mater.* **32**, 2002054 (2020).

51. Spiller, K. L. & Koh, T. J. Macrophage-based therapeutic strategies in regenerative medicine. *Adv. Drug Deliv. Rev.* **122**, 74–83 (2017).

52. Kuhn, M. & Goebel, W. Induction of cytokines in phagocytic mammalian cells infected with virulent and avirulent Listeria strains. *Infect. Immun.* **62**, 348–356 (1994).

53. Demuth, A., Goebel, W., Beuscher, H. U. & Kuhn, M. Differential regulation of cytokine and cytokine receptor mRNA expression upon infection of bone marrow-derived macrophages with Listeria monocytogenes. *Infect. Immun.* **64**, 3475–3483 (1996).

54. Fortier, A., Faucher, S. P., Diallo, K. & Gros, P. Global cellular changes induced by Legionella pneumophila infection of bone marrow-derived macrophages. *Immunobiology* **216**, 1274–1285 (2011).

55. Sun, D. *et al.* Bone marrow-derived cell regulation of skeletal muscle regeneration. *FASEB J.* **23**, 382–395 (2009).

56. Gibon, E. *et al.* Aging affects bone marrow macrophage polarization: relevance to bone healing. *Regen. Eng. Transl. Med.* **2**, 98–104 (2016).

57. Das, A. *et al.* Monocyte and macrophage plasticity in tissue repair and regeneration. *Am. J. Pathol.* **185**, 2596–2606 (2015).

58. Shen, T.-C. D. *et al.* Engineering the gut microbiota to treat hyperammonemia. *J. Clin. Invest.* **125**, 2841–2850 (2015).

59. Sheth, R. U., Cabral, V., Chen, S. P. & Wang, H. H. Manipulating Bacterial Communities by in situ Microbiome Engineering. *Trends Genet.* **32**, 189–200 (2016).

60. Puurunen, M. K. *et al.* Safety and pharmacodynamics of an engineered E. coli Nissle for the treatment of phenylketonuria: a first-in-human phase 1/2a study. *Nat. Metab.* **3**, 1125–1132 (2021).

61. Charbonneau, M. R. *et al.* Development of a mechanistic model to predict synthetic biotic activity in healthy volunteers and patients with phenylketonuria. *Commun. Biol.* **4**, 898 (2021).

62. Sedighi, M. *et al.* Therapeutic bacteria to combat cancer; current advances, challenges, and opportunities. *Cancer Med.* **8**, 3167–3181 (2019).

63. Sawant, S. S., Patil, S. M., Gupta, V. & Kunda, N. K. Microbes as Medicines: Harnessing the Power of Bacteria in Advancing Cancer Treatment. *Int. J. Mol. Sci.* **21**, (2020).

64. Yaghoubi, A. *et al.* Bacteriotherapy in Breast Cancer. *Int J Mol Sci* **20**, (2019).

65. Soleimanpour, S., Hasanian, S. M., Avan, A., Yaghoubi, A. & Khazaei, M. Bacteriotherapy in gastrointestinal cancer. *Life Sci* **254**, 117754 (2020).

66. Zhang, Z. H., Yin, L., Zhang, L. L. & Song, J. Efficacy and safety of Bacillus Calmette-Guerin for bladder cancer: A protocol of systematic review. *Med.* **99**, e21930 (2020).

67. Sfakianos, J. P. *et al.* Bacillus Calmette-Guerin (BCG): Its fight against pathogens and cancer. *Urol. Oncol.* **39**, 121–129 (2021).

68. La Mantia, I. *et al.* The role of bacteriotherapy in the prevention of adenoidectomy. *Eur Rev Med Pharmacol Sci* **23**, 44–47 (2019).

69. Andaloro, C., Santagati, M., Stefani, S. & La Mantia, I. Bacteriotherapy with Streptococcus salivarius 24SMB and Streptococcus oralis 89a oral spray for children with recurrent streptococcal pharyngotonsillitis: a randomized placebo-controlled clinical study. *Eur. Arch. oto-rhino-laryngology Off. J. Eur. Fed. Oto-Rhino-Laryngological Soc. Affil. with Ger. Soc. Oto-Rhino-Laryngology - Head Neck Surg.* **276**, 879–887 (2019).

70. Yaghoubi, A. *et al.* Bacteria as a double-action sword in cancer. *Biochim Biophys Acta Rev Cancer* **1874**, 188388 (2020).

71. Chowdhury, S. *et al.* Programmable bacteria induce durable tumor regression and systemic antitumor immunity. *Nat. Med.* **25**, 1057–1063 (2019).

72. Din, M. O. *et al.* Synchronized cycles of bacterial lysis for in vivo delivery. *Nature* **536**, 81–85 (2016).

73. Chien, T. *et al.* Enhancing the tropism of bacteria via genetically programmed biosensors. *Nat. Biomed. Eng.* **6**, 94–104 (2022).

74. Danino, T., Lo, J., Prindle, A., Hasty, J. & Bhatia, S. N. In vivo gene expression dynamics of tumor-targeted bacteria. *ACS Synth. Biol.* **1**, 465–470 (2012).

75. Abedi, M. H. *et al.* Ultrasound-controllable engineered bacteria for cancer immunotherapy. *Nat. Commun.* **13**, 1–11 (2022).

76. He, L. *et al.* Intestinal probiotics E. coli Nissle 1917 as a targeted vehicle for delivery of p53 and Tum-5 to solid tumors for cancer therapy. *J. Biol. Eng.* **13**, 1–13 (2019).

77. Yu, X., Lin, C., Yu, J., Qi, Q. & Wang, Q. Bioengineered Escherichia coli Nissle 1917 for tumour-targeting therapy. *Microb. Biotechnol.* **13**, 629–636 (2020).

78. Danino, T. *et al.* Programmable probiotics for detection of cancer in urine. *Sci. Transl. Med.* **7**, 289ra84-289ra84 (2015).

79. Zhang, Y. *et al.* Escherichia coli Nissle 1917 targets and restrains mouse B16 melanoma and 4T1 breast tumors through expression of azurin protein. *Appl. Environ. Microbiol.* **78**, 7603–7610 (2012).

80. Flickinger, J. C., Rodeck, U. & Snook, A. E. Listeria monocytogenes as a Vector for Cancer Immunotherapy: Current Understanding and Progress. *Vaccines* vol. 6 (2018).

81. Morrow, Z. T., Powers, Z. M. & Sauer, J.-D. Listeria monocytogenes Cancer Vaccines: Bridging Innate and Adaptive Immunity. *Curr. Clin. Microbiol. Reports* **6**, 213–224 (2019).

82. Hayashi, K. *et al.* Cancer metastasis directly eradicated by targeted therapy with a modified Salmonella typhimurium. *J. Cell. Biochem.* **106**, 992–998 (2009).

83. Nagakura, C. *et al.* Efficacy of a genetically modified Salmonella typhimurium in an orthotopic human pancreatic cancer in nude mice. *Anticancer Res.* **29**, 1873–1878 (2009).

84. Liang, K. *et al.* Genetically engineered Salmonella Typhimurium: Recent advances in cancer therapy. *Cancer Lett.* **448**, 168–181 (2019).

85. Nguyen, V. H. *et al.* Genetically engineered Salmonella typhimurium as an imageable therapeutic probe for cancer. *Cancer Res.* **70**, 18–23 (2010).

86. Guo, Y. *et al.* Targeted cancer immunotherapy with genetically engineered oncolytic Salmonella typhimurium. *Cancer Lett.* **469**, 102–110 (2020).

87. Harimoto, T. *et al.* A programmable encapsulation system improves delivery of therapeutic bacteria in mice. *Nat. Biotechnol.* (2022).

88. Toso, J. F. *et al.* Phase I study of the intravenous administration of attenuated Salmonella typhimurium to patients with metastatic melanoma. *J. Clin. Oncol.* **20**, 142–152 (2002).

89. Yelin, I. *et al.* Genomic and epidemiological evidence of bacterial transmission from probiotic capsule to blood in ICU patients. *Nat. Med.* **25**, 1728–1732 (2019).

90. Low, K. B. *et al.* Lipid A mutant Salmonella with suppressed virulence and TNFα induction retain tumor-targeting in vivo. *Nat. Biotechnol.* **17**, 37–41 (1999).

91. Bielecki, J., Youngman, P., Connelly, P. & Portnoy, D. A. Bacillus subtilis expressing a haemolysin gene from Listeria monocytogenes can grow in mammalian cells. *Nature* (1990).

92. Zuber, P. & Losick, R. Role of AbrB in Spo0A- and Spo0B-dependent utilization of a sporulation promoter in Bacillus subtilis. *J. Bacteriol.* (1987).

93. Travassos, L. H. *et al.* Toll-like receptor 2-dependent bacterial sensing does not occur via peptidoglycan recognition. *EMBO Rep.* **5**, 1000–1006 (2004).

94. Elshaghabee, F. M. F., Rokana, N., Gulhane, R. D., Sharma, C. & Panwar, H. Bacillus As Potential Probiotics: Status, Concerns, and Future Perspectives. *Front. Microbiol.* **8**, 1490 (2017).

95. Kolkman, M. A. B. *et al.* The twin-arginine signal peptide of Bacillus subtilis YwbN can direct either Tat- or Sec-dependent secretion of different cargo proteins: Secretion of active subtilisin via the B. subtilis Tat pathway. *Appl. Environ. Microbiol.* (2008).

96. Tugal, D., Liao, X. & Jain, M. K. Transcriptional control of macrophage polarization. *Arterioscler. Thromb. Vasc. Biol.* (2013).

97. Mitchell, P. J. & Tjian, R. Transcriptional regulation in mammalian cells by sequence-specific DNA binding proteins. *Science (80-.).* **245**, 371–378 (1989).

98. Fleetwood, A. J., Lawrence, T., Hamilton, J. A. & Cook, A. D. Granulocyte-macrophage colony-stimulating factor (CSF) and macrophage CSF-dependent macrophage phenotypes display differences in cytokine profiles and transcription factor activities: implications for CSF blockade in inflammation. *J. Immunol.* **178**, 5245–5252 (2007).

99. Heinz, S. *et al.* Simple combinations of lineage-determining transcription factors prime cis-regulatory elements required for macrophage and B cell identities. *Mol. Cell* **38**, 576–589 (2010).

100. Rilo-Alvarez, H., Ledo, A. M., Vidal, A. & Garcia-Fuentes, M. Delivery of transcription factors as modulators of cell differentiation. *Drug Deliv. Transl. Res.* **11**, 426–444 (2021).

101. Li, H., Jiang, T., Li, M. Q., Zheng, X. L. & Zhao, G. J. Transcriptional regulation of macrophages polarization by microRNAs. *Frontiers in Immunology* (2018).

102. Date, D. *et al.* Kruppel-like transcription factor 6 regulates inflammatory macrophage polarization. *J. Biol. Chem.* (2014).

103. Liao, X. *et al.* Krüppel-like factor 4 regulates macrophage polarization. *J. Clin. Invest.* (2011).

104. Yang, M. *et al.* Deficiency of GATA3-Positive Macrophages Improves Cardiac Function Following Myocardial Infarction or Pressure Overload Hypertrophy. *J. Am. Coll. Cardiol.* (2018).

105. VanDeusen, J. B. *et al.* STAT-1-mediated repression of monocyte interleukin-10 gene expression in vivo. *Eur. J. Immunol.* **36**, 623–630 (2006).

106. Tao, K., Fang, M., Alroy, J. & Sahagian, G. G. Imagable 4T1 model for the study of late-stage breast cancer. *BMC Cancer* **8**, 228 (2008).

107. Zhang, H. *et al.* Oncolytic adenoviruses synergistically enhance anti-PD-L1 and anti-CTLA-4 immunotherapy by modulating the tumour microenvironment in a 4T1 orthotopic mouse model. *Cancer Gene Ther.* **29**, 456–465 (2022).

108. Perez, G. I. *et al.* In Vitro and In Vivo Analysis of Extracellular Vesicle-Mediated Metastasis Using a Bright, Red-Shifted Bioluminescent Reporter Protein. *Adv. Genet.* **3**, 2100055 (2022).

109. Kortebi, M. *et al.* Listeria monocytogenes switches from dissemination to persistence by adopting a vacuolar lifestyle in epithelial cells. *PLoS Pathog.* **13**, e1006734–e1006734 (2017).

110. Huynh, K. K. *et al.* LAMP proteins are required for fusion of lysosomes with phagosomes. *EMBO J.* **26**, 313–324 (2007).

111. Deretic, V., Saitoh, T. & Akira, S. Autophagy in infection, inflammation and immunity. *Nat. Rev. Immunol.* **13**, 722–737 (2013).

112. G., B. B. *et al.* Inflammasome Components Coordinate Autophagy and Pyroptosis as Macrophage Responses to Infection. *MBio* **4**, e00620-12 (2013).

113. Levine, B., Mizushima, N. & Virgin, H. W. Autophagy in immunity and inflammation. *Nature* **469**, 323–335 (2011).

114. Siqueira, M. da S., Ribeiro, R. de M. & Travassos, L. H. Autophagy and Its Interaction with Intracellular Bacterial Pathogens. *Front. Immunol.* **9**, 935 (2018).

115. Gordon, S. & Martinez, F. O. Alternative Activation of Macrophages: Mechanism and Functions. *Immunity* **32**, 593–604 (2010).

116. Orecchioni, M., Ghosheh, Y., Pramod, A. B. & Ley, K. Macrophage Polarization: Different Gene Signatures in M1(LPS+) vs. Classically and M2(LPS–) vs. Alternatively Activated Macrophages. *Front. Immunol.* **10**, (2019).

117. Viola, A., Munari, F., Sánchez-Rodríguez, R., Scolaro, T. & Castegna, A. The Metabolic Signature of Macrophage Responses. *Front. Immunol.* **10**, (2019).

118. Torretta, S. *et al.* D-mannose suppresses macrophage IL-1β production. *Nat. Commun.* **11**, 6343 (2020).

119. LeBleu, V. S. *et al.* PGC-1α mediates mitochondrial biogenesis and oxidative phosphorylation in cancer cells to promote metastasis. *Nat. Cell Biol.* **16**, 992–1003 (2014).

120. Francis, K. P. *et al.* Visualizing pneumococcal infections in the lungs of live mice using bioluminescent Streptococcus pneumoniae transformed with a novel gram-positive lux transposon. *Infect. Immun.* (2001).

121. Francis, K. P. *et al.* Monitoring bioluminescent Staphylococcus aureus infections in living mice using a novel luxABCDE construct. *Infect. Immun.* **68**, 3594–3600 (2000).

122. Hong, E.-H. *et al.* Intratumoral injection of attenuated Salmonella vaccine can induce tumor microenvironmental shift from immune suppressive to immunogenic. *Vaccine* **31**, 1377–1384 (2013).

123. Pockley, A. G., Foulds, G. A., Oughton, J. A., Kerkvliet, N. I. & Multhoff, G. Immune cell phenotyping using flow cytometry. *Curr. Protoc. Toxicol.* **66**, 18 (2015).

124. Daud, A. I. *et al.* Tumor immune profiling predicts response to anti–PD-1 therapy in human melanoma. *J. Clin. Invest.* **126**, 3447–3452 (2016).

125. Khalsa, J. K. *et al.* Immune phenotyping of diverse syngeneic murine brain tumors identifies immunologically distinct types. *Nat. Commun.* **11**, 1–14 (2020).

126. Ryu, Y. H. *et al.* Differential immunostimulatory effects of Gram-positive bacteria due to their lipoteichoic acids. *Int. Immunopharmacol.* **9**, 127–133 (2009).

127. Moreira, L. O. *et al.* The TLR2-MyD88-NOD2-RIPK2 signalling axis regulates a balanced pro-inflammatory and IL-10-mediated anti-inflammatory cytokine response to Gram-positive cell walls. *Cell. Microbiol.* **10**, 2067–2077 (2008).

128. Holden, J. A. *et al.* Porphyromonas gingivalis lipopolysaccharide weakly activates M1 and M2 polarized mouse macrophages but induces inflammatory cytokines. *Infect. Immun.* **82**, 4190–4203 (2014).

129. M., J. J. *et al.* Mannose receptor (CD206) activation in tumor-associated macrophages enhances adaptive and innate antitumor immune responses. *Sci. Transl. Med.* **12**, eaax6337 (2020).

130. García-González, G. *et al.* Triggering of protease-activated receptors (PARs) induces alternative M2 macrophage polarization with impaired plasticity. *Mol. Immunol.* **114**, 278–288 (2019).

131. Leber, N. *et al.* α-Mannosyl-Functionalized Cationic Nanohydrogel Particles for Targeted Gene Knockdown in Immunosuppressive Macrophages. *Macromol. Biosci.* **19**, e1900162 (2019).

132. Stahl, P. D. & Ezekowitz, R. A. B. The mannose receptor is a pattern recognition receptor involved in host defense. *Curr. Opin. Immunol.* **10**, 50–55 (1998).

133. Murtaugh, M. P. & Foss, D. L. Inflammatory cytokines and antigen presenting cell activation. *Vet. Immunol. Immunopathol.* **87**, 109–121 (2002).

134. Zhang, X. & Mosser, D. M. Macrophage activation by endogenous danger signals. *Journal of Pathology* (2008).

135. Wang, L., Zhang, S., Wu, H., Rong, X. & Guo, J. M2b macrophage polarization and its roles in diseases. *J. Leukoc. Biol.* **106**, 345–358 (2019).

136. Graves, D. T. The potential role of chemokines and inflammatory cytokines in periodontal disease progression. *Clin. Infect. Dis.* **28**, 482–490 (1999).

137. Domingues, C., AB da Cruz e Silva, O. & Henriques, A. Impact of cytokines and chemokines on Alzheimer's disease neuropathological hallmarks. *Curr. Alzheimer Res.* **14**, 870–882 (2017).

138. Chatzigeorgiou, A. *et al.* The pattern of inflammatory/anti-inflammatory cytokines and chemokines in type 1 diabetic patients over time. *Ann. Med.* **42**, 426–438 (2010).

139. Tanaka, T. *et al.* Chemokines in tumor progression and metastasis. *Cancer Sci.* **96**, 317–322 (2005).

140. Ben-Baruch, A. Host microenvironment in breast cancer development: inflammatory cells, cytokines and chemokines in breast cancer progression: reciprocal tumor–microenvironment interactions. *Breast cancer Res.* **5**, 1–6 (2002).

141. Raman, D., Baugher, P. J., Thu, Y. M. & Richmond, A. Role of chemokines in tumor growth. *Cancer Lett.* **256**, 137–165 (2007).

142. Ramesh, G., MacLean, A. G. & Philipp, M. T. Cytokines and chemokines at the crossroads of neuroinflammation, neurodegeneration, and neuropathic pain. *Mediators Inflamm.* **2013**, 480739 (2013).

143. Benoit, M., Desnues, B. & Mege, J.-L. Macrophage Polarization in Bacterial Infections. *J. Immunol.* **181**, 3733 LP – 3739 (2008).

144. Smith, T. D., Tse, M. J., Read, E. L. & Liu, W. F. Regulation of macrophage polarization and plasticity by complex activation signals. *Integr. Biol. (Camb).* **8**, 946–955 (2016).

145. Rőszer, T. Understanding the Mysterious M2 Macrophage through Activation Markers and Effector Mechanisms. *Mediators Inflamm.* **2015**, 816460 (2015).

146. Martins, A., Han, J. & Kim, S. O. The multifaceted effects of granulocyte colony-stimulating factor in immunomodulation and potential roles in intestinal immune homeostasis. *IUBMB Life* **62**, 611–617 (2010).

147. Becker, C. *et al.* Regulation of IL-12 p40 Promoter Activity in Primary Human Monocytes: Roles of NF-κB, CCAAT/Enhancer-Binding Protein β, and PU.1 and Identification of a Novel Repressor Element (GA-12) That Responds to IL-4 and Prostaglandin E₂ *J. Immunol.* **167**, 2608 LP – 2618 (2001).

148. Laha, D., Grant, R., Mishra, P. & Nilubol, N. The role of tumor necrosis factor in manipulating the immunological response of tumor microenvironment. *Front. Immunol.* **12**, 656908 (2021).

149. Kenny, P. A., Lee, G. Y. & Bissell, M. J. Targeting the tumor microenvironment. *Front. Biosci. a J. virtual Libr.* **12**, 3468 (2007).

150. Rosenzweig, J. M., Glenn, J. D., Calabresi, P. A. & Whartenby, K. A. KLF4 modulates expression of IL-6 in dendritic cells via both promoter activation and epigenetic modification. *J. Biol. Chem.* **288**, 23868–23874 (2013).

151. Bhavsar, I., Miller, C. S. & Al-Sabbagh, M. Macrophage Inflammatory Protein-1 Alpha (MIP-1 alpha)/CCL3: As a Biomarker. *General Methods in Biomarker Research and their Applications* 223–249 (2015).

152. Bristow, C. A. P. & Shore, P. Transcriptional regulation of the human MIP-1alpha promoter by RUNX1 and MOZ. *Nucleic Acids Res.* **31**, 2735–2744 (2003).

153. Deshmane, S. L., Kremlev, S., Amini, S. & Sawaya, B. E. Monocyte chemoattractant protein-1 (MCP-1): an overview. *J. Interf. cytokine Res. Off. J. Int. Soc. Interf. Cytokine Res.* **29**, 313–326 (2009).

154. Sutcliffe, A. M. *et al.* Transcriptional regulation of monocyte chemotactic protein-1 release by endothelin-1 in human airway smooth muscle cells involves NF-kappaB and AP-1. *Br. J. Pharmacol.* **157**, 436–450 (2009).

155. Kanemaru, H. *et al.* Antitumor effect of Batf2 through IL-12 p40 up-regulation in tumor-associated macrophages. *Proc. Natl. Acad. Sci.* **114**, E7331 LP-E7340 (2017).

156. Chonov, D. C., Ignatova, M. M. K., Ananiev, J. R. & Gulubova, M. V. IL-6 Activities in the Tumour Microenvironment. Part 1. *Open access Maced. J. Med. Sci.* **7**, 2391–2398 (2019).

157. Hu, J. *et al.* Regulation of tumor immune suppression and cancer cell survival by CXCL1/2 elevation in glioblastoma multiforme. *Sci. Adv.* **7**, eabc2511 (2021).

158. Burke, S. J. *et al.* NF-κB and STAT1 control CXCL1 and CXCL2 gene transcription. *Am. J. Physiol. Endocrinol. Metab.* **306**, E131-49 (2014).

159. Laoui, D. *et al.* Tumor-associated macrophages in breast cancer: Distinct subsets, distinct functions. *Int. J. Dev. Biol.* (2011).

160. Wculek, S. K., Dunphy, G., Heras-Murillo, I., Mastrangelo, A. & Sancho, D. Metabolism of tissue macrophages in homeostasis and pathology. *Cell. Mol. Immunol.* **19**, 384–408 (2022).

161. Huang, S. C.-C. *et al.* Cell-intrinsic lysosomal lipolysis is essential for alternative activation of macrophages. *Nat. Immunol.* **15**, 846–855 (2014).

162. Diskin, C. & Pålsson-McDermott, E. M. Metabolic Modulation in Macrophage Effector Function. *Front. Immunol.* **9**, 270 (2018).

163. Wang, L. *et al.* Mitochondrial Respiratory Chain Inhibitors Involved in ROS Production Induced by Acute High Concentrations of Iodide and the Effects of SOD as a Protective Factor. *Oxid. Med. Cell. Longev.* **2015**, 217670 (2015).

164. Mookerjee, S. A., Gerencser, A. A., Nicholls, D. G. & Brand, M. D. Quantifying intracellular rates of glycolytic and oxidative ATP production and consumption using extracellular flux measurements. *J. Biol. Chem.* **292**, 7189–7207 (2017).

165. Rabold, K., Netea, M. G., Adema, G. J. & Netea-Maier, R. T. Cellular metabolism of tumor-associated macrophages–functional impact and consequences. *FEBS Lett.* **591**, 3022–3041 (2017).

166. Gonzalez, P. S. *et al.* Mannose impairs tumour growth and enhances chemotherapy. *Nature* **563**, 719–723 (2018).

167. Liu, Q., Li, X., Zhang, H. & Li, H. Mannose Attenuates Colitis-Associated Colorectal Tumorigenesis by Targeting Tumor-Associated Macrophages. *J. cancer Prev.* **27**, 31 (2022).

168. Martinez-Outschoorn, U. E., Sotgia, F. & Lisanti, M. P. Power surge: supporting cells “fuel” cancer cell mitochondria. *Cell Metab.* **15**, 4–5 (2012).

169. Whitaker-Menezes, D. *et al.* Hyperactivation of oxidative mitochondrial metabolism in epithelial cancer cells in situ: visualizing the therapeutic effects of metformin in tumor tissue. *Cell cycle* **10**, 4047–4064 (2011).

170. Martinez-Outschoorn, U., Sotgia, F. & Lisanti, M. P. Tumor Microenvironment and Metabolic Synergy in Breast Cancers: Critical Importance of Mitochondrial Fuels and Function. *Semin. Oncol.* **41**, 195–216 (2014).

171. Brandenburg, S. *et al.* Myeloid cells expressing high level of CD45 are associated with a distinct activated phenotype in glioma. *Immunol. Res.* **65**, 757–768 (2017).

172. Krzywinska, E. *et al.* CD45 isoform profile identifies natural killer (NK) subsets with differential activity. *PLoS One* **11**, e0150434 (2016).

173. Petkov, S. *et al.* High CD45 expression of CD8+ and CD4+ T cells correlates with the size of HIV-1 reservoir in blood. *Sci. Rep.* **10**, 20425 (2020).

174. Hadrup, S. & Donia, M. Effector CD4 and CD8 T cells and their role in the tumor microenvironment. *Cancer Microenviron.* **6**, 123–133 (2013).

175. Jiang, Y., Li, Y. & Zhu, B. T-cell exhaustion in the tumor microenvironment. *Cell Death Dis.* **6**, e1792–e1792 (2015).

176. Ock, C.-Y. *et al.* Pan-Cancer Immunogenomic Perspective on the Tumor Microenvironment Based on PD-L1 and CD8 T-Cell InfiltrationTumor Microenvironment Immune Type in Pan-Cancer. *Clin. cancer Res.* **22**, 2261–2270 (2016).

177. Yang, L., Pang, Y. & Moses, H. L. TGF-β and immune cells: an important regulatory axis in the tumor microenvironment and progression. *Trends Immunol.* **31**, 220–227 (2010).

178. Dhodapkar, M. V, Krasovsky, J. & Olson, K. T cells from the tumor microenvironment of patients with progressive myeloma can generate strong, tumor-specific cytolytic responses to autologous, tumor-loaded dendritic cells. *Proc. Natl. Acad. Sci.* **99**, 13009–13013 (2002).

179. Guiducci, C., Vicari, A. P., Sangaletti, S., Trinchieri, G. & Colombo, M. P. Redirecting in vivo elicited tumor infiltrating macrophages and dendritic cells towards tumor rejection. *Cancer Res.* **65**, 3437–3446 (2005).

180. Shafer-Weaver, K. A. *et al.* Immunity to murine prostatic tumors: continuous provision of T-cell help prevents CD8 T-cell tolerance and activates tumor-infiltrating dendritic cells. *Cancer Res.* **69**, 6256–6264 (2009).

181. Fu, C. & Jiang, A. Dendritic cells and CD8 T cell immunity in tumor microenvironment. *Front. Immunol.* **9**, 3059 (2018).

182. Bronte, V. *et al.* Recommendations for myeloid-derived suppressor cell nomenclature and characterization standards. *Nat. Commun.* **7**, 12150 (2016).

183. Niles, M. A. *et al.* Macrophages and dendritic cells are not the major source of pro-inflammatory cytokines upon SARS-CoV-2 infection. *Front. Immunol.* **12**, 647824 (2021).

184. Tran, T. H., Rastogi, R., Shelke, J. & Amiji, M. M. Modulation of Macrophage Functional Polarity towards Anti-Inflammatory Phenotype with Plasmid DNA Delivery in CD44 Targeting Hyaluronic Acid Nanoparticles. *Sci. Rep.* (2015).

185. Fontenot, J. D., Gavin, M. A. & Rudensky, A. Y. Foxp3 programs the development and function of CD4+ CD25+ regulatory T cells. *Nat. Immunol.* **4**, 330–336 (2003).

186. Rudensky, A. Y. Regulatory T cells and Foxp3. *Immunol. Rev.* **241**, 260–268 (2011).

187. Walzer, T. *et al.* Identification, activation, and selective in vivo ablation of mouse NK cells via NKp46. *Proc. Natl. Acad. Sci.* **104**, 3384–3389 (2007).

188. DuPré, S. A., Redelman, D. & Hunter, K. W. J. The mouse mammary carcinoma 4T1: characterization of the cellular landscape of primary tumours and metastatic tumour foci. *Int. J. Exp. Pathol.* **88**, 351–360 (2007).

189. Rokop, M. E., Auchtung, J. M. & Grossman, A. D. Control of DNA replication initiation by recruitment of an essential initiation protein to the membrane of Bacillus subtilis. *Mol. Microbiol.* (2004).

190. Harwood, C. R. & Cutting, S. M. Molecular biological methods for Bacillus. (1990).

191. Francis, K. P. *et al.* Visualizing pneumococcal infections in the lungs of live mice using bioluminescent Streptococcus pneumoniae transformed with a novel gram-positive lux transposon. *Infect. Immun.* (2001).

192. Mills, E. L. *et al.* Succinate Dehydrogenase Supports Metabolic Repurposing of Mitochondria to Drive Inflammatory Macrophages. *Cell* **167**, 457-470.e13 (2016).

193. Zhang, G.-L., Zhang, Y., Cao, K.-X. & Wang, X.-M. Orthotopic Injection of Breast Cancer Cells into the Mice Mammary Fat Pad. *JoVE* e58604 (2019).

CHAPTER 4

MAGNETOTHERMAL CONTROL OF TEMPERATURE-SENSITIVE REPRESSORS IN SUPERPARAMAGNETIC IRON NANOPARTICLE-COATED *BACILLUS SUBTILIS*

PUBLICATION NOTICE

The following dissertation chapter describes coating *B. subtilis* engineered with thermally responsive genetic switches with superparamagnetic iron as a way of non-invasive transcriptional control of bacteria using alternating magnetic fields. Emily Greeson constructed new strains of *B. subtilis* with genetic switches (temperature sensitive repressors) that respond to thermal energy and characterized the response of these switches to thermal energy. I worked jointly with Emily Greeson on this chapter and focused on coating *B. subtilis* with superparamagnetic iron and testing alternating magnetic field parameters to generate thermal energy (magnetothermal energy) to regulate transcription in the strains Emily Greeson constructed. Dr. Ashley Makela supported the characterization of the magnetothermal energy effect on *B. subtilis*. Dr. Christopher Contag supervised and aided in the conception and development of controlling *B. subtilis* with magnetothermal energy.

This chapter was published as a preprint in “Greeson, E. M., Madsen, C. S., Makela, A. V & Contag, C. H. Magnetothermal control of temperature-sensitive repressors in superparamagnetic iron nanoparticle-coated *Bacillus subtilis*. *bioRxiv* 2022.06.18.496685 (2022).” and reprint permission is reserved to the authors for use in this dissertation. The following chapter has been submitted to “Greeson, E. M., Madsen, C. S., Makela, A. V & Contag, C. H. Magnetothermal control of temperature-sensitive repressors in superparamagnetic iron nanoparticle-coated *Bacillus subtilis*. *ACS Nano*. (2022).” and reprint permission was granted for use in this dissertation.

ABSTRACT

Superparamagnetic iron oxide nanoparticles (SPIONs) are used as contrast agents in magnetic resonance imaging (MRI) and magnetic particle imaging (MPI) and resulting images can be used to guide magnetothermal heating. Alternating magnetic fields (AMF) cause local temperature increases in regions with SPIONs, and we investigated the ability of magnetic hyperthermia to regulate temperature-sensitive repressors (TSRs) of bacterial transcription. The TSR, TlpA39, was derived from a Gram-negative bacterium, and used here for thermal control of reporter gene expression in Gram-positive, *Bacillus subtilis. In vitro* heating of *B. subtilis* with TlpA39 controlling bacterial luciferase expression, resulted in a 14.6-fold (12 hour; h) and 1.8-fold (1 h) increase in reporter transcripts with a 9-fold (12 h) and 11.1-fold (1 h) increase in bioluminescence. To develop magnetothermal control, *B. subtilis* cells were coated with three SPION variations. Electron microscopy coupled with energy dispersive X-ray spectroscopy revealed an external association with, and retention of, SPIONs on *B. subtilis*. Furthermore, using long duration AMF we demonstrated magnetothermal induction of the TSRs in SPION-coated *B. subtilis* with a maximum of 4.6-fold increases in bioluminescence. After intramuscular injections of SPION-coated *B. subtilis,* histology revealed that SPIONs remained in the same locations as the bacteria. For *in vivo* studies, 1 h of AMF is the maximum exposure due to anesthesia constraints. Both *in vitro* and *in vivo*, there was no change in bioluminescence after 1 h of AMF treatment. Pairing TSRs with magnetothermal energy using SPIONs for localized heating with AMF can lead to transcriptional control that expands options for targeted bacteriotherapies.

INTRODUCTION

Magnetic nanoparticles have broad applications in biomedicine including imaging, drug delivery, theranostics and therapeutic hyperthermia[1–3]. Nanoparticles have also been used to study and treat bacterial infections through the coating of bacterial membranes for imaging and as anti-microbial agents[4–10]. Superparamagnetic iron oxide nanoparticles (SPIONs) are useful imaging contrast agents for magnetic resonance imaging (MRI) and more recently in magnetic particle imaging (MPI)[11–16]. MPI detects SPIONs directly, providing a readout of both iron content and location with high specificity and sensitivity[11,17–19]. Further, MPI can guide the application of electromagnetic energy generated by alternating magnetic fields (AMF) to cause local temperature increase known as magnetic hyperthermia[20–22] to precisely heat the iron-containing area[23].

Bacillus subtilis is a model Gram-positive organism[24] with numerous synthetic biology strategies for manipulating gene expression[25,26], global metabolic networks[27] and the entire genome[28–30] making it well-suited for engineering systems for spatial and temporal regulation[27]. *B. subtilis* is a generally recognized as safe organism that is used for industrial protein production and is highly resistant to environmental stressors such as heat with a heat shock response at 48ºC[31,32]. High heat resistance and well characterized protein production pathways may make *B. subtilis* an ideal chassis organism for thermal energy controlled protein production that could act as therapeutics[33–35]. *B. subtilis* also has multiple characterized inducible systems including several sugar-regulated inducible systems[36]. *B. subtilis* has been well studied for a variety of *in vitro* industry applications in areas such as pharmaceutical/nutraceutical production, recombinant protein production and secretion, and production of functional peptides and oligopeptides[37–40]. However, these inducible systems have limited control for both *in vitro* and *in vivo* applications due to potential host toxicity, cost and carbon-source dependence[41].

Temperature-sensitive repressors (TSRs) are a class of repressors that bind an operator-promoter region with temperature dependence, and show promise for *in vivo* control with local heating for localized delivery[42]. With the addition of thermal energy to the system, a structural change occurs that releases the repressor from DNA resulting in transcription[43]. Thus, TSRs are different from heat shock promoters (HSP) and rely on housekeeping sigma factors such as σA in *B. subtilis*[44,45]. TSRs offer a greater dynamic range than HSP and do not necessitate stress conditions for induction[42,43]. There is precedent for thermal control of *B. subtilis* with induction of gene expression at low and high temperatures in both native and recombinant systems[45–50]. Additionally, TSRs have been shown to be controlled previously in Gram-negative organisms with ultrasound to create localized thermal energy for transcriptional control[27].

The configuration, size and composition of SPIONs have a large effect on MPI performance[53–55] and magnetothermal heating[56]. Synomag-D is a commercially available multi-core “nanoflower” particle[57] and has demonstrated improved MPI performance[58,59] as well as high intrinsic power loss under magnetic hyperthermia[60,61]. Pairing TSRs with magnetothermal energy using SPIONs for localized heating with AMF can lead to regional transcriptional control as guided by MPI or MRI for new approaches to bacteriotherapy. There are many bacteriotherapy approaches under investigation, and FDA review, for a variety of human cancers[62–67]. We engineered TSRs[42,43] into the model organism, *B subtilis*, towards the development of noninvasive genetic control of a minimally invasive biological therapy (Fig. 4.1).

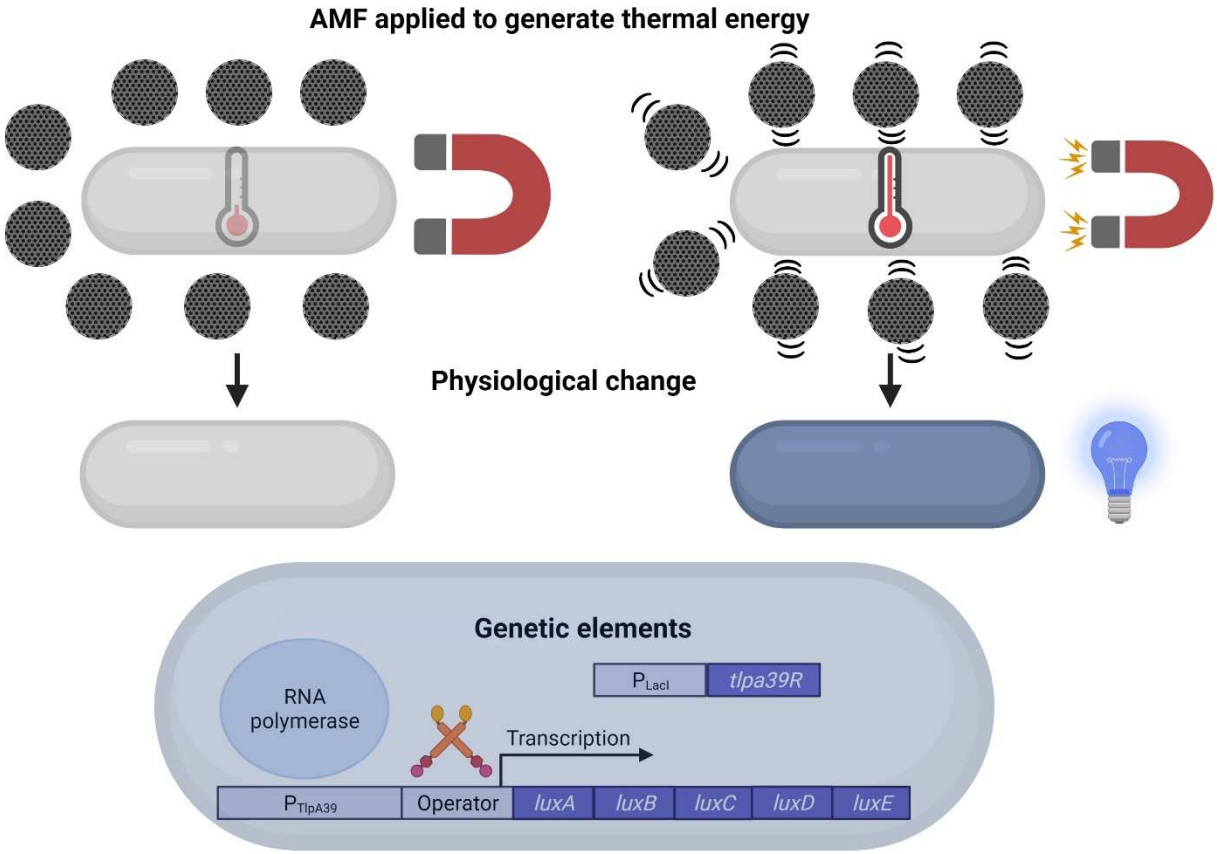

Figure 4.1. Illustration of magnetothermal control of *B. subtilis*

B. subtilis coated with Synomag-D SPIONs can be regulated by thermal energy generated from the SPIONs upon application of AMF which initiates transcription of *luxA-E* operon from P_{TlpA39}.

RESULTS

Temperature sensitive repressors control of transcription in *B. subtilis*

Magnetic nanoparticles have been used for several biomedical applications and can be further expanded into a measure of control through non-invasive stimuli. Magnetic hyperthermia has been proposed to be used for tumor microenvironment disruption by combining synthetic and biological magnetic nanoparticles with AMF but with limitations[3,14,20,21,23]. We investigated the concept of using magnetothermal energy to control a genetic switch in Gram-positive bacteria. This would comprise a modular platform as the basis for developing a variety of potential therapeutics. Directed delivery and targeted activation can improve therapeutic effects and reduce toxicity of bacteriotherapies while imaging can guide development of novel bacteriotherapies by assessing delivery, retention and activation within the target tissue[68]. Here we use magnetic hyperthermia and imaging to characterize the use of superparamagnetic nanoparticle-coated *B. subtilis* as a new approach for controlling Gram-positive bacterial gene expression with potential use in bacteriotherapies.

A TSR (TlpA39)[42,43,69] was used to control transcription of the *luxA-E* operon such that luciferase activity (bioluminescence) could be used as a rapid readout for regulation[70]. This construct demonstrated thermal transcriptional control in *B. subtilis* in response to continuous heating. *B. subtilis* P_{TlpA39} *luxA-E +tlpa39R* (+TlpA39R) and *B. subtilis* P_{TlpA39} *luxA-E -tlpa39R* (-TlpA39R) were heated continuously in a thermocycler for 12 h at 25°C, 37°C, 39°C or 42°C to test induction of P_{TlpA39}. *B. subtilis* +TlpA39R showed a 9.0-fold increase ($p<0.0001$) in luciferase activity when normalized to OD_{600} from 25°C to 37°C while *B. subtilis* -TlpA39R showed a 0.5-fold increase ($p<0.0001$; Fig. 4.2A). Bioluminescence did not significantly increase when cells were induced at temperatures above 37°C while mRNA levels, as measured by real-time quantitative PCR (RT-qPCR), showed continual increase in P_{TlpA39} activity up to 42°C in *B.*

subtilis +TlpA39R (Fig. 4.2B). The second gene in the *luxA-E* operon engineered for expression in Gram-positive organisms[69], *luxB,* was chosen as the target for RT-qPCR analysis since it encodes for the β subunit of the alkanal monooxygenase enzyme that provides structure for the active conformation of the α subunit of the heterodimeric luciferase[71]. In the +TlpA39R strain *luxB* levels increased by 1.9-, 3.6-, and 14.6-fold change at 37°C, 39°C and 42°C, respectively. The *tlpa39R* transcript fold change was 1.6, 2.9, and 7.4 at 37°C, 39°C and 42°C, respectively in *B. subtilis* +TlpA39R. *B. subtilis* -TlpA39R showed no significant change in bioluminescence signal and minimal change in P_{TlpA39} activity from mRNA levels as expected from the unregulated promoter (Fig. 4.2C). In the -TlpA39R strain *luxB* levels increased by 2.1-, 1.8-, and 1.6-fold change at 37°C, 39°C and 42°C, respectively. The increase in bioluminescence in the -TlpA39R strain from 25°C to 37°C can be attributed to increased activity of the Lux enzymes over those temperatures and more so to a shift in *B. subtilis* metabolism which is consistent throughout the study[50,70,77].

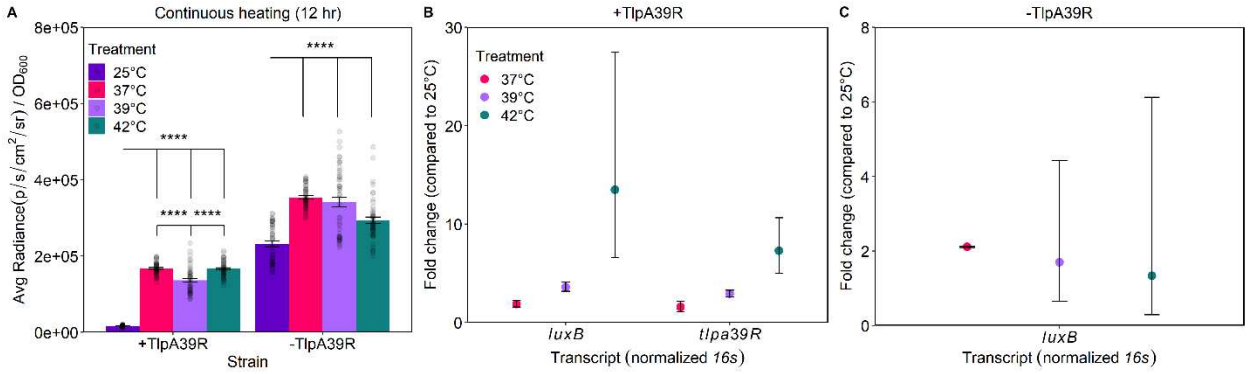

Figure 4.2. Continuous heating of *B. subtilis* +TlpA39R and *B. subtilis* -TlpA39R to induce expression of LuxA-E from P_{TlpA39}

Error bars are mean ± standard error mean. (A). Transcript levels determined by RT-qPCR for *luxB* and *tlpa39R* from +TlpA39R strain (B) along with *luxB* from -TlpA39R strain (C) at induction temperatures compared to 25°C. RT-qPCR shown as mean with error bars as 95% confidence intervals. Statistics were displayed when comparing to 25°C for both +/- TlpA39R strains and between each increasing temperature in +TlpA39R strain. ****p<0.0001.

SPION coating of *B. subtilis*

To test magnetothermal activation, *B. subtilis* ZB307[72] (derivative of *B. subtilis* strain 168) was coated SPIONs using plain-dextran, carboxyl or amine-coated Synomag-D[58,59]; each were assessed for coating efficiency, interactions between SPION and bacteria and magnetothermal heating. Scanning electron microscopy coupled with energy dispersive X-ray spectroscopy (SEM-EDS) was performed and displayed associations with, and retention of, the nanoparticles and *B. subtilis.* All three variations were found surrounding and associating with *B. subtilis* as confirmed by Fe signal from EDS, but with varied consistency of coating observed (Fig. 4.3). The plain-dextran and amine-coated evenly covered and associated with *B. subtilis* while the carboxyl-coated appeared to heterogeneously associate with *B. subtilis* in large aggregates (Fig. 4.3). Iron signal was absent from a *B. subtilis* sample without SPIONs (Fig. 4.4). SPIONs were not found in the cytoplasm of the *B. subtilis* after coating as shown by transmission electron microscopy (TEM) cross-sections (Fig. 4.5). To further investigate the three *B. subtilis* coatings, inductively coupled plasma mass spectrometry (ICP-MS) was performed to measure iron content. There was more iron in the carboxyl-coated samples compared to the plain-dextran and amine-coated, 464.8 and 294.7 times, respectively (Table 4.1). This highlights the disparity between the way the three SPION variations associate with *B. subtilis*.

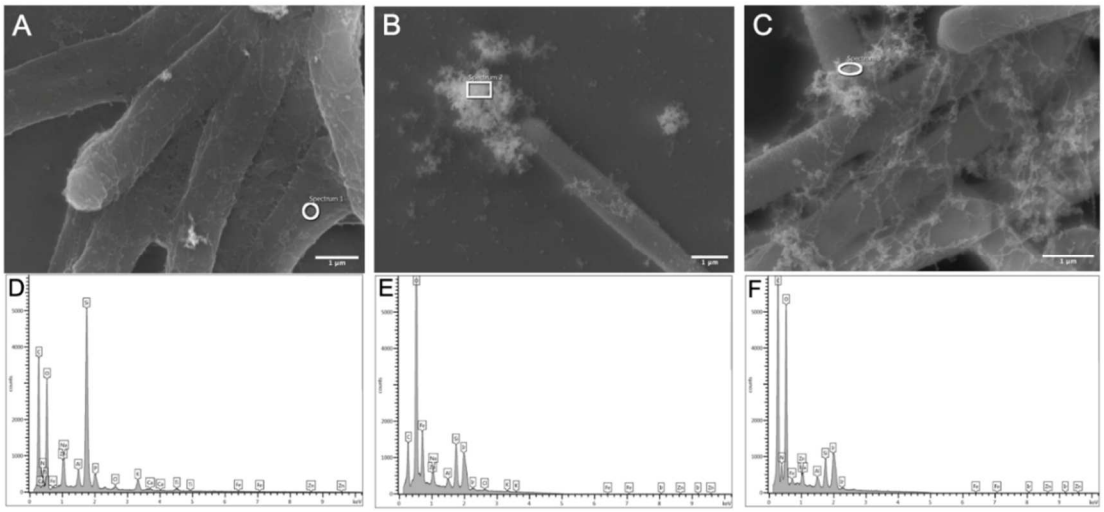

Figure 4.3. Visualization and elemental analysis of *B. subtilis* and SPION associations

Plain-dextran SPIONs; mag. = 27,000X (A), carboxyl SPIONS; mag. = 23,000X (B) and amine SPIONS; mag. = 33,000X (C) show various associations with *B. subtilis* as observed by scanning electron microscopy. Elemental analysis was performed on each of the samples (D-F) in the regions indicated with white borders to show iron (Fe) signal to identify the SPIONs. Scale bars = 1 µm.

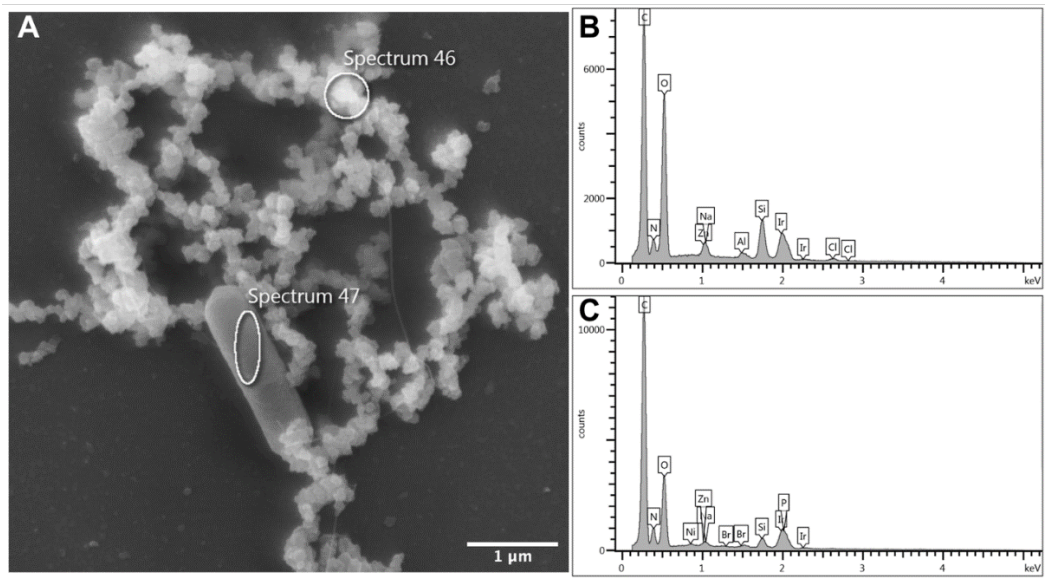

Figure 4.4. Elemental analysis of *B. subtilis* uncoated control

Sample analyzed with SEM-EDS in two regions (A) showing no iron (Fe) signal from the extracellular material (B) or from the bacterium (C). Magnification = 12,000X; scale bar = 1 µm.

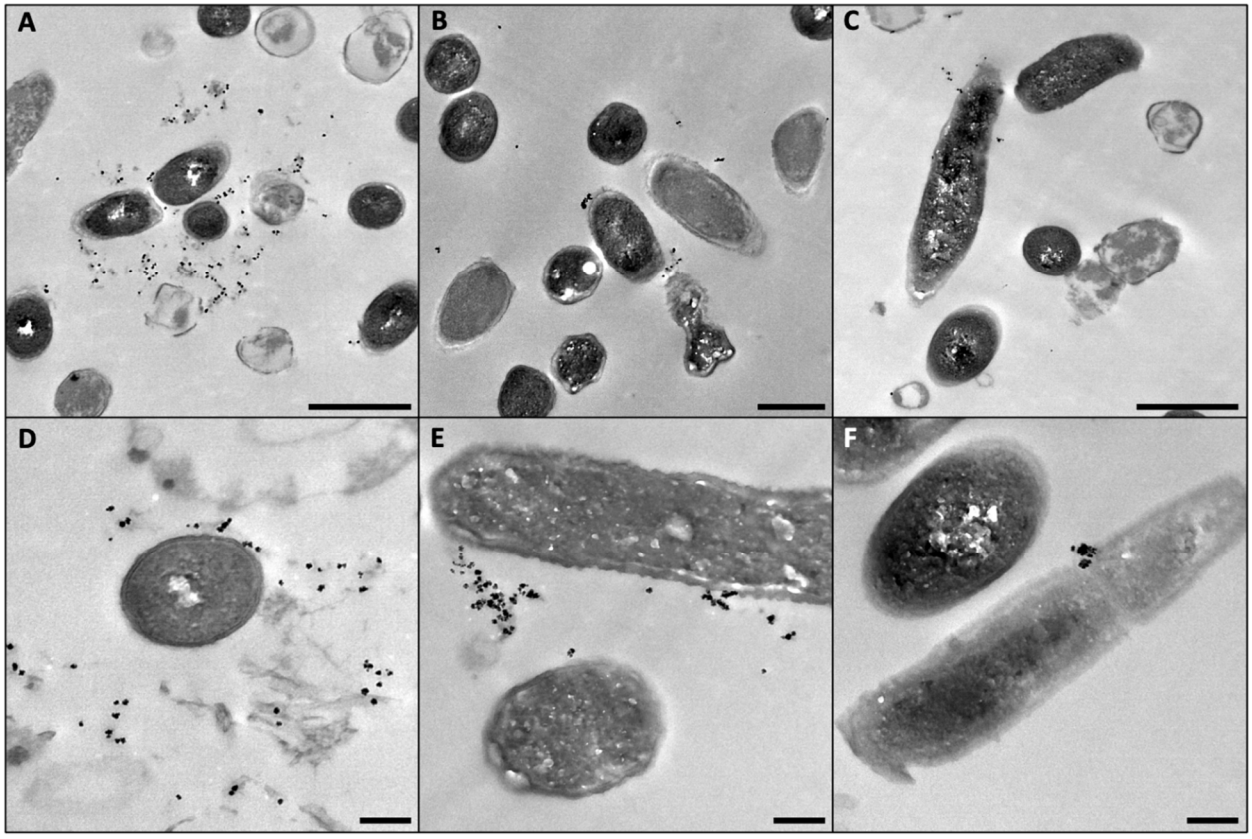

Figure 4.5. Transmission electron microscopy of *B. subtilis* coated with three SPIONs

Embedded and cross-section of each *B. subtilis*-SPION coating variation: plain-dextran (A, D), carboxyl (B, E), and amine (C, F) showing nanoparticles located outside of the bacterial cells. Mag. = 8,000X; scale bars = 1 µm (A-C). Mag. = 20,000X; scale bars = 200 nm (D-F).

Table 4.1. Quantification of iron via ICP-MS

Each of the three SPION variations and an untreated control sample were analyzed via ICP-MS. Values for the three experimental samples were adjusted by subtracting the background iron present from the untreated sample. n=1 for all samples.

ICP-MS Iron Quantification		
Sample	**Adjusted Total Iron (ng in 25 µl)**	**Adjusted Iron Concentration (ppm)**
Plain	19.80	0.792
COOH	9203.15	368.126
Amine	31.23	1.249

B. subtilis viability after coating with SPIONs and AMF application

B. subtilis viability was assessed by flow cytometry after coating with each of the SPIONs. Two bacterial concentrations, equal to OD_{600} = 1 or 2, were tested while maintaining the same concentration of the Synomag-D variations to determine if a high ratio of iron to *B. subtilis* would cause toxicity. After 2 h of coating, none of the Synomag-D variations at either *B. subtilis* concentrations demonstrated reduction in viability compared to the untreated control and all treatments were significant when compared to the 98°C control for cell death (Fig. 4.6A, B). Furthermore, viability was assessed after 12 h of AMF using the plain-dextran particle as it produced the most reproducible heating response from *B. subtilis* +TlpA39R at an OD_{600} = 2 with a 16.0 mT radio frequency (RF) amplitude (data not shown). The *B. subtilis* +TlpA39R strain had slight, but not significant differences in viability compared to the -TlpA39R strain with or without AMF treatment (Fig. 4.6C).

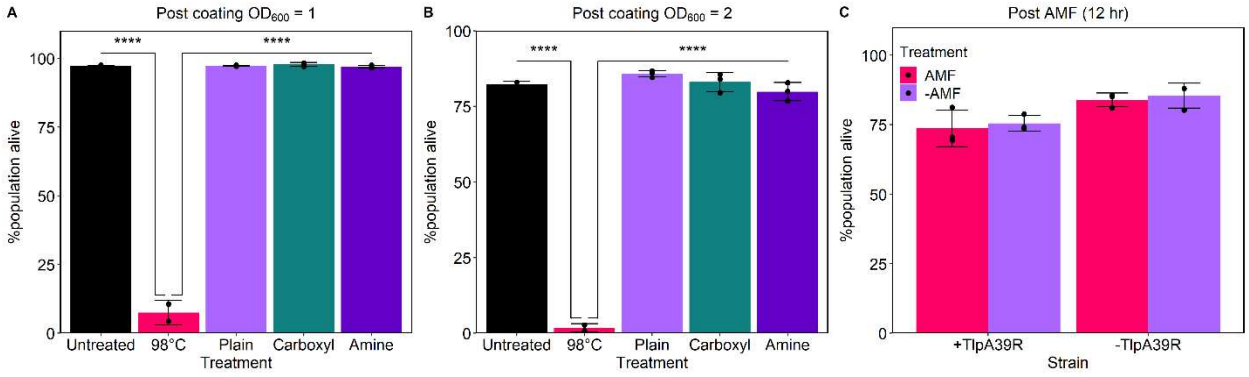

Figure 4.6. Flow cytometry determining viability of *B. subtilis* after coating with the three-particle variations and AMF application

Viability of *B. subtilis* was determined after coating with the three SPION variations at two bacterial concentrations (A, B). *B. subtilis* +TlpA39R and *B. subtilis* -TlpA39R were compared in and outside the AMF after 12 h of heating when coated with the plain-dextran particle (C). Error bars are mean ± standard deviation. ****p<0.0001.

Magnetothermal induction of *B. subtilis* transcription

To illustrate transcriptional control of potential bacteriotherapies, magnetic hyperthermia using the HYPER system, was applied to *B. subtilis* coated with each of the three variations of the SPION. The growth temperature of the *B. subtilis* for the HYPER experiments was 37°C as opposed to the thermocycler experiments where the growth temperature is 25°C. This was intended to support *in vivo* studies as the core body temperature of mice and humans is approximately 37°C[73]. Magnetic hyperthermia increased bioluminescent signals in bacteria coated with all particle variations with plain-dextran producing the most reproducible and significant result in the higher bacterial concentration at the max RF amplitude (16.0 mT). The carboxyl-coated SPION caused the highest fold changes in signal compared to the -AMF condition but with the most variability between replicates. The plain-dextran coated *B. subtilis* +TlpA39R showed only a 0.2-fold change ($p=0.0456$) at the lower concentration when exposed to AMF while at the higher bacterial concentration with a 16.0 mT RF amplitude showed a reproducible 1.4-fold change ($p<0.0001$; Fig. 4.7A, D). Carboxyl-coated *B. subtilis* +TlpA39R showed a 4.6-fold change ($p=0.0214$) and a 3.4-fold change ($p=0.014$) in bioluminescence when exposed to AMF at the lower and higher bacterial concentrations respectively but with variability (Fig. 4.7B, E). Additionally, the -TlpA39R strain showed a 1.9-fold change ($p=0.1689$) and a 1.1-fold change ($p=0.014$) in bioluminescence when exposed to AMF at the lower and higher bacterial concentrations respectively and with high variability. Finally, the amine-coating produced a 0.6-fold increase ($p=0.0026$) at the lower bacterial concentration in the +TlpA39R strain but showed a small decrease in signal at the higher bacterial concentration when exposed to AMF ($p=0.0217$; Fig. 4.7C, F). Due to the plain-dextran coating producing the most significant and reproducible result at the higher bacterial concentration, this condition was chosen for transcript measurements. There was a 1.2-fold increase in *luxB* levels even with increasing *tlpa39R* levels (1.7-fold change) in the +TlpA39R strain (Fig. 4.7G) and 1.4-fold

increase in *luxB* in the -TlpA39R strain after AMF exposure (Fig. 4.7H). Thermal probes indicated that only the carboxyl-coated SPION increased the culture medium by +3°C (Fig. 4.8).

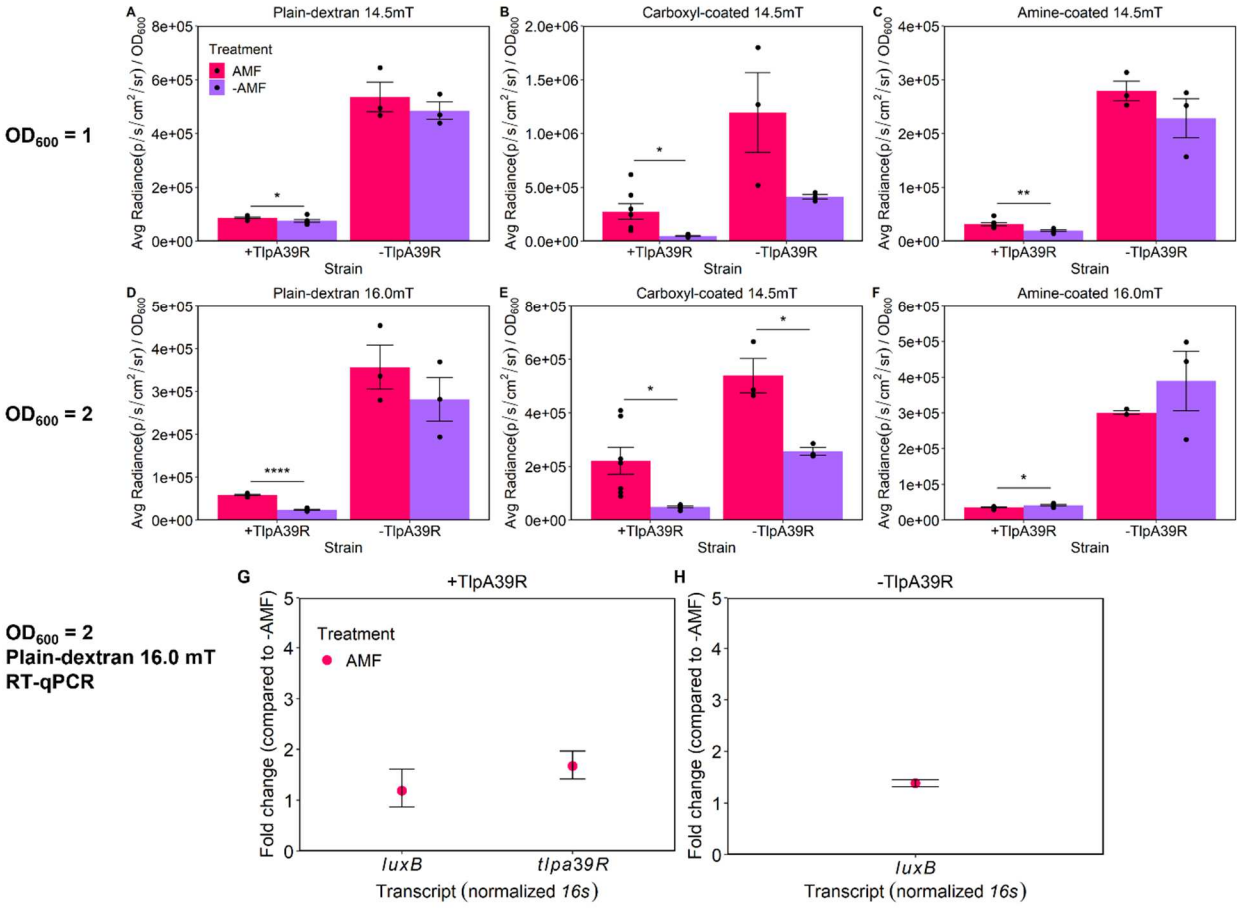

Figure 4.7. Magnetic hyperthermia increasing bioluminescent signal (Avg. Radiance) using the HYPER Theranostic Hyperthermia System

B. subtilis +TlpA39R and *B. subtilis* -TlpA39R were compared in and outside the AMF with the three Synomag-D coating variations at OD_{600} = 1 (A-C) or 2 (D-F). Error bars are mean ± standard error mean. RT-qPCR was used to determine transcript levels of the two strains and compare AMF to -AMF(G-H). RT-qPCR shown as mean with error bars as 95% confidence intervals. *p<0.05, **p<0.01, ****p<0.0001.

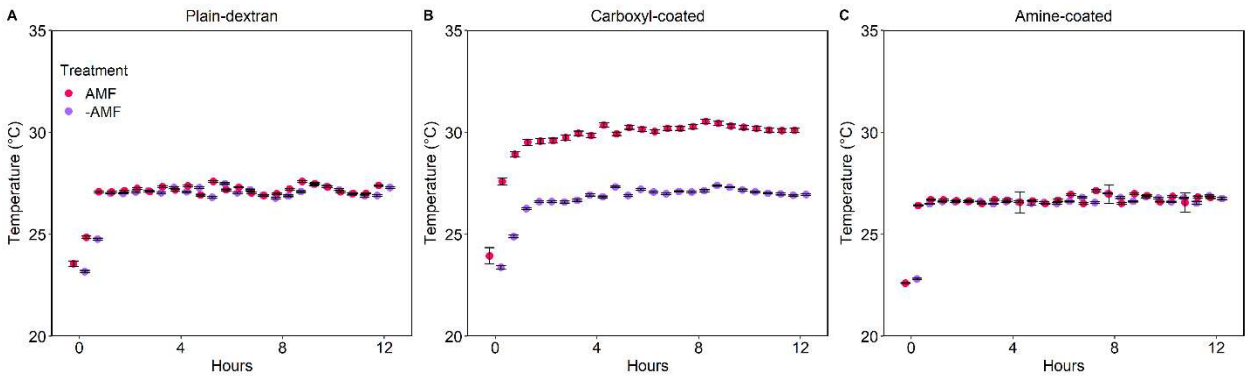

Figure 4.8. Magnetic hyperthermia impact on culture medium temperature with three Synomag-D variations

Points indicate temperature every 0.5 h over 12 h with 60 temperature reads taken every 1 min cycle considered as technical replicates. Error bars are mean ± standard deviation.

Reducing thermal energy application to *in vivo* timeframe

For small animal *in vivo* applications, anesthesia for times >1 h can cause negative impacts on animal health[75,76]. Therefore, reducing AMF application time to around 1 h was necessary for demonstration of translatability of this approach. Increases in bioluminescent signals and *luxB* levels were seen after 1 h of continuous heating in a thermocycler (Fig. 4.9A, B). *B. subtilis* +TlpA39R had a 11.1-fold increase ($p<0.0001$) in luciferase activity when normalized to OD_{600} from 25°C to 37°C while *B. subtilis* -TlpA39R showed a 1.3-fold increase ($p<0.0001$). When increasing the temperature from 37°C to 39°C and from 39°C to 42°C in the regulated strain (+TlpA39R) there was a 0.5-fold ($p<0.0001$) and 0.1-fold change ($p<0.0001$) between each step up, respectively, whereas the –TlpA39R strain had a negative fold change when comparing bioluminescent signal between 37°C to 39°C (-0.02-fold;$p=0.9061$) and 39°C to 42° (-0.3-fold;$p<0.0001$). In the +TlpA39R strain *luxB* transcript levels increased by 0.9-, 0.9-, and 1.8-fold change at 37°C, 39°C and 42°C, respectively, indicating induction between 39°C and 42°C. The *tlpa39R* transcript fold change was 0.8, 0.9, and 0.9 at 37°C, 39°C and 42°C,

respectively in *B. subtilis* +TlpA39R showing consistent levels as temperature increased. The *B. subtilis* -TlpA39R showed similar changes to +TlpA39R in *luxB* levels at 37°C and 39°C (0.9- and 0.9-fold, respectively), but showed a lesser fold change of 0.4 at 42°C compared to the regulated strain (Fig. 4.9C). This indicates that there is some temperature dependent induction of *luxB* in the +TlpA39R strain after 1 h of continuous heating. However, AMF application for 1 h only increased bioluminescent signal by 0.02-fold in the +TlpA39R strain and a minimal 1.0-fold increase (doubling) in *luxB* transcripts which was similar to the –TlpA39R *luxB* mean increase of 1.5 (Fig. 4.9D-F).

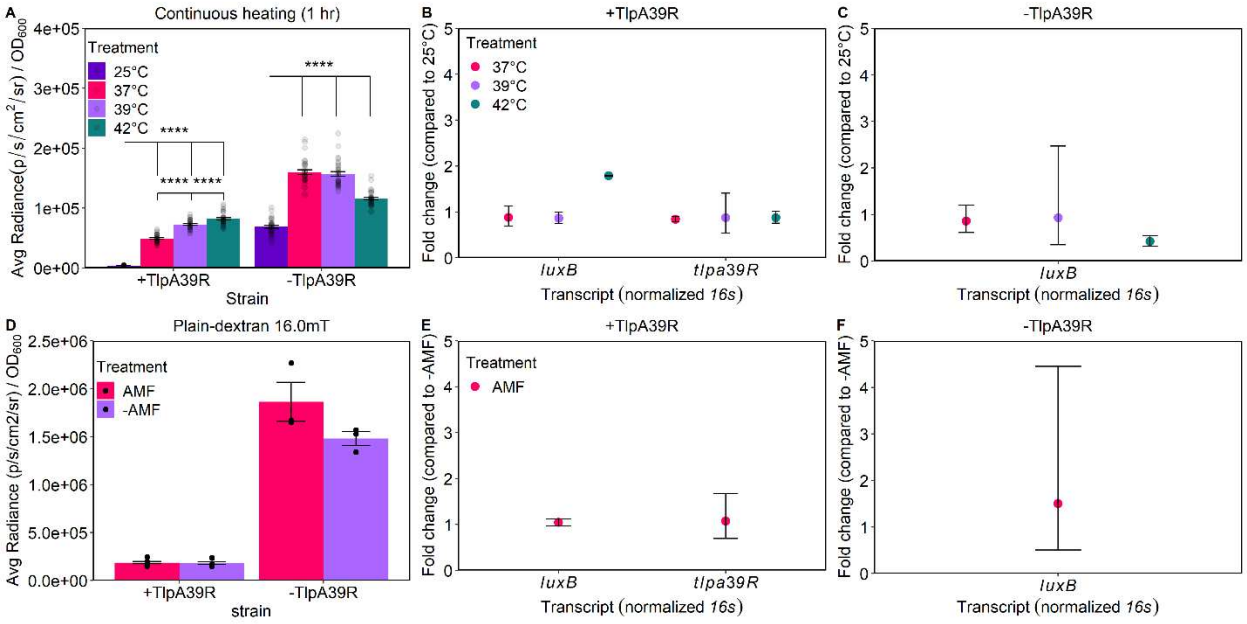

Figure 4.9. One-hour thermal inductions using continuous heating and magnetic hyperthermia

Reporter gene activity (Avg. Radiance) and transcript levels were measured for continuous and magnetic hyperthermia (A-C). *B. subtilis* +TlpA39R and *B. subtilis* -TlpA39R were compared in and outside the AMF (D-F). Error bars are mean ± standard error mean. RT-qPCR shown as mean with 95% confidence intervals. Statistics were displayed when comparing to 25°C for both +/- TlpA39R strains and between each increasing temperature in +TlpA39R strain for continuous heating.

Iron association with *B. subtilis* and magnetic hyperthermia *in vivo*

MPI was performed to quantify iron content in each sample, and these values were compared to those identified by ICP-MS (Table 4.1). Samples containing $1x10^8$ *B. subtilis* coated with the three Synomag-D coatings were resuspended in a volume relevant to intramuscular (IM) injections (25 µL). Only the carboxyl-coated *B. subtilis* could be detected in these conditions (Fig. 4.10B), with iron concentration at 384.8 ppm. The plain-dextran could not be detected when the 25 µL samples were imaged using MPI neither *in vitro* (Fig. 4.10A) nor *in vivo* (Fig. 4.11). When the plain-dextran samples were pooled to a total volume of 100 µL, MPI signals were detected (Fig. 4.10C inset) and iron quantified was 0.5 ppm, or 13.6 ng per 25 µL sample injected *in vivo* (Fig. 4.10D). The amine-coated sample was not detectable in a 25 µL sample volume (Fig. 4.10C) and was not pursued further due to the poor AMF response observed previously (Fig. 4.7C, F). MPI quantification showed that the carboxyl-coated SPION sample was 707.3 times that of the plain-dextran SPION (Fig. 4.10D).

A murine model of IM thigh injections was paired with the HYPER system and histology to assess iron association with the bacteria and potential changes in bioluminescence. Bacteria coated with SPIONs were prepared and imaged for bioluminescence quantification pre-injection, immediately post-injection, and 1 h post-treatment (+/-AMF). The bioluminescence levels decreased 4.1-fold and 8.0-fold from pre-injection to post-injection in +AMF and -AMF treatments, respectively, but the variance was high between replicates so there was no significance ($p=0.4841$; $p=0.3446$; Fig. 4.12). The change in bioluminescence before and after treatment was negligible with a 0.43-fold decrease and a 0.56-fold increase in the +AMF and –AMF conditions, respectively ($p=0.4813$; $p=0.4760$; Fig. 4.12). Histology using a modified Gram stain confirmed presence of *B. subtilis* within sectioned intramuscular tissue after 1 h treatments. Further, consecutive staining with a Perls' Prussian Blue protocol revealed *B. subtilis* and iron staining in the same location within the tissue (Fig. 4.10E-G). The white arrows

(Fig. 4.10F-G) indicate the presence of iron due to the insoluble Prussian blue pigment which is formed after the potassium ferrocyanide reagent reacts with ferric iron in the sample[77]. The use of the consecutive staining scheme which included multiple counterstains and decolorizing steps led to an atypical Gram stain result for *B. subtilis*. A sequential tissue section was stained using only the modified Gram stain and the standard purple rods of *B. subtilis* were observed adjacent to the muscle tissue stained yellow from the alcoholic saffron (Fig. 4.13A-C).

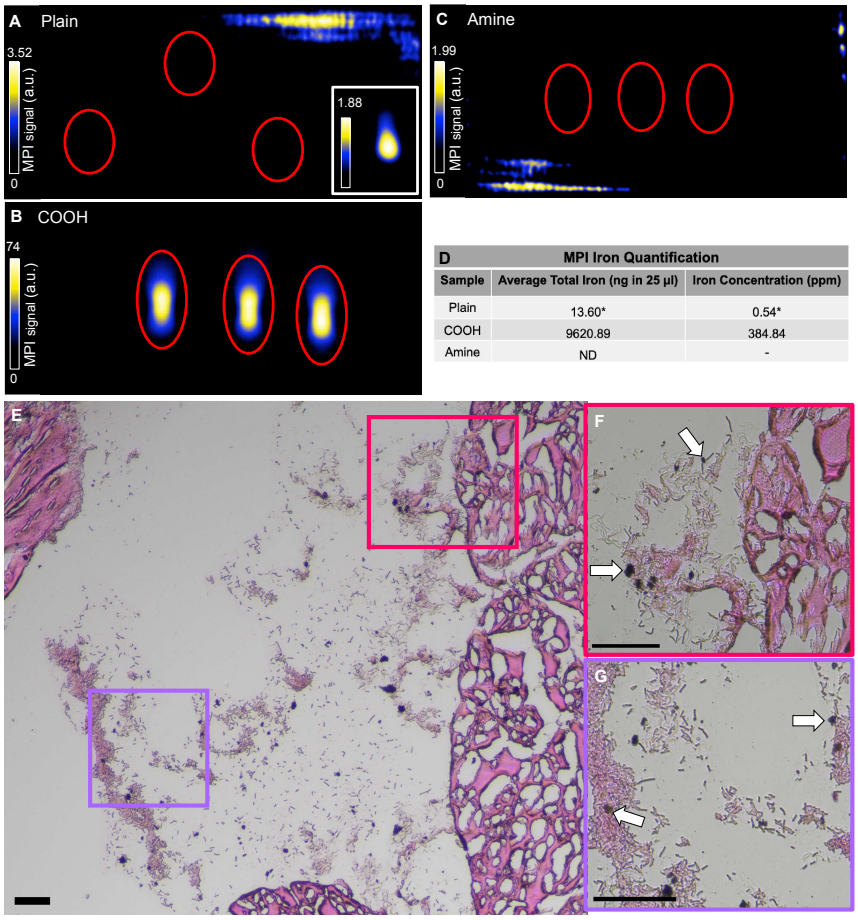

D MPI Iron Quantification

Sample	Average Total Iron (ng in 25 µl)	Iron Concentration (ppm)
Plain	13.60*	0.54*
COOH	9620.89	384.84
Amine	ND	-

Figure 4.10. MPI and histological analysis

B. subtilis +TIpA39R coated with the three SPION variations were analyzed via MPI in triplicate. MPI signals could not be detected in the plain-dextran sample in a 25 µL volume (A). Inset shows a pooled volume of 100 µL plain-dextran sample, adjusted to visualize MPI signals. Carboxyl-coated samples showed signal (B) while the amine-coated samples (C) were not detected in 25 µL volumes. MPI scale bars are individual for each condition and represent the full dynamic range of the image. Iron content was quantified using MPI data (D). *Quantification of the plain-dextran sample was performed on a 100 µL pellet and then calculated for a 25 µL volume. Sectioned tissue stained with a modified Gram stain followed Perls' Prussian Blue (PPB); magnification = 100X (E) and zoomed in regions indicated by magenta (F) and purple (G) boxes with magnification = 400X. White arrows indicate PPB-stained iron. a.u. = arbitrary units; ND = not detected. Scale bars = 50 µm.

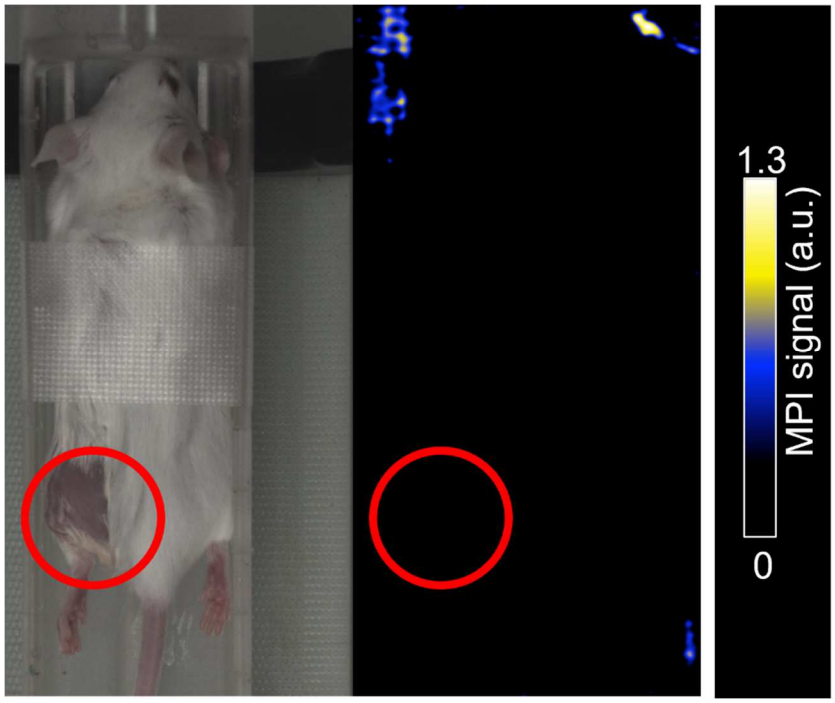

Figure 4.11. MPI of mouse thigh shows no signal from plain-dextran SPION

After injection of plain-dextran coated *B. subtilis* the -AMF control mouse was imaged via MPI and no discernible signal above background was found. Because of the injections of SPION-coated bacteria being below the limit of detection no additional mice were imaged (n=1). a.u. = arbitrary units.

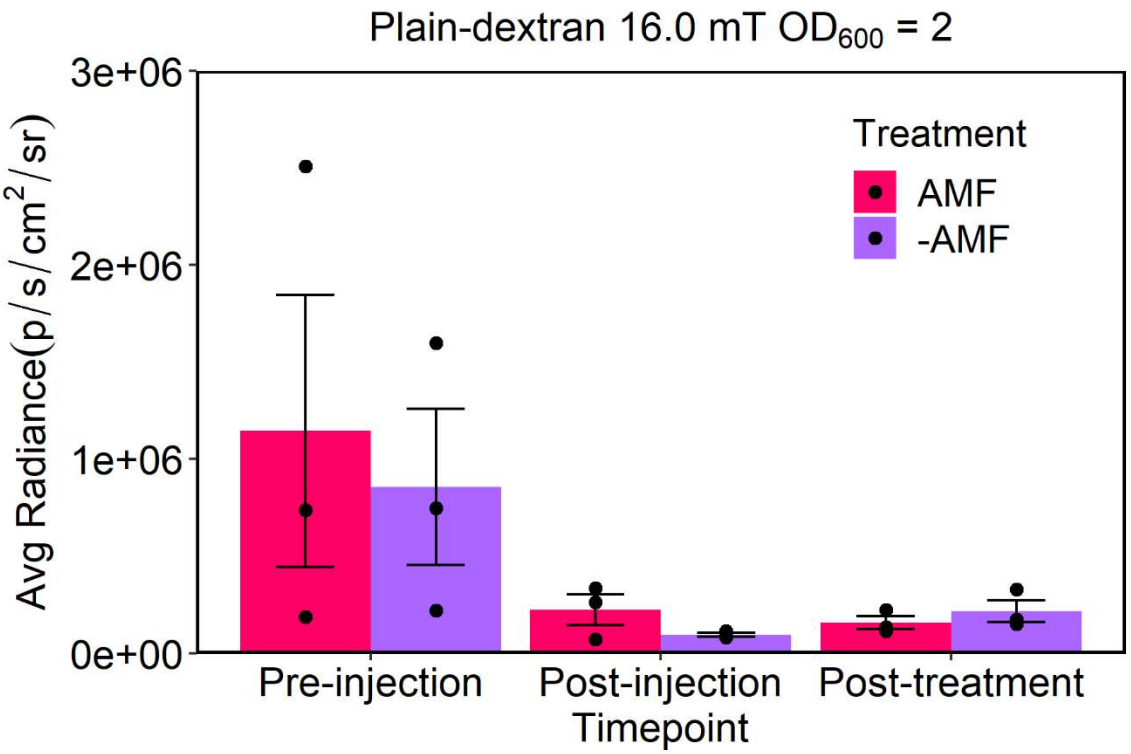

Figure 4.12. Magnetic hyperthermia of intramuscular injections

Magnetic hyperthermia did not significantly change bioluminescent signal (Avg. Radiance) when using the plain-dextran SPION. *B. subtilis* +TlpA39R was compared in and outside the AMF after injection and after 1 h of magnetic hyperthermia. Error bars are mean ± standard error mean; n=3; two-way repeated measures ANOVA with Tukey's post hoc showed no significance for any comparisons.

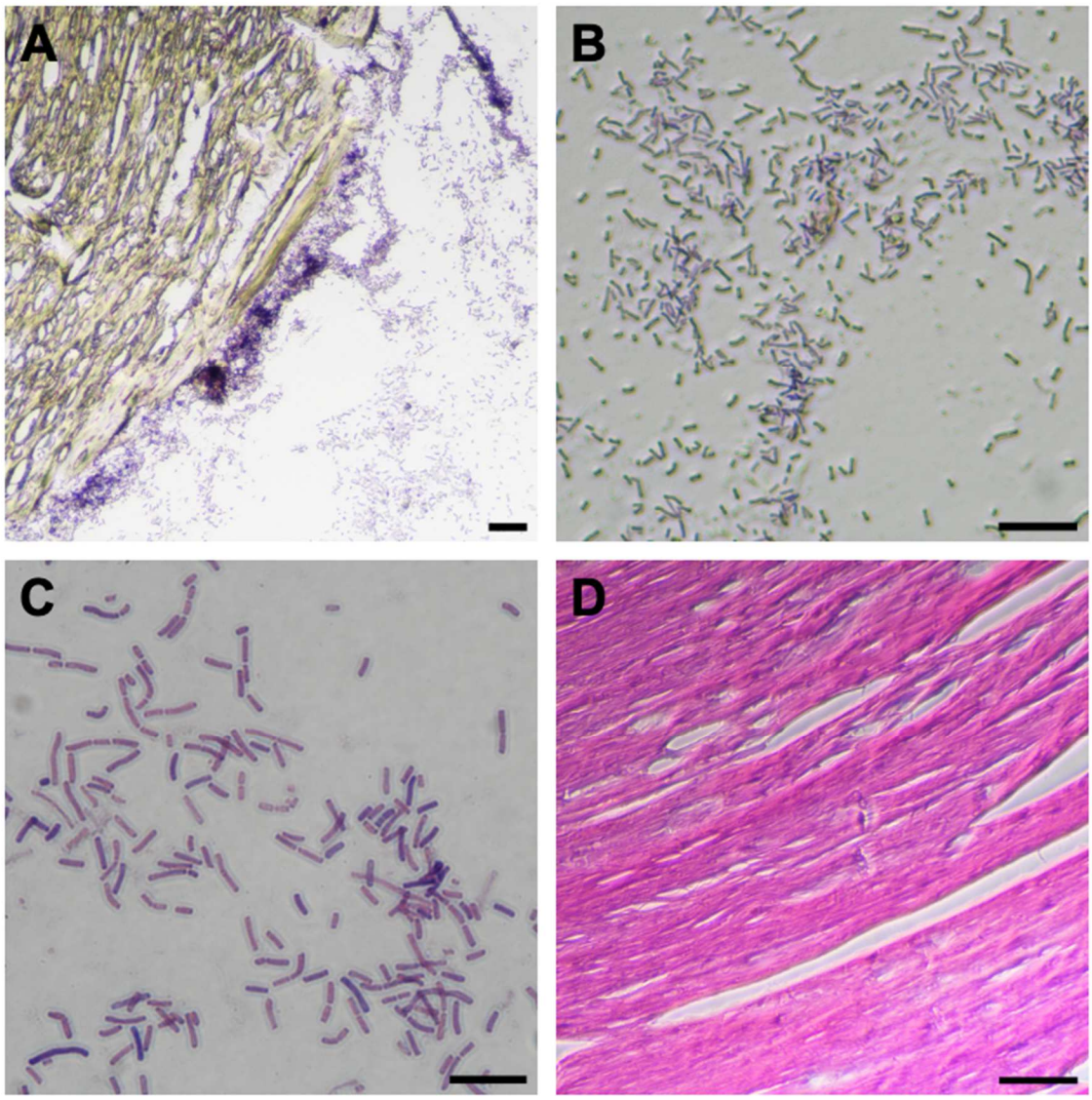

Figure 4.13. Modified Gram stain and hematoxylin and eosin staining of tissue sections

Mouse thigh muscles were sectioned and subsequently stained with a modified Gram stain method. Samples were imaged at various magnifications: 100X (A), 400X (B), and 1000X (C) with scale bars of 50 µm, 25 µm, and 10 µm, respectively. Muscle tissue is yellow from the alcoholic saffron counterstain and the purple rods are Gram positive from crystal violet which supports identification as *B. subtilis*. Hematoxylin and eosin staining was performed on mouse thigh controls with no samples injected. Imaging showed pink, eosin-stained longitudinal view of quadriceps muscle fibers; Magnification = 400X; scale bar = 25 µm (D).

DISCUSSION

The introduction of the TlpA39 regulatory system into *B. subtilis* demonstrated that a temperature-sensitive repressor optimized in a Gram-negative organism can be utilized in a Gram-positive organism to drive controlled transcription of the *luxA-E* operon by continuous or magnetothermal heating. The results indicate that the TlpA39 promoter and regulator system is functional in *B. subtilis* and able to regulate an operon with a slight temperature shift from what was observed in *Escherichia coli* previously (Fig. 4.2)[42]. This is further demonstrated by the increased levels of *luxB* transcription at increasing temperatures despite the increased levels of *tlpa39R* transcripts indicating more regulator protein available to bind the P_{TlpA39} operator-promoter region as indicated by RT-qPCR. The TlpA39 promoter and regulator system could be further optimized in *B. subtilis* as was done previously in *E. coli*[42] and *B. subtilis*[48]*.* Further optimization by directed mutagenesis[42,48] or other measures could improve the P_{TlpA39} genetic switch to have a more stringent on/off state which would be more ideal for *in vivo* studies.

After coating the bacteria with three SPION variations (plain-dextran, carboxyl-coated, amine-coated), SEM-EDS confirmed that the plain-dextran and amine-coated SPIONs covered the *B. subtilis* in an even, thin coating compared to the carboxyl-coated particle that formed large aggregates that heterogeneously associated with *B. subtilis* (Fig. 4.3)**.** The variations in association and retention of the three types of SPIONs with *B. subtilis* are primarily influenced by electrostatic and dispersive forces between the bacteria and the SPION coatings[78]. *B. subtilis* has a net negative electrostatic charge and a zeta-potential of – 41 mV when grown at a physiological pH[79,80]. Previous studies have demonstrated that with increasing negative zeta-potential, the higher the adhesion potential extends from the bacteria[80]. Additionally, the DLVO (Derjaguin–Landau–Verwey–Overbeek) theory can be used to explain the potential interaction between a given nanoparticle and bacteria[78,80]. The SPIONs used in this study have a net

electrostatic charge of negative (plain-dextran)[58,59], low negative to neutral charge (carboxyl-coated), or a positive charge (amine-coated) when at physiological pH or pH 6.5 for the amine-coated (MicroMod). Even though the plain-dextran is negatively charged, the difference in zeta potential between *B. subtilis* and the particle was enough to allow for coating similar to previous coatings of *B. subtilis* with gold nanoparticles[80]. The carboxyl-coated SPION has a high potential for Van der Waals interactions due to its hydroxyl functional groups which contributes to the DLVO theory and increases the aggregation and agglomeration of the nanoparticle in suspension and around *B. subtilis*[81]. The positive charge of the amine-coated SPION at pH 6.5 promoted association with *B. subtilis* but the pH requirement is a limiting factor for this particle type. Ultimately, the variations in coating between the promising plain-dextran and carboxyl-coated SPIONs at physiological pH were more well-suited for downstream applications. Additionally, none of the SPION variations reduced *B. subtilis* viability after coating (Fig. 4.6).

The SEM-EDS and TEM (Fig. 4.3, 4.5) provide some explanation for the results seen following magnetic hyperthermia. The plain-dextran and amine-coated SPIONs evenly coated *B. subtilis* while the carboxyl-coated SPIONs formed large aggregates that indicated potentially more iron around *B. subtilis* but with differences between bacteria in the sample. Therefore, AMF could result in greater thermal energy being delivered to *B. subtilis* through the carboxyl-coated SPION than with the plain-dextran or amine-coated SPION, but with higher variability due to less reproducible associations with the bacteria. The HYPER parameters were chosen based on several preliminary experiments that optimized RF amplitude for each particle at each bacterial concentration then the best conditions for each particle were performed with maximum biological replicates that could be placed inside the HYPER system (Fig. 4.7). Thermal probes measuring the temperature of the culture medium showed that the carboxyl-coated SPION was the only particle that increased culture medium temperature (+3°C) when exposed to AMF (Fig. 4.8). This was supported by the electron microscopy indicating more free iron throughout the

media in addition to the aggregates associated with the bacteria (Figure 3B, 5E). The plain-dextran and amine-coated SPIONs did not increase temperature but still induced P_{TlpA39} indicating potential direct thermal energy transfer to *B. subtilis*. Classical heat transfer theory based on Fourier's law of thermal conduction could explain this phenomenon at the micrometer scale taken together with coating observed under SEM-EDS but thermal confinement to *B. subtilis* is unlikely[82]. Explaining the observed thermal energy transfer phenomenon by Fourier's law is also supported by the observed differences in heating between the three particle variations. The carboxyl-coating caused the largest fold change, though variable, and also increased the culture medium temperature which would be consistent with the law of thermal conduction[82,83]. Accordingly, the other two particle variations were diffusing thermal energy that did not cause a detectable culture medium temperature change but could have still caused the biological response from *B. subtilis* especially when comparing the +/- TlpA39R strains. We chose the plain-dextran SPION for 1 h thermal induction and *in vivo* studies because of the reproducibility of heating, even coating of *B. subtilis* to maximize retention, minimal impact on viability after AMF treatment and less thermal energy transfer throughout the culture medium which could translate to less damage to surrounding tissue *in vivo.* In future studies, the SPION of choice should be determined based on desired effects as the varied particle characteristics could have different advantages in other scenarios.

Both thermocycler heating and magnetic hyperthermia by the HYPER system created significant increase in bioluminescent output over 12 h. Yet, the comparison of 12 h of continuous heating to AMF (Fig. 4.2, 4.7) demonstrated that magnetic hyperthermia does not induce the TSRs to the same degree as continuous, direct heating. Accordingly, results obtained after 1 h of heating indicate that thermocycler heating over this limited time can significantly increase the output of the reporter, which demonstrates the potential for *in vivo* use. However, it is likely that the pulse sequence of magnetic hyperthermia used here would need to

be improved to maximize potential for *in vivo* applications. An immediate change to the current process, that could enhance the magnetic hyperthermia, is increasing the RF amplitude beyond the limitations of the HYPER system (>16.0 mT). However, as an increase in RF amplitude will result in an increase in specific absorption rate (SAR)[84], this would have to be further studied to prevent any biological effects. The plain-dextran particle used here to coat *B. subtilis* is promising and shows potential for enhanced thermal energy transfer from a stronger AMF. Alternatively, other SPIONs could be investigated to further enhance magnetic hyperthermia response in *B. subtilis.* Various SPIONs have been modified to improve magnetic hyperthermia properties[85–88] and these variations should be investigated for efficient coating of *B. subtilis* and improved magnetic hyperthermia after exposure to AMF.

The histology suggests there is association and retention of the SPION with the bacteria after injection *in vivo* but could not be confirmed with the optical microscopy technique utilized (Fig. 4.10E-G). Yet, the modified Gram stain further supported the finding of the association of the *B. subtilis* and plain-dextran SPION *in vivo* by showing a typical Gram stain result for *B. subtilis* in comparison to the consecutive staining (Fig. 4.10E-G). Hematoxylin and eosin staining performed on adjacent tissue sections showed eosin-stained (pink), longitudinal quadriceps muscle fibers (Fig. 4.13D) confirming samples were injected intramuscularly.

Perls' Prussian Blue staining[89] and modified Gram stain[90] demonstrated the presence of iron and *B. subtilis* at the same location, which provides the opportunity to utilize magnetic hyperthermia to control *B. subtilis* transcription *in vivo.* Further tuning of the genetic elements to the *B. subtilis* and characterizing the interaction of improved particles for magnetic hyperthermia with *B. subtilis* would enhance further *in vivo* studies. SPIONs can be coated with polymers, small molecules, lipids and composites to increase stability, water solubility and biocompatibility[86]. For example, Fe_3O_4-oleic acid-Na-oleate nanoparticles[88] increased stability in

a transplanted carcinoma model and polycaprolactone-coated superparamagnetic iron oxide nanoparticles synthesized with a micellular conformation were used to increase cytocompatibility and thermosensitivity as a cancer therapy[86]. Additionally, increasing RF amplitude and amount of iron associating with the bacteria could improve heating along with imaging properties *in vivo*. Yet, increases in bioluminescence were observed after AMF treatment with only ~1 ppm of Fe in the plain-dextran coated condition *in vitro*. This reduced the amount of Fe that is delivered compared to other magnetic hyperthermia applications, such as for tumor ablation[91], from 1 mg/cm^3 to 13.6 ng/cm^3. Accordingly, the bacteria can be used as a carrying mechanism for and a responsive mechanism to SPIONs where minimal SPIONs are needed to produce a desired therapeutic outcome through controlling bacteriotherapies. Alternatively, manganese-doped magnetic nanoclusters have been studied for glioblastoma therapy as a nanoparticle that has complementary functionalities and can utilize photothermal and magnetic hyperthermia treatments[87]. Additionally, other heating mechanisms could be used for magnetic hyperthermia such as ultrasound which was been shown previously[42,52,92].

MATERIALS AND METHODS

Bacterial growth conditions

B. subtilis constructs were grown in Luria-Bertani Miller broth (LB) with spectinomycin (100 µg/mL). The overnight cultures were grown for 16 h at 37°C and 250 RPM unless otherwise specified.

B. subtilis constructs

The thermal response elements originated from pTlpA39-Wasabi (Addgene plasmid # 86116; http://n2t.net/addgene:86116; RRID:Addgene_86116) [42]. The TlpA39 promoter and regulator (driven by the LacI promoter) were cloned into the pDR111 plasmid to replace the Phyper-spank promoter and LacI regulator using Gibson assembly[93]. Accordingly, the *luxA-E* operon was inserted into in the NheI restriction site of the pDR111 backbone by the seamless ligation cloning extract (SLiCE) method[94] to create the new pDR111 P_{LacI} *tlpa39R* P_{TlpA39} *luxA-E. coli* construct. Three strains were created: empty vector (pDR111 backbone only), experimental P_{TlpA39} repressed strain (pDR111 P_{LacI} *tlpa39R* P_{TlpA39} *luxA-E*), and P_{TlpA} constitutive strain without the repressor (pDR111 P_{TlpA39} *luxA-E*). Constructs were inserted into the genome of *B. subtilis* at the *amyE* locus using a homologous recombination plasmid (pDR111[95], a gift from Dr. Lee Kroos). The pDR111 plasmid was transformed into *B. subtilis* using a natural competence protocol and constructs were selected for by spectinomycin then confirmed by PCR amplification out of the genome[96]. Three *B. subtilis* strains were created: containing the empty vector, the vector with the experimental P_{TlpA39} repressed strain (P_{TlpA39} *luxA-E* + *tlpa39R*), and the P_{TlpA} constitutive strain without the repressor (P_{TlpA39} *luxA-E* - *tlpa39R*). All constructs were confirmed by PCR, restriction enzyme digestion, functional assays (when applicable), and Sanger sequencing (Azenta Life Sciences).

Iron coating of *B. subtilis*

Synomag-D particles possess a maghemite (γ-Fe_2O_3) core of nanoflower-shaped nanocrystallites with a dextran shell and a hydrodynamic particle diameter of 50 nm[59]. We utilized the plain dextran shell nanoparticle, a variation coated with carboxyl groups (carboxyl-coated) and a variation coated with amine groups (amine-coated) (MicroMod; #104-00-501, #103-02-501, #104-01-501). *B. subtilis* was incubated with plain-dextran or carboxyl-coated Synomag-D (200 µg/mL) in LB broth (pH = 7) or in LB broth (pH = 6.5) for the amine-coated Synomag-D (200 µg/mL) for 2 h at 37°C and 250 RPM after being normalized to OD_{600} = 1 or 2 in 1 mL. Coated *B. subtilis* was spun down at 10,000 x g for 2 min and washed with PBS (pH = 7.4) for plain-dextran and carboxyl-coated Synomag-D or with PBS (pH = 6.5) for amine-coated Synomag-D. The cultures were then resuspended in 100 µL of LB broth with appropriate pH mentioned above for use in HYPER or 250 µL of PBS (pH appropriate) for MPI and *in vivo* experiments.

Scanning electron microscopy and elemental analysis

Five hundred microliters of coated *B. subtilis* suspended in growth media was mixed with an equal volume of 4% glutaraldehyde in 0.1M sodium phosphate buffer, pH 7.4. Fixation was allowed to proceed for 30 min at room temperature. Twelve-millimeter round glass coverslips were floated on one drop of 1% poly-L-lysine (Sigma Aldrich P1399) each and allowed to stand for 10 min. The coverslips were removed and gently washed with HPLC-grade water. One drop of fixed sample was placed on the now coated side of the coverslip and allowed to settle for 10 m. After sample addition the coverslip was gently washed with HPLC-grade water and placed in a graded ethanol series (25%, 50%, 75%, 95%) for 10m each with three 10m changes in 100% ethanol[97].

Coverslips with samples were then critical point dried in a Leica Microsystems model EM CPD300 critical point dryer (Leica Microsystems, Vienna, Austria) using carbon dioxide as the transitional fluid. Coverslips were then mounted on aluminum stubs using System Three Quick Cure 5 epoxy glue (System Three Resins, Inc., Aubur, WA) and carbon conductive paint (Structure Probe, Inc. 05006-AB) was added in a thin line for grounding. Samples were coated with iridium (2.7 - 5.5 nm thickness) in a Quorum Technologies/Electron Microscopy Sciences Q150T turbo pumped sputter coater (Quorum Technologies, Laughton, East Sussex, England BN8 6BN) purged with argon gas.

Samples were examined in a JEOL 7500F (field emission emitter) scanning electron microscope (JEOL Ltd., Tokyo, Japan) and energy dispersive X-ray spectroscopy (elemental analysis) was performed using an Oxford Instruments AZtec system (Oxford Instruments, High Wycomb, Bucks, England), software version 3.1 using a 150mm^2 Silicon Drift Detector (JEOL 7500F SEM) and an ultra-thin window. Images were analyzed using Fiji (ImageJ, version 2.0.0-rc-69/1.52i).

Transmission electron microscopy

Transmission Electron Microscopy (TEM; JEM-1400Flash, JEOL, MA USA) was used to confirm external associations of SPIONs with *B. subtilis*. Pelleted samples were fixed in 2.5% EM-grade glutaraldehyde for 5 min, washed with 0.1M phosphate buffer, and post-fixed with 1% osmium tetroxide in 0.1M phosphate buffer. After fixation, samples were dehydrated in a gradient series of acetone and infiltrated and embedded in Spurr's resin. Seventy nanometer thin sections were obtained with a Power Tome Ultramicrotome (RMC, Boeckeler Instruments. Tucson, AZ), floated onto 200-mesh, carbon-coated formvar copper grids. Images were taken

with JEOL 1400-Flash Transmission Electron Microscope (Japan Electron Optics Laboratory, Japan). Images were analyzed using Fiji (ImageJ, version 2.0.0-rc-69/1.52i).

In vitro imaging

Plain, carboxyl or amine Synomag-D coated *B. subtilis* were imaged in triplicates ($1x10^8$ cells per sample in 25 µL PBS) using the Momentum MPI scanner (Magnetic Insight Inc, CA, USA). Plain Synomag-D coated *B. subtilis* were combined to a total of $4x10^8$ cells in 100 µL PBS for detection. Images were acquired using a 2D projection scan with default (5.7 T/m gradient) or high sensitivity (3 T/m gradient) settings, rf amplitude (16.5 mT x-channel, 17 mT z-channel) and 45 kHz excitation with a field of view (FOV) = 12 x 6 cm, 1 average and acquisition time of ~1 minute.

Bioluminescence was measured on the *in vivo* imaging system (IVIS, PerkinElmer) with auto-exposure settings (time = 2-40 sec, binning = medium, f/stop = 1, emission filter = open). Average radiance (p/sec/cm2/sr) was normalized to bacterial growth using optical density measured as absorbance at 600 nm (OD_{600}) on a plate reader (Spectra Max 3, Molecular Devices, San Jose, CA, USA). Bioluminescent signals were quantified using the 8x12 grid ROI for all wells (*in vitro* thermocycler induction) and ellipse ROIs with standardized area for all tubes (*in vitro*) to calculate average radiance ($p/sec/cm^2/sr$) using Living Image software (PerkinElmer, Version 4.5.2).

Flow cytometry determination of *B. subtilis* viability

The effects of coating and heating on *B. subtilis* viability was assessed using flow cytometry. *B. subtilis* was coated as described above with all three nanoparticle variations (+/- AMF). Following treatment cells were resuspended in 100 µL of 150 mM NaCl and stained using

a viability/cytotoxicity assay kit for live and dead bacteria (Biotium, #30027) according to the manufacturers protocol. Following staining cells were collected by centrifugation and washed once with flow buffer (1X PBS, 0.5% bovine serum albumin) followed by fixation with 4% paraformaldehyde for 10 minutes. Cells were then resuspended in 100 µL flow buffer for analysis using the Cytek Aurora flow cytometer. Unstained dead (heat treated; 98°C), live (uncoated; untreated) and live (coated; plain, carboxyl, amine) plus single stained DMAO (live/dead, FITC) and Ethidium Homodimer III (EthD-III; dead, Cy3) were used as controls. EthD-III dead cells were gated on the DMAO+ cell population. Data were analyzed using FCS express software (De Novo Software, CA, USA; version 7.12.0005). A one-way ANOVA was used to determine any significance between treatments' potential impact on viability. The data presented herein were obtained using instrumentation in the MSU Flow Cytometry Core Facility. The facility is funded in part through the financial support of Michigan State University's Office of Research & Innovation, College of Osteopathic Medicine, and College of Human Medicine.

RNA extraction and RT-qPCR

Technical replicates from thermal inductions were pooled for RNA extractions. *B. subtilis* was lysed using LETS buffer (100mM LiCl, 10mM EDTA, 10mM Tris pH 7.8, 1% SDS) and bead beating (0.1mm zirconium beads, 3 cycles of 60 sec at max speed). Total RNA was extracted using RNeasy miniprep kit (QIAGEN). Samples were cleaned and made into cDNA with QuantiTect Reverse Transcription kit (QIAGEN). The resulting cDNA was diluted 1:20 in RNAse free water for qPCR. QuantiTect SYBR Green PCR kit (QIAGEN) was used to prepare 20 µL reactions according to instructions. Primers for *luxB*, *16s*, and *tlpa39R* were created using NCBI Primer BLAST and used for all samples. No-template controls of RNase-free water were run in triplicate for each primer set. Reactions were run in triplicate for each sample. Data was screened for validity using melting curves and then analyzed for relative quantification using the

$2^{-\Delta\Delta Ct}$ method[98]. The expression levels for *luxB* and *tlpa39R* was calculated relative to the *16s* rRNA housekeeping gene and the experimental groups (37, 39, 42°C). Confidence intervals of 95% were calculated using the mean and standard deviation for all cycle threshold values of a given sample (n=6) and then converting to fold change using the above $2^{-\Delta\Delta Ct}$ method.

In vitro thermocycler inductions

Cultures of *B. subtilis* were grown in LB for 36 h at 25°C and 250 RPM under spectinomycin (100 µg/mL) selection. These cultures were then diluted to optical density of 0.1 at 600 nm (OD_{600}) in LB with appropriate antibiotic and grown until they reached OD_{600} of 0.25. Twenty-five microliters of the samples were aliquoted into 96-well PCR plates and sealed. Thermal inductions were carried out in Biorad C-100 thermocyclers at 25, 37, 39, and 42°C for either 12 h or 1 h. After thermal induction, the samples were diluted 1:4 in LB and 90 µL was transferred to a 96-well, black Costar plate. The OD_{600} and bioluminescence output was measured. Controls for the measurements were: growth media only, empty vector strain, P_{TlpA39} constitutive strain without the repressor, and experimental P_{TlpA39} repressed strain. After bioluminescent imaging and optical density measurements (method above), a one-way ANOVA with Tukey's post-hoc was used to determine any significance between temperatures within a strain.

HYPER Theranostic Hyperthermia System

Magnetic hyperthermia was performed using the HYPER Theranostic Hyperthermia System (Magnetic Insight). Magnetothermal heating is localized using a Field Free Point (FFP) to direct radiofrequency (RF) energy. HYPER was programmed to apply AMF to the coated *B. subtilis* strains by using a 0.66 T/m magnetic field gradient strength, a RF amplitude of 14.5 or 16.0 mT, 350 kHz excitation and a RF amplitude application time of 60 seconds with a 1 second

cool down time. This programmed AMF cycle would be repeated such that the AMF was applied for the desired total run time of either 1 or 12 h. Optimal parameters for each particle were determined when bacteria were normalized to OD_{600} = 1 or 2. For each run the following strains and replicates were included: *B. subtilis* P_{TlpA39} *luxA-E* +TlpA39R coated with one of the three variations of Synomag-D were divided into PCR tubes in two 50 µL aliquots where one aliquot would be placed in the AMF (+AMF) and outside the AMF (-AMF) in biological replicates (n=7). The same process was repeated for the *B. subtilis* P_{TlpA39} *luxA-E* -TlpA39R strain (n=3) to be run in same conditions with +TlpA39R strain. Optimal HYPER parameters for each variation of particle mentioned above with bacteria normalized to OD_{600} = 2 were utilized to determine temperature increase in LB during the heating of *B. subtilis* with the three variations of coating. Fiber-optic temperature probes (Weidmann-Optocon, standard TS2 probes) were placed into the LB throughout the 12 h of heating to track temperature through the HYPER software. Temperature readings were recorded every AMF application cycle (60 readings per cycle were treated as technical replicates) with reads at each 30 min time point plotted for visualization. Unpaired Student or Welch's t-test was used to determine statistical significance between samples with and without AMF treatment.

In vivo magnetothermal heating and imaging

Female BALB/c mice (6-8 weeks; Jackson Laboratories USA) were obtained and cared for in accordance with the standards of Michigan State University Institutional Animal Care and Use Committee. *B. subtilis* were coated with plain Synomag-D as described above. Mice (n=6) were anesthetized with isoflurane administered at 2% in oxygen followed by hair removal on each thigh using a depilatory. An intramuscular (IM) injection of $1x10^8$ iron-coated bacteria in 25 µL PBS was performed into the left thigh followed by BLI (IVIS Spectrum; post-injection timepoint) using auto-exposure settings (time = 30-120 sec, binning = medium, f/stop = 1,

emission filter = open). One mouse was imaged using MPI using the default setting, as described above. No signal was detected and no further mice were imaged by MPI. Following imaging, mice were either placed into the HYPER system for magnetothermal heating (+AMF; 16 mT for 1 h, n=3) or maintained at room temperature in cage (-AMF, n=3). BLI was performed as above, after AMF application, or 1 h for mice which were not subjected to AMF (post-treatment timepoint). After the final imaging time point mice were sacrificed and thigh muscle from the IM injected side and the contralateral not injected side were excised followed by sectioning for histological staining and microscopy (see below for detailed methods). Two-way repeated measures ANOVA and Tukey's post-hoc was used to determine statistical significance between AMF treatments and timepoints for bioluminescence.

Histological analysis

Thigh muscle samples were fixed in 4% paraformaldehyde for 24 h followed by cryopreservation through serial submersion in graded sucrose solutions (10%, 20% and 30%). Samples were then frozen in optimal cutting temperature compound (Fisher HealthCare, USA). Tissues were sectioned using a cryostat (6 µm sections). Sections were stained with a modified Gram stain as described by Becerra *et al*., 2016[90], followed by Perls' Prussian Blue (PPB)[89] on the same sections for detection of bacteria and detection of ferric iron. CitriSolv (Decon Labs, Inc., King of Prussia, PA, USA; Cat.#1601) was used as a safe alternative for xylene in the final step of the modified Gram stain. Eosin was used as a counterstain in the Perls' Prussian Blue protocol. Sequential sections of the tissue were stained with the modified Gram stain only and hematoxylin and eosin staining only to verify Gram status of the *B. subtilis* and confirm intramuscular injections, respectively. Microscopy was performed on the sections using a Nikon Eclipse Ci microscope equipped with a Nikon DS-Fi3 camera (Nikon, Tokyo, Japan)) for color image acquisition and NIS elements BR 5.21.02 software (Nikon). Microscopy images were

prepared using the auto-white feature on NIS elements and Fiji (ImageJ, version 2.0.0-rc-69/1.52i).

Image analysis

Living Image software (PerkinElmer, Version 4.5.2) was used to quantify bioluminescent signals. An 8x12 grid region of interest (ROI) was used for 96-well plates (*in vitro* thermocycler induction) or ellipse ROIs with standardized area for all tubes (*in vitro*) or on the injection site of the mouse thigh (*in vivo*) to calculate average radiance (p/sec/cm2/sr).

MPI data sets were visualized and analyzed utilizing Horos imaging software (Horos is a free and open-source code software program that is distributed free of charge under the LGPL license at Horosproject.org and sponsored by Nimble Co LLC d/b/a Purview in Annapolis, MD USA). Fixed ROIs were used to identify all samples and total MPI signal was determined (area x mean signal). Calibration standard curves were created by imaging different amounts of iron and plotting signal (y) versus iron content (x) with the y-intercept (b) set to zero. The slope (m) of the data was found using a simple linear regression and quantification of iron content was calculated using the trendline equation (y=mx+b). Standard curves were created using matched imaging parameters (default or high sensitivity) dependent on the data set being analyzed.

Inductively Coupled Plasma-Mass Spectrometry (ICP–MS)

After *B. subtilis* + TlpA39R was coated with the three SPION variations at OD_{600} = 2 then the cells were pelleted (centrifugation at 10,000xg) and resuspended in phosphate buffered saline (PBS; pH 7.4). Three technical replicates of the coating procedure were pooled in a final volume of 750 µL PBS. One sample of untreated *B. subtilis* + TlpA39R (OD_{600} = 2) from the coating process (no SPION control) was also prepared and resuspended in 250 µL PBS. The cells were digested in concentrated nitric acid (J.T. Baker, USA; 69-70%) overnight, and diluted

25-fold with a solution containing 0.5% EDTA and Triton X-100, 1% ammonium hydroxide, 2% butanol, 5 ppb of scandium, and 7.5 ppb of rhodium, indium, and bismuth as internal standards (Inorganic Ventures, VA, USA). The samples were analyzed on an Agilent 7900 ICP mass spectrometer (Agilent, CA, USA). Elemental concentrations were calibrated using a 5-point linear curve of the analyte-internal standard response ratio. Bovine liver (National Institute of Standards and Technology, MD, USA) was used as a control.

Statistical analysis and visualization

Statistical analyses were performed using Prism software (9.2.0, GraphPad Inc., La Jolla, CA). Statistical tests are identified for each method. Significance was considered as $p<.05$ Plotting was performed using R version 4.0.4 with the following packages: ggplot2, dplyr, reshape2, ggsignif, ggpubr and plotrix.

Availability of data and materials

All raw data, *Bacillus subtilis* constructs and R scripts will be made available upon request by the corresponding author. Plasmids used to produce *B. subtilis* constructs will be submitted to Addgene after manuscript publication. All R scripts were written with established packages.

Competing interests

The authors declare that they have no competing interests.

Acknowledgments

The authors would like to acknowledge A. Withrow, C. Flegler, and S. Flegler at the MSU Center for Advanced Microscopy, the MSU Flow Cytometry Core, S. Rebolloso at the MSU Veterinary Diagnostic Laboratory, L. Kroos, M. Witte, A. Tundo, and K. Conner at MSU, M. Huebner and J. Tait at MSU Center for Statistical Training and Consulting. The graphical abstract and Figure 1 were created using Biorender.com.

Funding

The authors would like to acknowledge the James and Kathleen Cornelius Endowment Fund, the College of Engineering Dissertation Completion Fellowship supported C. S. Madsen and the College of Natural Sciences Dissertation Continuation and Completion Fellowships supported E. M. Greeson.

Affiliations

Department of Biomedical Engineering, Michigan State University, East Lansing, MI, USA. Department of Microbiology and Molecular Genetics, Michigan State University, East Lansing, MI, USA. Institute for Quantitative Health Science and Engineering, Michigan State University, East Lansing, MI, USA.

Contributions

E.M. Greeson and C.S. Madsen contributed equally to experimental design, performing experiments, data analysis and manuscript writing. A.V. Makela contributed to experimental design, performed *in vivo* studies and contributed to manuscript writing. C.H. Contag contributed

to experimental design and data analysis, and manuscript writing. All authors have given approval to the final version of the manuscript. ‡E.M. Greeson and C.S. Madsen contributed equally.

REFERENCES

REFERENCES

1. Mahmoudi, M., Hofmann, H., Rothen-Rutishauser, B. & Petri-Fink, A. Assessing the in vitro and in vivo toxicity of superparamagnetic iron oxide nanoparticles. *Chem. Rev.* **112**, 2323–2338 (2012).

2. Prijic, S. & Sersa, G. Magnetic nanoparticles as targeted delivery systems in oncology. *Radiol. Oncol.* **45**, 1–16 (2011).

3. Cardoso, V. F. *et al.* Advances in Magnetic Nanoparticles for Biomedical Applications. *Adv. Healthc. Mater.* **7**, (2018).

4. Moore, J. D. *et al.* Time-dependent bacterial transcriptional response to CuO nanoparticles differs from that of Cu 2+ and provides insights into CuO nanoparticle toxicity mechanisms. *Environ. Sci. Nano* **4**, 2321–2335 (2017).

5. Wang, C. *et al.* Combined use of vancomycin-modified Ag-coated magnetic nanoparticles and secondary enhanced nanoparticles for rapid surface-enhanced Raman scattering detection of bacteria. *Int. J. Nanomedicine* **13**, 1159 (2018).

6. Wang, L. *et al.* Bacterial inactivation using silver-coated magnetic nanoparticles as functional antimicrobial agents. *Anal. Chem.* **83**, 8688–8695 (2011).

7. Lee, J.-J. *et al.* Synthetic ligand-coated magnetic nanoparticles for microfluidic bacterial separation from blood. *Nano Lett.* **14**, 1–5 (2014).

8. Guo, N. *et al.* Magnetism and NIR dual-response polypyrrole-coated Fe3O4 nanoparticles for bacteria removal and inactivation. *Mater. Sci. Eng. C* **126**, 112143 (2021).

9. Arakha, M. *et al.* Antimicrobial activity of iron oxide nanoparticle upon modulation of nanoparticle-bacteria interface. *Sci. Rep.* **5**, 1–12 (2015).

10. Slavin, Y. N., Asnis, J., Häfeli, U. O. & Bach, H. Metal nanoparticles: understanding the mechanisms behind antibacterial activity. *J. Nanobiotechnology* **15**, 1–20 (2017).

11. Zheng, B. *et al.* Magnetic particle imaging tracks the long-term fate of in vivo neural cell implants with high image contrast. *Sci. Rep.* **5**, 1–9 (2015).

12. Tay, Z. W. *et al.* Superferromagnetic Nanoparticles Enable Order-of-Magnitude Resolution & Sensitivity Gain in Magnetic Particle Imaging. *Small Methods* 1 (2021).

13. Kratz, H. *et al.* Novel magnetic multicore nanoparticles designed for MPI and other biomedical applications: From synthesis to first in vivo studies. *PLoS One* **13**, e0190214–e0190214 (2018).

14. Casula, M. F. *et al.* Manganese doped-iron oxide nanoparticle clusters and their potential as agents for magnetic resonance imaging and hyperthermia. *Phys. Chem. Chem. Phys.* **18**, 16848–16855 (2016).

15. Makela, A. V *et al.* Magnetic Particle Imaging of Macrophages Associated with Cancer: Filling the Voids Left by Iron-Based Magnetic Resonance Imaging. *Mol. imaging Biol.* (2020).

16. Sehl, O. C., Makela, A. V., Hamilton, A. M. & Foster, P. J. Trimodal Cell Tracking In Vivo: Combining Iron- and Fluorine-Based Magnetic Resonance Imaging with Magnetic Particle Imaging to Monitor the Delivery of Mesenchymal Stem Cells and the Ensuing Inflammation. *Tomogr. (Ann Arbor, Mich.)* **5**, (2019).

17. Borgert, J. *et al.* Fundamentals and applications of magnetic particle imaging. *J. Cardiovasc. Comput. Tomogr.* **6**, 149–153 (2012).

18. Yu, E. Y. *et al.* Magnetic particle imaging: a novel in vivo imaging platform for cancer detection. *Nano Lett.* **17**, 1648–1654 (2017).

19. Ludewig, P. *et al.* Magnetic Particle Imaging for Real-Time Perfusion Imaging in Acute Stroke. *ACS Nano* **11**, 10480–10488 (2017).

20. Alphandéry, E., Chebbi, I., Guyot, F. & Durand-Dubief, M. Use of bacterial magnetosomes in the magnetic hyperthermia treatment of tumours: a review. *Int. J. Hyperth. Off. J. Eur. Soc. Hyperthermic Oncol. North Am. Hyperth. Gr.* **29**, 801–809 (2013).

21. Hergt, R. & Dutz, S. Magnetic particle hyperthermia—biophysical limitations of a visionary tumour therapy. *J. Magn. Magn. Mater.* **311**, 187–192 (2007).

22. Hergt, R. *et al.* Magnetic properties of bacterial magnetosomes as potential diagnostic and therapeutic tools. *J. Magn. Magn. Mater.* **293**, 80–86 (2005).

23. Tay, Z. W. *et al.* Magnetic Particle Imaging-Guided Heating in Vivo Using Gradient Fields for Arbitrary Localization of Magnetic Hyperthermia Therapy. *ACS Nano* **12**, 3699–3713 (2018).

24. Earl, A. M., Losick, R. & Kolter, R. Ecology and genomics of Bacillus subtilis. *Trends Microbiol.* **16**, 269–275 (2008).

25. Lowary, P. T. & Uhlenbeck, O. C. An RNA mutation that increases the affinity of an RNA–protein interaction. *Nucleic Acids Res.* **15**, 10483–10493 (1987).

26. Radeck, J. *et al.* The Bacillus BioBrick Box: generation and evaluation of essential genetic building blocks for standardized work with Bacillus subtilis. *J. Biol. Eng.* **7**, 29 (2013).

27. Martin, B. J. *et al.* Global Network Reorganization During Dynamic Adaptations of Bacillus subtilis Metabolism. *Science (80-.).* **335**, 1099–1103 (2012).

28. Jakutyte-Giraitiene, L. & Gasiunas, G. Design of a CRISPR-Cas system to increase resistance of Bacillus subtilis to bacteriophage SPP1. *J. Ind. Microbiol. Biotechnol.* **43**, 1183–1188 (2016).

29. Zhang, K., Duan, X. & Wu, J. Multigene disruption in undomesticated Bacillus subtilis ATCC 6051a using the CRISPR/Cas9 system. *Sci. Rep.* **6**, 27943 (2016).

30. Watzlawick, H. & Altenbuchner, J. Multiple integration of the gene ganA into the Bacillus subtilis chromosome for enhanced β-galactosidase production using the CRISPR/Cas9 system. *AMB Express* **9**, 158 (2019).

31. Schumann, W. The Bacillus subtilis heat shock stimulon. *Cell Stress Chaperones* **8**, 207–217 (2003).

32. Elshaghabee, F. M. F., Rokana, N., Gulhane, R. D., Sharma, C. & Panwar, H. Bacillus As Potential Probiotics: Status, Concerns, and Future Perspectives. *Front. Microbiol.* **8**, 1490 (2017).

33. Souza, C. C. de, Guimarães, J. M., Pereira, S. D. S. & Mariúba, L. A. M. The multifunctionality of expression systems in Bacillus subtilis: Emerging devices for the production of recombinant proteins. *Exp. Biol. Med. (Maywood).* **246**, 2443–2453 (2021).

34. Gang, F. *et al.* An operator-based expression toolkit for Bacillus subtilis enables fine-tuning of gene expression and biosynthetic pathway regulation. *Proc. Natl. Acad. Sci.* **119**, e2119980119 (2022).

35. Lam, K. H. E., Chow, K. C. & Wong, W. K. R. Construction of an efficient Bacillus subtilis system for extracellular production of heterologous proteins. *J. Biotechnol.* **63**, 167–177 (1998).

36. Vavrová, Ľ., Muchová, K. & Barák, I. Comparison of different Bacillus subtilis expression systems. *Res. Microbiol.* (2010).

37. Niu, T. *et al.* Engineering a Glucosamine-6-phosphate Responsive glmS Ribozyme Switch Enables Dynamic Control of Metabolic Flux in Bacillus subtilis for Overproduction of N-Acetylglucosamine. *ACS Synth. Biol.* **7**, 2423–2435 (2018).

38. Wenzel, M., Müller, A., Siemann-Herzberg, M. & Altenbuchner, J. Self-inducible Bacillus subtilis expression system for reliable and inexpensive protein production by high-cell-density fermentation. *Appl. Environ. Microbiol.* **77**, 6419–6425 (2011).

39. van Dijl, J. & Hecker, M. Bacillus subtilis: from soil bacterium to super-secreting cell factory. *Microb. Cell Fact.* **12**, 3 (2013).

40. Park, S. A. *et al.* Bacillus subtilis as a robust host for biochemical production utilizing biomass. *Crit. Rev. Biotechnol.* **41**, 827–848 (2021).

41. Seo, S.-O. & Schmidt-Dannert, C. Development of a synthetic cumate-inducible gene expression system for Bacillus. *Appl. Microbiol. Biotechnol.* **103**, 303–313 (2019).

42. Piraner, D. I., Abedi, M. H., Moser, B. A., Lee-Gosselin, A. & Shapiro, M. G. Tunable thermal bioswitches for in vivo control of microbial therapeutics. *Nat. Chem. Biol.* **13**, 75–80 (2017).

43. Piraner, D. I., Wu, Y. & Shapiro, M. G. Modular Thermal Control of Protein Dimerization. *ACS Synth. Biol.* **8**, 2256–2262 (2019).

44. Haldenwang, W. G. The sigma factors of Bacillus subtilis. *Microbiol. Rev.* **59**, 1–30 (1995).

45. D., H. J. *et al.* Global Transcriptional Response of Bacillus subtilis to Heat Shock. *J. Bacteriol.* **183**, 7318–7328 (2001).

46. Li, W. *et al.* Characterization of two temperature-inducible promoters newly isolated from B. subtilis. *Biochem. Biophys. Res. Commun.* **358**, 1148–1153 (2007).

47. Völker, U. *et al.* Cloning and characterization of heat-inducible promoters of Bacillus subtilis. *FEMS Microbiol. Lett.* **106**, 287–293 (1993).

48. Breitling, R., Sorokin, A. V & Behnke, D. Temperature-inducible gene expression in Bacillus subtilis mediated by the c1857-encoded repressor of bacteriophage lambda. *Gene* **93**, 35–40 (1990).

49. Thuy Le, A. T. & Schumann, W. A novel cold-inducible expression system for Bacillus subtilis. *Protein Expr. Purif.* **53**, 264–269 (2007).

50. Budde, I., Steil, L., Scharf, C., Völker, U. & Bremer, E. Adaptation of Bacillus subtilis to growth at low temperature: a combined transcriptomic and proteomic appraisal. *Microbiology* **152**, 831–853 (2006).

51. Abedi, M. *et al.* Acoustic Remote Control of Bacterial Immunotherapy. *bioRxiv* (2021).

52. Abedi, M. H. *et al.* Ultrasound-controllable engineered bacteria for cancer immunotherapy. *Nat. Commun.* **13**, 1–11 (2022).

53. Eberbeck, D., Wiekhorst, F., Wagner, S. & Trahms, L. How the size distribution of magnetic nanoparticles determines their magnetic particle imaging performance. *Appl. Phys. Lett.* **98**, 182502 (2011).

54. Ferguson, R. M., Minard, K. R., Khandhar, A. P. & Krishnan, K. M. Optimizing magnetite nanoparticles for mass sensitivity in magnetic particle imaging. *Med. Phys.* **38**, 1619–1626 (2011).

55. Tomitaka, A. *et al.* Variation of Magnetic Particle Imaging Tracer Performance With Amplitude and Frequency of the Applied Magnetic Field. *IEEE Trans. Magn.* **51**, (2015).

56. Gavilán, H. *et al.* How size, shape and assembly of magnetic nanoparticles give rise to different hyperthermia scenarios. *Nanoscale* **13**, 15631–15646 (2021).

57. Gavilán, H. *et al.* Colloidal Flower-Shaped Iron Oxide Nanoparticles: Synthesis Strategies and Coatings. *Part. Part. Syst. Charact.* **34**, 1700094 (2017).

58. Liu, S. *et al.* Long circulating tracer tailored for magnetic particle imaging. *Nanotheranostics* **5**, 348–361 (2021).

59. Matschegewski, C. *et al.* Biocompatibility of magnetic iron oxide nanoparticles for biomedical applications. *Curr. Dir. Biomed. Eng.* **5**, 573–576 (2019).

60. Bender, P. *et al.* Relating Magnetic Properties and High Hyperthermia Performance of Iron Oxide Nanoflowers. *J. Phys. Chem. C* **122**, 3068–3077 (2018).

61. Ota, S. *et al.* Quantitation method of loss powers using commercial magnetic nanoparticles based on superparamagnetic behavior influenced by anisotropy for hyperthermia. *J. Magn. Magn. Mater.* **538**, 168313 (2021).

62. Laliani, G. *et al.* Bacteria and cancer: Different sides of the same coin. *Life Sci.* **246**, 117398 (2020).

63. Sawant, S. S., Patil, S. M., Gupta, V. & Kunda, N. K. Microbes as Medicines: Harnessing the Power of Bacteria in Advancing Cancer Treatment. *Int. J. Mol. Sci.* **21**, (2020).

64. Sedighi, M. *et al.* Therapeutic bacteria to combat cancer; current advances, challenges, and opportunities. *Cancer Med.* **8**, 3167–3181 (2019).

65. Soleimanpour, S., Hasanian, S. M., Avan, A., Yaghoubi, A. & Khazaei, M. Bacteriotherapy in gastrointestinal cancer. *Life Sci* **254**, 117754 (2020).

66. Yaghoubi, A. *et al.* Bacteria as a double-action sword in cancer. *Biochim Biophys Acta Rev Cancer* **1874**, 188388 (2020).

67. Zhang, Z. H., Yin, L., Zhang, L. L. & Song, J. Efficacy and safety of Bacillus Calmette-Guerin for bladder cancer: A protocol of systematic review. *Med.* **99**, e21930 (2020).

68. Allemailem, K. S. Innovative Approaches of Engineering Tumor-Targeting Bacteria with Different Therapeutic Payloads to Fight Cancer: A Smart Strategy of Disease Management. *Int. J. Nanomedicine* **16**, 8159–8184 (2021).

69. Hurme, R., Berndt, K. D., Namork, E. & Rhen, M. DNA Binding Exerted by a Bacterial Gene Regulator with an Extensive Coiled-coil Domain (∗). *J. Biol. Chem.* **271**, 12626–12631 (1996).

70. Francis, K. P. *et al.* Monitoring bioluminescent Staphylococcus aureus infections in living mice using a novel luxABCDE construct. *Infect. Immun.* **68**, 3594–3600 (2000).

71. Tinikul, R. & Chaiyen, P. Structure, Mechanism, and Mutation of Bacterial Luciferase. *Adv. Biochem. Eng. Biotechnol.* **154**, 47–74 (2016).

72. Zuber, P. & Losick, R. Role of AbrB in Spo0A- and Spo0B-dependent utilization of a sporulation promoter in Bacillus subtilis. *J. Bacteriol.* (1987).

73. Reitman, M. L. Of mice and men – environmental temperature, body temperature, and treatment of obesity. *FEBS Lett.* **592**, 2098–2107 (2018).

74. Albrecht, M., Henke, J., Tacke, S., Markert, M. & Guth, B. Effects of isoflurane, ketamine-xylazine and a combination of medetomidine, midazolam and fentanyl on physiological variables continuously measured by telemetry in Wistar rats. *BMC Vet. Res.* **10**, 198 (2014).

75. Navarro, K. L. *et al.* Mouse Anesthesia: The Art and Science. *ILAR J.* ilab016 (2021).

76. Carleton, H. M., Drury, R. A. B. & Wallington, E. A. *Carleton's histological technique*. (Oxford University Press, USA, 1980).

77. Meighen, E. A. Enzymes and genes from the lux operons of bioluminescent bacteria. *Annu. Rev. Microbiol.* **42**, 151–176 (1988).

78. Hwang, G., Ahn, I.-S., Mhin, B. J. & Kim, J.-Y. Adhesion of nano-sized particles to the surface of bacteria: Mechanistic study with the extended DLVO theory. *Colloids Surfaces B Biointerfaces* **97**, 138–144 (2012).

79. Mozes, N. & Rouxhet, P. G. Microbial hydrophobicity and fermentation technology. (1990).

80. Pajerski, W. *et al.* Attachment efficiency of gold nanoparticles by Gram-positive and Gram-negative bacterial strains governed by surface charges. *J. Nanoparticle Res.* **21**, 186 (2019).

81. Han, Y. *et al.* Stability of carboxyl-functionalized carbon black nanoparticles: the role of solution chemistry and humic acid. *Environ. Sci. Nano* **4**, 800–810 (2017).

82. Davis, H. C. *et al.* Nanoscale Heat Transfer from Magnetic Nanoparticles and Ferritin in an Alternating Magnetic Field. *Biophys. J.* **118**, 1502–1510 (2020).

83. Regmi, R., Naik, A., Thakur, J. S., Vaishnava, P. P. & Lawes, G. Temperature dependent dissipation in magnetic nanoparticles. *J. Appl. Phys.* **115**, 17B301 (2014).

84. Vander Vorst, A., Rosen, A. & Kotsuka, Y. *RF/Microwave Interaction with Biological Tissues*. *RF/Microwave Interaction with Biological Tissues* (2006).

85. Pucci, C., Degl'Innocenti, A., Gümüş, M. B. & Ciofani, G. Superparamagnetic iron oxide nanoparticles for magnetic hyperthermia: recent advancements, molecular effects, and future directions in the omics era. *Biomater. Sci.* (2022).

86. Hedayatnasab, Z., Dabbagh, A., Abnisa, F. & Wan Daud, W. M. A. Polycaprolactone-coated superparamagnetic iron oxide nanoparticles for in vitro magnetic hyperthermia therapy of cancer. *Eur. Polym. J.* **133**, 109789 (2020).

87. Gupta, R. & Sharma, D. Manganese-Doped Magnetic Nanoclusters for Hyperthermia and Photothermal Glioblastoma Therapy. *ACS Appl. Nano Mater.* **3**, 2026–2037 (2020).

88. Kulikov, O. A. *et al.* Magnetic Hyperthermia Nanoarchitectonics via Iron Oxide Nanoparticles Stabilised by Oleic Acid: Anti-Tumour Efficiency and Safety Evaluation in Animals with Transplanted Carcinoma. *International Journal of Molecular Sciences* vol. 23 (2022).

89. Booth, J. C. The Theory and Practice of Histological Techniques| The Theory and Practice of Histological Techniques. Eds John D. Bancroft & Alan Stevens. Churchill Livingstone, Melbourne. 662 pp. illustrated (some in colour). ISBN 0 443 02006 X. $89, 60. (1983).

90. Becerra, S. C., Roy, D. C., Sanchez, C. J., Christy, R. J. & Burmeister, D. M. An optimized staining technique for the detection of Gram-positive and Gram-negative bacteria within tissue. *BMC Res. Notes* **9**, 216 (2016).

91. Chan, K. W. & Chou, C. K. Use of thermocouples in the intense fields of ferromagnetic implant hyperthermia. *Int. J. Hyperth.* **9**, 831–848 (1993).

92. Bourdeau, R. W. *et al.* Acoustic reporter genes for noninvasive imaging of microorganisms in mammalian hosts. *Nature* **553**, 86–90 (2018).

93. Gibson, D. G. *et al.* Enzymatic assembly of DNA molecules up to several hundred kilobases. *Nat. Methods* **6**, 343 (2009).

94. Zhang, Y., Werling, U. & Edelmann, W. Seamless Ligation Cloning Extract (SLiCE) cloning method. *Methods Mol. Biol.* **1116**, 235–244 (2014).

95. Rokop, M. E., Auchtung, J. M. & Grossman, A. D. Control of DNA replication initiation by recruitment of an essential initiation protein to the membrane of Bacillus subtilis. *Mol. Microbiol.* (2004).

96. Harwood, C. R. & Cutting, S. M. Molecular biological methods for Bacillus. (1990).

97. Klomparens, K. L., Flegler, S. L., Hooper, G. R. & Hooper, G. R. a laboratory manual. (1986).

98. Livak, K. J. & Schmittgen, T. D. Analysis of relative gene expression data using real-time quantitative PCR and the 2(-Delta Delta C(T)) Method. *Methods* **25**, 402–408 (2001).

CHAPTER 5

CONCLUSIONS AND FUTURE DIRECTIONS

The development of the EES platform required the appropriate model chassis organism and host organism for testing and optimizing the strategy of this new technology. *B. subtilis* LLO proved to be an appropriate chassis organism in delivering proteins to the nuclei of host cells. Additionally, because *B. subtilis* is a model organism and many synthetic biology tools exist for the organism, the construction of the EES was streamline and modular which could be altered for other uses. The safety of *B. subtilis* also provides advantages over other bacteria that have been considered and initially tested in approaches for manipulating mammalian cell fate. *B. subtilis* fulfilled the need for the appropriate chassis organism but choosing the appropriate type of host cell to modulate was also necessary. To demonstrate both cytoplasmic persistence of the EES and host cell fate alteration, phagocytic immune cells[1], specifically macrophages, provided a useful model. Because phagocytic immune cells readily internalize bacteria and demonstrate altered cell fate that is the result of specific TFs, these cells represented a testable system for EES function[1]. Initially, the J774A.1 cells were used because *B. subtilis* LLO was tested in these cells previously[2,3] and the cell line expedited characterization of the *B. subtilis* LLO uptake and delivery of the TFs. After uptake, the LLO strain escaped phagosome destruction when LLO expression was induced and replicated inside the J774A.1 cells. Additionally, efficient uptake and persistence was observed as the J774A.1 cells contained an average of 11 bacteria per cell with 99% of cells containing bacteria. Yet, the replication of the LLO strain did affect the host cell viability as 10-12% of J774A.1 cells were lost by 4 h post bacterial addition and the cultures were treated with a high concentration of gentamicin (25 μg/mL) to prevent further loss of host cells when the bacteria delivered protein to the nucleus. The replication of the LLO strain within the J774A.1 cells indicated that replication may need to be controlled to optimize the EES interaction with macrophages. However, when BMDMs were used as the host cells to demonstrate translatability to primary macrophages, the replication of the LLO strain was regulated by the BMDMs and minimally impacted BMDM viability (~95% viable). Notwithstanding, *B. subtilis* LLO still gained access to the cytoplasm of BMDMs with

IPTG induction of LLO expression and remained viable to deliver TFs as shown by replication that occurred before destruction. Even with destruction by LC3 related autophagy mechanisms[4–7], the bacteria persisted for several hours which provided time for TF delivery. Furthermore, the natural removal of the bacteria indicated safety of the EES platform. However, if further interaction between the host cell and engineered *B. subtilis* LLO strains is necessary for an application, proteins such as phospholipases (plc) A and B from *L. monocytogenes* could be introduced into the *B. subtilis* LLO chassis to evade the autophagy mechanisms[7] but replication would need to be considered. The uptake rate into BMDMs was substantially less than the J774A.1 cells as only 35% of BMDMs were positive for the bacteria compared to 99% of J774A.1 cells. Nonetheless, the results from the interaction between the TF strains and the BMDMs indicated that the population function was adjusted by the TF strains and the pilot *in vivo* work showed promising trends.

The TFs were produced and delivered by *B. subtilis* TF strains even within 4 h of incubation with the host cells which resulted in higher levels of these TFs in the nuclei than levels produced by the known signal cascade inducers (IFN-γ and LPS[8–11]; IL-4 and IL-13[12,13]). Accordingly, this result demonstrated the potential of the TF strains to impact host cell function within the 3 h timeframe of interaction between the bacteria and host cells. As a result, cell surface marker expression of J774A.1 cells and BMDMs was measured because marker expression is commonly used to differentiate macrophage phenotype[14,15]. Cell surface expression levels in J774A.1 cells of CD86 and CD206 were altered by the LLO-*SK* and LLO-*KG* strains and CD206 expression was regulated as expected based on the known activity of the expressed TFs even though CD206 has been shown to recognize the surface carbohydrates of pathogens and be triggered by proteases produced by *B. subtilis*[16,17]. CD86 response was more complex as it is expected to be upregulated as a general response to bacteria but by 48 h the LLO-*SK* strain had increased expression significantly compared to the

LLO strain which indicated TF specificity. On the contrary, BMDMs marker expression exhibited only minor shifts from the bacterial treatments but especially strong responses to the characterized controls for increasing these markers. The TF strains did not increase or decrease CD86 marker expression in comparison to untreated BMDMs and CD206 was increased by the strains but only at 24 h. The lack of CD86 expression in response to the non-pathogenic *B. subtilis* LLO from the BMDMs was unexpected because Toll-like receptor 2 (TLR2) triggers inflammatory responses[18,19] but a similar lack of CD86 and CD206 marker expression has been observed when bacterial TLR agonists were used to stimulate initially resting BMDMs[20]. Yet, the CD206 expression response was a bit more complex. CD206 is the mannose binding receptor[21–23] which explains the increase seen in the mannose treatment conditions and acts as a receptor for bacterial surface carbohydrates[17]. Even with the complexity in the surface marker response, the TF strains differentially regulated CD86 and CD206 expression in J774A.1 cells and LLO-*KG* was the one strain that caused a significant increase in CD206 expression compared to the untreated in the treatments without D-mannose in BMDMs. CD206 has been recently implicated in promoting innate and adaptive antitumor immune responses when expressed by TAMs which suggests translatability for the LLO-*KG* strain[21].

Cytokines and chemokines play essential roles in signaling between various immune cell populations[24–27]. These proteins have been categorized based on roles in disease progression and for classifying macrophages[14,15,28] but with further evaluation, these proteins have been shown to exhibit pleiotropic effects in diseases progression and in cell classification[29–37]. Furthermore, complex stimuli such as live bacteria compounds with the pleiotropic effects to create unexpected responses from macrophages which makes the macrophage phenotype and function difficult to classify[28,38]. Yet, unraveling this complexity provides valuable insight into outcomes *in vivo* and understanding therapeutic potential. The TF strains stimulated production

of many disease especially tumor relevant cytokines and chemokines from the macrophages with the TFs causing specific regulations. The bacterial treatments stimulated production of most of the cytokines and chemokines analyzed and generated a higher protein production than the positive controls, conversely of the surface markers[26,39,40], indicating the signaling response from the macrophages to the bacteria[41,42]. The TF strains impacted the J774A.1 cells and BMDMs cytokine and chemokine expression in predictable and unexpected ways based on activity of the TFs. For example, the upregulation of IL-10 by LLO-*KG* and down regulation by LLO-*SK* was an expected result along with G-CSF being downregulated by LLO-*SK* which occurred in both the J774A.1 cells and BMDMs[8,12,43,44]. Additionally, other predicted results which occurred in the BMDM characterization include when LLO-*KG* upregulated IL-6 at 24 h which is a predicted result based on the known activity of KLF4[45] and MCP-1 was downregulated by LLO-*SK* which is predicted based on the known regulation by NF-κB and STAT-1 can compete with these pathways[46,47]. However, in some cases there were results that were not anticipated, and the pleiotropic effects of each selected TF need to be considered. The change in IL-12p40 levels was an example of an unexpected result but after further searching it has been shown that the IL-12p40 promoter has a canonical GATA binding site which could explain the increase measured in the LLO-*KG* treatments in both J774A.1 cells and BMDMs[48]. Some unexpected results were shown to be host cell specific. LLO-*SK* downregulated TNF-α in the J774A.1 cells which was unexpected but could be explained by TNF-α being regulated by NF-κB[49–51] but upregulated the cytokine in BMDMs which was expected and could be useful in altering the TME[52,53]. This result epitomized that most of the unexpected results occurred in the J774A.1 cells compared to the BMDMs which had reproducibly predictable results. This emphasized the importance of transitioning from the cell line to the primary cells especially when determining potential impact on the TME. D-mannose did regulate some of the cytokines and chemokines independently of the bacterial treatments as demonstrated in IL-1β[54,55] in J774A.1 cells and MCP-1/MIP-2 in BMDMs which indicated that metabolism should be studied.

Overall, the engineered *B. subtilis* LLO strains generated production of beneficial cytokines and chemokines for altering the TME including TNF-α and IL-12p40[52,53,56]. Yet, the pleiotropic effects of some cytokines and chemokines adds ambiguity to whether others may also be beneficial. Two specific examples are IL-6 and MCP-1 because both are implicated in promoting immune cells such as T cells to invade the TME but can also promote tumor angiogenesis when expressed by cancer cells[46,57]. Some cytokines and chemokines such as MIP-1α, MIP-2, G-CSF and IL-10 are implicated in promoting poor outcomes in tumors when produced by TAMs or other cells so the downregulation by LLO-*SK* is beneficial[44,58–61]. Therefore, the LLO-*SK* strain appeared to be the better strain for altering the TME, but the LLO-*KG* still produced beneficial cytokines and chemokines for this application. Nonetheless, D-mannose indicated the important role of metabolism as mentioned above and the cytokines and chemokines are only one component in altering the TME so other analyses such as functional metabolism was necessary.

With the complexities seen in marker and cytokine/chemokine expression and impact from D-mannose, functional metabolism provides another measure of macrophage phenotype in response to the TF strains and D-mannose that is relevant *in vivo*. In totality, the bacterial treatments caused increases in metabolism and the Warburg effect[62–69] similar to that of the LPS treatment at 12 h post bacterial treatment. The LLO-*KG* strain promoted the most significant shift in metabolism with increased OCR, ECAR and ATP production because both TFs are associated with IL-4 cascades and work with STAT-6 to induce PPARγ causing mitochondrial biogenesis. This results in increased OCR and ATP production and a major reduction in OCR if electron transport inhibitors were added[12,70–73]. Accordingly, the LLO-*KG* strain had the most significant reduction in OCR when Rotenone/AA (complex I and complex III inhibitors[74]) were added. ECAR was increased most significantly by the LLO-*KG* treatments in comparison to the untreated which is directed by the increase in glycolysis that is synergistic

with mitochondrial biogenesis as a response to the bacteria[70]. When the inhibitors Rotenone/AA were added, differential change in ECAR between LLO-*SK* and LLO-*KG* was observed at 12 h which indicated that STAT-1 and KLF6 promoted the electron transport chain running in reverse electron flow as seen in classical pro-inflammatory macrophages because of a positive loss in ECAR[73,75]. D-mannose also caused the same positive loss in ECAR after Rotenone/AA addition at 12 h because D-mannose contributes to lactate production in macrophages[55] and significantly reduced OCR, ECAR and ATP production with a significant shift towards glycolysis (except in LLO-*KG* condition) at 24 h which demonstrated the potency of D-mannose in altering macrophage function. TAMs have been shown to enhance tumor progression through metabolic measures[70,73,76] and therapeutic measures have been proposed to increase PPARγ induction to cause increased phagocytic activity of TAMs which the LLO-*KG* strain directed[70,73,76]. However, TAM metabolism is understudied, and complex so further studies are needed to understand the ideal target to adjust TAM metabolism[70,73,76]. These observations from the *in vitro* functional metabolism analyses continued to underscore the complexity of macrophage response. Nonetheless, the functional assays established that the engineered *B. subtilis* LLO strains modulated macrophage function. Yet, on-going RNA-seq analysis will further reinforce changes seen in functional assays and provide an in-depth characterization of gene expression changes caused by the TF delivering strains compared to controls.

After in-depth characterization of the engineered *B. subtilis* LLO strains interaction with and specific modulation of BMDMs, the translatability of the strains in mobilizing the immune system to alter the TME was tested. The non-pathogenic LLO-*lux* strain was observed to be cleared from healthy mice within 24 h but persisted in tumor bearing mice specifically within the tumors for a week post injection IV which established the potential for the engineered *B. subtilis* LLO strains to be utilized to alter the TME. Injection methods of IV and IT were compared because of the efficacy shown in previous studies from IT injection[77–80] but IV added an

additional measure of translatability by showing *B. subtilis* accumulates wherever the TME is located. Tumor growth stabilization materialized in the LLO-*KG* treatments especially post the second bacterial injection with some indication of tumor regression in the few days immediately after injection without any negative effects on overall health, but the LLO-*lux* strain did not produce the same result which signaled strain specificity. Additionally, the D-mannose treatment appeared to stabilize tumor growth (n=2) which has been observed in previous studies[81,82]. The dissociated tumors from the bacterial treatments exhibited shifts in tumor metabolism and immunophenotyping. The bacterial treatments reduced OCR and accordingly reduced ATP production, max respiration and spare capacity while the D-mannose treatment sustained or increased these properties compared to the untreated which may indicate a shift to glycolysis in the heterogenous TME caused by the bacteria. However, the LLO-*KG* IV treatment was the only treatment that potentially increased glycolysis (ECAR increased) while the other bacterial treatments also reduced ECAR. Carcinoma cell metabolism is classically discussed as being driven by glycolysis, but this is largely in homogeneous cell culture. In fact, several studies on subtypes of carcinoma especially breast cancer show a reliance on oxidative phosphorylation[83–85]. As a result, the LLO-*KG* IV could have caused a shift to glycolysis at the population level because immune cells were stimulated to invade and the immunophenotyping begins to support this hypothesis. The LLO-*KG* IV also was the most beneficial treatment based on immunophenotyping as total immune cells increased by 15% and had higher expression of CD45 which has shown to indicate activated immune cells[86–88] compared to all other treatments. T cells (CD3+) were a significant portion of these immune cells with the population being largely naïve T cell (CD4+) but a significant portion of the CD3+ were also beneficial tumor disrupting cytotoxic T cells[89–93] that highly expressed CD8α. The LLO-*KG* IV treatment also increased dendritic cells which would be beneficial for altering the TME by activating T cells and increasing innate and adaptive immune responses[94–96]. The D-mannose treatment also increased immune cells especially T cells which provides insight on how D-mannose alone alters the TME and

contributes to tumor regression seen previously[81,82]. While these markers provide substantial insight into the TME alteration, further markers are being optimized to provide further insights into immune cell invasion and ratio of immune cells to 4T1 cells present in the TME. Altogether the engineered *B. subtilis* LLO strains altered the TME in the pilot study due to strain specificity as the different strains and delivery method did not impact the number of bacteria present in the tumors. Yet, a final study will be necessary to test efficacy from both LLO-*SK* and LLO-*KG* on tumor growth stabilization, alteration of TME by characterizing more immune cell populations by flow cytometry and repeating functional metabolism analysis. Furthermore, these expansions on EES *in vivo* studies will be performed with increased numbers of mice for each treatment and expanding conditions to include all bacterial treatments without D-mannose to understand the role of the sugar in the TME as seen in the pilot study especially in tumor growth stabilization. Also, more thorough safety characterization will be performed by determining if there are negative repercussions on the liver with all bacteria passing through this organ.

Improved transcriptional control of the EES is necessary for advancement of the platform especially when used for *in vivo* applications. The increased complexity caused by using D-mannose as a transcriptional inducer was accounted for by controls and appeared to be potentially beneficial for altering TME as shown previously[81,82]. Yet, using a transcriptional inducer that increased complexity and diffused throughout the entire mouse is not sustainable for further translation of the EES. Using thermal energy that can be localized to specific regions and be limited in impact on host cells provides several advantages. The magnetothermal control demonstrated by using the TlpA39 regulatory system in *B. subtilis* to respond to thermal energy generated when an AMF was applied to SPION coated *B. subtilis* took the first step towards a method of controlling the EES non-invasively and in a localized region *in vivo*. The TlpA39 promoter and regulator system was functional in *B. subtilis* and able to regulate an operon with a slight temperature shift from what was observed in *Escherichia coli* previously[97] which was

demonstrated by increased bioluminescence and transcript levels when heated in a thermocycler. Though, the TlpA39 promoter and regulator system could be further optimized in *B. subtilis* as was done previously in *E. coli*[97] and *B. subtilis*[98]. Further optimization by directed mutagenesis[97,98] or other measures could improve the P_{TlpA39} genetic switch to have a more stringent on/off state which would improve responses during magnetothermal heating studies.

When transitioning to magnetothermal heating, an approach was needed to facilitate thermal energy release when an AMF was applied. Accordingly, the SPION coatings provided the solution which was confirmed by SEM-EDS. The variations coated *B. subtilis* in different ways, but these observations were explainable by the DLVO (Derjaguin–Landau–Verwey–Overbeek) theory which has been shown to predict the potential interaction between a given nanoparticle and bacteria[99,100]. Culminating the observed coating of the variations with the response of the bacteria to magnetothermal heating and heating of the culture medium, the plain-dextran SPION showed the most promise for reproducible localized heating that could be used *in vivo*. Magnetothermal energy over 12 h showed significant increase in reporter output but this change is still substantially less than that of the continuous heating in a thermocycler and this result is even more clear after only 1 h of heating. Therefore, the thermal energy diffusion from the SPIONs to *B. subtilis* needs to be improved because the 1 h of continuous heating demonstrated that the TSRs can produce a significant amount of transcription leading to a change in bioluminescence signal even within the constraints for small animal anesthesia[101,102]. An immediate change that could enhance the magnetic hyperthermia is increasing the RF amplitude beyond the limitations of the HYPER system (>16.0 mT). However, an increase in RF amplitude will result in an increase in specific absorption rate (SAR)[103], this would have to be further studied to prevent any biological effects. Another option is considering more variations of SPIONs that have been modified to improve magnetic hyperthermia

properties[104–107]. Accordingly, these variations should be investigated for efficient coating of *B. subtilis* and improved magnetic hyperthermia after exposure to AMF.

The Perls' Prussian Blue staining[108] and modified Gram stain[109] demonstrated the presence of iron and *B. subtilis* at the same location, which provides the opportunity to utilize magnetic hyperthermia to control *B. subtilis* transcription *in vivo.* As mentioned above, further tuning of the genetic elements and characterizing the interaction of improved particles for magnetic hyperthermia with *B. subtilis* would enhance further *in vivo* studies. Other coatings of SPIONs such as with polymers, small molecules, lipids and composites can increase stability, water solubility and biocompatibility[105]. For example, Fe_3O_4-oleic acid-Na-oleate nanoparticles[107] increased stability in a transplanted carcinoma model and polycaprolactone-coated superparamagnetic iron oxide nanoparticles synthesized with a micellular conformation were used to increase cytocompatibility and thermosensitivity as a cancer therapy[105]. Additionally, increasing RF amplitude in accordance with SAR requirements[103] and amount of iron associating with the bacteria could improve heating along with imaging properties *in vivo*. Yet, increases in bioluminescence were observed after AMF treatment with only ~1 ppm of Fe in the plain-dextran coated condition *in vitro*. This reduced the amount of Fe that is delivered compared to other typical magnetic hyperthermia applications, such as for tumor ablation[110], from 1 mg/cm^3 to 13.6 ng/cm^3. Accordingly, the bacteria act as a carrying mechanism for and a responsive mechanism to SPIONs where minimal SPIONs are needed to produce a desired therapeutic outcome through controlling bacteriotherapies. Alternatively, other heating mechanisms could be used for magnetic hyperthermia such as ultrasound which was been shown previously[97,111,112] that could be paired with the SPION coated *B. subtilis* strategy. Overall, the demonstration of magnetothermal control of *B. subtilis* transcription advances the translatability of the EES platform by increasing control of bacteria through a non-invasive measure during *in vivo* applications.

The EES platform and further advancements on transcriptional control creates a new approach for intracellular communication with mammalian host cells to articulate function towards therapeutic outcomes. Even with the complexities in regulation of macrophage phenotype which were encountered, the TF strains produced predictable outcomes based on characterized activity of the TFs but also demonstrated that there are limitations in understanding regulatory networks within macrophages. More TF pairings should be constructed to optimize response of the macrophages for targeted applications such as cancer treatment and to further fundamental understanding of macrophage function and regulation. Alternatively, the EES could also be designed as a delivery method for CRISPR-Cas9[113,114] which could improve the modulation of cell fates. Yet, the demonstration of predictable outcomes and generating rapid, potent responses from the macrophages, which has been characterized by low efficacy and lack of innate control previously[115], shows advantages over current methods[116]. Ultimately, the EES technology creates a new modular approach to altering macrophage function that can be used in human health applications.

REFERENCES

REFERENCES

1. Epelman, S., Lavine, K. J. & Randolph, G. J. Origin and Functions of Tissue Macrophages. *Immunity* **41**, 21–35 (2014).

2. Bielecki, J., Youngman, P., Connelly, P. & Portnoy, D. A. Bacillus subtilis expressing a haemolysin gene from Listeria monocytogenes can grow in mammalian cells. *Nature* (1990).

3. Portnoy, D. A., Tweten, R. K., Kehoe, M. & Bielecki, J. Capacity of listeriolysin O, streptolysin O, and perfringolysin O to mediate growth of Bacillus subtilis within mammalian cells. *Infect. Immun.* (1992).

4. Deretic, V., Saitoh, T. & Akira, S. Autophagy in infection, inflammation and immunity. *Nat. Rev. Immunol.* **13**, 722–737 (2013).

5. G., B. B. *et al.* Inflammasome Components Coordinate Autophagy and Pyroptosis as Macrophage Responses to Infection. *MBio* **4**, e00620-12 (2013).

6. Levine, B., Mizushima, N. & Virgin, H. W. Autophagy in immunity and inflammation. *Nature* **469**, 323–335 (2011).

7. Siqueira, M. da S., Ribeiro, R. de M. & Travassos, L. H. Autophagy and Its Interaction with Intracellular Bacterial Pathogens. *Front. Immunol.* **9**, 935 (2018).

8. VanDeusen, J. B. *et al.* STAT-1-mediated repression of monocyte interleukin-10 gene expression in vivo. *Eur. J. Immunol.* **36**, 623–630 (2006).

9. Date, D. *et al.* Kruppel-like transcription factor 6 regulates inflammatory macrophage polarization. *J. Biol. Chem.* (2014).

10. Li, H., Jiang, T., Li, M. Q., Zheng, X. L. & Zhao, G. J. Transcriptional regulation of macrophages polarization by microRNAs. *Frontiers in Immunology* (2018).

11. Mogensen, T. H. IRF and STAT transcription factors - From basic biology to roles in infection, protective immunity, and primary immunodeficiencies. *Frontiers in Immunology* (2019).

12. Liao, X. *et al.* Krüppel-like factor 4 regulates macrophage polarization. *J. Clin. Invest.* (2011).

13. Yang, M. *et al.* Deficiency of GATA3-Positive Macrophages Improves Cardiac Function Following Myocardial Infarction or Pressure Overload Hypertrophy. *J. Am. Coll. Cardiol.* (2018).

14. Martinez, F. O., Sica, A., Mantovani, A. & Locati, M. Macrophage activation and polarization. *Frontiers in Bioscience* (2008).

15. Mantovani, A. *et al.* The chemokine system in diverse forms of macrophage activation and polarization. *Trends Immunol.* **25**, 677–686 (2004).

16. Corvey, C., Stein, T., Düsterhus, S., Karas, M. & Entian, K.-D. Activation of subtilin precursors by Bacillus subtilis extracellular serine proteases subtilisin (AprE), WprA, and Vpr. *Biochem. Biophys. Res. Commun.* **304**, 48–54 (2003).

17. Stahl, P. D. & Ezekowitz, R. A. B. The mannose receptor is a pattern recognition receptor involved in host defense. *Curr. Opin. Immunol.* **10**, 50–55 (1998).

18. Ryu, Y. H. *et al.* Differential immunostimulatory effects of Gram-positive bacteria due to their lipoteichoic acids. *Int. Immunopharmacol.* **9**, 127–133 (2009).

19. Moreira, L. O. *et al.* The TLR2-MyD88-NOD2-RIPK2 signalling axis regulates a balanced pro-inflammatory and IL-10-mediated anti-inflammatory cytokine response to Gram-positive cell walls. *Cell. Microbiol.* **10**, 2067–2077 (2008).

20. Holden, J. A. *et al.* Porphyromonas gingivalis lipopolysaccharide weakly activates M1 and M2 polarized mouse macrophages but induces inflammatory cytokines. *Infect. Immun.* **82**, 4190–4203 (2014).

21. M., J. J. *et al.* Mannose receptor (CD206) activation in tumor-associated macrophages enhances adaptive and innate antitumor immune responses. *Sci. Transl. Med.* **12**, eaax6337 (2020).

22. García-González, G. *et al.* Triggering of protease-activated receptors (PARs) induces alternative M2 macrophage polarization with impaired plasticity. *Mol. Immunol.* **114**, 278–288 (2019).

23. Leber, N. *et al.* α-Mannosyl-Functionalized Cationic Nanohydrogel Particles for Targeted Gene Knockdown in Immunosuppressive Macrophages. *Macromol. Biosci.* **19**, e1900162 (2019).

24. Turner, M. D., Nedjai, B., Hurst, T. & Pennington, D. J. Cytokines and chemokines: At the crossroads of cell signalling and inflammatory disease. *Biochim. Biophys. Acta - Mol. Cell Res.* **1843**, 2563–2582 (2014).

25. Kuhn, M. & Goebel, W. Induction of cytokines in phagocytic mammalian cells infected with virulent and avirulent Listeria strains. *Infect. Immun.* **62**, 348–356 (1994).

26. Murtaugh, M. P. & Foss, D. L. Inflammatory cytokines and antigen presenting cell activation. *Vet. Immunol. Immunopathol.* **87**, 109–121 (2002).

27. Zhang, X. & Mosser, D. M. Macrophage activation by endogenous danger signals. *Journal of Pathology* (2008).

28. Smith, T. D., Tse, M. J., Read, E. L. & Liu, W. F. Regulation of macrophage polarization and plasticity by complex activation signals. *Integr. Biol. (Camb).* **8**, 946–955 (2016).

29. Wang, L., Zhang, S., Wu, H., Rong, X. & Guo, J. M2b macrophage polarization and its roles in diseases. *J. Leukoc. Biol.* **106**, 345–358 (2019).

30. Graves, D. T. The potential role of chemokines and inflammatory cytokines in periodontal disease progression. *Clin. Infect. Dis.* **28**, 482–490 (1999).

31. Domingues, C., AB da Cruz e Silva, O. & Henriques, A. Impact of cytokines and chemokines on Alzheimer's disease neuropathological hallmarks. *Curr. Alzheimer Res.* **14**, 870–882 (2017).

32. Chatzigeorgiou, A. *et al.* The pattern of inflammatory/anti-inflammatory cytokines and chemokines in type 1 diabetic patients over time. *Ann. Med.* **42**, 426–438 (2010).

33. Tanaka, T. *et al.* Chemokines in tumor progression and metastasis. *Cancer Sci.* **96**, 317–322 (2005).

34. Ben-Baruch, A. Host microenvironment in breast cancer development: inflammatory cells, cytokines and chemokines in breast cancer progression: reciprocal tumor–microenvironment interactions. *Breast cancer Res.* **5**, 1–6 (2002).

35. Raman, D., Baugher, P. J., Thu, Y. M. & Richmond, A. Role of chemokines in tumor growth. *Cancer Lett.* **256**, 137–165 (2007).

36. Ramesh, G., MacLean, A. G. & Philipp, M. T. Cytokines and chemokines at the crossroads of neuroinflammation, neurodegeneration, and neuropathic pain. *Mediators Inflamm.* **2013**, 480739 (2013).

37. Pathria, P., Louis, T. L. & Varner, J. A. Targeting Tumor-Associated Macrophages in Cancer. *Trends Immunol.* **40**, 310–327 (2019).

38. Benoit, M., Desnues, B. & Mege, J.-L. Macrophage Polarization in Bacterial Infections. *J. Immunol.* **181**, 3733 LP – 3739 (2008).

39. Foss, D. L., Zilliox, M. J. & Murtaugh, M. P. Differential regulation of macrophage interleukin-1 (IL-1), IL-12, and CD80-CD86 by two bacterial toxins. *Infect. Immun.* **67**, 5275–5281 (1999).

40. Bromander, A., Holmgren, J. & Lycke, N. Cholera toxin stimulates IL-1 production and enhances antigen presentation by macrophages in vitro. *J. Immunol.* **146**, 2908–2914 (1991).

41. Udayan, S. *et al.* Macrophage cytokine responses to commensal Gram-positive Lactobacillus salivarius strains are TLR2-independent and Myd88-dependent. *Sci. Rep.* **11**, 1–16 (2021).

42. Zhou, Q., Desta, T., Fenton, M., Graves, D. T. & Amar, S. Cytokine profiling of macrophages exposed to Porphyromonas gingivalis, its lipopolysaccharide, or its FimA protein. *Infect. Immun.* **73**, 935–943 (2005).

43. Rőszer, T. Understanding the Mysterious M2 Macrophage through Activation Markers and Effector Mechanisms. *Mediators Inflamm.* **2015**, 816460 (2015).

44. Martins, A., Han, J. & Kim, S. O. The multifaceted effects of granulocyte colony-stimulating factor in immunomodulation and potential roles in intestinal immune homeostasis. *IUBMB Life* **62**, 611–617 (2010).

45. Rosenzweig, J. M., Glenn, J. D., Calabresi, P. A. & Whartenby, K. A. KLF4 modulates expression of IL-6 in dendritic cells via both promoter activation and epigenetic modification. *J. Biol. Chem.* **288**, 23868–23874 (2013).

46. Deshmane, S. L., Kremlev, S., Amini, S. & Sawaya, B. E. Monocyte chemoattractant protein-1 (MCP-1): an overview. *J. Interf. cytokine Res. Off. J. Int. Soc. Interf. Cytokine Res.* **29**, 313–326 (2009).

47. Sutcliffe, A. M. *et al.* Transcriptional regulation of monocyte chemotactic protein-1 release by endothelin-1 in human airway smooth muscle cells involves NF-kappaB and AP-1. *Br. J. Pharmacol.* **157**, 436–450 (2009).

48. Becker, C. *et al.* Regulation of IL-12 p40 Promoter Activity in Primary Human Monocytes: Roles of NF-κB, CCAAT/Enhancer-Binding Protein β, and PU.1 and Identification of a Novel Repressor Element (GA-12) That Responds to IL-4 and Prostaglandin E₂ *J. Immunol.* **167**, 2608 LP – 2618 (2001).

49. Ramana, C. V, Chatterjee-Kishore, M., Nguyen, H. & Stark, G. R. Complex roles of Stat1 in regulating gene expression. *Oncogene* **19**, 2619–2627 (2000).

50. Samuel, T. *et al.* Control of specificity and magnitude of NF-κB and STAT1-mediated gene activation through PIASy and PIAS1 cooperation. *Proc. Natl. Acad. Sci.* **104**, 11643–11648 (2007).

51. Falvo, J. V, Tsytsykova, A. V & Goldfeld, A. E. Transcriptional control of the TNF gene. *Curr. Dir. Autoimmun.* **11**, 27–60 (2010).

52. Laha, D., Grant, R., Mishra, P. & Nilubol, N. The role of tumor necrosis factor in manipulating the immunological response of tumor microenvironment. *Front. Immunol.* **12**, 656908 (2021).

53. Kenny, P. A., Lee, G. Y. & Bissell, M. J. Targeting the tumor microenvironment. *Front. Biosci. a J. virtual Libr.* **12**, 3468 (2007).

54. O'Neill, L. A. J. & Pearce, E. J. Immunometabolism governs dendritic cell and macrophage function. *J. Exp. Med.* **213**, 15–23 (2015).

55. Torretta, S. *et al.* D-mannose suppresses macrophage IL-1β production. *Nat. Commun.* **11**, 6343 (2020).

56. Kanemaru, H. *et al.* Antitumor effect of Batf2 through IL-12 p40 up-regulation in tumor-associated macrophages. *Proc. Natl. Acad. Sci.* **114**, E7331 LP-E7340 (2017).

57. Chonov, D. C., Ignatova, M. M. K., Ananiev, J. R. & Gulubova, M. V. IL-6 Activities in the Tumour Microenvironment. Part 1. *Open access Maced. J. Med. Sci.* **7**, 2391–2398 (2019).

58. Bhavsar, I., Miller, C. S. & Al-Sabbagh, M. Macrophage Inflammatory Protein-1 Alpha (MIP-1 alpha)/CCL3: As a Biomarker. *General Methods in Biomarker Research and their Applications* 223–249 (2015).

59. Hu, J. *et al.* Regulation of tumor immune suppression and cancer cell survival by CXCL1/2 elevation in glioblastoma multiforme. *Sci. Adv.* **7**, eabc2511 (2021).

60. Burke, S. J. *et al.* NF-κB and STAT1 control CXCL1 and CXCL2 gene transcription. *Am. J. Physiol. Endocrinol. Metab.* **306**, E131-49 (2014).

61. Laoui, D. *et al.* Tumor-associated macrophages in breast cancer: Distinct subsets, distinct functions. *Int. J. Dev. Biol.* (2011).

62. Liu, Y. *et al.* Metabolic reprogramming in macrophage responses. *Biomark. Res.* **9**, 1–17 (2021).

63. Liu, D. *et al.* Comprehensive proteomics analysis reveals metabolic reprogramming of tumor-associated macrophages stimulated by the tumor microenvironment. *J. Proteome Res.* **16**, 288–297 (2017).

64. Errea, A. *et al.* Lactate inhibits the pro-inflammatory response and metabolic reprogramming in murine macrophages in a GPR81-independent manner. *PLoS One* **11**, e0163694 (2016).

65. Kelly, B. & O'neill, L. A. Metabolic reprogramming in macrophages and dendritic cells in innate immunity. *Cell Res.* **25**, 771–784 (2015).

66. Galván-Peña, S. & O'Neill, L. A. J. Metabolic reprograming in macrophage polarization. *Front. Immunol.* **5**, 420 (2014).

67. Blagih, J. & Jones, R. G. Polarizing macrophages through reprogramming of glucose metabolism. *Cell Metab.* **15**, 793–795 (2012).

68. Lorenz, M. C., Bender, J. A. & Fink, G. R. Transcriptional response of Candida albicans upon internalization by macrophages. *Eukaryot. Cell* **3**, 1076–1087 (2004).

69. Ip, W. K. E., Hoshi, N., Shouval, D. S., Snapper, S. & Medzhitov, R. Anti-inflammatory effect of IL-10 mediated by metabolic reprogramming of macrophages. *Science (80-.).* **356**, 513–519 (2017).

70. Wculek, S. K., Dunphy, G., Heras-Murillo, I., Mastrangelo, A. & Sancho, D. Metabolism of tissue macrophages in homeostasis and pathology. *Cell. Mol. Immunol.* **19**, 384–408 (2022).

71. Huang, S. C.-C. *et al.* Cell-intrinsic lysosomal lipolysis is essential for alternative activation of macrophages. *Nat. Immunol.* **15**, 846–855 (2014).

72. Viola, A., Munari, F., Sánchez-Rodríguez, R., Scolaro, T. & Castegna, A. The Metabolic Signature of Macrophage Responses. *Front. Immunol.* **10**, (2019).

73. Diskin, C. & Pålsson-McDermott, E. M. Metabolic Modulation in Macrophage Effector Function. *Front. Immunol.* **9**, 270 (2018).

74. Wang, L. *et al.* Mitochondrial Respiratory Chain Inhibitors Involved in ROS Production Induced by Acute High Concentrations of Iodide and the Effects of SOD as a Protective Factor. *Oxid. Med. Cell. Longev.* **2015**, 217670 (2015).

75. Mookerjee, S. A., Gerencser, A. A., Nicholls, D. G. & Brand, M. D. Quantifying intracellular rates of glycolytic and oxidative ATP production and consumption using extracellular flux measurements. *J. Biol. Chem.* **292**, 7189–7207 (2017).

76. Rabold, K., Netea, M. G., Adema, G. J. & Netea-Maier, R. T. Cellular metabolism of tumor-associated macrophages–functional impact and consequences. *FEBS Lett.* **591**, 3022–3041 (2017).

77. Hong, E.-H. *et al.* Intratumoral injection of attenuated Salmonella vaccine can induce tumor microenvironmental shift from immune suppressive to immunogenic. *Vaccine* **31**, 1377–1384 (2013).

78. Chien, T. *et al.* Enhancing the tropism of bacteria via genetically programmed biosensors. *Nat. Biomed. Eng.* **6**, 94–104 (2022).

79. Din, M. O. *et al.* Synchronized cycles of bacterial lysis for in vivo delivery. *Nature* **536**, 81–85 (2016).

80. Harimoto, T. *et al.* A programmable encapsulation system improves delivery of therapeutic bacteria in mice. *Nat. Biotechnol.* (2022).

81. Gonzalez, P. S. *et al.* Mannose impairs tumour growth and enhances chemotherapy. *Nature* **563**, 719–723 (2018).

82. Liu, Q., Li, X., Zhang, H. & Li, H. Mannose Attenuates Colitis-Associated Colorectal Tumorigenesis by Targeting Tumor-Associated Macrophages. *J. cancer Prev.* **27**, 31 (2022).

83. Martinez-Outschoorn, U. E., Sotgia, F. & Lisanti, M. P. Power surge: supporting cells "fuel" cancer cell mitochondria. *Cell Metab.* **15**, 4–5 (2012).

84. Whitaker-Menezes, D. *et al.* Hyperactivation of oxidative mitochondrial metabolism in epithelial cancer cells in situ: visualizing the therapeutic effects of metformin in tumor tissue. *Cell cycle* **10**, 4047–4064 (2011).

85. Martinez-Outschoorn, U., Sotgia, F. & Lisanti, M. P. Tumor Microenvironment and Metabolic Synergy in Breast Cancers: Critical Importance of Mitochondrial Fuels and Function. *Semin. Oncol.* **41**, 195–216 (2014).

86. Brandenburg, S. *et al.* Myeloid cells expressing high level of CD45 are associated with a distinct activated phenotype in glioma. *Immunol. Res.* **65**, 757–768 (2017).

87. Krzywinska, E. *et al.* CD45 isoform profile identifies natural killer (NK) subsets with differential activity. *PLoS One* **11**, e0150434 (2016).

88. Petkov, S. *et al.* High CD45 expression of CD8+ and CD4+ T cells correlates with the size of HIV-1 reservoir in blood. *Sci. Rep.* **10**, 20425 (2020).

89. Hadrup, S. & Donia, M. Effector CD4 and CD8 T cells and their role in the tumor microenvironment. *Cancer Microenviron.* **6**, 123–133 (2013).

90. Jiang, Y., Li, Y. & Zhu, B. T-cell exhaustion in the tumor microenvironment. *Cell Death Dis.* **6**, e1792–e1792 (2015).

91. Ock, C.-Y. *et al.* Pan-Cancer Immunogenomic Perspective on the Tumor Microenvironment Based on PD-L1 and CD8 T-Cell InfiltrationTumor Microenvironment Immune Type in Pan-Cancer. *Clin. cancer Res.* **22**, 2261–2270 (2016).

92. Yang, L., Pang, Y. & Moses, H. L. TGF-β and immune cells: an important regulatory axis in the tumor microenvironment and progression. *Trends Immunol.* **31**, 220–227 (2010).

93. Dhodapkar, M. V, Krasovsky, J. & Olson, K. T cells from the tumor microenvironment of patients with progressive myeloma can generate strong, tumor-specific cytolytic responses to autologous, tumor-loaded dendritic cells. *Proc. Natl. Acad. Sci.* **99**, 13009–13013 (2002).

94. Guiducci, C., Vicari, A. P., Sangaletti, S., Trinchieri, G. & Colombo, M. P. Redirecting in vivo elicited tumor infiltrating macrophages and dendritic cells towards tumor rejection. *Cancer Res.* **65**, 3437–3446 (2005).

95. Shafer-Weaver, K. A. *et al.* Immunity to murine prostatic tumors: continuous provision of T-cell help prevents CD8 T-cell tolerance and activates tumor-infiltrating dendritic cells. *Cancer Res.* **69**, 6256–6264 (2009).

96. Fu, C. & Jiang, A. Dendritic cells and CD8 T cell immunity in tumor microenvironment. *Front. Immunol.* **9**, 3059 (2018).

97. Piraner, D. I., Abedi, M. H., Moser, B. A., Lee-Gosselin, A. & Shapiro, M. G. Tunable thermal bioswitches for in vivo control of microbial therapeutics. *Nat. Chem. Biol.* **13**, 75–80 (2017).

98. Breitling, R., Sorokin, A. V & Behnke, D. Temperature-inducible gene expression in Bacillus subtilis mediated by the c1857-encoded repressor of bacteriophage lambda. *Gene* **93**, 35–40 (1990).

99. Hwang, G., Ahn, I.-S., Mhin, B. J. & Kim, J.-Y. Adhesion of nano-sized particles to the surface of bacteria: Mechanistic study with the extended DLVO theory. *Colloids Surfaces B Biointerfaces* **97**, 138–144 (2012).

100. Pajerski, W. *et al.* Attachment efficiency of gold nanoparticles by Gram-positive and Gram-negative bacterial strains governed by surface charges. *J. Nanoparticle Res.* **21**, 186 (2019).

101. Albrecht, M., Henke, J., Tacke, S., Markert, M. & Guth, B. Effects of isoflurane, ketamine-xylazine and a combination of medetomidine, midazolam and fentanyl on physiological variables continuously measured by telemetry in Wistar rats. *BMC Vet. Res.* **10**, 198 (2014).

102. Navarro, K. L. *et al.* Mouse Anesthesia: The Art and Science. *ILAR J.* ilab016 (2021).

103. Vander Vorst, A., Rosen, A. & Kotsuka, Y. *RF/Microwave Interaction with Biological Tissues*. *RF/Microwave Interaction with Biological Tissues* (2006).

104. Pucci, C., Degl'Innocenti, A., Gümüş, M. B. & Ciofani, G. Superparamagnetic iron oxide nanoparticles for magnetic hyperthermia: recent advancements, molecular effects, and future directions in the omics era. *Biomater. Sci.* (2022).

105. Hedayatnasab, Z., Dabbagh, A., Abnisa, F. & Wan Daud, W. M. A. Polycaprolactone-coated superparamagnetic iron oxide nanoparticles for in vitro magnetic hyperthermia therapy of cancer. *Eur. Polym. J.* **133**, 109789 (2020).

106. Gupta, R. & Sharma, D. Manganese-Doped Magnetic Nanoclusters for Hyperthermia and Photothermal Glioblastoma Therapy. *ACS Appl. Nano Mater.* **3**, 2026–2037 (2020).

107. Kulikov, O. A. *et al.* Magnetic Hyperthermia Nanoarchitectonics via Iron Oxide Nanoparticles Stabilised by Oleic Acid: Anti-Tumour Efficiency and Safety Evaluation in Animals with Transplanted Carcinoma. *International Journal of Molecular Sciences* vol. 23 (2022).

108. Booth, J. C. The Theory and Practice of Histological Techniques| The Theory and Practice of Histological Techniques. Eds John D. Bancroft & Alan Stevens. Churchill Livingstone, Melbourne. 662 pp. illustrated (some in colour). ISBN 0 443 02006 X. $89, 60. (1983).

109. Becerra, S. C., Roy, D. C., Sanchez, C. J., Christy, R. J. & Burmeister, D. M. An optimized staining technique for the detection of Gram positive and Gram negative bacteria within tissue. *BMC Res. Notes* **9**, 216 (2016).

110. Chan, K. W. & Chou, C. K. Use of thermocouples in the intense fields of ferromagnetic implant hyperthermia. *Int. J. Hyperth.* **9**, 831–848 (1993).

111. Bourdeau, R. W. *et al.* Acoustic reporter genes for noninvasive imaging of microorganisms in mammalian hosts. *Nature* **553**, 86–90 (2018).

112. Abedi, M. H. *et al.* Ultrasound-controllable engineered bacteria for cancer immunotherapy. *Nat. Commun.* **13**, 1–11 (2022).

113. Jakutyte-Giraitiene, L. & Gasiunas, G. Design of a CRISPR-Cas system to increase resistance of Bacillus subtilis to bacteriophage SPP1. *J. Ind. Microbiol. Biotechnol.* **43**, 1183–1188 (2016).

114. Liu, C., Zhang, L., Liu, H. & Cheng, K. Delivery strategies of the CRISPR-Cas9 gene-editing system for therapeutic applications. *J. Control. Release* **266**, 17–26 (2017).

115. Spiller, K. L. & Koh, T. J. Macrophage-based therapeutic strategies in regenerative medicine. *Adv. Drug Deliv. Rev.* **122**, 74–83 (2017).

116. Boehler, R. M. *et al.* Lentivirus delivery of IL-10 to promote and sustain macrophage polarization towards an anti-inflammatory phenotype. *Biotechnol. Bioeng.* **111**, 1210–1221 (2014).